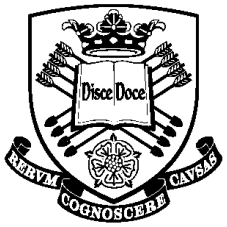

The University Of Sheffield.

Department of Mechanical Engineering

Oil Film Thickness Measurements in Journal Bearings under Normal, Severe & Dynamic Loading Conditions using Ultrasound

Scott **Beamish**

October 2021

Prof Rob Dwyer-Joyce

Thesis submitted to the Department of Mechanical Engineering, University of Sheffield
in partial fulfilment of the requirements for the degree of PhD

[Page intentionally left blank]

Abstract

Journal bearings are found in a staggering variety of systems, from motorcycles to cruise ships. As such, understanding their performance could have a substantial positive impact in many industries. With increased understanding comes the ability to optimise systems, leading to improved efficiencies and reduced emissions.

One key parameter in hydrodynamic journal bearings is the thickness of the lubricant layer at the shaft-bearing interface. Due to the journal bearing's enclosed geometry and the minute thickness of the oil film, typically in the order of 1's to 10's microns, conventional techniques often struggle to provide effective measurements. A promising alternative is the ultrasonic method. Ultrasound has previously been shown to accurately measure thin oil films and furthering this research will allow a greater understanding of the technology's potential.

The aim of this project is to develop new ultrasonic techniques for journal bearing lubricant film thickness measurement under a wide range of operating conditions, including variable load, speed, temperature, alignment and oil type.

To achieve this, two bespoke journal bearing platforms have been designed. The first is a static loading test platform instrumented with ultrasonic transducers embedded within the shaft. Testing under normal operating conditions demonstrated that the combined application of multiple ultrasonic techniques enables accurate circumferential film measurements when compared against a numerical solution. The test platform and ultrasonic method were demonstrated to be highly repeatable, enabling a robust comparison between different lubricant types.

How oil films behave under more severe conditions has also been investigated. Testing under shaft misaligned and offset-loading conditions demonstrated the ability of ultrasound to measure misalignment angle. Results compared against numerical simulations demonstrated the dramatic effect tiny changes in edge film thickness can have on peak pressure. Run-down testing, in which rotation speed was steadily reduced, allowed the system to clearly transition through lubrication regimes. The transition point between the hydrodynamic and mixed regime was found to be viscosity-dependent. Starvation testing showed that by observing changes in signal response at the thick film side of the bearing, the onset of low lubricant supply could be identified earlier than via conventional methods.

The second system is a dynamic loading test platform, with both bearing and shaft mounted ultrasonic transducers. This platform can apply a wide variety of complex loading patterns via a hydraulic power-pack controlled by an electro-proportional programmable valve. The effects of rotation speed and load pattern on oil film rupture and recovery have been studied, with results in good agreement with numerical predictions.

Contents

Acknowledgements

"The self-made man is a myth". These words from bodybuilder turned Hollywood superstar Arnold Schwarzenegger have resonated with me throughout my PhD journey. Without the generosity, help and guidance of so many people, I could not have accomplished anything close to what is presented in this thesis.

First, I would like to thank my supervisor Professor Rob Dwyer-Joyce for allowing me the freedom to explore and to make my own mistakes whilst keeping me from straying too far off the path. Also, to the Engineering and Physical Sciences Research Council for funding this project.

Thank you to the RAs and my fellow PhD students within the Tribology group, particularly C4. Ben, Dave, Jack, John, Rasmus, Royce, Sam, Tom & Will, we did it together!

Also, a special mention to Andrew Hunter, LabVIEW wizard and Henry Brunskill, ultrasonic applications extraordinaire for their patience and expertise. My thanks to all the departmental technical staff. In particular, Dave Butcher, master of rig design and Chris Todd. Also thank you to Henry Dodson for his contribution to the development of the dynamic loading test platform presented in this thesis.

My thanks to Anna for putting up with me through thick and thin, somehow surviving lock-down together. And last but certainly not least my parents, for their love and support even though they still don't quite know what Tribology is.

List of Figures

List of Tables

Acronyms

EHL	Elastohydrodynamic lubrication
FFT	Fast Fourier transform
FPGA	Field programmable gate array
LIF	Laser induced fluorescence
LLS	Limited lubricant supply
NDT	Non destructive testing
PRF	Pulse repetition frequency
PZT	Lead zirconate titanate
SEM	Standard error of the mean
SNR	Signal-to-noise ratio
TCM	Total capacitance method
TDC	Top dead centre
TEHD	Thermo-elastohydrodynamic
TGC	Time gain compensation
ToF	Time of flight
TRM	Total resistance method
TTL	Transistor-transistor logic
UPR	Universal pulser receiver

Nomenclature

α	Pressure-viscosity coefficient (Pa^{-1})
β	Volume concentration ($-$)
$\dot{\gamma}$	Shear rate (s^{-1})
κ	Compessibility (Pa^{-1})
λ	Lambda ratio ($-$)
μ	Dynamic viscosity (Pas)
ν	Poisson's ratio ($-$)
ω	Angular frequency ($rads^{-1}$)
$\overline{W}$	Dimensionless load capacity ($-$)
Φ	Phase shift ($radians$)
ρ	Density (kgm^{-3})
σ	Stress (Pa)
θ	Attitude angle ($^{\circ}$)
ε	Eccentricity ratio ($-$)
B	Bulk modulus (Pa)
C	Radial clearance (m)
c	Speed of sound (ms^{-1})
D	Diameter (m)
E	Elastic modulus (Pa)
f	Frequency (Hz)
h	Film thickness (m)
k	Stiffness (Nm^{-1})
L	Length (m)
m	Resonance mode ($-$)
N	Rotation Speed (Hz)
P	Pressure (Pa)
R	Reflection coefficient ($-$)
r	Radius (m)
R_a	Arithmetic average roughness (m)
R_q	Root mean squared roughness (m)
S	Sommerfeld number ($-$)
T	Temperature ($^{\circ}C$)
t	Time (s)
U	Relative surface velocity (ms^{-1})
V	Approach velocity (ms^{-1})
W	Applied load (N)
z	Acoustic impedance ($Rayl$)

Chapter 1

Introduction

In this chapter, the motivation for investigating film thickness in journal bearings is introduced. This includes the industrial and environmental benefits to film measurements, along with justifications highlighting why further research is required. The aim and objectives of the project are then outlined, followed by an overview of the thesis structure.

1.1 Statement of the Problem

Small improvements on a grand scale can reap tremendous benefits. This philosophy is most famous in the world of sport, such as the concept of marginal gains developed in pro-cycling. However, it is equally applicable in many areas of society including agriculture [1], finance [2], healthcare [3] and, of course, engineering [4].

The specific case that this work tackles is that of journal bearings; a component so common in systems, from bacteria to turbochargers to cruise ships (see Figure 1.1), that a single percent improvement in efficiency, component life or oil consumption can significantly reduce costs and environmental impact. For example, in 2019 Holmberg and Erdemir calculated that passenger cars waste a third of their energy simply overcoming friction [5], approximately 25% of which derives from the main and connecting rod bearings within the engine [6, 7]. They estimate frictional losses can be reduced globally by around 18% in the next 5-10 years, but even just a 1% decrease would save 40 million barrels of oil and lower CO_2 emissions by 16.1 million tonnes per year.

With emissions regulations ever-tightening, automotive manufacturers need to push the efficiency of every component to its limit [8, 9]. This includes the big-end, main and turbocharger bearings, for which optimising oil thickness is critical. Too thick and excess lubricant is sheared unnecessarily, but too thin and the surfaces will not be sufficiently separated, leading to high friction and wear due to surface contact. Thus, a goldilocks zone exists where the film thickness is just right, resulting in optimum efficiency and component life [10]. With improved machining processes and extending knowledge of these systems, automotive manufacturers may carefully reduce film thickness further into the mixed lubrication regime without risking damage and reap the rewards of improved effi-

ciency.

That said, developing our knowledge of journal bearing systems can also enable transformative changes. Public perception is that the primary dangers to the marine environment are plastic pollution, overfishing and oil spills [11, 12, 13]. However, other sources of marine pollution are less prominent but should be equally concerning [14]. For example, Etkin found that the majority of oil entering the oceans derives from intentional day-to-day marine vessel operations [15]. As shown in Figure 1.2, Etkin calculated that 10.3% of all oil input in 2010 originated just from leaking stern tube bearings, up to 28.6 million litres per year. This figure may indeed be much higher as measurements were only obtained in-port and the additional discharge during open-sea operations is unknown.

A potential solution to reduce the impact of stern tube leakage is switching to EALs (Environmentally Acceptable Lubricants) which readily break down in seawater thus reducing the impact on marine life [16]. However, early adopters are reporting that using these lubricants leads to rapid wearing of the stern tube bearings, resulting in expensive additional maintenance and downtime. A leading theory is that the oil layer between the bearing and shaft breaks down under more severe operating conditions, such as sharp turning at high speed. With no intermediate oil film as protection, the shaft and bearing surfaces directly rub against one another, causing extreme levels of wear. The cause of breakdown in EALs, if it happens at all, is currently disputed. This multibillion-pound [15], environmentally critical problem may be solved in part by improving our understanding of bearing behaviour; thereby diagnosing the primary cause and developing a solution to maintain bearing performance using EALs.

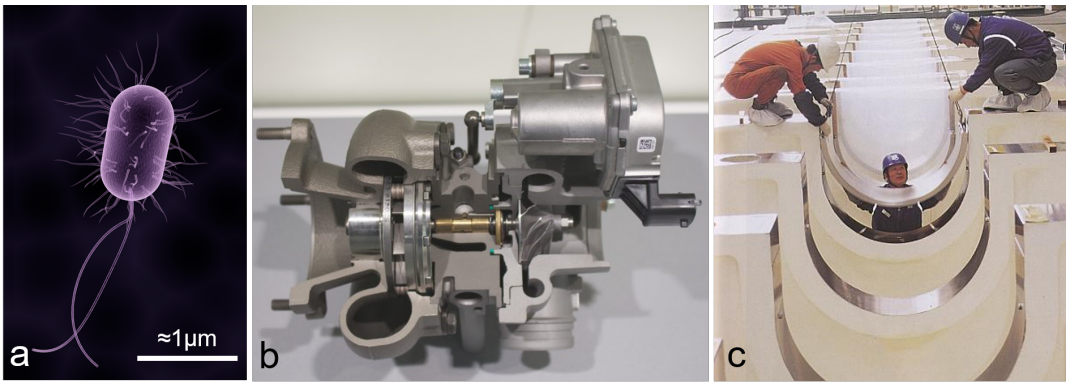

Figure 1.1: Journal bearings at different scales. (a) E-coli locomotion is powered by flagella, appendages which rotate up to 1000 rpm, with protein rings acting as nanometre-scale bearings [17, 18]. (b) Cross section of turbocharger from Porsche 911 turbo (997), with 8 mm diameter copper sleeve bearings supporting radial load [19]. (c) Installation of 1.0 m diameter crankshaft bearings in a 108,920 hp marine diesel engine [20].

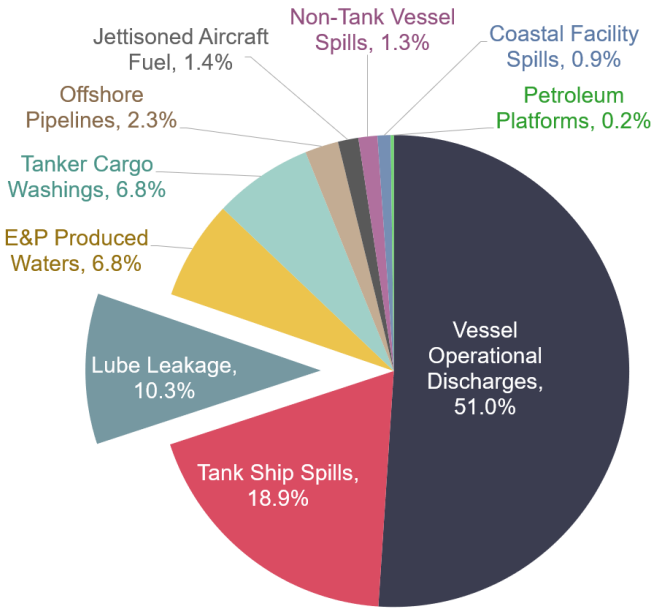

Figure 1.2: Proportion of oil entering the ocean by source. Stern tube lubricant leakage highlighted, at 10.3%. Data taken from Etkin, 2010 [15].

Several conventional techniques capable of film thickness measurements have been developed over the last few decades, however, each has its critical limitations. The difficulty of this task is due to the enclosed nature of the bearing contact, along with the minute thickness of the film one is attempting to measure, typically in the order of 1's to 10's of microns.

The ultrasonic method has been gaining momentum as an effective alternative for this application, although to become attractive to a wider industrial market the extent of its capabilities must be explored rigorously. In particular, investigating more extreme cases such as misalignment, shut-down and dynamic loading conditions which are at the forefront of current challenges in tribology.

1.2 Aim and Objectives

The aim of this project is to develop the capabilities of the ultrasonic technique in the analysis of oil films in the context of journal bearings. This will be achieved by completing the following objectives:

- Design two bespoke journal bearing test platforms capable of ultrasonic film thickness measurements; one designed to investigate films under static loading conditions and one to study dynamic loading conditions.
- Perform tests under a range of static loading, dynamic loading and severe operating conditions.
- Apply a range of new ultrasonic techniques to obtain film thickness measurements.

- Understand the resulting film thickness profiles and features such as cavitation, shear thinning and squeeze films.

1.2.1 Project Benefits

Findings could directly further the understanding of bearing behaviour, particularly under more extreme operating conditions. The work may also demonstrate the capabilities of the ultrasonic method on a wider scale, especially as the techniques discussed could readily be applied to other tribological components, such as cylinder liners and thrust pad bearings. Thus, there is wider value to this investigation. Additionally, the development of a robust and adaptable test platform would enable future projects which can continue research into new and exciting areas.

1.3 Thesis Layout

This thesis is divided into eleven chapters. The following provides a summary of the contents within each chapter, with the structure shown graphically in Figure 1.3.

Chapter 2: Lubricants & Lubrication begins by introducing the concepts within lubrication theory that are relevant to the project, thus providing the reader with sufficient comprehension to understand and assess the work presented. This is followed by an overview of how journal bearings operate, along with common bearing configurations and materials.

Chapter 3: Ultrasonic Principles presents the fundamental concepts of ultrasound. This includes how waves propagate through media and their behaviour at boundaries between dissimilar materials.

Chapter 4: Literature Review investigates the most popular and effective conventional techniques used in bearing film thickness measurements, identifying their strengths and limitations, then exploring how these gaps in capabilities constrain our current understanding of bearing behaviour. This is followed by the various ways ultrasound may be used in film thickness measurements. The chapter concludes with a review of previous studies which have applied ultrasonic techniques to journal bearing film measurements.

Chapter 5: Generic Ultrasonic Hardware and Method details the ultrasonic hardware and signal processing techniques used across a broad range of applications. Along with providing the reader with sufficient understanding, this will be useful in subsequent chapters which include justifications for certain design choices made, such as why particular transducer materials were selected or why a specific couplant was used, for example.

Chapter 6: Statically Loaded Journal Rig Development introduces the bearing test platform, named BAXTER, designed for this investigation to study bearing behaviour under both normal and severe operating conditions. The manufacturing process and de-

sign choices for primary components are detailed and justified.

Chapter 7: Film Thickness Acquisition Methodology describes the procedure used to calculate film thickness using ultrasonic methods, with novel processes applied to improve the accuracy and capabilities of the technique. An investigation to determine the acoustic impedance of the bearing is also presented, using a method new to this application.

Chapter 8: Normal Operating Conditions presents the results obtained from the BAXTER rig under static loading, constant shaft rotation speed test parameters. This includes full circumferential film thickness measurements obtained by combining multiple ultrasonic techniques. The minimum film thickness results are compared against both a numerical prediction and measurements taken via conventional eddy-current sensors. A novel method for detecting evidence of shear thinning using this test platform is also proposed.

Chapter 9: Severe Operating Conditions presents the results obtained from tests performed using the BAXTER rig under more extreme situations. These are misalignment, offset-load, starvation and shutdown testing.

Chapter 10: Dynamic Loading Conditions begins with an overview of the second bearing test rig, named BETTY, developed for this project. The BETTY rig has been designed to investigate bearing behaviour under dynamic loads. This is followed by the results obtained by the BETTY rig under a range of dynamic loading events.

Chapter 11: Conclusions summarises the project and its findings. Suggestions for future directions are proposed, with the details of preliminary work to evaluate feasibility included.

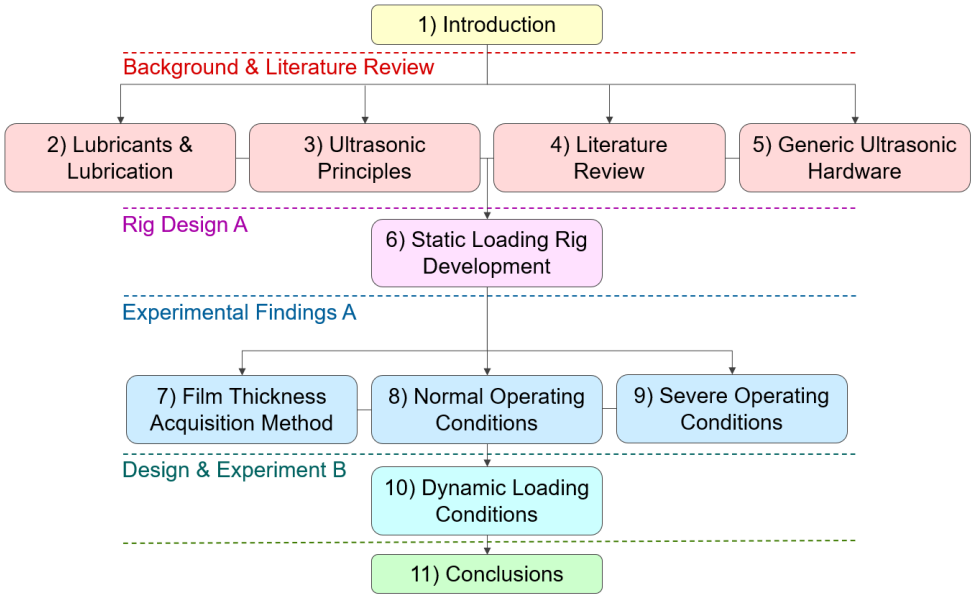

Figure 1.3: Thesis structure by chapters.

Chapter 2

Lubricants & Lubrication

This chapter contains an overview of the lubrication theory related to the present work. This includes the importance of lubricants within a sliding contact and how their physical attributes, such as viscosity, can impact the efficacy of a tribological system. This is followed by the introduction of journal bearing components, focussing on key design elements such as geometry, material type and the inclusion of features such as oil ports. Finally, the most common types of severe operating conditions found in hydrodynamic journal bearings are presented, along with the current state of understanding for each condition.

2.1 Physical Properties of Lubricants

The function of a lubricant is to separate surfaces which are in relative motion. This provides numerous benefits such as:

- Reduced friction
- Reduced wear
- Protecting surfaces from corrosion
- Maintaining optimum contact operating temperature
- Flushing of 3rd body particles [21]

Lubricants come in a wide variety of forms. Oils or greases probably first come to mind, however, PTFE [22], graphite [23], water [24] and even air [25] are widely used in lubricating surfaces. The optimum lubricant composition heavily depends on system requirements, such as the speed of the surfaces relative to each other, operating temperatures and the magnitude of applied load [10].

2.1.1 Fluid Viscosity

Arguably the most critical physical property of a fluid-type lubricant is its viscosity, which is a measure of the fluid's resistance to flow [10]. In layman's terms this may be thought

of as the fluid "thickness", for example honey is "thicker" (more viscous) than water. A more viscous lubricant can generally maintain larger oil films in a contact, however, large films require more energy to shear. As such, optimising viscosity for a given application is critical [26].

It is common to use the parameter dynamic viscosity, also known as absolute viscosity, which can be defined as the ratio of shearing stress and velocity gradient between the two surfaces [27]. This is exemplified by Equation 2.1 and Figure 2.1.

$$\tau = \mu \frac{du}{dh} \tag{2.1}$$

Where τ is shear stress, μ is dynamic viscosity and du/dh is relative velocity gradient.

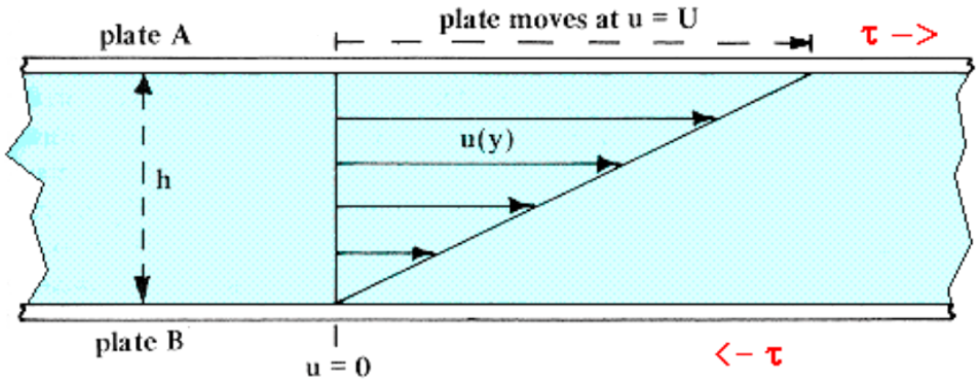

Figure 2.1: Velocity profile of fluid between two plates in relative motion [27].

Dividing the dynamic viscosity by the lubricant density provides the kinematic viscosity, ν. This alternative measure removes the external force terms and, as such, is preferred in cases where fluid momentum is of primary interest [10].

The viscosity of a lubricant is strongly affected by its temperature and a range of both theoretically derived and empirical techniques are available to model this relationship [10]. One of the most popular of these is the semi-empirical Vogel equation:

$$\mu = ae^{b/(T-c)} \tag{2.2}$$

where μ is dynamic viscosity and T is absolute temperature in Kelvin. a, b and c are constants. By measuring three viscosities at known temperatures this simple equation can be applied to determine the viscosity at any temperature with high accuracy [28].

In many applications, the viscosity-temperature relationship for a particular oil is characterised by its Viscosity Index (VI). This dimensionless scale was developed by Dean and Davis in 1929 by comparing the viscosity-temperature relationship of lubricants available at the time [29]. Texas Gulf crudes were considered the least temperature stable lubricants so were assigned a VI of 0. Pennsylvania crudes on the other hand, were very

temperature stable and therefore given a VI of 100. Since then, major developments in lubricant chemistry have been made. Particularly with the addition of viscosity modifiers and advancements in synthetic oils, lubricants now regularly exceed 100, with silicone oils even reaching VIs up to 400 [30].

Another parameter that may have a significant effect on fluid viscosity is pressure. This positive relationship is most important in high pressure point contacts, such as in gears and ball bearings where pressures are in the order of GPa. In such components viscosity can increase so considerably that the fluid may behave more like a solid.

The pressures in components such as journal bearings are not so extreme (typically 1's to 10's MPa), however, its effect on viscosity should still be taken into account. The consequence of increased viscosity with pressure in journal bearings is that the film thickness and therefore load-carrying capacity (magnitude of the applied load the bearing can withstand) will be greater compared to a situation where the pressure-viscosity relationship did not exist. As such, it is important to consider this effect to avoid overestimating the required viscosity for a given application and to select the optimum lubricant, possibly one with a higher pressure-viscosity coefficient. A popular formula used to link viscosity and pressure is the Barus equation:

$$\mu_p = \mu_0 e^{\alpha p} \tag{2.3}$$

Where μ_p is viscosity at pressure p, μ_0 is viscosity at atmospheric pressure, α is pressure-viscosity coefficient and p is the pressure in question. This equation is suitable for pressures up to around 500 MPa. Above this point, the equation quickly loses accuracy and alternative techniques are required.

2.1.2 Non-Newtonian Fluids

Newton's law of viscosity states that the viscosity of a fluid is independent of applied stress. A non-Newtonian fluid breaks this law, exhibiting stress-viscosity dependence [10]. If stress is applied in the shear plane, the rate at which deformation progresses may be quantified by the shear rate, $\dot{\gamma}$. As seen in Figure 2.2(a), the viscosity of a non-Newtonian fluid can either increase with shear rate (shear thicken) or decrease (shear thin).

Figure 2.2(b) shows that a non-Newtonian fluid typically produces two plateaus, one found at low shear rates and the other initiating at a high shear rate. The curve for a particular fluid can be described mathematically by the Carreau–Yasuda equation:

$$\mu = \mu_\infty + (\mu_0 - \mu_\infty)(1 + (A\dot{\gamma})^a)^{\frac{n-1}{a}} \tag{2.4}$$

Where μ is the dynamic viscosity at shear rate $\dot{\gamma}$, μ_0 is the low shear rate viscosity, μ_∞ is the high shear viscosity. A, a and n are constants specific to the fluid.[28]

Shear thinning behaviour is far more common than shear thickening in lubricants and is often seen as a problem in tribology. It is easier to design systems without the additional complexity of viscosity changing with a wide range of parameters that affect shear rate. Also, the low shear rate viscosity of such lubricants may need to be higher, thereby reducing efficiency, to offer the same load carrying capacity at high shear rates compared to their Newtonian counterparts [10]. Oils blended with additives such as viscosity modifiers are particularly susceptible to shear thinning, as the long polymer chains unravel and extend with applied stress [31], although improved understanding of various additive packages may lead to the mitigation of these effects [32].

It should be noted that a change in viscosity with stress is not instant. A fluid that decreases in viscosity over time is referred to as thixotropic and one in which viscosity increases over time is rheopexic [10]. This time-dependence relationship is frequently disregarded, particularly in situations with constant or only gradually changing shear rates.

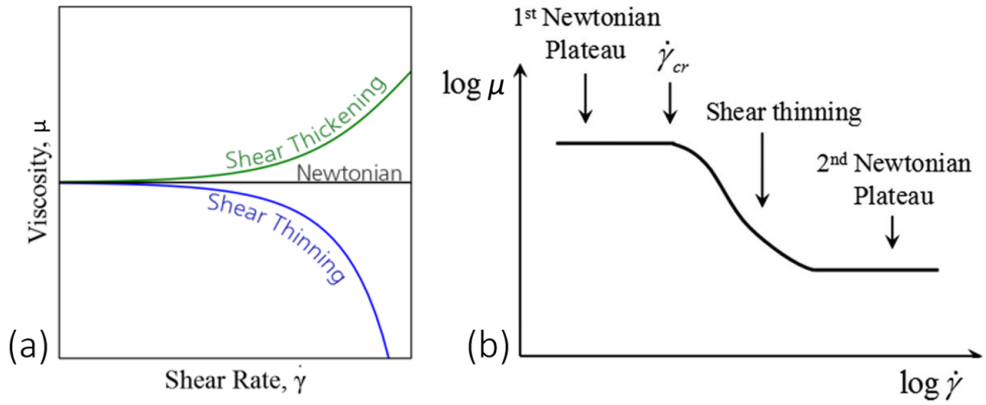

Figure 2.2: (a) Viscosity against shear rate for Newtonian, shear thinning and shear thickening fluids [33]. (b) Typical viscosity-shear rate relationship for shear thinning fluids, with plateaus at low and high shear rates indicated [34].

2.2 Lubrication Regimes

The performance of a lubricated contact heavily depends on the lubricant film thickness, exemplified by the Stribeck curve in Figure 2.3. This behaviour can be classified into the following four regimes:

Boundary lubrication: Sliding speed and viscosity are low relative to the applied load; as such, there is insufficient hydrodynamic pressure to separate the surfaces. Asperity contact leads to high levels of friction and wear dominated by solid surface interactions [21].

Mixed lubrication: A transition regime in which hydrodynamic pressure partially separates the surfaces, leading to moderate rates of friction and wear [21].

Hydrodynamic lubrication: Generally considered the ideal regime in lubricated contacts. Operating conditions allow total surface separation. Friction force depends primarily on lubricant rheology. If the film thickness increases further, friction will also increase due to additional forces required to shear the lubricant [21]. However, operating with a lubricant film only just within the hydrodynamic region can be dangerous, as unexpected shock loading or temperature spikes can push the system into the mixed lubrication regime. As such, a factor of safety is usually implemented by targeting a slightly thicker film [35].

Elastohydrodynamic lubrication (EHL): High localised stresses, in the order of GPa, lead to dramatic increases in lubricant viscosity. These stresses also lead to elastic deformation of the surfaces. Principally found in systems with small contact areas, such as in rolling element bearings, cam followers and gears [36].

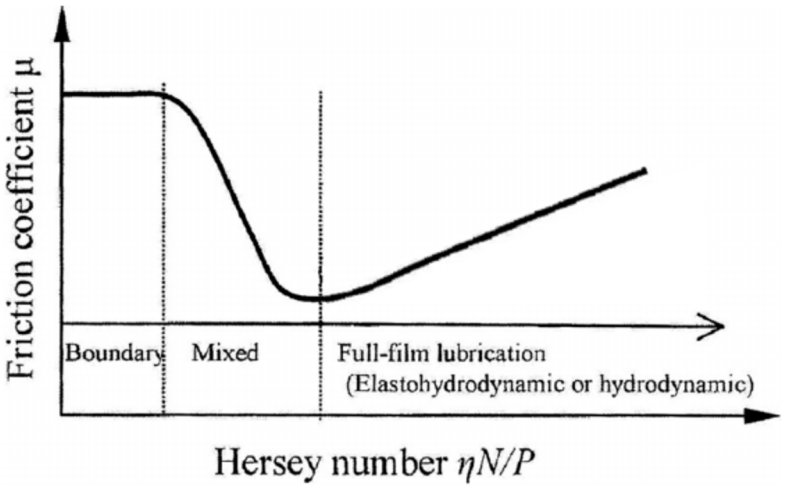

Figure 2.3: A Stribeck curve highlighting the four primary lubrication regimes [37]. Hershey number directly relates to interfacial film thickness, thereby a change in Hershey number is equal to a proportional change in film thickness.

As advances in machining processes and our understanding of tribology are made over time, the required film thickness factor of safety can be reduced; thus allowing systems to operate more closely to the mixed regime by using less viscous lubricants without risking damage [35].

Theoretically predicting the precise inflection point on the Stribeck curve for any given system has been a long-standing problem in tribology [36]. The primary challenge is accounting for the roughness profile of each surface. Rougher surfaces would of course require a thicker film for the asperities to adequately separate, however, a robust method to predict regime transition is yet to be discovered.

Traditionally, the lambda ratio, λ, has been used to predict which regime a system may be operating in by accounting for film thickness and the average surface roughness, R_a. This parameter can be calculated by the following equation:

$$\lambda = \frac{h_{min}}{\sqrt{R_{a,1}^2 + R_{a,2}^2}} \tag{2.5}$$

Where h_{min} is minimum film thickness at the contact, $R_{a,1}$ and $R_{a,2}$ are the mean roughnesses of the two surfaces. Stolarski states that a lambda ratio exceeding three would indicate a very low probability of surface contact, thus the system would be in the hydrodynamic regime [38]. Recently however, critics of this method have demonstrated that the lambda ratio is a relatively poor predictor of lubrication regime. Not only are these prediction bands too imprecise for many applications, even if correct, Cann et al. argue that the surface chemistry and roughness direction also dictate the lubrication regime, which are not accounted for in the lambda ratio [39]. In 2012, Zhu & Wang applied numerical techniques to this problem and concluded that this may be difficult to verify with conventional experimental techniques due to their fundamental limitations [40]. Further work is required to draw more concrete conclusions, particularly by developing and applying a more suitable experimental method.

2.3 The Anatomy of a Journal Bearing

In its most basic form, a journal bearing is simply a shaft (journal) within a solid block, As journal bearings are so simple, with no rolling elements or magnets to speak of, they are generally more compact, cheaper and lightweight compared to all other bearing types [41]. Journal bearings also have a high load carrying capacity and offer damping from undesirable vibrations. They are lubricated either with an external fluid such as oil or via the bearing material itself (PTFE bushings for example) [42].

Fluid journal bearings are lubricated either hydrostatically or hydrodynamically. Hydrostatic bearings use an external pump to push high pressure oil into the contact, whereas hydrodynamic bearings rely on the rotation of the shaft to generate pressure. Therefore, at start-up there can be significant wear in hydrodynamic journal bearings when a fluid pressure has not yet been developed. However, the requirement for ancillary equipment means hydrostatic bearings are more complex and therefore expensive [36]. This investigation will focus on hydrodynamic journal bearings.

The gap around the circumference between the shaft and bearing is known as the clearance, C. This geometric parameter affects the hydrodynamic pressure generated at the shaft-bearing interface and therefore the load carrying capacity of the bearing [43]. The optimum clearance depends primarily on operating rotation speed and journal diameter. An estimate can be calculated in several ways. For example, Chu provided the rule of thumb that diametric clearance should be approximately 0.001 times the journal diameter [44]. More accurate values may be obtained via design charts such as in Figure 2.4.

When the shaft in a hydrodynamic bearing rotates it also shifts radially in the direction of rotation. The angle between the applied load vector and the point of minimum

film thickness is known as the attitude angle (denoted as θ in Figure 2.5). Attitude angle is generally fixed under constant operating conditions, however, in high-speed systems oil whirl can occur if the lubrication wedge becomes unstable [45].

Oil whirl instability is a generally undesirable phenomenon caused by dynamic forces, excessive wear or changes in viscosity, temperature or damping. These events can create a sudden shock, causing the bearing to rapidly change the attitude angle. This leads to additional oil being pumped into the newly formed gap, increasing pressure. This pressure increase drives the bearing into an orbital pattern, the frequency of which is 40% to 48% of shaft rotation speed. If oil whirl matches the natural frequency of the system an even more potentially devastating phenomenon can occur, oil whip. This can cause high levels of vibration and even rapid catastrophic failures [46].

Both oil whirl and oil whip can be detected by condition monitoring tools designed to measure film thickness at different points around the bearing. They may be solved temporarily by adjusting operating conditions, such as lubricant temperature. However, a more long-term and preferable solution is to optimise system damping, particularly during the design stage [46]. A particular example of oil whip management is in 4-stroke ICE's, for which the firing frequency is often close to 50% of the engine's natural frequency. Thus, designers must optimise the stiffness of the engine to discourage the onset of oil whip [47].

Another phenomenon that must be carefully considered is cavitation. As the bearing and shaft surfaces diverge after the point of minimum film thickness, pressure in the lubricant rapidly decreases. If flow pressure drops below ambient pressure, gasses dissolved in the lubricant are released. This leads to gaseous cavitation [48]. Then, if the pressure drops even lower, past the lubricant's vapour pressure point, the lubricant will start to evaporate rapidly, this is known as vaporous cavitation [48]. These gas bubbles result in pockets of high pressure, which can erode the bearing surfaces if left unchecked [48].

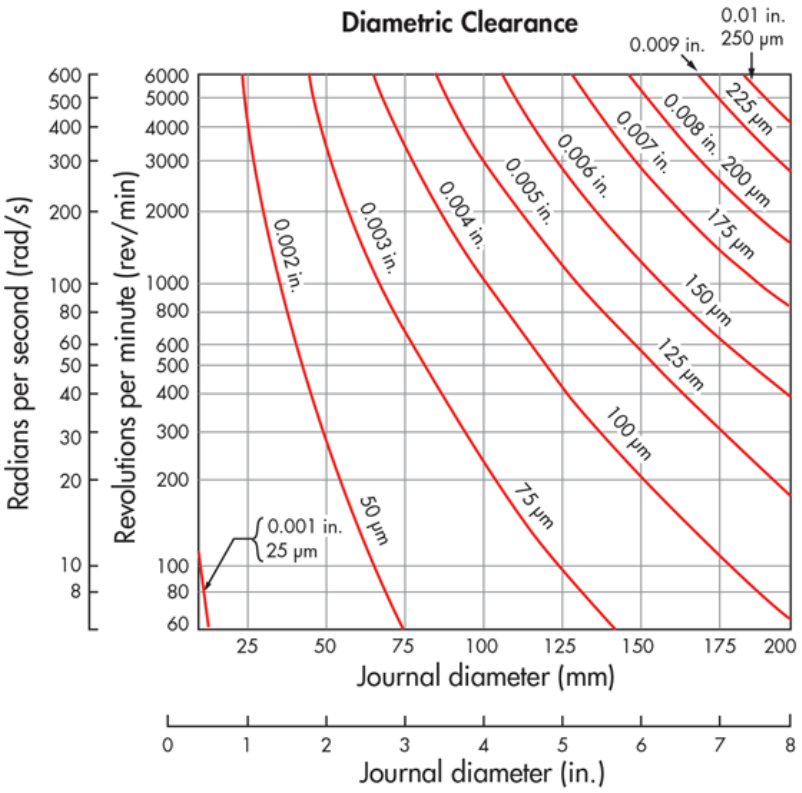

Figure 2.4: A design chart to determine optimum shaft-bearing clearance [49]. Optimum clearance is driven by journal diameter and shaft rotation speed.

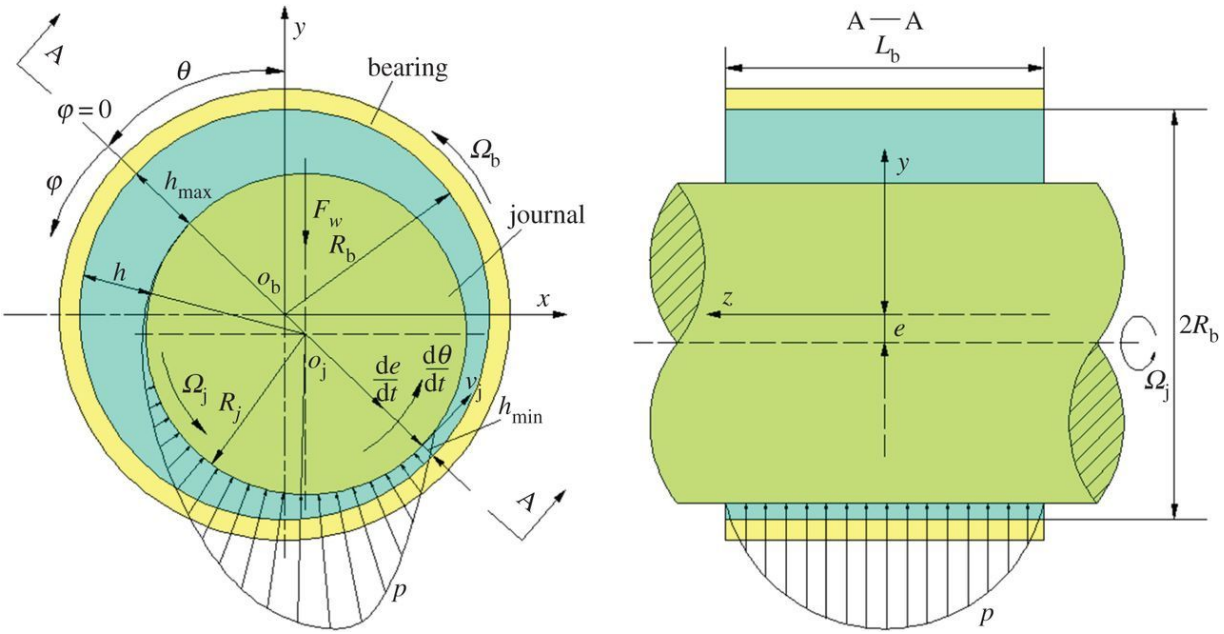

Figure 2.5: Annotated diagram of journal bearing showing key parameters [50].

2.3.1 Journal Bearing Characteristics and Configurations

In most cases replacing the shaft in a system would be particularly complicated and expensive. To give a rather specific example, as of the time of writing the cost of a replacement crankshaft for a Volkswagen Golf Mk4 is around £500 (although with free shipping) [51] compared to £18 for a replacement crankshaft bearing set for the same vehicle [52], both not including the cost of fitting. As such, it is generally desirable for the bearing to be the sacrificial component; designed to be low cost, easy to repair or replace and protect the shaft from damage [53].

An ideal bearing running material is typically one which is softer than that of the shaft, so if contact between the two surfaces does occur it is the bearing that wears, but not so soft that it deforms excessively under the required load [54]. A further characteristic of a good bearing is that it protects the shaft from damage if any 3^{rd} body particles enter the interface. To achieve this, the bearing's goal is to capture the particle as quickly as possible. The measure at which this is achieved is known as embeddability [55].

As described earlier, the simplest bearing would be a solid block of material. However, it may be expensive and impractical to replace the full component each time. Also, the optimum bearing running surface material may not have the desired structural properties. As such, a coating is typically applied to the bulk material. When this coating wears significantly the bearing may be extracted and re-coated. This maintenance process, sometimes known as rebabbitting, is most common in larger systems such as turbines and stern tubes [56]. The term babbitt is the general name given to the range of white-metal coatings applied to bearing surfaces [54].

In smaller systems, it is not worth the cost to extract the component and re-coat the running surface. So instead the bearing is designed to be disposable [54]. These components come in the form of thin bearing shells, an example of which is shown in Figure 2.7b. Bearing shells fit into a solid housing which provides additional structural support. If damaged the shells can be easily removed and replaced. Coated bearing shells are generally either categorised as bi-metal or tri-metal, so-called due to the number of layers each bearing type has (excluding the flash and bonding layers) [53]. The layers present in each are shown in Figure 2.6. The following is a brief description of the purpose of each layer:

Flash Layer: A thin cosmetic top layer that also protects the bearing from corrosion prior to installation. Typically made of 100% tin. Up to 1 μm thick [53].

Overlay: Considered the main coating layer in most cases. This layer should be softer than the shaft material to reduce shaft wear. It should also exhibit low-friction properties, and good embeddability [54]. A wide range of materials may be used in this layer. Leaded bronze alloys are popular in larger-scale applications as they offer a high load carrying capacity, however, there are environmental and health dangers due to their high lead content, thereby use is being phased out in some industries [57]. Tin-based alloys provide a less toxic alternative, with excellent corrosion resistance. Layer thickness is around 20 μm

in tri-metal bearings and 0.2 mm to 0.4 mm in bi-metal bearings [53].

Interlay: Structurally supports the overlay. Good conformability, thermal conductivity and fatigue strength characteristics are desirable [53]. In bi-metal bearings there is no interlay and therefore the overlay is required to perform these additional functions. Often this layer is plated with nickel to prevent diffusion between the interlay and overlay. This plating is particularly necessary for high loading applications where the layers may be very heavily compressed. Common interlay materials include leaded bronze or copper alloys. Layer thickness is around 0.2 mm to 0.4 mm [53, 58].

Bonding Layer: Ensures good adhesion between the interlay and backing. Typically made from pure aluminium or nickel. Approximately 25 μm to 50 μm in thickness [53].

Backing: Provides the overall strength of the bearing shell. Typically made of steel, cast iron or bronze [54]. Thickness varies considerably depending on bearing size. Big-end bearings in automotive applications are around 2 mm for example [59].

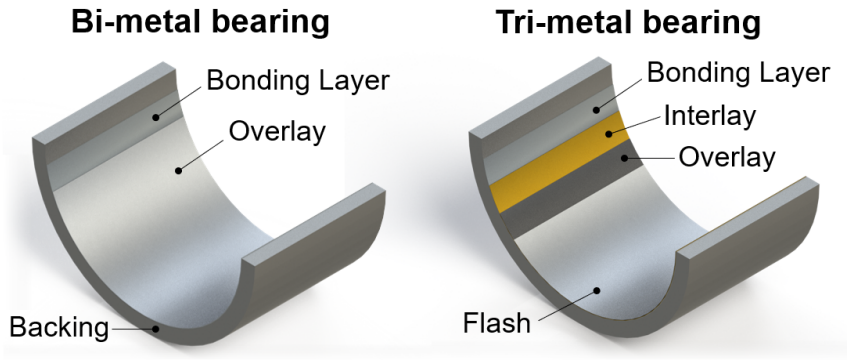

Figure 2.6: Schematic of bi-metal and tri-metal bearings with layers annotated.

More advanced hydrodynamic journal bearing variants are becoming ever more popular, offering improved performance and functionality. One of these is the tilting pad bearing (see Figure 2.7a). This design usually consists of three to eight pads mounted on pivots which move naturally as operating conditions change. Tilting pad bearings are more dynamically stable at high speeds (with reduced oil whirl), less affected by misalignment (due to its shorter length-diameter ratio) and can efficiently operate under a wide range of rotation speeds and applied loads [60].

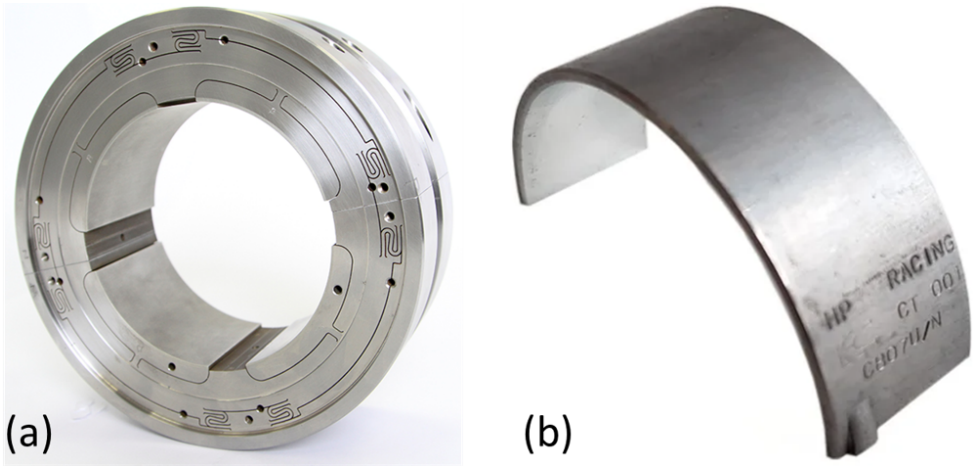

Figure 2.7: (a) Photograph of a typical tilting pad journal bearing [61]. (b) Photograph of a typical big end bearing [62].

2.3.2 Oil Holes & Grooves

As viscosity is the main driver of lubricant film thickness, which itself is incredibly sensitive to temperature, it makes logical sense that bearing temperature is a key parameter, if not the most important parameter, in the determination of bearing performance. Basri & Yani stated that for high-speed bearings over 50 mm in diameter thermal convection between the bearing and lubricant was the most significant contributor to temperature control within the system [63]. Thus, to provide sufficient heating or cooling the oil must be allowed to flow readily around the interface.

The most basic method to achieve this is to simply flood the system with lubricant. No additional geometric features are required, however, this is only effective for short bearings. For wider bearings, the oil is simply unable to overcome the squeeze forces and can not make its way into the axial centre of the bearing.

A simple solution is to implement a hole in the unloaded region of the bearing. This does not significantly disrupt the hydrodynamic flow but does rely on the rotating shaft entraining lubricant into the contact. As such, this may still be insufficient for highly loaded systems or bearings with a length-diameter ratio exceeding 0.5 [64]. Additionally, the oil hole must always remain outside the loaded region, therefore restricting the allowable attitude angle and by extension variation in load, speed and directionality. As such, oil holes are generally less suitable in dynamic loading systems [65].

To encourage yet more lubricant into the loaded region, one may apply a groove around the bearing circumference; a by no means exhaustive set of common groove designs is shown in Figure 2.8. However, the trade-off with grooves is that they reduce load carrying capacity, interrupting the hydrodynamic flow and acting as pressure sinks [66]. Multiple groove designs supply even greater levels of lubricant to the bearing, and groove layout can be designed offset from the axial centre and away from the peak pressure region. However,

an imbalance of flow rates between adjacent grooves is a common problem. New designs in which oil supply pressures are adjusted with check valves have shown much promise, although this does make the system more complex [66].

In summary, the challenge of bearing port design is to supply the bearing with enough oil to provide sufficient cooling and inhibit starvation, whilst maintaining the required load carrying capacity. This often transpires to be a difficult task and is highly dependent on bearing geometry, loading requirements and application. It should also be noted that alternative lubrication methods do exist. For example, many crankshaft systems use oil ports found in the shaft itself, rather than in the connecting rod bearing [67].

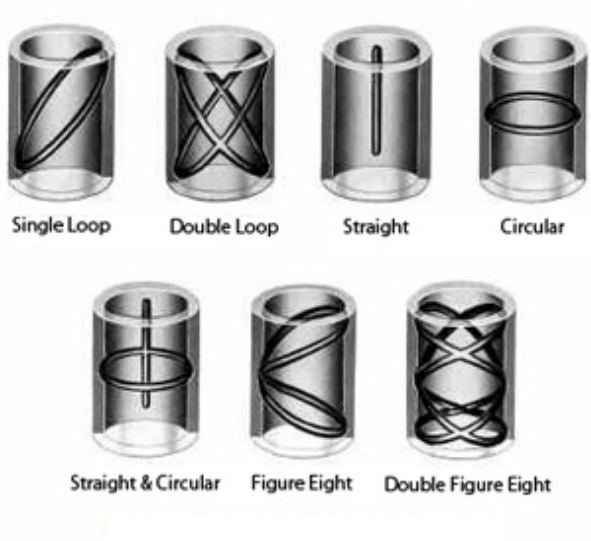

Figure 2.8: Various common journal bearing groove designs. [64]

2.4 Severe Conditions in Journal Bearings

In an ideal scenario, bearings would operate under constant load and speed, be perfectly aligned and have access to a generous supply of lubricating oil. Unfortunately, due to poor management or simply the demands of the application, real systems commonly operate under more severe conditions. The following presents severe conditions which currently pose a challenge to industry and where oil film thickness measurements may be particularly useful.

2.4.1 Misalignment

If the applied load on a bearing system is offset from its axial centre or there are poor tolerances in manufacturing, the shaft may become misaligned relative to the bearing. A misaligned system causes a localised minimum film at the bearing edge, which may lead to significant increases in wear and maximum pressure. The temperature increase in this localised region exacerbates the situation, reducing oil viscosity and further decreasing

film thickness [68].

The importance of this issue was identified as far back as 1942, where Pigott demonstrated a supposedly insignificant 0.2 milliradian misalignment angle can reduce load carrying capacity by as much as 40% [69]. In 2008 Nikolakopoulos & Papadopoulos found that once wear had initiated, the friction in a misaligned bearing system will steadily increase as wear depth progresses [70]. As such, a misaligned system will continuously reduce efficiency until potentially catastrophic failure.

In many systems some level of misalignment is unavoidable and so must be carefully managed. For example, in marine stern tubes a significant side load will be experienced when the ship changes direction [71]. If this transient event is particularly severe it may lead to "wiping", in which the white-metal overlay at the aft end of the bearing is removed. An example of stern tube bearing wear due to wiping is shown in Figure 2.9. In 2019, Lee et al. showed that the problem is most prevalent in modern stern tubes supported by a single bearing [72], suggesting more traditional multi-bearing designs should be favoured as they distribute the load more evenly. Also, EALs have recently been blamed for increasing the severity of wiping events due to shear thinning, although this is currently disputed [14, 16].

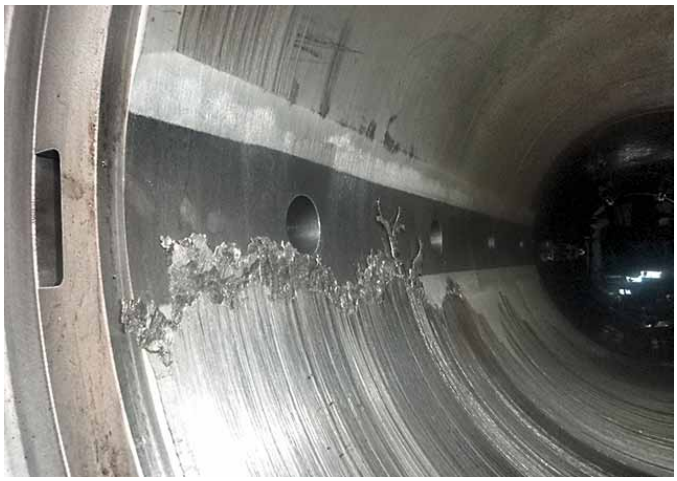

Figure 2.9: Photograph of wear in a stern tube bearing due to wiping [71].

2.4.2 Starvation

As discussed in Section 2.3.2, a sufficient supply of oil is required to maintain a well-lubricated interface, else direct bearing-shaft contact will occur, leading to a rapid increase in wear and heat generation. In extreme cases this temperature increase can be so significant that the surfaces weld together, causing seizure [73]. Bearings operating with limited lubricant supply (LLS) also have a capped top rotation speed, above which film thickness will start to decrease as there is not enough oil to be entrained into the contact, this is known as the critical speed [74].

In contrast, designers of modern bearing systems are conscious of the environmental impact of petroleum-based lubricants and as such aim to minimise the quantity of oil supplied. Additionally, oversupply of lubricant increases viscous drag within the system, lowering bearing efficiency [74]. All these considerations result in a challenging balancing act, particularly as calculating the exact quantity of oil to supply must account for side-leakage and how this may change with different loads and speeds [10, 75].

To make the situation even more complex, many causes of starvation occur well within the life-cycle of the components. This includes insufficient oil in the reservoir, blocked filters, incorrect oil grade used, worn seals, and kinked or blocked oil feed pipes. Also, in some components such as turbochargers, insufficient lubricant supply can cause catastrophic damage within seconds [76]. Current monitoring techniques which measure temperature, friction or vibration only detect a change when solid contact is occurring [73], at which point it is too late and the system is already damaged. Consequently, a continuous, fast-reacting condition monitoring technique that detects precursors to starvation would be highly advantageous. He et al. highlighted in 2005 that observing the oil film away from the minimum film region may indicate early signs of starvation [75], which was reinforced by Velasquez in 2014 [77]. Also, in 2019 Liu et al. demonstrated that lubricant supply volume was sensitive to film thickness [74].

2.4.3 Start-Stop

Start-stop technology is becoming an ever-more popular strategy used by the automotive industry to reduce fuel consumption and noise pollution. Start-stop systems automatically shut off the engine when idling is detected and restart once the accelerator pedal is depressed. This strategy is particularly effective in urban driving, with a study by Sander et al. finding that effective implementation of start-stop can reduce fuel consumption by as much as 10% [78, 79].

However, this frequent start-up and shut-down of the engine causes the crank bearings to transition through the boundary and mixed lubrication regimes many times in a single journey, rather than just once, significantly accelerating wear rates. The increase in temperatures as the engine heats up compounds the problem, with a reduced oil viscosity leading to greater metal-metal contact each cycle [80]. In addition, drivers do not want to be embarrassed by being slow off the mark at traffic lights, so restarts are often designed to be more rapid and aggressive [78].

Increased bearing wear leads to reduced component life. Traditional bearings have been shown to withstand only 100,000 start-stop cycles, falling short of the 250,000 cycles required by manufacturers using start-stop systems [81]. As such, new bearing material types are being developed, with particular interest in Polyamide-Imide (PAI) coatings [82]. The dimension changes from wear can also cause misalignment and vibrations [83].

A simple solution would be to increase the oil viscosity grade used, however, this goes

against the current trends within the automotive industry. As previously discussed, a more viscous lubricant would decrease efficiency during the majority of engine operation due to viscous drag [10]. The capability to monitor film thickness either in a real system or a controlled test platform could instead highlight the conditions in which start-stop is most severe and optimise the system to reduce its impacts.

2.4.4 Dynamic Loading

Due to their large contact area, journal bearings offer excellent protection against rapid dynamic loads compared to other bearing types such as ball bearings [84]. However, even journal bearings have their limits and, as they are pushed to operate under ever more demanding conditions, the mechanics of dynamic loading must be well understood.

Shock loading is a generally undesirable sudden spike in applied load, commonly experienced in many dynamic applications; for example in suspension systems when a car hits a bump or marine stern tubes when the propeller crashes into a wave in stormy weather [85]. This sharp increase in load reduces film thickness and can cause shaft-bearing contact if not properly controlled. However, predicting minimum film thickness is not as simple as considering a static load of the same magnitude. This is because the oil cannot exit the contact instantly, no matter how hard it is squeezed. The effect is known as a squeeze film and the delay period is referred to as squeeze time. This squeeze time is related to the magnitude of the applied load, bearing geometry and oil viscosity [86].

Squeeze films can be inherently useful as they offer a level of cushioning against extreme loads, although only for a short window of time. In many applications, it is critical to correctly predict the squeeze film effect. An underestimation will mean an unnecessarily high viscosity oil is used, thus reducing efficiency, whereas an overestimation will lead to instability, vibrations and wear due to shaft-bearing contact [87]. How the film recovers after load removal is equally important, as the oil layer must be sufficiently thick to protect the system from the next load instance.

Connecting rod bearings within automotive applications serve as some of the most popular examples of bearings subjected to dynamic loading. Converting linear reciprocating motion to cyclic rotation, understanding their behaviour is particularly challenging. Not only does the magnitude of the load change but also its radial direction [88]. This variation rapidly changes both minimum film thickness and attitude angle significantly. Also, connecting rod bearing failure can have catastrophic effects, potentially causing the connecting rod to snap (known colloquially as "throwing a rod") and driving it through the crankcase, thereby destroying the engine. Thus, engine manufactures have a vested interest in optimising efficiency by minimising film thickness, whilst mitigating the possibility of bearing failure.

Along with an increasing understanding of dynamic loading in traditional bearings, new bearing designs to mitigate dynamic loading effects have also been developed [61]. Applications that require even more protection against shock loading can implement a squeeze

film damping system between the bearing and housing, two examples of which is shown in Figure 2.10. However, these are not suitable for lower cost or compact systems as the feature requires additional thickness around the bearing circumference.

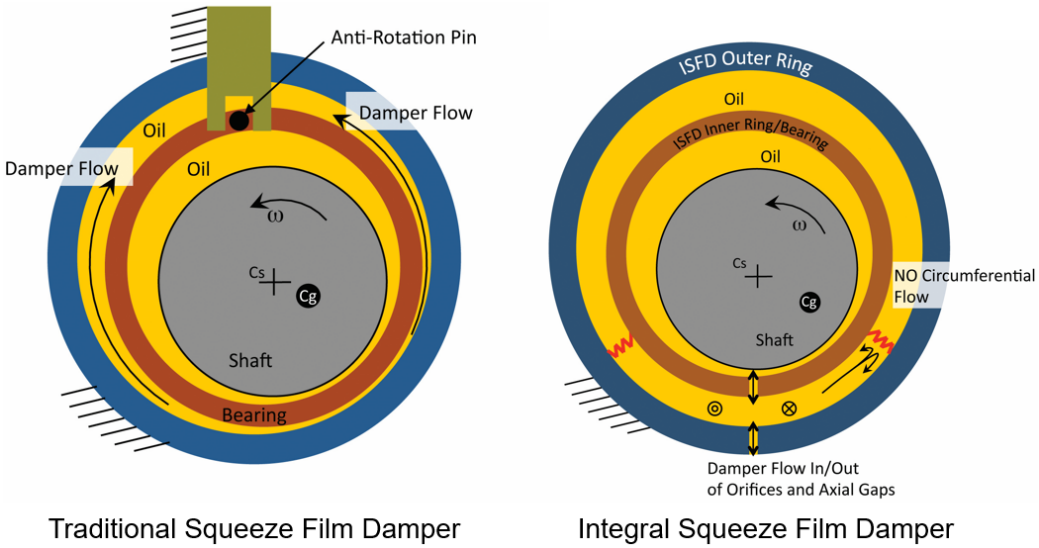

Figure 2.10: A schematic of a traditional squeeze film damper (left) and an integral squeeze film damper (right) [61].

2.5 Conclusions

This chapter has provided an introduction to the relevant lubrication theory related to this project, including:

- Fundamental physical properties of lubricants, with particular regard to viscosity. Also, how temperature, pressure and shear rate can affect film thickness.
- The different regimes of lubrication within a contact, highlighting the importance of optimising film thickness.
- A detailed description of the main components in a journal bearing, including the function of each layer in bearing shells and different oil inlet configurations available.
- A review of the types of severe operating conditions that a journal bearing might experience. Specifically, misalignment, starvation, start-stop and dynamic loading.

Chapter 3

Ultrasonic Principles

This chapter gives an overview of the ultrasonic principles relevant to the current work, providing the reader with a sufficient understanding of the techniques used in the measurement of oil films.

3.1 Wave Propagation

A sound wave travels through a host medium as a mechanical pressure wave, in which particles are held together in the host medium by elastic forces. As such, the oscillation of one particle transmits energy to its neighbours, causing them to also oscillate, resulting in wave motion through the medium. An ultrasonic wave is simply a sound wave with a frequency exceeding the threshold of human hearing, generally taken as a frequency above 20kHz [89].

There are two major wave types, categorised by how the particles oscillate in relation to wave direction, these are longitudinal and shear waves.

For longitudinal waves, each particle oscillates in parallel to the direction of wave propagation. The resulting compressions and rarefactions are shown in Figure 3.1. In this, λ denotes the wavelength, which may be defined as the distance between repeating sections of the wave [90].

For shear waves (also known as transverse waves), particles oscillate perpendicular to the direction of wave propagation. This is shown in Figure 3.1. Unlike longitudinal waves, shear waves can only travel effectively through solid media as they require a restoring force to transmit energy from one particle to another [89].

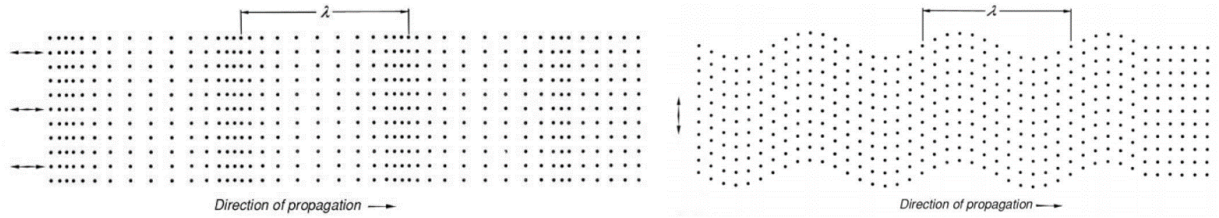

Figure 3.1: Diagram of longitudinal (left) and shear (right) wave propagation [90].

3.2 Acoustic Velocity

Acoustic velocity, or how quickly the sound travels through a medium, is dictated by the stiffness of the elastic bonds holding particles together. This stiffness is determined by host material properties and type of wave propagation. In longitudinal waves, acoustic velocity, c_l, may be defined by:

$$c_l = \sqrt{\frac{E}{\rho(1+\nu)(1-2\nu)}} \tag{3.1}$$

For which E is the elastic modulus, υ is Poisson's ratio and ρ is density.

Whereas the acoustic velocity for shear waves is equal to:

$$c_s = \sqrt{\frac{E}{\rho(1+\nu)}} \tag{3.2}$$

By evaluating Equations 3.1 and Equation 3.2, it can be seen that increasing elastic modulus leads to an increase in acoustic velocity, whereas an increase in either density or Poisson's ratio leads to an acoustic velocity decrease. Also, the Poisson's ratio of most real materials is below 0.5, and as such longitudinal wave propagation is typically faster than shear wave propagation in the same medium.

As these material properties vary with temperature, so does acoustic velocity. For example, at atmospheric pressure, the acoustic velocity of water at 20°C is 1482.2 ms $^{-1}$, whereas at 50°C acoustic velocity increases to 1542.4 ms $^{-1}$ [91]. This temperature effect must be considered in ultrasonic measurements for which high accuracy is required.

It should be noted that acoustic velocity is distinct from particle velocity, which is the speed at which the individual particles move. Particle velocity is generally many orders of magnitude slower than acoustic velocity [90].

3.3 Reflection Coefficient

At the interface between two dissimilar materials, a proportion of the sound wave energy is reflected and the rest transmits into the second material. The proportion of energy

reflected may be quantified by the reflection coefficient, R [92].

This reflection coefficient is related to the difference in specific acoustic impedances between the two materials, with a greater difference leading to increased energy reflected. Acoustic impedance is the resistance to acoustic flow within the material, determined by:

$$z = \rho c \tag{3.3}$$

If wave direction is perpendicular to the interface, the reflection coefficient may be calculated via the following relationship:

$$R = \frac{z_2 - z_1}{z_2 + z_1} \tag{3.4}$$

3.4 Acoustic Attenuation

As a sound wave propagates through a material, its acoustic energy reduces. This is the result of two main physical effects, scattering and absorption:

Scattering: when a wave interacts with particles of dissimilar elastic properties relative to the host material, a proportion of the wave energy is reflected along a secondary plane. Scattering is dominant in crystalline materials or media with suspended particles [93].

Absorption: mechanical energy due to particle motion is converted into heat energy, caused by stresses from viscous effects. Absorption becomes increasingly important over larger distances [94].

The rate of attenuation is related to the square of the wave frequency. As such, a high-frequency wave decays more quickly than an equivalent low-frequency wave.

It should also be noted that even in ideal media there will be an apparent reduction in signal amplitude received by a sensor due to spreading of the acoustic wave.

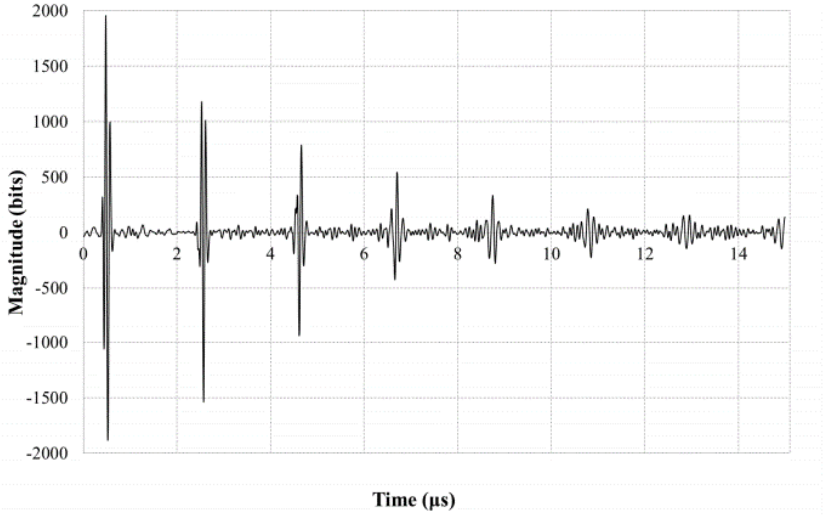

Figure 3.2: Decrease in signal amplitude due to attenuation [89].

3.5 Near Field and Far Field

The Huygens principle states that a wavefront is made of many discrete wavelets, each producing its own spherical wave [89]. This is shown in Figure 3.3. Close to the transducer face these wavelets constructively and destructively interfere with each other, causing the overall wave pattern to become complex. Therefore, it is extremely difficult to obtain accurate measurements in this area, known as the near field region.

However, at a certain distance from the transducer, the overall waveform becomes more uniform. This region is known as the far field and is more suitable for acquiring measurements. An example pressure field showing a clear difference and transition between the near and far fields is shown in Figure 3.4. The transition point between regions can be approximated by the following:

$$N = \frac{D^2 f}{4c} \tag{3.5}$$

Where N is near field length, D is transducer diameter, f is transducer frequency and c is acoustic velocity of the host medium.

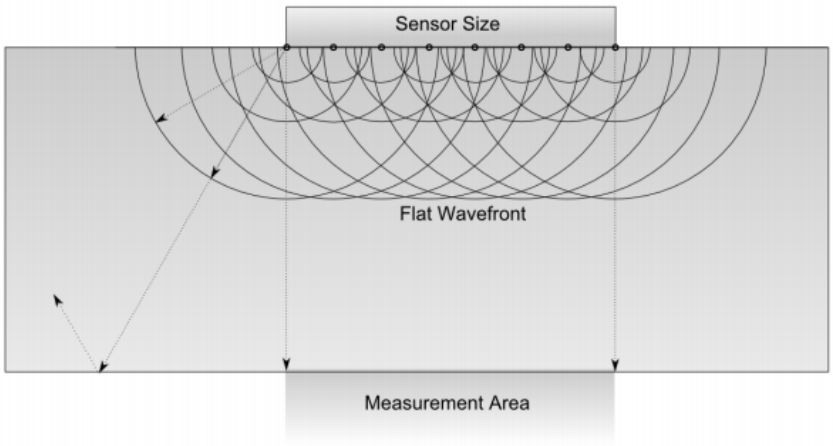

Figure 3.3: Wave propagation shape due to the Huygens principle [89].

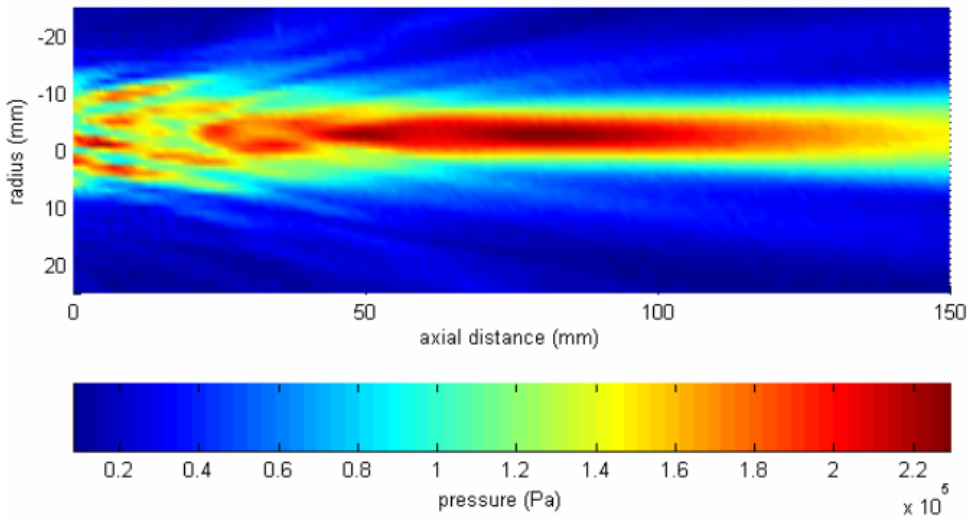

Figure 3.4: Example pressure field highlighting the transition from near to far field at an axial distance of 50 mm [95].

3.6 The Acoustoelastic Effect

Subjecting a material to a stress field changes its acoustic velocity. Known as the acoustoelastic effect, this phenomenon is due to a resultant change in strain state within the material, which in turn affects its elasticity characteristics [96]. Generally, the application of a tensile stress decreases acoustic velocity, whereas a compressive stress increases acoustic velocity. Schneider defined this relationship mathematically by the following set of equations:

$$\frac{c_{ii} - c_l}{c_l} = \frac{A}{C}\sigma_i + \frac{B}{C}(\sigma_j + \sigma_k) \tag{3.6}$$

$$\frac{c_{ij} - c_s}{c_s} = \frac{D}{K}\sigma_i + \frac{H}{K}\sigma_j + \frac{F}{K}\sigma_k \tag{3.7}$$

$$\frac{c_{ik} - c_s}{c_s} = \frac{D}{K}\sigma_i + \frac{H}{K}\sigma_k + \frac{F}{K}\sigma_j \tag{3.8}$$

Where i, j and k are axes in a three-dimensional Cartesian coordinate system, σ is stress, c is acoustic velocity and A, B, C, D, F, H and K are elasticity constants. c_l and c_s are the longitudinal and shear acoustic velocities when no stress is applied respectively. This model assumes the axes of the stress field, strain state and wave propagation are aligned.

Equations 3.6 to 3.8 highlight that acoustic velocity is affected in all directions by an applied stress, although by different magnitudes. This includes velocities orthogonal to a stress applied in a single direction.

The acoustoelastic effect has been used previously to calculate stress in components by recording acoustic velocity. For example, in 2020 Stepanova et al. used changes in acoustic velocity to find longitudinal stresses in railway rails to an accuracy within ±2% [97]. It is also important to consider acoustoelastic effects in highly stressed systems such as ball bearings when measuring film thickness via ultrasonic techniques [98]. As will be discussed in Section 3.7, practically all ultrasonic film thickness techniques require an accurate acoustic velocity value for reliable measurements.

3.7 Measuring OFT via the Ultrasonic Technique

The following section explores the techniques currently used to link acoustic response to thickness in lubricated contacts, along with their respective strengths and limitations.

3.7.1 Time of Flight Method ($f.h >> c_0$)

Be it counting the seconds between lightning and thunder to calculate how far away a storm is or shouting down a well and listening for the echo to estimate its depth, even the average layperson knows how to apply the time of flight technique. Due to its simplicity, it has also become the most established technique for calculating the thickness of layers

via ultrasound. In practice, the time-of-flight technique is implemented by sending a pulse through the layer and timing how long it takes for each reflection to return. By applying the following equation thickness may be calculated:

$$boundary\,thickness = \frac{1}{2} \times speed \times time\,of\,flight \tag{3.9}$$

Unfortunately, the standard time-of-flight technique is unsuitable for the measurement of thin films (generally less than 200 μm). With thick films the two reflections are discrete; however, as film thickness decreases these reflections overlap and become indistinguishable. This is often the case in all but the largest journal bearings.

To overcome this, new time-domain based methods have been developed which compare the reflected signal against a numerical simulation of the waveform, allowing the individual wave components to be distinguished and separated. In 2017, Praher and Steinbichler presented such a method which they proposed could be applied to components such as journal bearings [99]. Fluid film thicknesses between 30 μm and 200 μm were successfully measured. However, many internal reflections within the contact are required for accurate measurements, leading to a very long time-domain signal, as shown in Figure 3.5. This could be problematic in real systems as the path length between the transducer and contact is often reasonably small. Thus, the first and second full reflections may also merge, making the wave components more difficult or even impossible to separate. Additionally, even 20 μm is too thick for many journal bearing applications. For this reason, the focus of most research has been on alternative techniques for micron-scale film measurements.

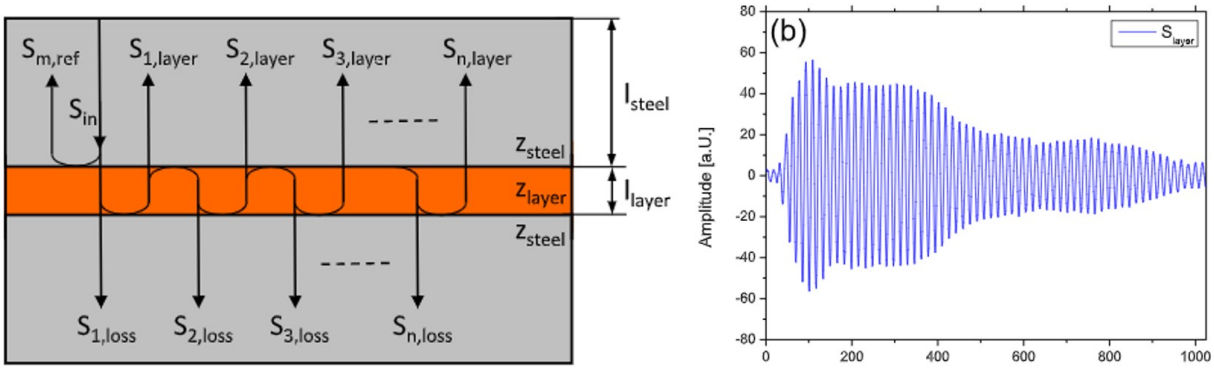

Figure 3.5: Schematic of the wave path in a three-layer system, with multiple reflections within the liquid layer indicated (left). Example of time-domain signal used in work by Praher and Steinbichler, 2017 (right) [99].

3.7.2 Thin Film Methods ($f.h < 0.5c_0$)

If an oil layer is thin the reflection coefficient amplitude or phase shift of the signal can be used to determine film thickness. The following describes how the solutions are derived.

Exact model – amplitude and phase

As previously discussed, for a single interface the reflection coefficient can be found by the acoustic impedance mismatch between media:

$$R = \frac{z_2 - z_1}{z_2 + z_1} \tag{3.10}$$

For a three-layer system, as in Figure 3.6, the total reflected signal is a combination of the reflection at both boundaries. However, one cannot simply apply Equation 3.10 for the two boundaries independently and then find the sum. This is due to a phase difference between the reflections, which leads to some level of interference affecting the amplitude and phase of the total reflected wave. Instead, the reflection coefficient in a three-layer system may be calculated by:

$$R = \frac{R_{01} + R_{20}e^{(-2\pi f i \frac{2h}{c_0})}}{1 + R_{01}R_{20}e^{(-2\pi f i \frac{2h}{c_0})}} \tag{3.11}$$

From this, the reflection coefficient amplitude and phase shift can be derived: This reflection coefficient is a complex number, having both a magnitude and phase component. These components can be separated, leading to the following equations:

$$|R| = \left[\frac{R_{02} + R_{10}e^{(-2\beta d)^2} - 4R_{10}R_{02}e^{(-2\beta d)^2}sin^2(2\pi f d/C_2)}{1 + R_{10}R_{02}e^{(-2\beta d)^2} - 4R_{10}R_{02}e^{(-2\beta d)^2}sin^2(2\pi f d/C_2)}\right]^{0.5} \tag{3.12}$$

$$\Phi = tan^{-1}\left[\frac{R_{10}e^{-2\beta d}(1 - R_{02}^2)sin(4\pi f d/C_2)}{R_{02} + R_{10}e^{-2\beta d}(1 + R_{02}^2)cos(4\pi f d/C_2) + R_{02}R_{10}^2e^{-4\beta d}}\right] \tag{3.13}$$

These solutions are known as the exact amplitude and phase models; however they are rarely applied in practice [100]. The equations are clearly unwieldy and do not have a unique solution, thus requiring either approximations or numerical techniques to solve. Often, the exact models can be simplified if the acoustic impedance of medium 1 and 2 can be assumed equal, however, this would still require a numerical technique to solve.

Spring model

One such method of approximation is to treat the oil layer as a series of springs with a defined stiffness. This can be derived by returning to Equation 3.11 and applying a Taylor expansion to the exponential terms:

$$e^{-2\pi f i \frac{2h}{c_0}} = 1 + \frac{4i\pi f h}{c_0} + O^2 + ... \tag{3.14}$$

The higher-order terms may be discarded as their effect is negligible. Thus, applying Equation 3.14 to Equation 3.11 leads to:

$$R_e \approx R_s = \frac{(z_1 - z_2) + \frac{z_1 z_2}{k} 2\pi f i}{(z_1 + z_2) + \frac{z_1 z_2}{k} 2\pi f i} \tag{3.15}$$

Where k is oil film stiffness and is equal to:

$$k = \frac{\rho_0 c_0^2}{h} \tag{3.16}$$

Equation 3.15 can then be rearranged and expressed in terms of amplitude:

$$h = \frac{\rho c^2}{2\pi f z_1 z_2} \sqrt{\left(\frac{|R|^2 (z_1 + z_2)^2 - (z_1 - z_2)^2}{1 - |R|^2} \right)} \tag{3.17}$$

or in terms of phase shift:

$$h = \frac{\rho c^2 (tan\Phi_R)(z_1^2 - z_2^2)}{\omega z_1 z_2 \pm \sqrt{(\omega z_1 z_2^2)^2 - (tan\Phi_R)^2 (z_1^2 - z_2^2)(\omega z_1 z_2)^2}} \tag{3.18}$$

These are known as the spring model amplitude and phase shift equations respectively and are the leading techniques in thin film measurements, particularly the amplitude model [101, 102].

Exact model - complex

In 2020, Yu et al. presented another method to directly calculate film thickness in thin films [103]. In this, they applied Euler's notation to Equation 3.11, rearranged the result and made practical assumptions regarding amplitude and phase. The full derivation has been omitted for brevity. With this method, referred to as the "exact model – complex", film thickness can be found by the following:

$$h = \frac{-c_0}{4\pi f} atan \left(\frac{|R_e| sin(\Phi_{R_e})(1 - R_{01}^2)}{R_{01} + |R_e|^2 R_{01} + |R_e| cos((\Phi_{R_e}) + |R_e| cos(\Phi_{R_e}) R_{01}^2} \right) \tag{3.19}$$

This new solution holds great promise, particularly as acoustic impedance values for either media are not required. However, the authors note that measurement uncertainty may be increased as it is a combination of the uncertainties in both the amplitude and phase shift measurements. Also, this work is the first and only instance of the technique being used. Additionally, the experimental setup was a simple static system, with an oil layer between two flat plates of the same material (glass-oil-glass and steel-oil-steel). As such, independent comparative studies using the method in more advanced applications would be valuable in assessing its effectiveness.

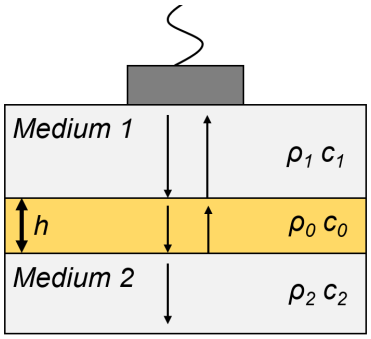

Figure 3.6: Schematic of the ultrasonic path within a three-layer system.

3.7.3 Resonant Dip Technique ($f.h \approx 0.5c_0$)

When the thickness of an oil film matches the frequency of the incident wave, constructive and destructive interference between successive reflections occurs. This manifests as dips in the frequency-domain of the reflected signal, hence the name of the technique [89]. This can be observed in Figure 3.7. The film thickness and resonant frequency may be related by the following equation:

$$f_m = \frac{cm}{2h} \tag{3.20}$$

For which f_m is the dip frequency and m is the resonance mode. The frequency of the sensor element determines the measurement range of this method.

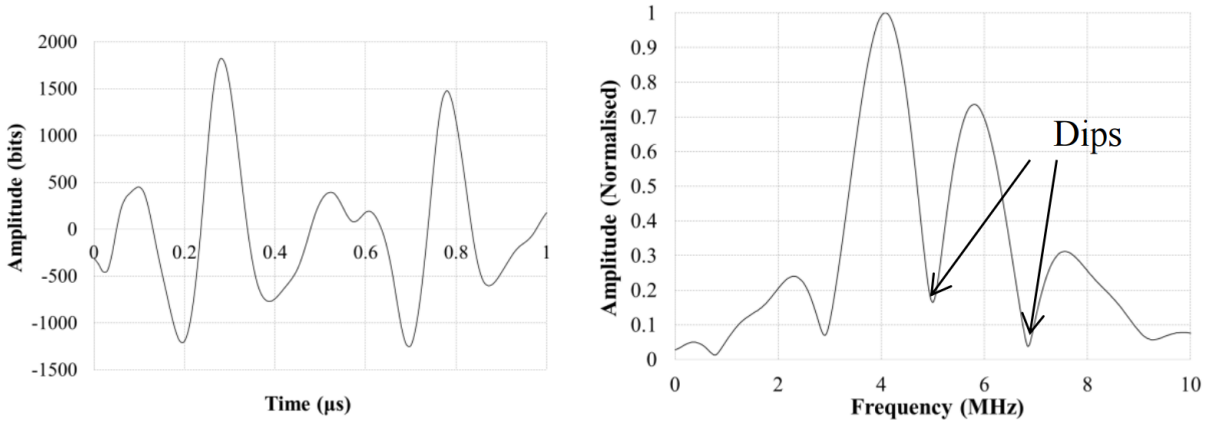

Figure 3.7: Examples of resonant dips in the time-domain (left) and frequency-domain (right) [89].

3.7.4 Measurement Limits of Ultrasonic Methods

As shown in Figure 3.8 and Figure 3.9, the most suitable ultrasonic technique is heavily influenced by the expected film thickness range experienced in a particular system. The specific measurement range of each method is dictated by system parameters, such as

transducer centre frequency, host material type and lubricant properties.

There is not a hard limit to these boundaries. Figure 3.9 highlights how values for the spring amplitude and phase models tend towards a constant value ($R \to 1$ and $\Phi \to 0$ respectively), restricting their upper measurement range. An appropriate cut-off point is primarily dependent on signal quality and the number of repeat measurements. This figure also shows that sharp changes in amplitude and phase occur around the resonant film thickness, considered in the exact model but not the spring models.

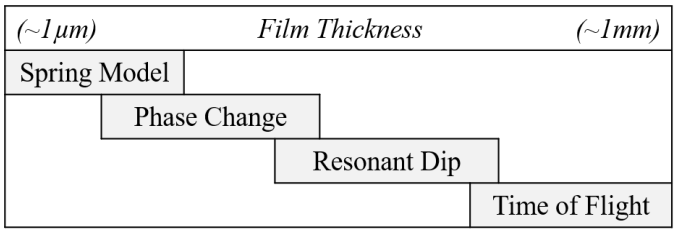

Figure 3.8: Approximate film thickness measurement range for each ultrasonic technique, assuming a steel-oil-steel three-layer system.

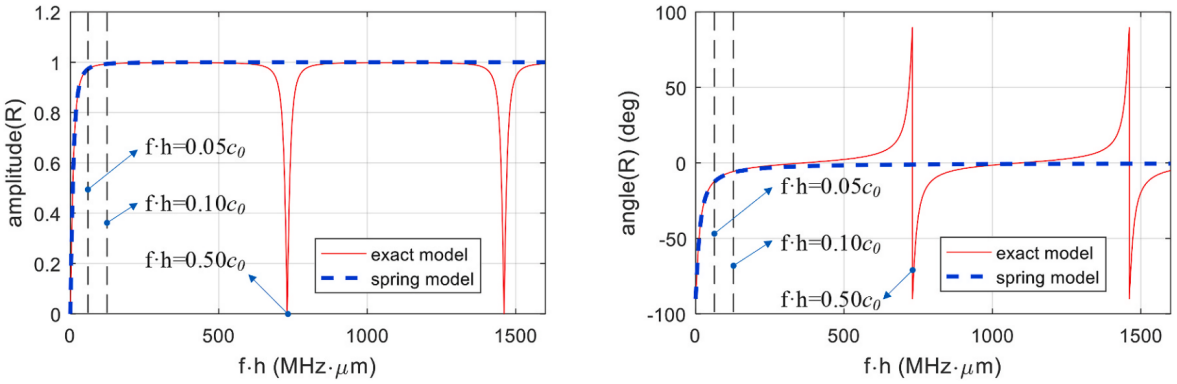

Figure 3.9: Relationship between amplitude (left) and phase (right) against the product of frequency and film thickness for both the spring model and the exact model. The example shown is for a steel-oil-steel three-layer system [103].

3.8 Conclusions

This chapter has introduced the fundamental principles of ultrasound relevant to this project. This includes:

- How waves propagate through a medium, specifically the differences between longitudinal and shear wave types, the mechanisms driving acoustic attenuation and the transition between the near and far field regions.
- Acoustic velocity and how it is affected by material properties such as density and elasticity.
- The behaviour of ultrasonic waves incident on a boundary between dissimilar materials.
- The acoustoelastic effect, detailing how applied stresses can affect the acoustic velocity within a material.
- The various methods developed to determine film thickness from ultrasonic signals. The primary drawback of each method is its limited measurement range, dictated in part by sensor frequency. The film thickness around a bearing's circumference can vary by two orders of magnitude. By combining multiple techniques it may be possible to measure across this full range with a single sensor frequency.

Chapter 4

Literature Review

This chapter details the techniques currently applied in the determination of lubricant film thickness in journal bearings. Following this, a review of previous research using the ultrasonic method to study bearing behaviour is presented, to highlight gaps in current knowledge.

4.1 Current Film Thickness Modelling & Measurement Techniques

This section details the most common techniques applied to predict or measure film thickness in journal bearing systems under normal, severe and dynamic loading conditions.

4.1.1 Analytical Prediction Methods

The foundation of analytical techniques to predict film thickness in hydrodynamic contacts, including journal bearings, is the Reynolds equation; the full three-dimensional form of which is:

$$\frac{\partial}{\partial x}\left(\frac{h^3}{\mu}\frac{\partial p}{\partial x}\right)+\frac{\partial}{\partial y}\left(\frac{h^3}{\mu}\frac{\partial p}{\partial y}\right)=6\left(U\frac{\partial h}{\partial x}+V\frac{\partial h}{\partial y}\right)+12\frac{\partial h}{\partial t} \tag{4.1}$$

Where h is film thickness, μ is viscosity, p is pressure, U and V are relative velocity components, and x and y are spatial components. In this case, the equation is expressed in Cartesian co-ordinates, although it is also common to use polar co-ordinates when applied to cylindrical components such as journal bearings.

This equation may be derived in multiple ways, most commonly either from the Navier-Stokes equation (for which the Reynolds equation is a simplification) or by applying the principles of equilibrium of forces and continuity of flow to an infinitesimally small element. The full form assumes there is no velocity discontinuity between the fluid and sliding surfaces, flow is laminar, there is no pressure gradient across the film thickness and that density is constant [10].

Derivation of the full Reynolds equation has been omitted for brevity, with plenty of good examples available elsewhere [10, 104]. What is more important here is that the equation in its full form is thought to be unsolvable analytically without applying boundary conditions. This is because the second-order components are elliptic. In fact, $1 million is on offer for anyone who can provide proof of a unique solution to the Navier-stokes equation (and by extension the Reynolds equation) [105]. Thus, assumptions have to be made to simplify the equation.

Unidirectional velocity approximation
First, the axes may be aligned so that one velocity component is equal to zero. Thus, Equation 4.1 simplifies to:

$$\frac{\partial}{\partial x}\left(\frac{h^3}{\mu}\frac{\partial p}{\partial x}\right)+\frac{\partial}{\partial y}\left(\frac{h^3}{\mu}\frac{\partial p}{\partial y}\right)=6U\frac{\partial h}{\partial x}+12\frac{\partial h}{\partial t} \tag{4.2}$$

This is not applicable if the two velocity components cannot be decoupled. For example, if a bearing slides along a rotating shaft, which is indeed rare.

Steady film thickness approximation

In many cases, film thickness does not change with time. Therefore, the Reynolds equation may be simplified further to:

$$\frac{\partial}{\partial x}\left(\frac{h^3}{\mu}\frac{\partial p}{\partial x}\right)+\frac{\partial}{\partial y}\left(\frac{h^3}{\mu}\frac{\partial p}{\partial y}\right)=6U\frac{\partial h}{\partial x} \tag{4.3}$$

This assumption cannot be made if film thickness does change significantly with time, for example in dynamic loading conditions or if there is significant bearing vibration.

Isoviscous approximation
If viscosity may be assumed constant around the length and circumference of the bearing, Reynolds equation becomes:

$$\frac{\partial}{\partial x}\left(h^3\frac{\partial p}{\partial x}\right)+\frac{\partial}{\partial y}\left(h^3\frac{\partial p}{\partial y}\right)=6U\mu\frac{\partial h}{\partial x} \tag{4.4}$$

Viscosity cannot be assumed constant if there is a significant temperature gradient around the bearing, particularly common in larger bearings. Also, if the fluid is non-Newtonian this assumption cannot be made if bearing pressures are high.

Long bearing approximation ($L/D > 3$):
Even with the above simplifications, numerical methods would still be required to obtain a solution. Two further approximations can be applied: either assume the bearing is infinitely long or assume it is infinitely short. First, for infinitely long bearings, pressure around the bearing diameter (in this case the y dimension) is assumed constant, therefore

the equation simplifies to:

$$\frac{\partial}{\partial x}\left(h^3\frac{\partial p}{\partial x}\right) = 6U\mu\frac{\partial h}{\partial x} \tag{4.5}$$

This approximation quickly loses accuracy as bearing length decreases. As such, it is generally considered that bearings with a length-diameter ratio over three may use this assumption [10]. Such long bearings are rare in practical applications as they are highly susceptible to shaft-bearing contact with the slightest shaft bending or misalignment.

Short bearing approximation ($L/D < 0.33$)
Conversely, if the bearing is narrow relative to its diameter, one may assume pressure across the bearing length is constant:

$$\frac{\partial}{\partial y}\left(h^3\frac{\partial p}{\partial y}\right) = 6U\mu\frac{\partial h}{\partial x} \tag{4.6}$$

This is also commonly referred to as Ocvirk's approximation. As many real bearings have a low length-diameter ratio, it is a much more popular assumption.

In many cases, analytical solutions are perfectly acceptable; however, they are often not appropriate for more complex cases, such as for highly loaded or high precision applications [106, 107, 108]. Phenomena such as deformation effects in elastic bearings or lubricant shear thinning can add significant uncertainty to results from analytical techniques.

Recent efforts focus on reducing the number of required assumptions so that accurate predictions can be made in more advanced applications without resorting to more expensive numerical techniques or experimental testing. For example, in 2011, Vignolo et al. presented an approximate analytical solution to the Reynolds equation applicable to bearings of finite-length [109]. Similarly, in 2015 Gong et al. presented an analytical solution that applies to dynamic loading operating conditions, also derived using the regular perturbation method [110].

4.1.2 Numerical Prediction Methods

Numerical prediction techniques promise more accurate results than analytical methods, particularly for more complex geometries and operating conditions [111]. Such prediction methods also have an advantage over experimental techniques in that operating parameters are often simple and quick to adjust, leading to greater potential for iterative system optimisation [112].

One of the first numerical techniques to be introduced is the Raimondi-Boyd method, first presented in 1958 [113]. This solution has stood the test of time due to its ease of use and accuracy. However, it should be noted that the following assumptions are made:

- Lubricant viscosity is constant.

- Independence of viscosity on pressure.
- Temperature of the lubricant remains constant as it passes through the bearing.
- Perfectly rigid bearing and shaft.
- Oil inlet is located at the angle of maximum film thickness.

Film thickness is generally found graphically via the Raimondi-Boyd technique, as seen in Figure 4.1. The bearing characteristic number (also known as the Sommerfeld number) shown on the x-axis, is a non-dimensional parameter related to the system's geometry as well as rotation speed, applied load and lubricant viscosity. Each solid black curved line on the graph indicates a specific bearing length-diameter ratio. The Sommerfeld number is a particularly convenient parameter as it enables comparisons between bearings of any geometry. Sommerfeld number can be found by the following relationship:

$$S = \left(\frac{r}{C}\right)^2 \frac{\mu N}{P} \tag{4.7}$$

Where r is bearing radius, C is radial clearance, μ is dynamic viscosity, N is rotation speed and P is projected pressure. Projected pressure is equal to the radial load over the bearing projected area and can be calculated via:

$$P = \frac{F}{LD} \tag{4.8}$$

Where F is radial load, L is bearing length and D is bearing diameter.

The main disadvantage of the Raimondi-Boyd technique is that, along with the assumptions listed above, it is limited to static loading cases. As such, the hunt for more sophisticated models continued. The mobility method, introduced by Booker [114] in 1965, provides a numerical solution to dynamically loaded bearings. Although this method is decades old, it is still frequently used and being built upon. A good example is Park et al., who in 2020 adapted the mobility method to investigate journal bearings under dynamic loads using non-Newtonian fluids, with con-rod bearings as the intended application [115].

In 2012, Benasciutti et al. applied an iterative approach, coupling a finite-element structural model with the Reynolds equation [116]. This method could therefore account for deformation effects. However, the work only evaluated results against a rigid model with no comparison against experimental measurements.

Others take a more unconventional approach by attempting to approximate the Reynolds equation using exotic mathematical techniques. For example, in 2020, Pasini et al. presented a numerical approximation of the isoviscous finite-bearing solution, Equation 4.4, by applying spectral methods to solve the differential equations [117]. Although promising, the solution still makes some key assumptions, such as constant viscosity, laminar flow and constant lubricant density.

Commercial solutions are available which allow non-experts to confidently predict complex bearing behaviour via numerical techniques with easy to use tools. For example, AIES Ltd offers a suite of solutions for different journal bearing conditions, such as TEHD (Thermo Elasto Hydrodynamic) modelling [118]. However, the methods used in such products are generally either patented or commercial secrets, meaning the method cannot be scrutinised in detail or applied independently.

So far, all of these methods are rooted in the Reynolds equation. A completely different approach is the application of neural networks by Kumar et al. in 2020 [119]. In this, the radial load is set as an input and minimum film thickness as an output. Literature data from a previous investigation was used as training data and a genetic algorithm was executed to develop the neural network. This process highlights the primary disadvantage of neural network techniques. The accuracy of any neural network is limited by the quality of the training data. In this case, training data was obtained numerically. So, although Kumar et al. present a framework that may be useful in future, the work presented cannot exceed the accuracy of the Reynolds based numerical model used. Also, the inner workings of neural network techniques by their nature cannot be easily understood by humans; in fact, these are even called "hidden layers" [120]. Therefore, it is difficult to predict whether the network would be accurate if applied to different operating conditions or a new bearing system.

Overall, numerical methods need to balance complexity with the number of assumptions made. To account for effects such as temperature and deformation, all component geometries and material types need to be modelled accurately. As such, the results are only as good as the model. Often it is difficult to obtain all parameters and these are subject to change over time due to effects such as wear [121]. Where possible, simulations should always be validated with experiments, particularly under more complex conditions such as when operating in the mixed lubrication regime. This not only increases confidence in the results but also allows refinement of the numerical technique to simulate real-world system more accurately in future situations.

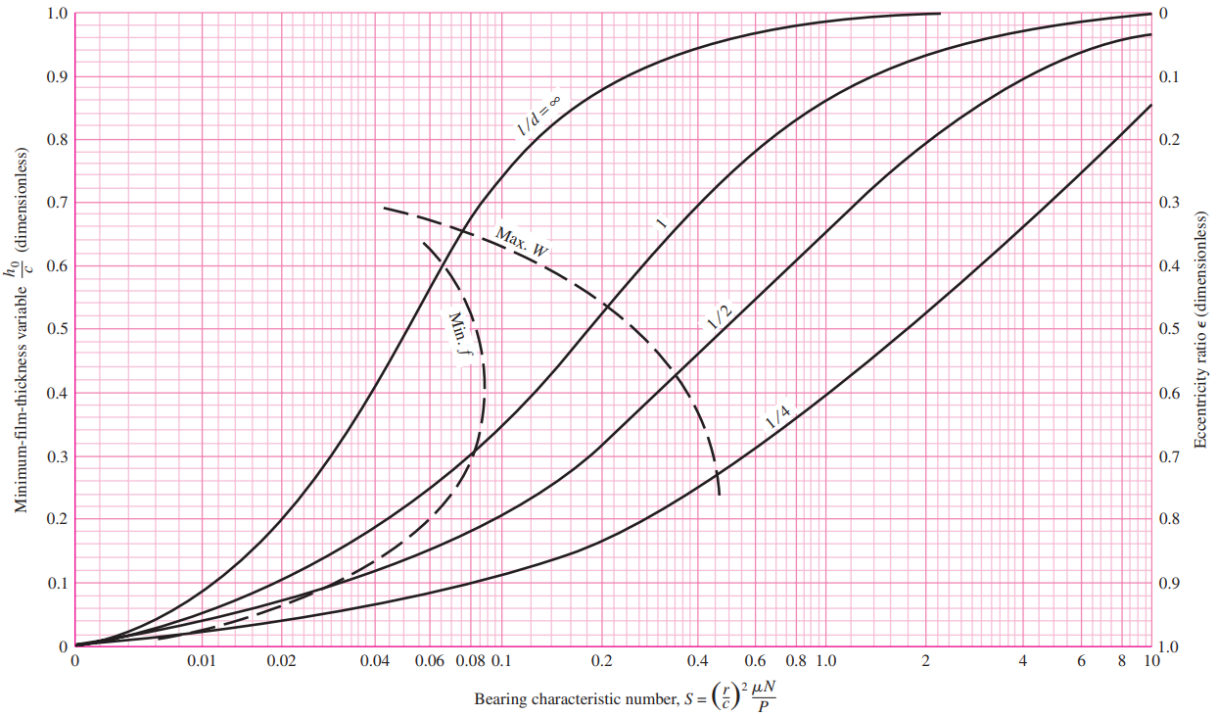

Figure 4.1: Raimondi-Boyd chart allowing the prediction of minimum film thickness in bearings when given the bearing characteristic number (Sommerfeld number) [122].

4.1.3 Optical Techniques

Both analytical and numerical methods have an innate disadvantage in that they can only predict bearing behaviour under the conditions simulated. This means they provide no condition monitoring abilities if something goes wrong, such as sudden shaft misalignment or bearing wear. This is where experimental methods can provide a solution, particularly if they can be directly applied to real-world components.

Optical interferometry is one of the most popular techniques available for the precision measurements of thin oil films. Individual product configurations may vary; however, the general principles of operation remain the same. In optical interferometry, a white light beam is aimed at the contact. When this beam reaches the interface, some of the light is reflected, and some passes through the lubricant layer. The transmitted portion of light then reflects off the opaque surface on the opposite side of the contact. Both beams travel back to an optical sensor. As the beams now have different path lengths, there is a difference between the arrival time of each beam. This results in an interference pattern due to superposition. The wavelengths of light found in this pattern indicate the lubricant film thickness, which can be inspected visually or processed by a spectrometer for more accurate measurements [123]. A schematic showing this process is shown in Figure 4.2.

The popularity of the technique is principally due to its accuracy. Optical interferometry offers high precision measurements down to films as thin as 1nm [123]. Also, systems

are available which require minimal training or technical knowledge to operate.

Higginson and Reed first applied this technique to journal bearings in 1967, although at the time they suggested the technique required further development before it could be applied to films with rapidly changing thickness [124]. This was later achieved in 1997 by Taplin et al., in which they successfully measured film thickness in a journal bearing under dynamic loading conditions to an accuracy of $\pm 0.1\mu$m [125].

Laser-induced florescence (LIF) is a similar optical technique, although this uses a florescent dye mixed into the lubricant. By shining laser light of a particular frequency at the contact, the dye will emit light at a different frequency. The intensity of the emitted radiation is a function of oil film thickness. LIF does not need the opposite face within the contact to be highly reflective, which is required by optical interferometry. However, as emitted intensity is also a function of input intensity, dye characteristics and dye concentration, LIF requires careful calibration for effective thickness measurements. Despite these challenges, Nakayama et al. applied the technique to connecting rod bearings in 2003, for which they were able to distinguish differences in film thickness across the axial profile of the bearing [126]. However, introducing dye to the lubricant can affect its performance, making it less attractive as a condition monitoring tool in real systems.

The primary disadvantage of both these optical methods is that they require at least one of the surfaces to be transparent or translucent, typically coated glass, quartz or sapphire [127]. Real bearing materials are almost exclusively opaque, and as such, there will always be inherent uncertainty in the measurement as characteristics of different materials, such as elasticity or roughness, have a considerable effect on the operation of a journal bearing. Because of these limitations, although they remain popular in the study of other components, such as EHL contacts in roller bearings and seals [128, 129], there has been a shift away from optical techniques in journal bearings as more competitive methods emerge.

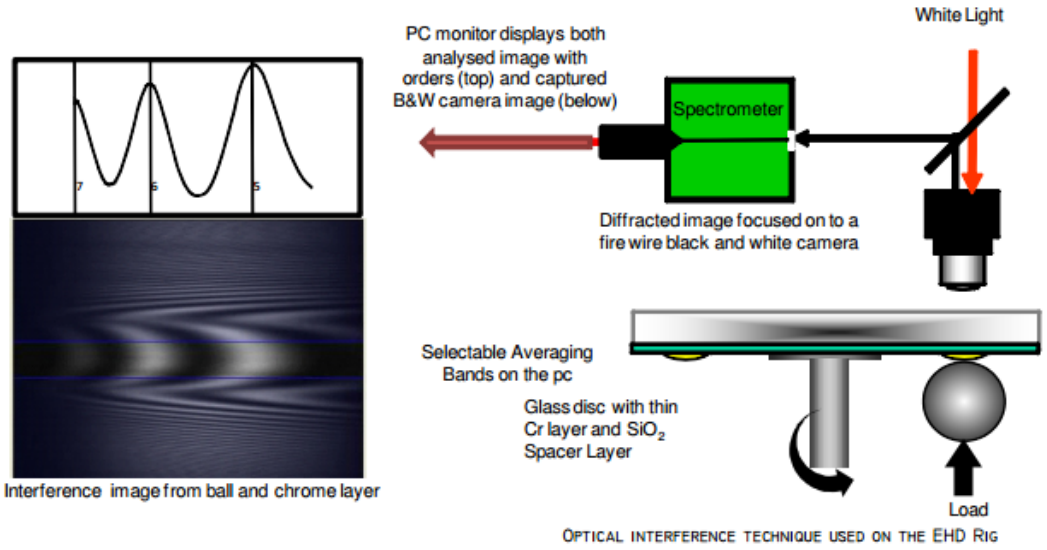

Figure 4.2: Schematic of optical interferometry system [123].

4.1.4 Electrical Techniques

The two primary electrical techniques are the total resistance method (TRM) and the total capacitance method (TCM). As their names suggest, TRM measures film thickness by observing the resistance across the interface, whereas TCM observes the capacitance of the lubricant layer. Unlike optical methods, they do not require a transparent window, and as such, they can be more readily applied to real engineering components. [130]

In TRM, the interface acts to connect the two surfaces to complete an electrical circuit. As film thickness decreases, asperity contact increases which makes it easier for the electrical current to travel across the interface. This leads to a reduction in electrical resistance.

However, if the film is too thick, asperity contact does not occur, and resistance tends to infinity. This restricts the technique to boundary and mixed lubrication regime testing unless a conductive lubricant is used. Additionally, the two surfaces must be electrically isolated to ensure a potential difference across the surfaces. [131]

TCM solves this fundamental issue by observing the change in capacitance, which allows measurements even in the hydrodynamic regime. A comparison between the two techniques in the context of journal bearings was performed by Spearot and Murphy in 1988 [132]. This study concluded that TCM is a superior technique for bearing film thickness measurements because the dialectic constant of oil is more consistent and can be measured more precisely than its electrical resistance. Consequently, the use of TRM today is uncommon.

In 2000, Paranjpe et al. applied TCM to the crankshaft bearings of an operating engine [112]. This system was able to track the change in film thickness under dynamic loading; however, there was some disagreement between measurement and prediction dur-

ing decreasing loads. The authors theorised that this was due to cavitation. Air bubbles in oil decrease the dielectric constant at local points around the bearing as pressure reduces. They attempted to compensate for this by using analytical techniques to predict the expected amount of cavitation that would occur. Therefore, they could estimate the concentration of air in the lubricant and adjust the dialectic constant accordingly. With this correction factor, film thickness measurements shifted by approximately 20%. However, assessing the accuracy of this correction factor is difficult, and results were only compared against a theoretical model.

The application of TCM was continued by Kataoka et al. in 2011, in which they also applied the technique to a crankshaft bearing in an operating engine [133]. This study agreed with the conclusions made by Paranjpe et al., noting that TCM does not take into account deformation in the bearing or crankshaft.

The simplicity of TRM and TCM techniques is also their downfall, as they only provide a measurement of the minimum film thickness and no information is gathered regarding the circumferential film thickness profile, cavitation effects or deformation of the journal bearing [131]. Alternative technologies such as the ultrasonic technique allow localised film thickness measurements, enabling more complex phenomena to be explored such as misalignment.

4.1.5 Electromagnetic Induction Techniques

Inductive sensors, also known as eddy current sensors or proximity probes, operate by passing an alternating current through a coil wrapped around a magnet. By Faraday's law of induction, this generates a constantly changing magnetic field. The introduction of a conductor, such as a steel shaft, will result in the formation of eddy currents that oppose the primary magnetic field. The strength of these eddy currents is inversely proportional to the distance between the sensor and conductor, with an increase in frequency and magnitude of the oscillations as the gap decreases. This change can be detected by the inductive sensors. Implementing a shield around the coil decreases the size of the primary field but directs flow towards the target, improving accuracy. A schematic of an inductive sensor is shown in Figure 4.3.

In 2002, Moreau et al. [134] implemented inductive sensors into a con-rod bearing test platform to study dynamic loading conditions and compare measurements against a theoretical model. Four sensors were embedded in the bearing at different locations around its circumference. This allowed a direct measurement of film thickness at distinct points, however, accuracy was limited to ± 1 μm and the presence of a sensor within the contact may have affected bearing operation.

Navhar et al. took a different approach in 2011, mounting inductive sensors outside of the contact on a static loading journal test platform [135]. A stepper motor then changed the relative angle of the inductive sensor with respect to the bearing. This enabled a circumferential film measurement with only one sensor on the bearing side. Results were

compared against a theoretical model. Although minimum film thickness results agreed reasonably well, circumferential measurements differed substantially. The authors concluded this difference was at least partly due to deflection in the shaft and bearing.

An experimental study by Chatterton et al. in 2017 studied film thickness in a journal bearing under high load, slow speed conditions. This was achieved via inductive sensors embedded into both the shaft and bearing [136]. Surfaces were reground after installation to reduce the influence of the sensor on bearing operation. A photograph of the inductive sensor embedded in the shaft is shown in Figure 4.4. This shaft-side sensor enabled film thickness measurements around the full circumference of the bearing, allowing deformation effects to be examined.

Bouyer et al. in 2017 [137], 2019 [138] and again in 2021 [139] used inductive sensors to study the effects of shaft scratches on bearing performance. In these investigations, each proximity sensor embedded in the shaft was front filled with a non-conductive epoxy, followed by shaft grinding. The 2017 study successfully demonstrated scratches on a shaft significantly impacts film thickness and pressure distribution. The 2019 study compared experimental results against a numerical simulation, which showed good agreement. The 2021 study investigated shaft scratches in even finer detail, with scratch depths ranging between 50 μm and 300 μm. They found that a multi-scratched shaft surface leads to elevated operating temperatures due to a reduced film thickness. The limitation of this implementation is that the epoxy has a different stiffness than the steel shaft; this is particularly important under high pressures. Also, the steel and epoxy will almost certainly have different wear rates and again film thickness uncertainty was relatively high, at ± 1 μm.

As shown by these examples, the technology is becoming increasingly popular for journal bearing test platforms due to its wide measurement range and ease of installation. However, the probes must be positioned within the contact for a direct measurement, which interferes with the fluid film [48]. Mounting sensors away from the contact negates these effects, although factors such as deformation in the components introduce significant measurement uncertainties. Therefore, the technique is either invasive if probes are positioned within the contact or loses accuracy if positioned outside the contact. Additionally, eddy current sensors are restricted to conductive materials, require precise calibration and are susceptible to noise from external sources [48, 140].

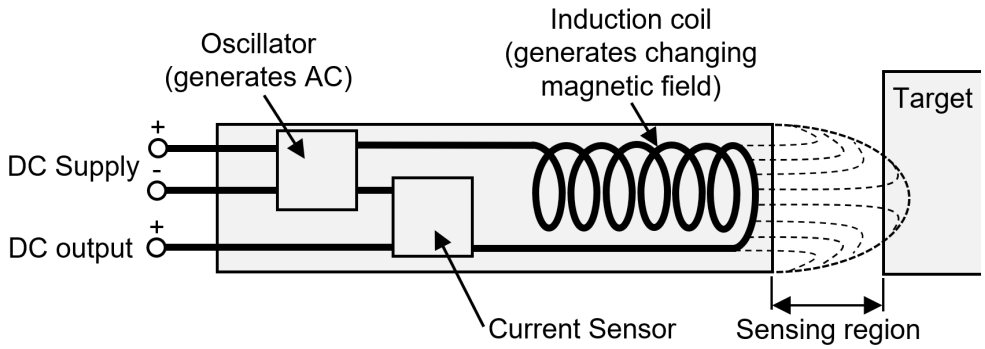

Figure 4.3: Schematic of an inductive sensor, adapted from Oladapo et al. [141].

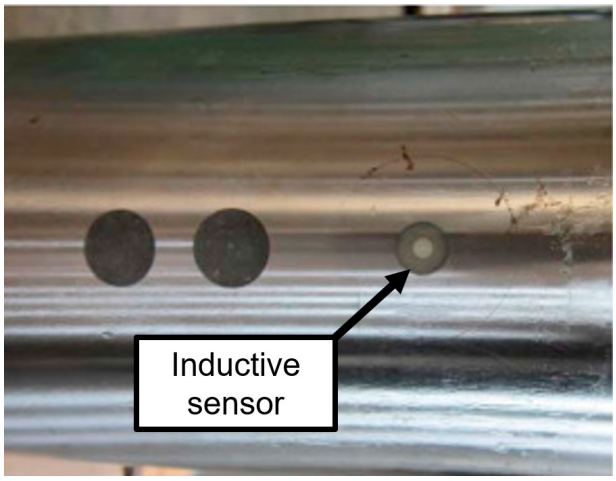

Figure 4.4: Photograph of proximity probe embedded within shaft [136].

4.2 Previous Research using Ultrasound in Journal Bearing Analysis

Ultrasound has been used to study interfacial contacts for some time. Work published by Tattersall is one of the earliest examples, applying the pulse-echo technique to study adhesive bonds in 1973 [142]. However, using the ultrasonic method to study journal bearing behaviour only began to emerge in the early 2000s. Harper in 2003 and Dwyer-Joyce in 2004 both demonstrated the technique's capabilities in a journal test rig using bearing mounted transducers with promising results [143, 101]. From here, efforts focussed on improving accuracy across a wider measurement range, demonstrating that the method can be used to analyse tribological features such as cavitation [144], and applying the technique in more specific applications.

A push to obtain a more robust referencing technique has also been made. Traditionally, references were taken before testing, often by calibrating the components in an oven at a range of temperatures. However, it was found that signal amplitude and phase were highly sensitive to the temperature gradient in the materials [145]. The gradient found in bearing operation is not easily replicated in an oven, which leads to significant

measurement uncertainty. In 2008, Reddyhoff et al. proposed a method of within-test auto-calibration, in which the amplitude and phase change responses are related via the following equation:

$$A = A_0 cos(\phi - \phi_0) \tag{4.9}$$

Where A is amplitude, A_0 is reference amplitude, ϕ is phase and ϕ_0 is reference phase [145]. This method was then applied in 2011 by Geng et al. to a bearing test rig using a 10 MHz bearing mounted transducer [146]. This was found to be reasonably accurate, although the auto-calibration method requires the shaft and bearing surfaces to be the same material.

As the ultrasonic method developed, such as with improved hardware and processing techniques, the use of shaft mounted transducers emerged. This enabled more complete circumferential measurements. In 2008, Kasolang et al. used shaft mounted transducers to obtain circumferential measurements under normal operating conditions via the spring amplitude technique [144]. In this work, signs of cavitation in the diverging region could be clearly identified. However, due to the limited range of the amplitude technique, measured film thickness ranged only between 10 μm and 40 μm in this study.

In 2020, Ouyang et al. extended the versatility of shaft mounted ultrasound by applying the spring amplitude and resonant dip techniques simultaneously [147]. This enabled a wider range of oil films to be measured. However, a gap in the measurable range between thin film measurements via the amplitude method and thick film measurements via the resonant dip method still existed. It is possible that applying the phase shift method could fill this intermediate film region.

Previous research has generally assumed the effect of pressure on acoustic velocity and density of the lubricant to be negligible. Past work has also concentrated only on normal operating conditions, in which operational parameters such as rotation speed and applied load are constant. As discussed previously, more severe operating conditions have been investigated via conventional techniques.

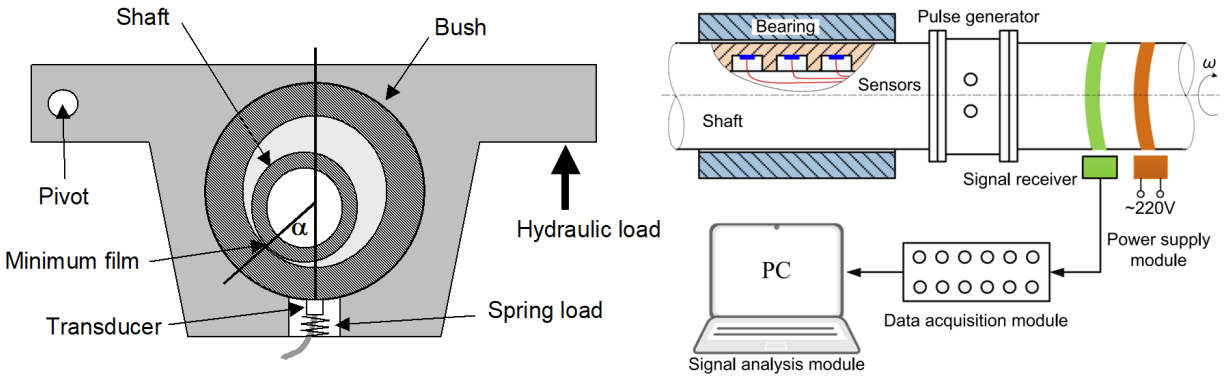

Figure 4.5: Schematics of previous bearing systems used to investigate film thickness via ultrasound. A system with a single bearing mounted ultrasonic transducer used by Reddyhoff et al. (left) [102]. A system with a shaft mounted ultrasonic array used by Ouyang et al. (right) [147].

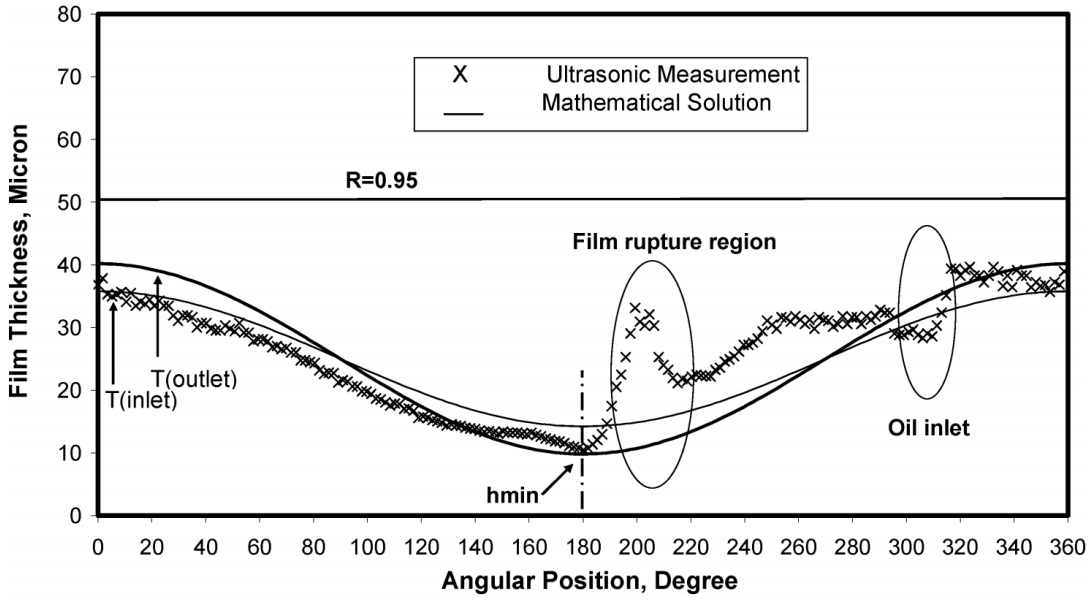

Figure 4.6: Film thickness measured around the circumference of a journal bearing by Kasolang et al. [144]. The film rupture region, where cavitation occurs, is indicated.

4.3 Conclusions

This chapter has covered the following:

- A review of current film thickness measurement techniques, including an evaluation of the strengths and weaknesses of each method. This highlighted the need for a non-invasive, high accuracy technique that can be readily applied to real bearing systems, for which ultrasonic methods may be a potential solution.
- Previous studies that have applied ultrasonic methods in journal bearing film measurements. These focus only on aligned bearings operating under "normal" operating conditions, with a constant applied load and rotation speed.

In general, findings from this review give clear justification for the project. It has been observed that although good progress has been made in journal bearing film measurements via ultrasound, there are still multiple potential areas of optimisation and study. This includes improving measurement accuracy, combining multiple ultrasonic techniques to develop a more complete method and investigating a broader range of bearing operating conditions, such as misalignment and dynamic loading, which are yet to be investigated via ultrasonic methods.

Chapter 5

Generic Ultrasonic Hardware and Method

This chapter details the hardware found in a wide range of active ultrasonic systems, including those applied to medical diagnosis, wear detection and oil film thickness measurement. The purpose of this chapter is to inform the reader as to what hardware is available, particularly so that decisions for component selection later in this study can be justified with context. Additionally, the reader may understand how components within the system interact to enable ultrasonic measurements.

5.1 Ultrasonic Hardware

The five primary components in any ultrasonic system are the transducer, coupling, cabling, acquisition hardware and of course the object being investigated. A simple schematic demonstrating how the components interact is shown in Figure 5.1. Although this study focusses on active ultrasonics, in which the transducer both generates and detects an acoustic wave, the following is equally applicable to passive ultrasonic techniques in which the system exclusively detects incoming acoustic waves from external sources.

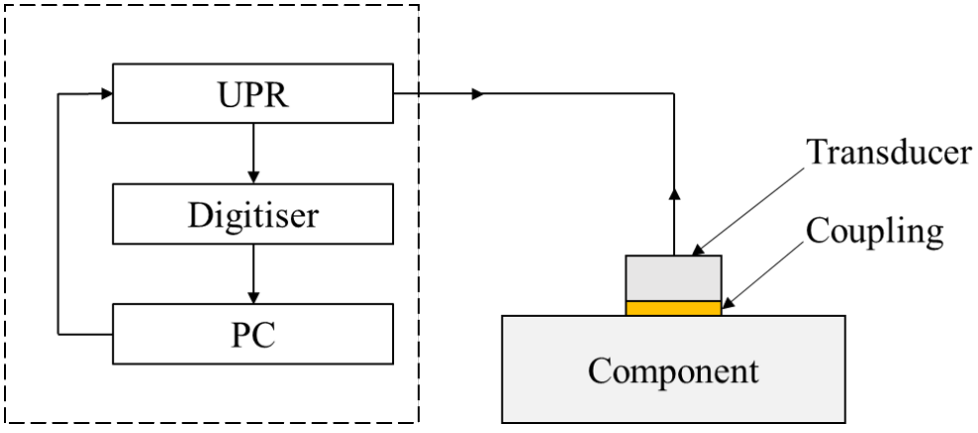

Figure 5.1: Schematic of the key hardware components in a generic ultrasonic system.

5.1.1 Piezoelectric Transducers

The piezoelectric transducer is the heart of an ultrasonic system. This component converts an applied electric field into mechanical motion, thus generating an acoustic wave that travels through the material. A transducer is also responsible for converting the incoming acoustic wave back into an electric signal to be analysed.

Selecting the right transducer is critical for success, particularly the piezoelectric element sitting at (or near) the transducer's front face. However, there is no perfect piezoelectric material that fits every situation. With dozens of mechanical properties dictating the performance of these materials, it is usually a compromise to meet the requirements of a given application. The following highlights the most important material properties one must consider when selecting a piezoelectric element.

Curie temperature, t_c: To understand this parameter it is helpful to introduce the process of how a piezoelectric material is made. Such elements are most commonly manufactured by passing a strong DC electric field through the material at an elevated temperature. This aligns the dipoles in the direction of the electric field, thus polarising the material. Cooling the element locks these dipoles into place and polarisation is maintained even when the electric field is removed [148]. The Curie temperature is the point at which the dipoles are again free to move and the permanence of polarisation is lost. Thereby, this parameter is strongly linked to, and generally slightly higher than, the maximum operating temperature of the material [148, 149].

Electromechanical coupling factor, k: Put simply, this can be thought of as the sensitivity of a piezoelectric element, quantifying its effectiveness in converting electrical energy into mechanical motion and vice versa [150]. This parameter is typically direction-dependant, for example, a particular element may be more effective, and therefore have a greater coupling factor in a shear plane in comparison to a longitudinal plane. As such, the coupling factor direction is commonly indicated by subscripts.

Dielectric constant temperature stability, $\varepsilon/°C$: This parameter quantifies the variation in energy output for a given piezoelectric element as temperature changes, with a lower value indicating better temperature stability [151]. Generally, more temperature stable elements have a lower coupling factor and as such each must be balanced depending on the application and available hardware [152].

Mechanical quality factor, Q: This parameter may be related to the sharpness of the resonant frequency [153]. The effect of quality factor in both the time and frequency domains are shown in Figure 5.2. This figure demonstrates that a high quality factor will lead to a less damped time-domain signal, which may be undesirable in thin layer systems as the successive reflections are more likely to overlap and will not be distinct. Also, energy is concentrated closer to the resonant frequency, with a narrower bandwidth in the frequency-domain. Methods such as the resonant dip technique use the frequency value in its calculation, and as such a narrow band signal has a more limited measurement range.

Thus, it is generally preferable to have a low mechanical quality factor, providing sharper time-domain signals and greater bandwidth. One exception is in high power applications where a lot of energy around the resonant frequency is required without excessive heating of the components, for example in ultrasonic cleaning which of course is outside the scope of sensing applications [154, 155].

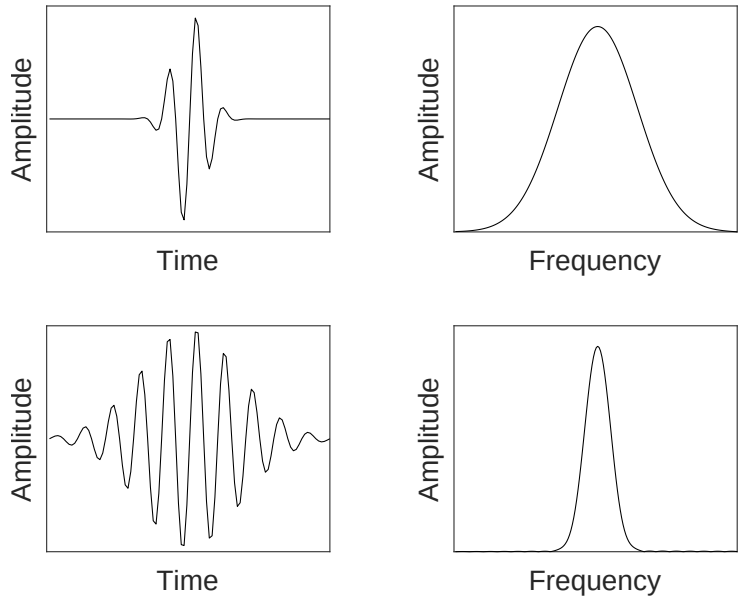

Figure 5.2: Signals with low mechanical quality factor (top) and high mechanical quality factor (bottom) presented in the time-domain and frequency-domain.

Some of the most popular piezoelectric materials are listed in Table 5.1, along with approximate values for each material property.

Table 5.1: Common piezoelectric materials and their physical properties [152].

Parameter	BiT	$Pb(Nb0_3)_2$	Hard PZT	Soft PZT	PMN-PT
Curie temperature, °C	650	280 to 480	215 to 340	150 to 360	140
Coupling factor, -	0.22	0.35 to 0.43	0.46 to 0.51	0.48 to 0.53	0.55
Temperature stability, $°C^{-1}$	1	1.6 to 2.2	4 to 9	5 to 25	-
Quality factor, -	350	15 to 650	150 to 800	10 to 35	80

Although the primary component of a transducer is its piezoelectric element, there are other features that may improve its performance. For example, quality factor may be reduced further by introducing backing material to damp oscillations, a popular composition of which is epoxy resin doped with tungsten powder [156]. A backing material also protects the cable-transducer element from corrosion and physical damage, along with providing strain relief to the cable.

Wear plates are commonly found on the front face of commercial transducers designed for temporary acoustic measurements. These wear plates protect the transducer from

scratching or cracking from the physical environment as well as from elevated temperatures [157].

A matching layer may also be found on the front face of the active element. This component improves the efficiency of acoustic energy transmission by the principle of superposition. By making the matching layer thickness equal to one-quarter of the wavelength of the resonant frequency, reflections within the matching layer constructively interfere, multiplying the signal energy. The thickness must be accurate, as an incorrect thickness can disrupt the wavefront. Also, to maximise transmission the matching layer material should have an acoustic impedance approximately halfway between the transducer material and the material being measured. [158].

5.1.2 Transducer Arrangement

Just as important as transducer type is how they are positioned within the system. The most basic arrangements use either a single element or pair of elements in one of the three following layouts, also shown in Figure 5.3:

Pulse-echo: A single transducer both generates and receives the acoustic wave. The most frequently used method, pulse-echo has low system complexity and does not require access to the rear face of the component.

Pitch-catch: One transducer generates an ultrasonic wave and a nearby transducer receives the signal. This allows a combination of piezoelectric element material types. For example, it may be preferable to use a hard PZT to transmit the ultrasonic wave as it can handle greater driving voltages and a soft PZT as the receiver due to its greater sensitivity.

Through-Transmission: Often considered a sub-category of the pitch-catch arrangement, in which the transmitter is positioned opposite the receiver. This approach does not rely on a signal to be reflected, although it does require access to both sides of the host material. Through-transmission is commonly used in thickness gauging and simple flaw detection applications.

As acquisition hardware improves and applications become more demanding, the use of transducer arrays is becoming ever more popular. Instead of measuring at a single point as done by one sensor, a row of elements can capture a two-dimensional image with each pulse and a grid of elements can capture a full 3-dimensional volume.

Transducer arrays also enable techniques such as beam shaping and steering. By exciting particular elements at different times in a dense ultrasonic array, the wavefront may be directed and shaped to allow greater dimensional accuracy without physically sweeping the transducer. The downside of this technique is its complexity. Not only does it require more sophisticated pulsing hardware, the system is often more difficult to operate and thus technicians require more extensive training [159].

Another unlocked method is full matrix capture. In this, a single element generates a sound wave and all other elements in the array capture its reflected signal. This is repeated for every element in the array. Full matrix capture provides the same potential benefits as phased arrays, although with greater flexibility. However, pulsing every sensor in turn takes time and as such the method is less suitable for dynamic systems [160].

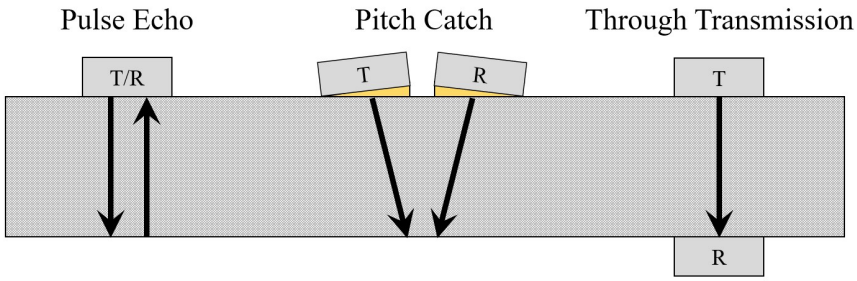

Figure 5.3: Most common sensor configurations, with transmitters and receivers denoted T and R respectively.

5.1.3 Couplants

With transducer type and arrangement decided, a method to bond the transducer onto the host component must then be selected. Again, the optimum solution depends on the requirements of the application. Figure 5.4 provides a flow diagram that may be used as a coupling selection guide.

Transducers may be either temporarily or permanently bonded to a surface. Temporary bonds, arguably the more conventional method, allow the user to rapidly adjust transducer position to measure over a wide area. This is ideal for NDT applications where the surface of multiple large components can be investigated. The position of permanent bonds on the other hand have to be selected with care as they cannot be adjusted once installed. However, permanently bonded transducers have the advantage that they can be installed for years without maintenance and experience no significant degradation in performance. Also, without the need for additional components such as wear plates, permanent elements are far more compact and are therefore more easily embedded within components [161]. For these reasons permanent bonds are the most popular choice for recent ultrasonic film thickness measurements and as such will be the focus of this section.

Temperature is another major consideration in selecting the right coupling. Cyanoacrylates allow rapid installation, however at even moderately elevated temperatures, typically around 65°C, the bond weakens and is permanently degraded. Also, the bond stiffness is lower than other competing adhesives [162]. As such, cyanoacrylates are most suited to quick trials in which the instrumentation process can be performed in minutes, rather than hours. Although the resulting bond line is less stiff, the reduced instrumentation time sometimes outweighs a slightly worse signal response.

Epoxy-phenolic adhesives can withstand temperatures between -269°C to 260°C; the vast majority of bearing applications fit comfortably within this range [86]. However, epoxy-phenolic adhesives require an elevated temperature curing process which must exceed the expected operating temperature by around 30°C [163]. Not only does this add time to the instrumentation process, it also adds an extra layer of complexity, particularly with larger components that may not fit inside a standard oven for example.

Brazing is an emerging bonding technique designed for the most extreme high-temperature environments, such as monitoring steels in power plants or in-situ testing of graphite-epoxy composites during curing [164]. In this, the transducer and host medium are heated and a hot filler material flows into the interface. Gold and silver-copper alloy foils have been demonstrated as ideal filler materials for brazing, capable of maintaining a good bond-line up to 800°C [165]. At these high temperatures more specialised piezoelectric elements, such as lithium niobate, are also required.

Generally, to get an optimum signal the bond line should be as thin as possible, resulting in a stiffer transducer-component interface. However, in some instances, a more viscous epoxy is preferred. One such application is in rigid PCB arrays for which some flexibility in the bond is required. An example is the PCB array transducer installed in the test platform described in Chapter 10, a photograph of which is shown in Figure 5.5

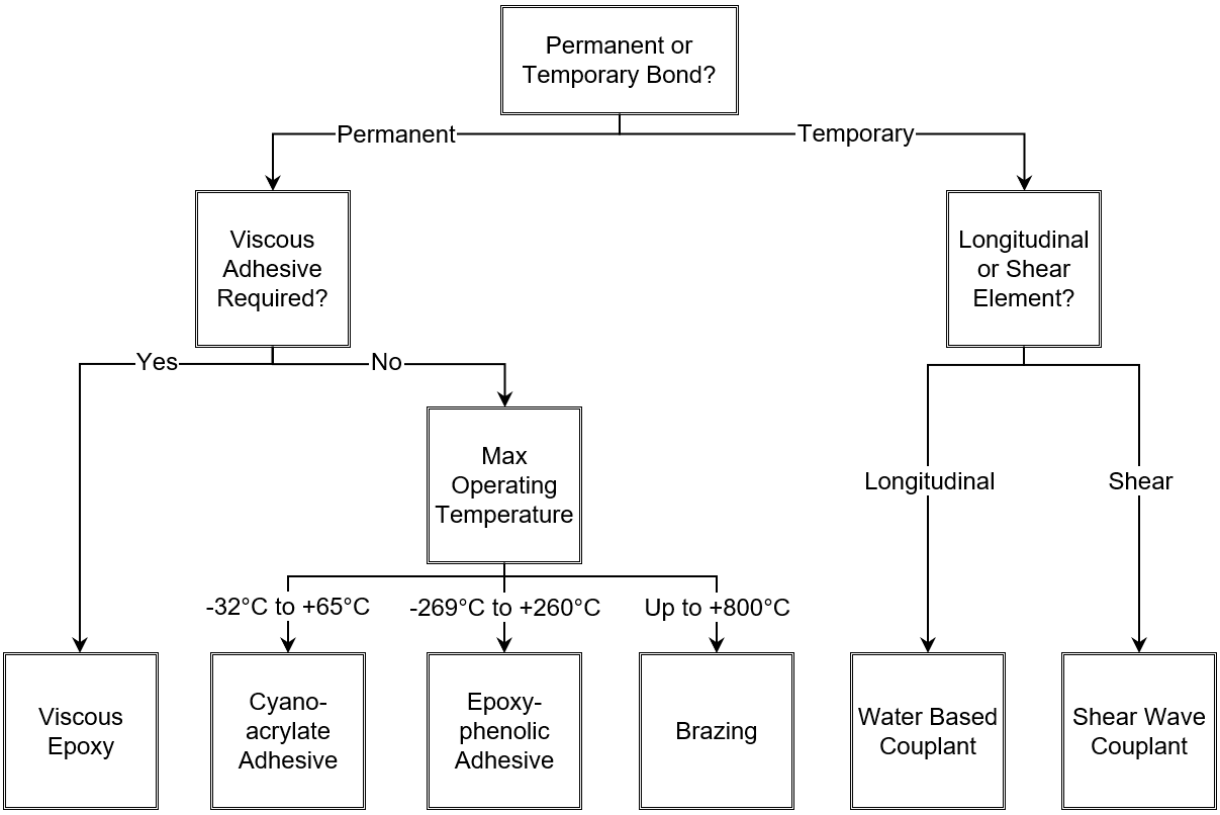

Figure 5.4: Couplant selection diagram.

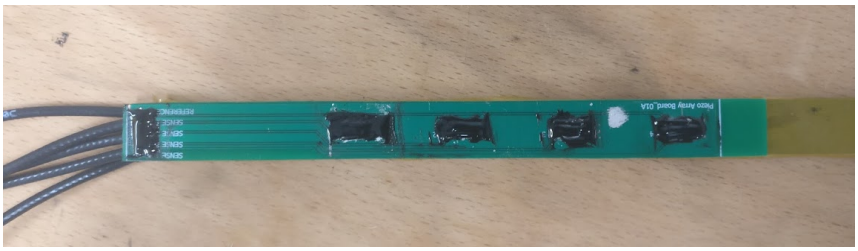

Figure 5.5: Photograph of a rigid PCB array coated with viscous epoxy before installation.

5.1.4 Cabling

The obvious consideration when selecting a cable is its maximum operating temperature, generally dictated by the insulation material. However, other environmental factors may also lead to unexpected failure if a poor choice is made. For example, if the cable assembly is in contact with lubricants then PFA rather than PVC insulation is superior as it is more resistant to chemical degradation.

Generally, a thicker cable offers more mechanical strength and more shielding from noise than an equivalent thinner cable. However, geometric constraints, such as narrow cable ejection channels, may limit the thickness of each cable. As such, thin cables should be as short as possible, with a junction box converting to a thicker cable if the acquisition hardware is some distance away.

Most single element transducers use coaxial cables due to their simplicity and excellent shielding from external sources or adjacent cables (known as crosstalk). However, with high-density arrays, wiring each transducer individually can quickly become impractical and require a large cross-sectional area. In this case, certain ribbon cables are often a more suitable alternative, reducing cable size while still minimising crosstalk [166]. Further advantages and disadvantages of cable types in transducer applications are outlined in Table 5.2, with photographs of each shown in Figure 5.6.

Figure 5.6: Common transducer cable types. Coaxial (left) [167], ribbon (centre) [168] and multicore (right) [169].

Table 5.2: Advantages and limitations of common transducer cable types.

	Advantages	Limitations
Coaxial cable	Braided shield protects electrical signal from external noise. Available in a variety of sizes and material types. Can be terminated with standard connectors.	One cable per sensor, therefore good cable management required for high-density arrays.
Ribbon cable	Suitable for high-density arrays.	Cannot be terminated directly with many standard connector types.
Multicore cable	Cheap. Easy to work with.	Cores not individually shielded, can lead to cross-talk.

5.1.5 Ultrasonic Pulser-Receiver

As its name suggests, the UPR (Ultrasonic Pulser-Receiver) has two main functions: generate an electric signal to excite the transducer element and receive the reflected signal, including filtering and amplifying the response. Below are some of the most popular waveforms used in signal generation, with corresponding examples shown in Figure 5.7:

Impulse/spike: The most straightforward way to excite a sensor is to hit it with a quick burst of energy. This is often achieved by rapidly discharging a capacitor [170], thus the simple circuitry leads to this being a low-cost option. In reality, the shape is not a simple vertical spike, instead, there is a sharp non-linear rise in voltage before reaching its peak, see Figure 5.7. Because of this rise shape, the frequency spectrum is broadened, although the phase spectrum is not so distinct [171]. Also, because the energy is only supplied over such a short time, impulse waves have a high peak-average power ratio (PAPR). As such, higher voltages are required to obtain a good SNR which can overheat the sensor element [172].

Square wave: Requiring slightly more complex hardware than an impulse, square waves maintain a constant voltage over a set pulse length, with very rapid rise and fall times. This pulse length can be adjusted to match the centre frequency of the element to optimise signal quality. As the voltage is sustained longer than for an impulse it has a lower PAPR. Square waves used in ultrasonic applications are generally uni-polar [173, 174], with the waveform taking a 'top-hat' or inverted 'top-hat' shape, although UPRs capable of bi-polar square waves are emerging in popularity [175].

Sine wave: This waveform fits more in line with the natural expansion and contraction pattern that a piezoelectric element experiences, which can improve signal response amplitude. That said, this is somewhat counteracted by a higher PAPR than square

waves, so the maximum allowable voltage is reduced [176]. As with square waves, a train of multiple sine waves can be sent to improve SNR. However, this leads to a longer signal response, thus there is a danger of individual reflections merging when path length is low.

Chirp wave: This waveform excites all frequencies within a range in turn. Chirp waves usually sweep through frequencies at a linear rate, $f(t) = c(t) + f_0$, or an exponential rate, $f(t) = f_0 k^t$, where f is frequency, t is time and c and k are rate-of-change variables. Because of their constant frequency gradients, linear sweeps produce more uniform amplitude-frequency responses. Conversely, exponential sweeps can be controlled to spend more time at higher frequencies, thus improving SNR within the range of interest [177]. The main downside of chirp waves is that they have a far longer pulse length than all other waveforms presented, meaning unless the path length is large, individual reflections will no longer be distinct. For this reason, they are only very recently being applied to film thickness measurements and so far only to surface films [178].

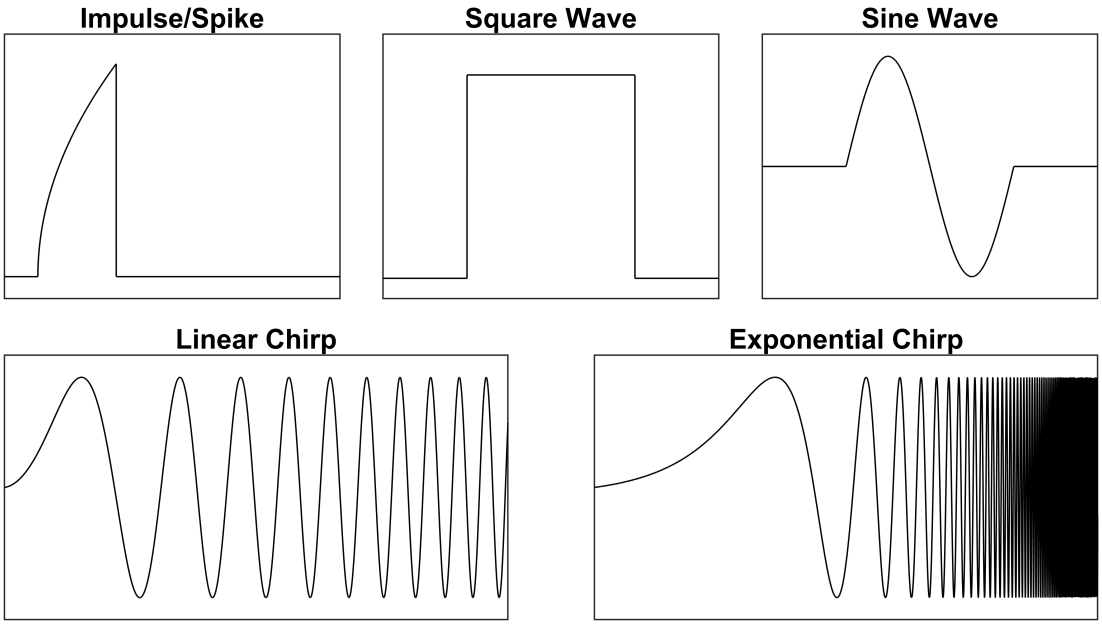

Figure 5.7: Common waveforms used in ultrasonic signal generation.

It should be noted that some advanced UPRs can be programmed to generate more than one of these waveforms, whereas more low-cost solutions are often limited to one type. Another aspect to consider is pulse repetition frequency (PRF), which is the rate at which individual pulses are sent. Depending on UPR hardware, this can range from less than 1 Hz to 100 kHz and greater [170, 174]. PRF is important in rapid dynamic conditions so that the event is captured with a sufficient number of measurements.

When the signal returns, gain settings on a UPR can create a uniform increase or decrease in amplitude across the full length of the signal. Increasing gain also amplifies any noise by the same proportion, meaning SNR will remain the same. A sufficient amplitude is required so that a good vertical resolution is obtained in digitisation, although peaks

will be cut off if the gain is set too high. Therefore a balance must be struck, including accounting for any potential increase or decrease in signal amplitude during the test program. For example, temperature variations may affect the electromechanical coupling factor, thereby changing signal response amplitude. More advanced systems, most commonly within the medical industry, have a time gain compensation (TGC) feature. This increases the gain proportionally at each time-step, counteracting the reduction in amplitude with distance due to attenuation, scattering and wave dispersion [179]. However, this is not required in most film thickness applications as the depth of interest is narrow, as such gain can be optimised just for this small region.

Signal noise occurs most often at frequencies higher or lower than the frequency bandwidth of interest. For example, slow rotating machinery may produce a substantial level of low-frequency noise. As such, filters designed to remove unwanted frequencies can significantly improve SNR. The four primary filter types are low-pass, high-pass, band-pass and band-stop filters, as shown in Figure 5.8. Low-pass filters attenuate high-frequency content and high-pass filters attenuate low-frequency-content. Band-pass filters attenuate both low and high frequencies, leaving intermediate frequencies, whereas band-stop filters do the opposite, removing only intermediate frequencies. In film thickness applications a band-pass filter is most popular as frequencies outside the transducer bandwidth are generally undesirable and would only originate from external sources.

A sharp cut-off frequency is not usually the best option as it can lead to a "ringing" effect, where frequencies close to the cut-off overshoot [180]. Therefore, a gradient is usually applied. There are numerous algorithms to define this slope, each with its own benefits. For example, the Butterworth algorithm eliminates the ringing effect with a smooth transition and no ripples [180]. Figure 5.8 shows a selection of the most common filtering algorithms.

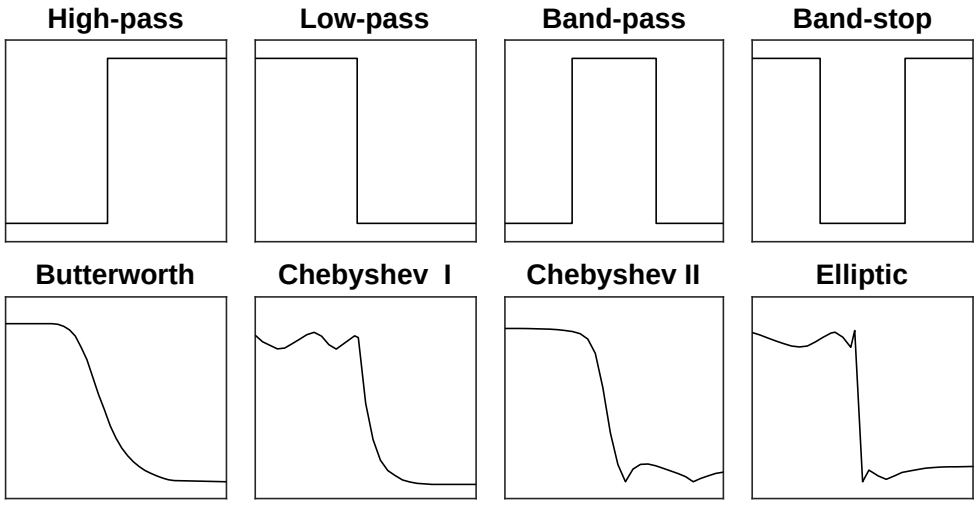

Figure 5.8: Amplitude against frequency for high-pass, low-pass, band-pass and band-stop filters (top row). A selection of common filter algorithms (bottom row).

5.1.6 Digitiser

In preparation for saving the received signal and performing further processing, the analogue signal must be discretised. This is the job of the digitiser. One of the key parameters when selecting digitiser hardware is the sampling rate. This is defined as the number of data-points per unit of time. The Nyquist theorem states that the sampling rate must be at least twice that of the highest frequency present in the signal. If the sampling rate is too low then aliasing will occur, causing different frequencies to become indistinguishable [181].

In practice, it is advised to use a much higher sampling rate, typically at least ten times greater than the centre frequency [174, 182]. So for example a transducer with a 5 MHz centre frequency would require a 50 MHz digitiser.

5.1.7 Acquisition PC

Of course, there must be a way to control this hardware, adjust settings and record data. This is achieved in most cases by a PC. It is common for the components of the acquisition hardware (UPR, digitiser and PC) to be integrated into one device. Integrated systems might also have reduced electrical noise as all hardware is shielded in one unit.

Via the PC, time-domain signals can be windowed to capture the section of interest. This is particularly important in high-speed applications where gigabytes of data can be recorded in a matter of seconds, rapidly filling hard drives. Saving massive amounts of unnecessary data is wasteful and increases the computational load, which is particularly critical if real-time film thickness measurements are required. The PC may also be responsible for handling and recording other sensor measurements, such as temperature or torque data.

5.2 Signal Processing

Figure 5.9 shows the steps performed to obtain film thickness measurements, starting with a raw ultrasonic signal. As previously discussed, the UPR handles filtering and amplification of the analogue signal, followed by digitisation by the digitiser. Depending on PRF and the capabilities of the acquisition PC, real-time processing can range from simply saving the digital signal for future analysis to outputting a live film thickness measurement. In this example, the acquisition PC zero-pads the time-domain signal and performs an FFT ready for further analysis.

Zero padding is a simple process in which the time-domain signal is extended by adding zeros at its end. This is performed because many FFT algorithms are far more efficient when the length of the time-domain signal is a power of two [183]. So for example, if the time-domain length is 900 samples, 124 zero values can be added to decrease processing time. Also, zero-padding can result in a smoother frequency curve by interpolation. Note that this increase in spectral density is not strictly the same as increasing resolution in the frequency-domain, which can only be achieved by sampling more data [183].

An FFT is then applied to the padded time-domain signal. This outputs both frequency amplitude and phase information, which can be separated. The amplitude and phase spectra may then be used to calculate film thickness using several ultrasonic models. In this example, three of the most popular techniques are presented, the spring amplitude, phase shaft and resonant dip techniques.

Reflection coefficient, R, is found by dividing the amplitude of the signal by the amplitude of an air or thick film reference. This can be performed over the full frequency spectrum or by selecting an index frequency, which is more computationally efficient. Similarly, phase shift is obtained by subtracting the phase of the signal by the phase of a reference, again this can be performed over the full spectrum or at an index frequency. Finding the resonant dip frequency is slightly different, and is achieved by locating the minimum reflection coefficient within a frequency range. When each of these values has been calculated they may be applied to the corresponding equations in Section 3.7 to determine film thickness. The exact complex method can also be applied similarly, although film thickness is a function of both reflection coefficient and phase.

From Figure 5.9 we can see an advantage in ultrasonic film thickness measurements, in that data capture and much of the processing is identical when using multiple techniques. Therefore not only can new models be applied to old data, it also simplifies signal processing, reducing computational load.

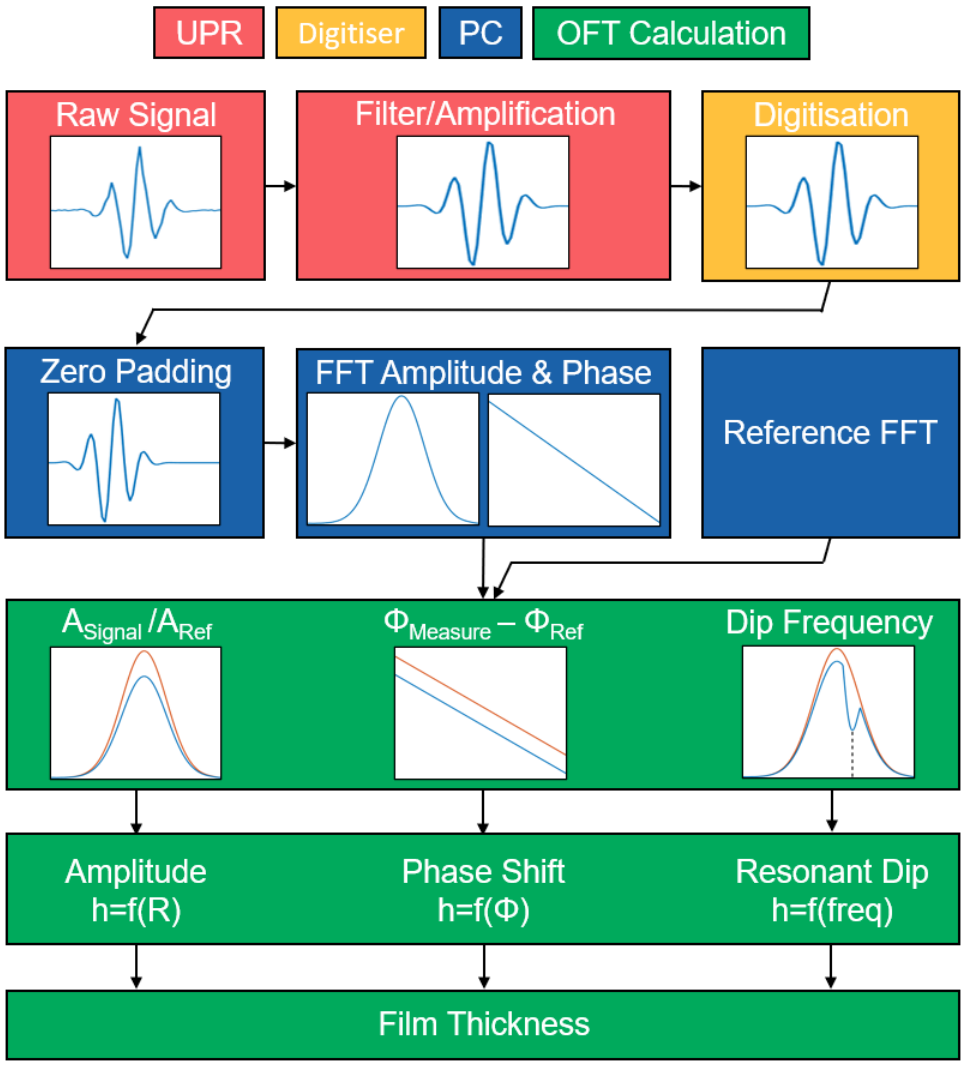

Figure 5.9: Flow diagram of signal processing method, with the role of the UPR, digitiser and acquisition PC indicated. The functions relating film thickness to R, Φ and resonant dip frequency are shown in Equations 3.17, 3.18 and 3.20 respectively.

5.3 Conclusions

This chapter has introduced the primary ultrasonic hardware components and how they are used in measurements, including:

- Key properties of piezoelectric transducers.
- Description and benefits of different transducer arrangements.
- Considerations for selecting coupling and cabling types depending on the application.
- The role of the UPR, Digitiser and PC in generating and acquiring ultrasonic data.
- How ultrasonic signals can be processed to obtain film thickness measurements.

Chapter 6

Statically Loaded Journal Rig Development

The following chapter starts with an overview of the design of the journal bearing platform, named BAXTER (BeAmish TEst Rig), used in static loading conditions. This includes the various iterations of the system during the development stages. This section is followed by a description of how the specifications such as load range and operating temperatures were selected. The author was responsible for leading the design and implementation of the system as part of this project. This includes conceptualisation, specification development, component design and manufacture, assembly, preliminary testing, troubleshooting and processing software development.

6.1 Overview of BAXTER Rig Design

A bespoke journal bearing test platform, named the BAXTER test rig, has been designed and commissioned with the capabilities of circumferential film thickness measurements via ultrasonic transducers embedded in the shaft. A schematic and photograph of the bearing platform are shown in Figures 6.2 and 6.3 respectively.

In this design, two spherical rolling element bearings support a rotating shaft in a fixed axial position. One of these support bearings is allowed to move axially slightly so that any thermal expansion does not result in beam bending.

A journal bearing located between these support bearings is loaded using a hydraulic cylinder via a flexible linkage. This linkage is free to articulate in multiple degrees of freedom; such that when load is applied via a hydraulic actuator the floating bearing assembly may find its natural position. This ensures the shaft and bearing are aligned during operation. The journal bearing assembly is flooded with lubricant, which is continuously circulating. Flooding the assembly ensures starvation will not occur during testing. Lubricant is stored in a heated circulation bath, which allows accurate lubricant inlet temperature control. A schematic of the journal bearing, including oil inlet position at 27°, is shown in Figure 6.1, with θ denoting attitude angle.

Along with ultrasonic sensors, conventional measurement hardware is also installed on the test platform. K-type thermocouples monitor temperature within the bearing assembly, oil bath and oil inlet. A load cell monitors applied load, an encoder records rotation angle and a torque transducer enables friction measurements. Four eddy current gap sensors are located on the outside of the bearing assembly to enable indirect film thickness measurements. The locations of these gap sensors are shown in Figure 6.5. This gap sensor configuration was inspired by Plantegenet et al., in which they mounted gap sensors in the same manner to investigate thermal unbalance effects [184].

A flow diagram showing the connections between each measurement hardware item is displayed in Figure 6.6. The test platform specifications and operating parameters used in the present investigation are shown in Table 6.1.

Figure 6.3 also highlights the iterative nature of the test rig design process. Three major versions were implemented, with each successive iteration increasing functionality as well as improving ease of assembly and operation. Version 1 was designed as a proof of concept, with no ultrasonic sensors installed, to understand the key bearing design considerations. Version 2 implemented a new shaft instrumented with ultrasonic transducers, high-performance twin rolling support bearings and an HRC coupling. Version 3 introduced a torque transducer rated up to 250 Nm, an improved bearing housing designed for rapid bearing replacement and a high-performance backlash-free bellows coupling.

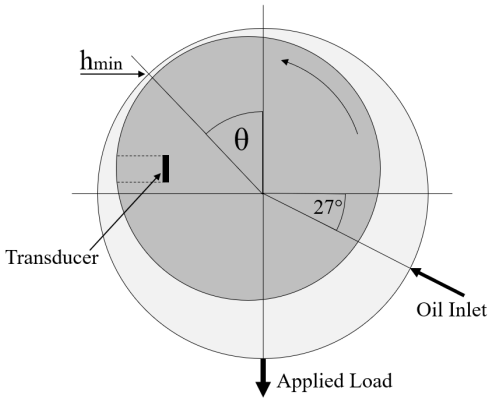

Figure 6.1: Schematic of bearing geometry including the position of oil inlet, with θ denoting attitude angle.

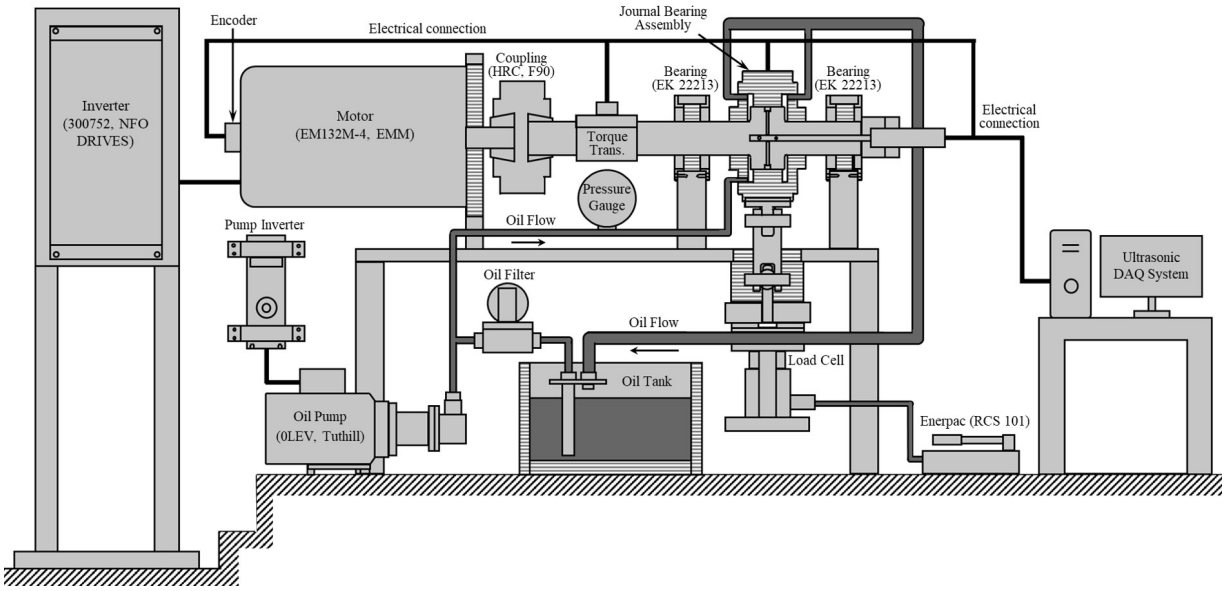

Figure 6.2: Schematic of BAXTER test platform.

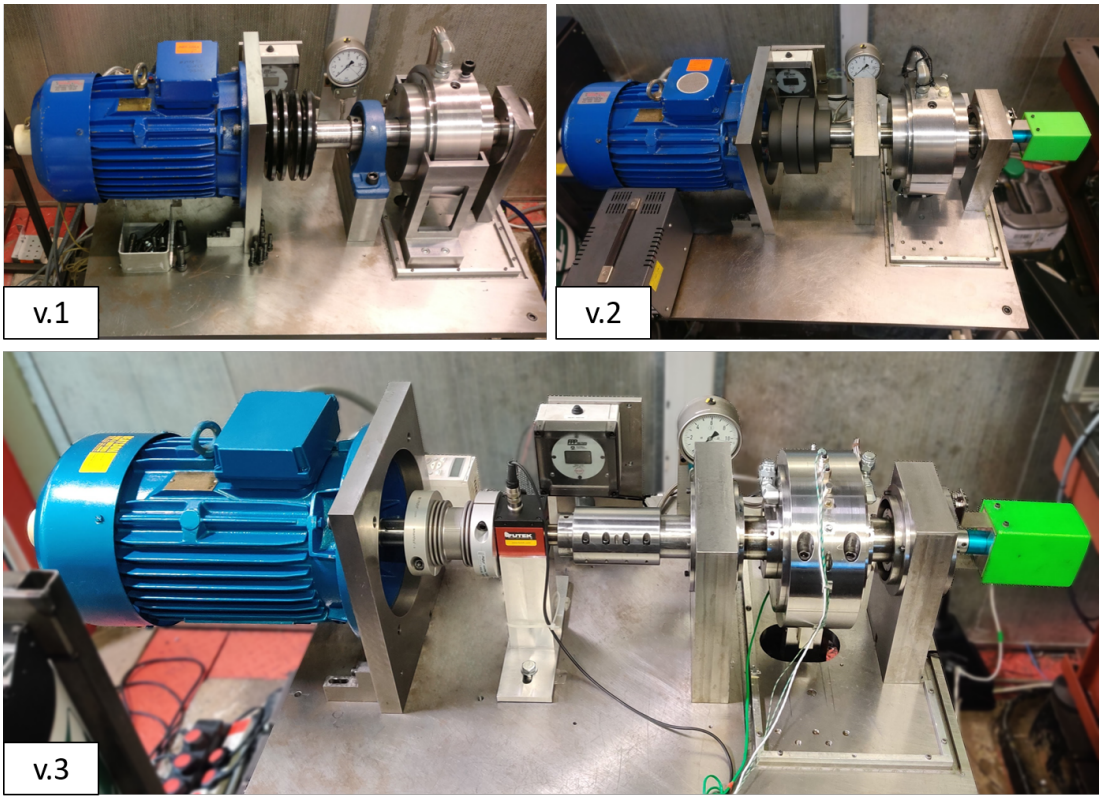

Figure 6.3: Photograph of BAXTER test platform, taken during each of the three major design iterations.

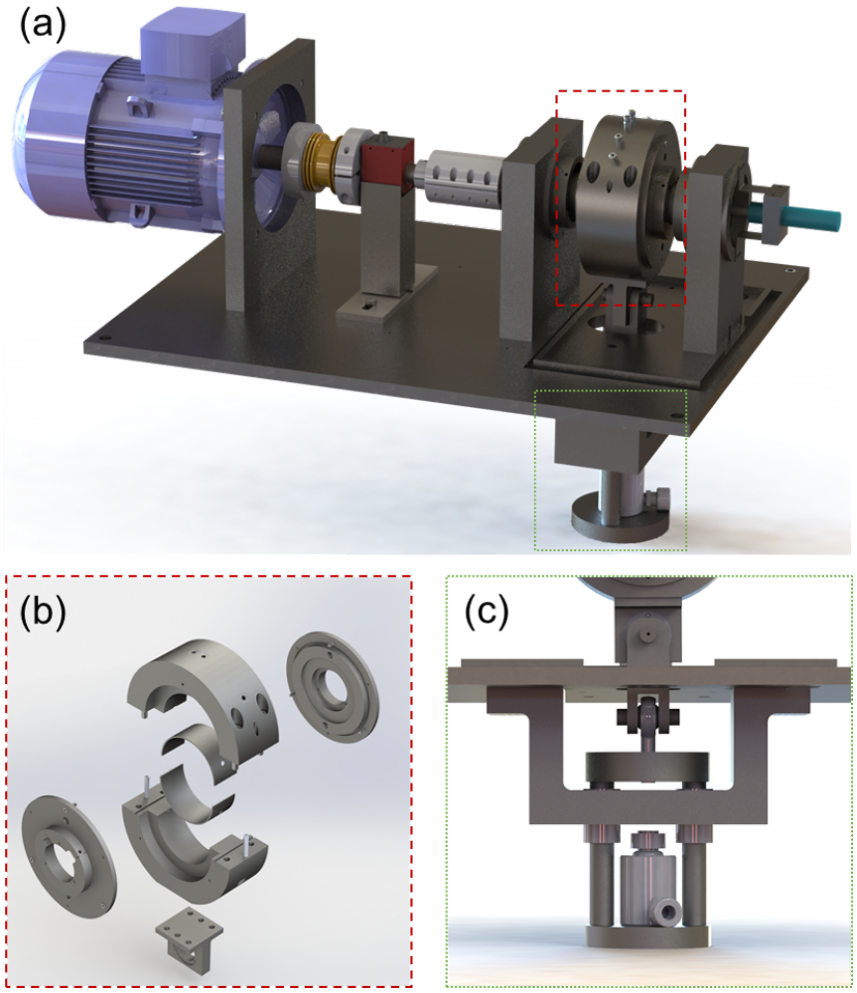

Figure 6.4: CAD renders of BAXTER test rig. a) Dimetric projection of full assembly. b) Exploded view of bearing assembly. c) Side view of loading system.

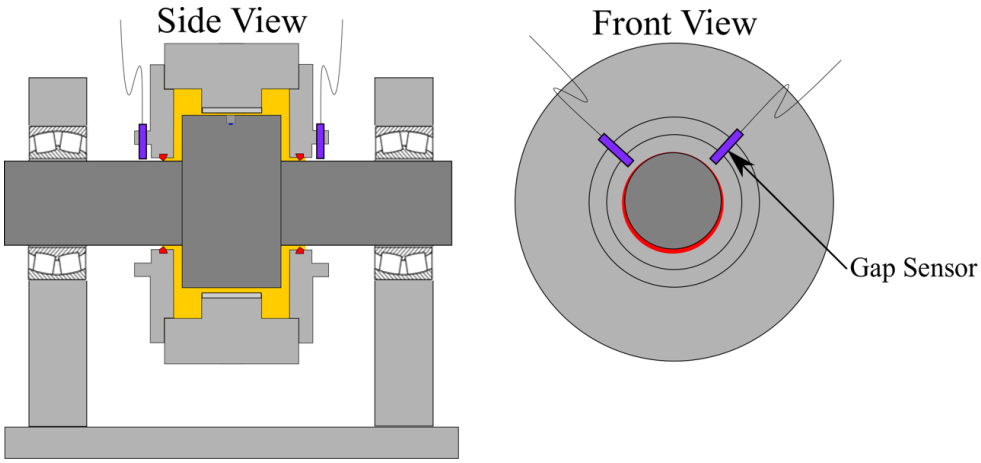

Figure 6.5: Partial schematic of BAXTER test platform with gap sensor locations indicated.

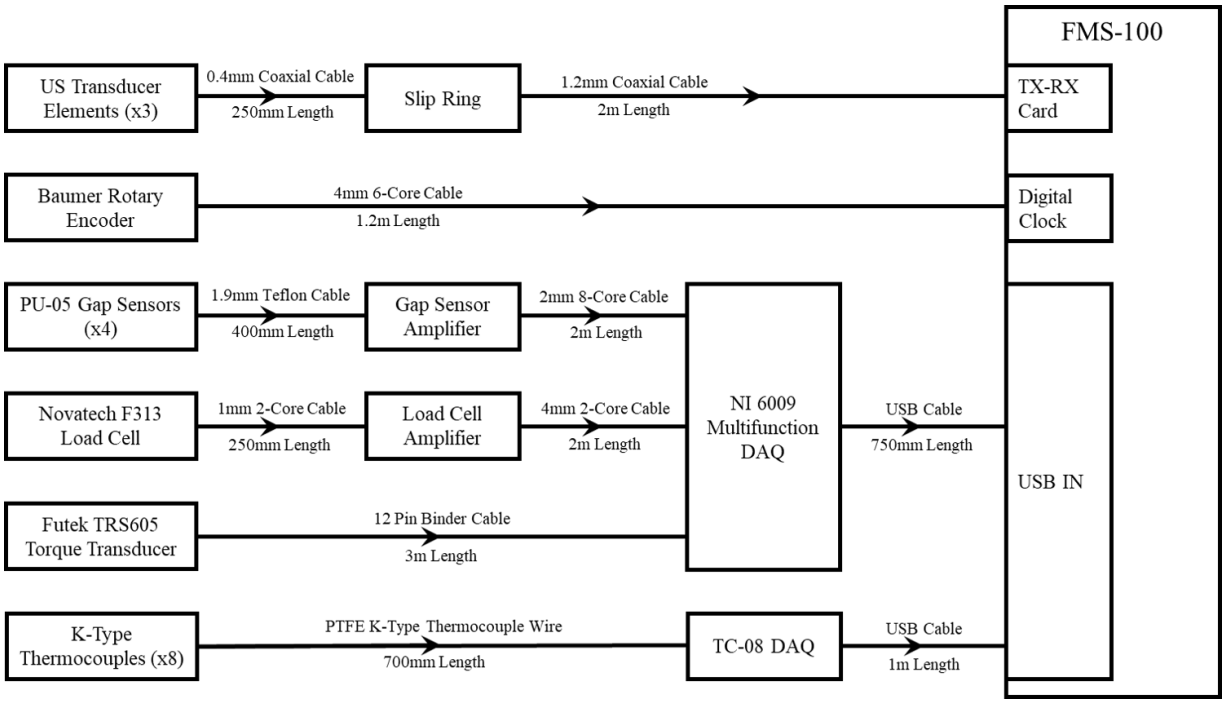

Figure 6.6: Measurement hardware flow diagram for BAXTER rig.

Table 6.1: BAXTER rig operating parameters.

Parameter	Value
Bearing radial clearance, C	50 μm $(+0 - 5\ \mu\text{m})$
Bearing internal diameter, D	112.08 mm
Bearing length, L	50.55 mm
Load range, W	1-25 kN
Rotation speed, N	100-1500 rpm
Ultrasonic acquisition rate	80 kHz

6.2 Developing Test Rig Specifications

A primary requirement of this test platform is that it can accurately simulate conditions found in a variety of real-world components. This is particularly useful for large-scale applications such as marine stern-tubes, in which the bearings often exceed 1 metre in diameter. Using such a large real system for a variety of test cases would be prohibitively expensive, let alone time-consuming. However, just like using Reynolds number to relate a scale model in a wind tunnel to an aircraft, a relationship between the journal bearing test platform and the system it is emulating must be made.

6.2.1 Matching via Shear Rate

The first parameter one may use to relate two systems is shear rate. As described in Chapter 2, the shear rate is simply a measure of how quickly particles are moving with

respect to their neighbours. For example, an oil layer between two plates in relative motion can be considered as a stack of infinitely thin layers, with shear rate as the speed at which each layer is moving compared to the layer on either side of it. As such matching systems via shear rate is particularly useful for investigating lubricants that are potentially non-Newtonian.

To determine a suitable shear rate range for which the system should be capable of operating over, the shear rates found in real bearing systems were researched. Figure 6.7 shows typical shear rates found in industrial gas turbine bearings, automotive connecting rod bearings and marine stern tube bearings. These are systems that industry has a particular interest in furthering understanding. Also shown are the quoted shear rates from a selection of popular viscometers. This highlights that many of these viscometers suffer from a low shear rate measurement range compared to those found in real bearing systems. Therefore, any effects due to shear thinning would not be represented. VROC (Viscometer/Rheometer-on-a-Chip) and TBS (Tapered Bearing Simulator) viscometers do have a higher shear rate range, however, operating conditions may still be less realistic than a scaled bearing system. For example, these viscometers typically operate under a different pressure range than in real journal bearings.

Using this information, the design applied load, shaft rotation speed and bearing temperature ranges were selected. From these, the expected film thicknesses and therefore shear rates could be calculated. An example using a standard SAE 0W-8 oil and applying parameters at the extremes within test platform specifications is provided in Table 6.2. In this table, the film thickness is predicted via the Raimondi-Boyd technique. The shear rate range calculated in this example is also shown in Figure 6.7.

As with most conventional viscometers, the potential shear rate range in this test platform also varies depending on the viscosity of the particular oil being investigated. A more viscous oil, such as a standard SAE 60 lubricant would have an increased film thickness under the same conditions and therefore a reduced maximum measurable shear rate. Conversely, using a lower viscosity oil, for example PAO-4, would result in thinner oil films, leading to a higher maximum measurable shear rate. However, the test platform is designed to be adaptable, with room to install a gearbox if a future project demands the exploration of a different shear rate range. Also, the bearing assembly may be reconfigured to allow misaligned or offset-load testing. Uneven loading across the axial plane induces a localised film thickness reduction close to the bearing edge, thus increasing shear rate within this region. Misalignment testing is explored further in Section 9.1.

Table 6.2: Shear rate prediction in bearing platform using SAE 0W-8 lubricant.

Parameter	Minimise shear rate	Maximise shear rate
Bearing temperature, $°C$	15	110
Applied load, kN	1	25
Rotation speed, rpm	50	1500
Predicted film thickness, μm	16.4	3.4
Shear rate, s^{-1}	**18,000**	**2,580,000**

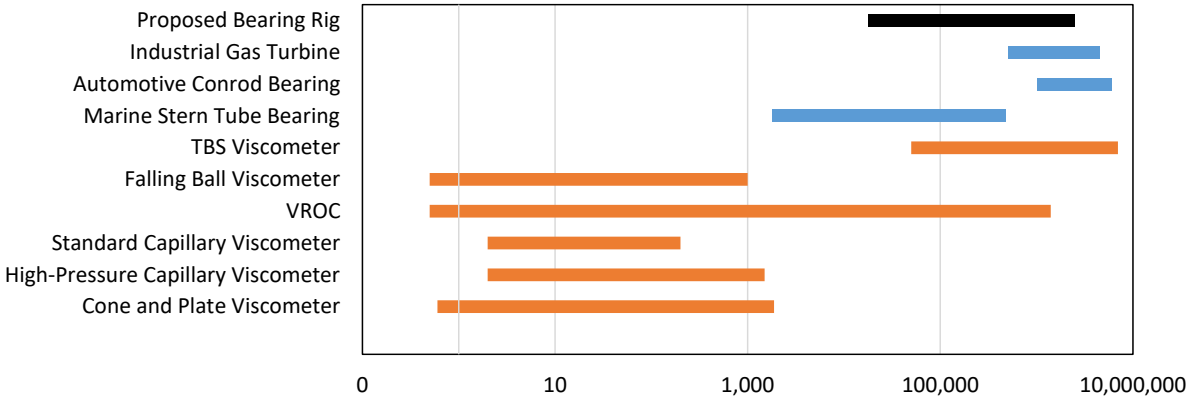

Figure 6.7: Approximate range of shear rates found in common bearing systems and the measurable shear rates in a range of popular viscometers [46, 185, 186, 187, 188, 189, 190, 191, 192, 193, 194].

6.2.2 Matching via Sommerfeld Number

An alternative measure to relate bearing systems is the Sommerfeld number, introduced in Section 4.1.2. This non-dimensional parameter allows direct comparisons between bearings of different geometries. The range of Sommerfeld numbers typical in common bearing applications is presented in Table 6.3, along with the range predicted for the Baxter test rig. This prediction is calculated using SAE 0W-8 lubricant. In a similar manner to shear rate, different lubricant viscosities alter the potential Sommerfeld number range, with higher viscosity shifting the range up and reduced viscosity shifting the range down.

Also shown in Table 6.3 is projected pressure. Even though the loads in very large systems such as marine stern tubes and gas generators are much greater, the projected area is also larger. As such, with the right balance, the same bearing pressures can be achieved using a much smaller bearing.

Although the test platform has the goal of simulating a variety of bearing types, it would be extremely difficult to design a single test platform that can adapt to simulate every bearing application. For example, turbocharger bearings have such a high Sommerfeld number due to their low loading and incredibly high rotation speeds, typically in the order of 100,000 rpm [195]. As such, it was decided that this was not the range of interest,

particularly as there is more value in simulating larger bearings which are more difficult to work with on real systems. In smaller-scale applications, it is often more efficient to use the real system, either with the components isolated in a test cell or as part of the full assembly during normal operation. That said, the test platform could be redesigned to enable high speed, low load operating conditions if required for a future project.

Table 6.3: Sommerfeld numbers in common journal bearing systems, *proposed test rig boundaries are calculated using SAE 0W-8. [196, 197, 195, 198, 199]

	Automotive big end	Automotive turbocharger	Marine stern tube	Proposed test rig*
Bearing diameter, mm	40 to 100	5 to 10	400 to 800	112
Bearing length, mm	25 to 50	4	300 to 1600	50.55
Radial clearance, μm	25 to 50	15	400 to 1200	45
Film thickness, μm	2 to 50	-	60 to 200	1.2 to 30
Projected pressure, MPa	5 to 27	0.025	0.5 to 2	0.15 to 4.4
Sommerfeld number	**0.004 to 1.5**	**>5**	**0.025 to 0.07**	**0.001 to 4**

6.2.3 Optimum Sensor Type and Frequency

Using the criteria detailed in Section 5.1, a variety of transducer materials were compared to identify which was most suitable for the shaft embedded ultrasound sensors. A soft PZT, specifically Pz27 (lead zirconate titanate), was selected due to its low mechanical quality factor [200, 201] as a broadband signal may be necessary to measure the wide range of film thicknesses this bearing system may experience. In addition, Pz27 has good sensitivity, which is key as the sensors need to have a small diameter to meet geometric constraints. Also, the signal must overcome electrical noise from rotating components and noise introduced as the signal passes through the slip ring.

Pz27 also has a high working range, at $250°C$, due to its high curie temperature of $360°C$ [152, 201]. This is critical as localised contact temperatures may exceed the maximum system temperature of $110°C$ for short periods. As such, it is wise to include a large safety factor. The amplitude of acoustic waves generated by Pz27 is reasonably temperature dependent [201], however, the live referencing technique presented later in Section 7.4 mitigates related uncertainties.

As discussed in Section 3.7, the transducer frequency is a primary factor driving measurable film thickness range and thus selecting the correct transducer centre frequency is of utmost importance. As this test platform aims to measure film thickness around a full circumference, the measurement range may span two orders of magnitude and is therefore too wide for a single ultrasonic model. As such, a combination of techniques is required. Although the exact complex model will be investigated later, the sensor frequency specifications will be defined by the more established resonant dip, spring amplitude and spring phase shift models.

The practical range of the spring amplitude and phase shift models are dictated not only by frequency but also by the amount of noise in the signal. In this investigation, a limit of $R = 0.99$ and $\Phi = 0.025$ will be applied. The measurable range of the resonant dip technique is defined by the transducer's centre frequency and bandwidth. The soft PZT used in this investigation has a usable frequency range of approximately 30% on either side of the centre frequency; as seen in Figure 7.23, for which usable frequency is defined by a 12 dB bandwidth. Using these limits the measurable film thickness boundaries with respect to frequency for each model are shown in Figure 6.9.

Conveniently, Figure 6.9 demonstrates that the amplitude and phase shift models always overlap for this given system, irrespective of frequency. However, when considering a single frequency there is a small gap between the phase model and minimum resonant dip model. That said, this gap can be eliminated by processing results over multiple frequencies, provided the transducer bandwidth is sufficiently broad. For this test platform, the gap can be eliminated between 1 MHz and 10 MHz given that the 12 dB fractional bandwidth is $\pm 11\%$, which is rather conservative. As such, the total upper limit is simply defined by considering the resonant dip technique and the lower limit is defined by the amplitude model.

Calculating the upper limit for circumferential lubricant film thickness is trivial as, unless something has gone wrong, it cannot significantly exceed the shaft-bearing diametric clearance. In this particular test platform, the design diametric clearance is 100 μm (+0 μm, -10 μm). Using a lubricant acoustic velocity value of 1350 m/s, which is typical for mineral oils under such conditions [202], Figure 6.9 shows that to achieve 100 μm the minimum usable frequency must be 9.0 MHz or lower.

During the design stage, it is difficult to exactly predict what the thinnest expected film will be, particularly as the test platform is designed to operate using a wide range of lubricants. Table 6.3 shows that, under aligned conditions with SAE 0W-8 grade lubricant and within test platform capabilities, the thinnest expected film is 1.2 μm. However, the test platform is also designed to operate under more severe conditions such as with misaligned-shaft and run-down conditions, in which these films may be significantly lower. Also, although SAE 0W-8 is a reasonably thin lubricant grade, even lower viscosity lubricants may be of interest in future. As such, 0.8 μm was considered an appropriate lower bound. With this value, Figure 6.9 shows that transducer frequency must be no lower than 6.4 MHz to satisfy this criterion. With an upper and lower frequency bound now defined, an appropriate transducer centre frequency may be selected. In this investigation, 7 MHz was proposed as transducers with this centre frequency are readily available.

Another aspect to consider is whether the acoustic signal would enter the far field region before it reaches the interface. The near field formula in Equation 3.5 shows that transducer frequency and diameter affect the transition point from near to far field. Given a proposed transducer diameter of 3.5 mm, transducer frequency of 7 MHz and that steel shaft acoustic velocity is 5800 ms^{-1}, the minimum distance is calculated as follows:

$$N = \frac{D^2 F}{4c} = \frac{(3.5 \times 10^{-3})^2 \times 7 \times 10^6}{4 \times 5800} = 3.70\ mm \tag{6.1}$$

As the design distance between transducer and interface is 11 mm, it is therefore comfortably within the far field region, thus a clean signal reflection can be expected at the interface.

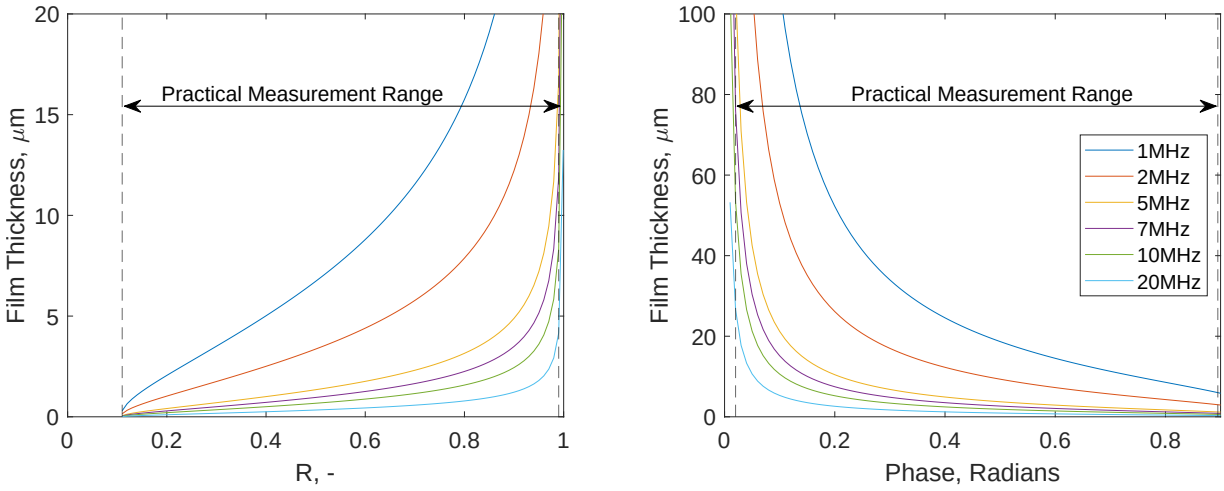

Figure 6.8: Relationship between film thickness and reflection coefficient (left) and phase (right) for a range of sensor frequencies, with practical measurement ranges indicated. Relationships are specific to the BAXTER rig.

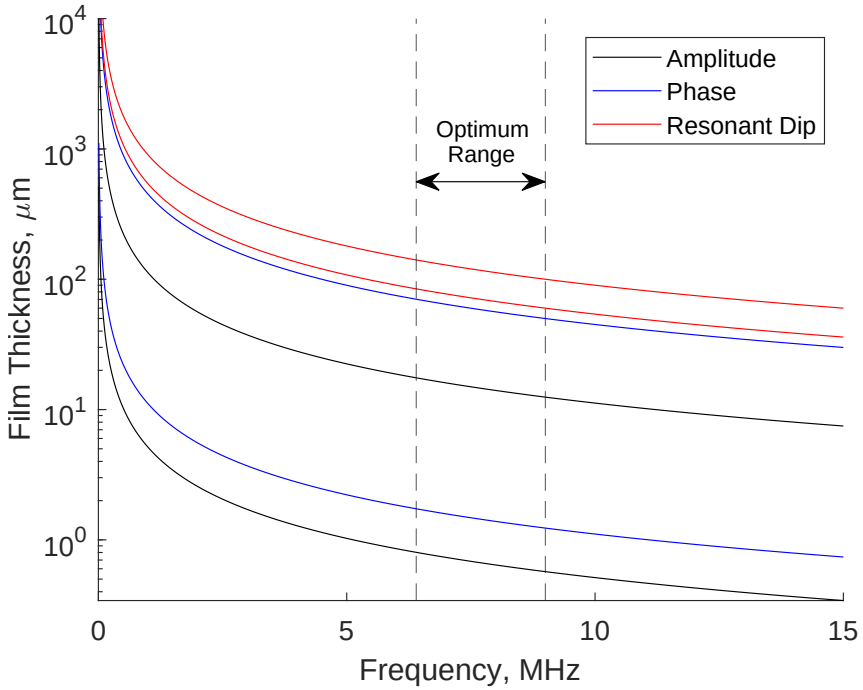

Figure 6.9: Film thickness measurement range with respect to frequency for the ultrasonic amplitude, phase shift and resonant dip techniques. Ranges are calculated using the proposed bearing platform system parameters. Optimum frequency region is indicted, with the upper bound dictated by the resonant dip model and the lower bound by the spring amplitude model.

6.3 Hollow Shaft Instrumentation

A key advantage of ultrasonic sensors in film measurements is that they can be mounted away from the interface of interest, thus offering a direct non-invasive measurement. As such, the method in which the sensors are embedded is critical to ensure the transducer assembly does not interfere with the hydrodynamic flow whilst maintaining good measurement accuracy.

For this test platform, the shaft has been instrumented with six ultrasonic transducers using a pin design, with locations indicated in Figure 6.10. In this design, the transducer element is mounted on top of a barrel-shaped steel pin using epoxy-phenolic adhesive and protected with epoxy resin, as shown in Figure 6.11. Cables are ejected out the end of the shaft and connect to the acquisition hardware via a brushless slip ring.

The pin is manufactured using the same material as the shaft (EN24 Steel). As such the stiffness of both pin and shaft are the same, meaning stresses due to thermal expansion are minimised. This is in contrast to inductive probes, which are generally constructed using dissimilar materials.

Once the pin is installed and fixed in place with thread sealant, the shaft is cylindrically

ground to its final diameter. This ensures that the pins do not influence the operation of the test platform. A photograph of the shaft after grinding is presented in Figure 6.12, in which evidence the pins cannot be observed on the shaft running face.

The integrity and quality of the sensor signals were monitored at each stage of shaft instrumentation. Figure 6.13 shows the reflected signal for Pin A in both the time and frequency domains before the epoxy resin was applied, after the epoxy resin was applied and after the shaft had been ground to its final dimensions. There is a clear increase in damping once the epoxy is applied, as evident by the sharper signal in the time-domain and wider bandwidth response in the frequency-domain. After grinding, time-of-flight is reduced, due to the reduction in path length. Also, the frequency response distribution changes. This is likely because the pin face has changed from flat to curved, matching the profile of the shaft running surface. This effect is explored in more detail in Section 7.5.1.

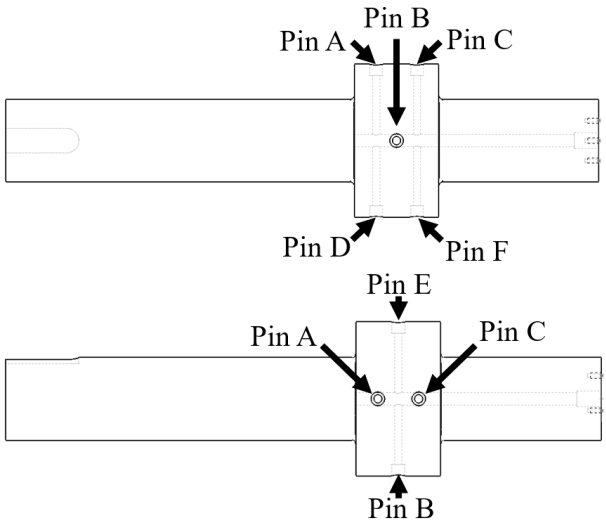

Figure 6.10: Schematic of instrumented shaft showing pin layout.

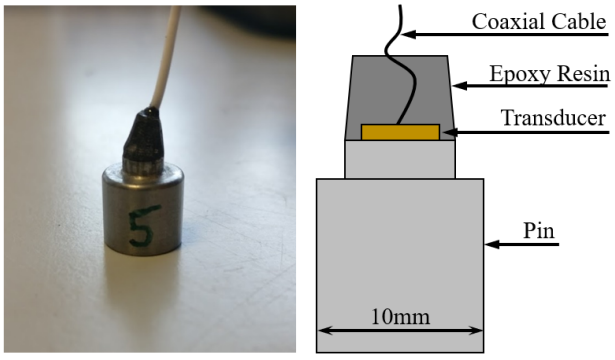

Figure 6.11: Photograph (left) and schematic (right) of instrumented pin.

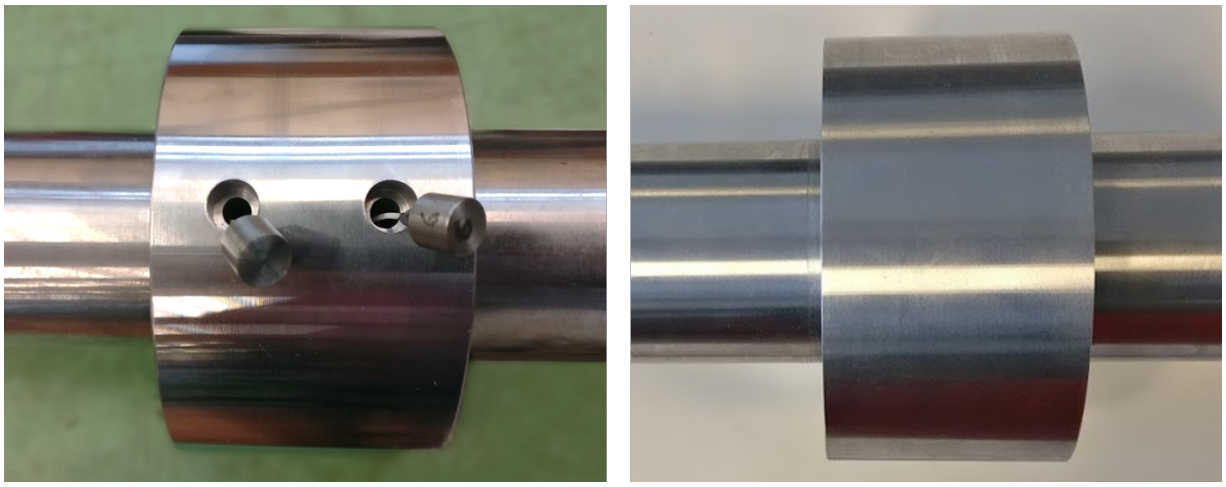

Figure 6.12: Photograph of shaft pin installation (left) and shaft after grinding (right).

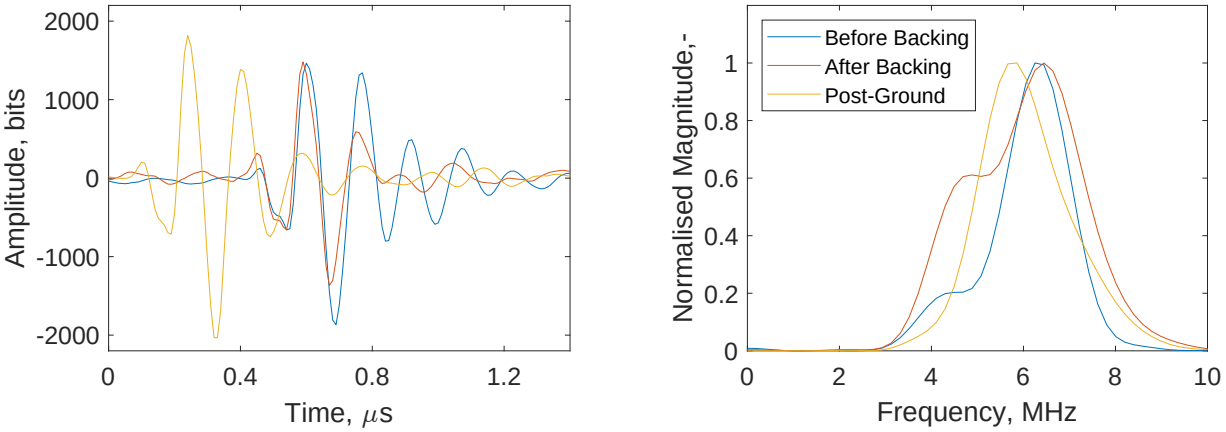

Figure 6.13: Time and frequency domain reflected signal responses, captured at different stages of the instrumentation process. For determining frequency-domain response via FFT, the time-domain is windowed between 0.4μs and 1.2μs for the before backing and after backing cases, whereas the post-ground time-domain signal is windowed between 0μs and 0.8μs.

6.4 Validating Bearing Clearance

One of the most important measures dictating bearing performance is the clearance between the bearing and shaft. This can significantly affect hydrodynamic pressure distribution and magnitude, meaning a high accuracy value is required to reliably predict film thickness. For example, the Sommerfeld number is related to radial clearance squared. Therefore, a small uncertainty in clearance may lead to a much larger error in film thickness predicted via the Raimondi-Boyd technique.

Measuring clearance before assembly can be challenging, particularly due to bearing crush. Before installation, bearing shells are not perfect semi-circles and only take the form of the bearing housing once seated. As such, in this investigation clearance was measured

after bearing installation. This was achieved in two ways.

The first method used dial gauges to measure the displacement of the bearing housing when loaded and unloaded. This process is photographed in Figure 6.14. Dial gauges were positioned on either side of the housing and zeroed with the bearing assembly unloaded, thus pulled down onto the shaft only by its own weight. The bearing assembly was then lightly loaded upwards and the change in displacement was observed. Using this technique, diametric clearance was found to be between 95 μm and 105 μm.

The second method was an equally simple approach. The bearing assembly was lightly loaded and shims of known thickness were inserted in turn into the gap between bearing and shaft. This process is photographed in Figure 6.14. Shim thickness increased by 5 μm intervals until the shim would no longer fit in the gap. This gave a diametric clearance value between 100 μm and 105 μm.

Both studies were performed with the bearing assembly drained of any lubricant, else a static squeeze film may introduce an error in the measurements. These results are close to the design diametric clearance, 100 μm (+0 -10 μm), checked by measuring the shaft geometry with a micrometer during the manufacturing process. The clearance values obtained from this study will also be useful later in determining the accuracy of the resonant dip technique presented in Section 8.1.1.

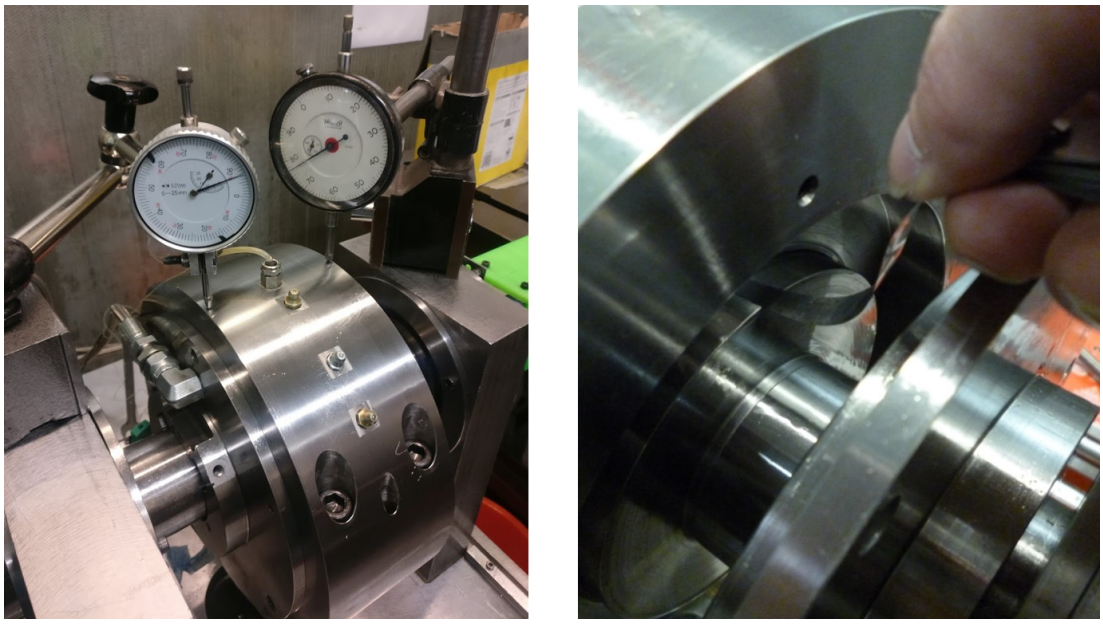

Figure 6.14: Photographs of experiment to validate bearing clearance with the use of dial gauges (left) and shims (right).

6.5 Conclusions

This chapter has covered the design of the bearing platform used in static and anomalous operating conditions testing presented in subsequent chapters, with particular focus on the development process and justifications for design decisions. This includes:

- An overview of the bearing platform, including installed sensor hardware and key operating parameters.
- The process to calculate optimum test platform specifications so that it may accurately simulate conditions in real systems. This has been achieved by matching shear rate and Sommerfeld number.
- The method applied to instrument the shaft with ultrasonic transducers.
- How radial clearance of the bearing-shaft interface was validated.

Chapter 7

Film Thickness Acquisition Methodology

This chapter describes the steps that were developed to obtain film thickness measurements using the journal bearing test rig presented in Chapter 6. Accurate values for the lubricant acoustic velocity and density are required before film thickness calculations can be made and as such the method to obtain these values will be discussed first. This is followed by an observation of how signal reflection coefficient and phase varies as the shaft rotates. Reflection coefficient and phase shift measurements are then applied to determine bearing acoustic impedance via a novel technique.

The method for determining film thickness in the thin film region is then discussed, including a study into the frequency dependence of these measurements. Finally, the process for obtaining thick film measurements via the resonant dip technique is presented.

7.1 Lubricant Characterisation

As referenced in Section 3.7, it is evident that all ultrasonic methods discussed require an accurate lubricant acoustic velocity value to calculate film thickness effectively. The acoustic velocity of oil is sensitive to changes in temperature and pressure. As such, the relationship may be expressed as the sum of functions:

$$c = f(T) + g(p) + h(T, p) \tag{7.1}$$

Where c is acoustic velocity, T is lubricant temperature and p is pressure. The contribution of function $h(T, p)$ is typically an order of magnitude lower than that of $f(T)$ and $g(p)$ [203, 204]; therefore it has been considered negligible in the following work for experimental simplicity.

7.1.1 Acoustic Velocity-Temperature Relationship

In practically all bearing applications temperature may vary significantly with changing operating conditions. Thus, it is standard practice to characterise the lubricant acoustic

velocity with respect to temperature before or after testing when applying ultrasonic techniques.

Such a characterisation has been performed in the present study via a bespoke speed of sound test rig, photographed in Figure 7.1. The bath is manufactured using Invar to reduce measurement uncertainty from thermal expansion. Invar is a nickel-iron alloy that has a particularly low thermal expansion coefficient (hence its name, a contraction of 'invariable'). The chamber length was also calibrated using distilled water, which has a well defined acoustic velocity-temperature relationship. An embedded 10 MHz longitudinal transducer measures the acoustic velocity of the lubricant.

The bath chamber was filled with the test lubricant (Shell Melina S 30, a marine diesel engine mineral oil) and placed in a programmable oven. The temperature was steadily raised to 130°C over 7 hours, held at 130°C for 1 hour, then cooled to 20°C over a period of 7 hours. ToF measurements were recorded every 20 seconds. Results from this test are shown in Figure 7.2. A second-order fit yields the following acoustic velocity-temperature relationship:

$$c(T, p = 0) = 0.0039T^2 - 3.39T + 1555.2 \tag{7.2}$$

Figure 7.1: Photograph of acoustic velocity-temperature calibration rig.

7.1.2 Acoustic Velocity-Pressure Relationship

Previous journal bearing studies that apply ultrasonic techniques often account for changes in acoustic velocity with temperature. However, no instances in which the effect of pressure is considered could be found in the available literature. In this investigation, the relationship has been measured via a pressure rig. A schematic and photograph of the setup are shown in Figure 7.3 and Figure 7.4 respectively. This equipment has been modified to enable lubricant acoustic velocity measurements with changing pressure up to 50 MPa using an embedded longitudinal ultrasonic transducer. By measuring ToF over a known path length at 5 MPa increments and applying a linear fit to the results, see Figure 7.5, the acoustic velocity-pressure relationship at a constant temperature of 20°C was obtained:

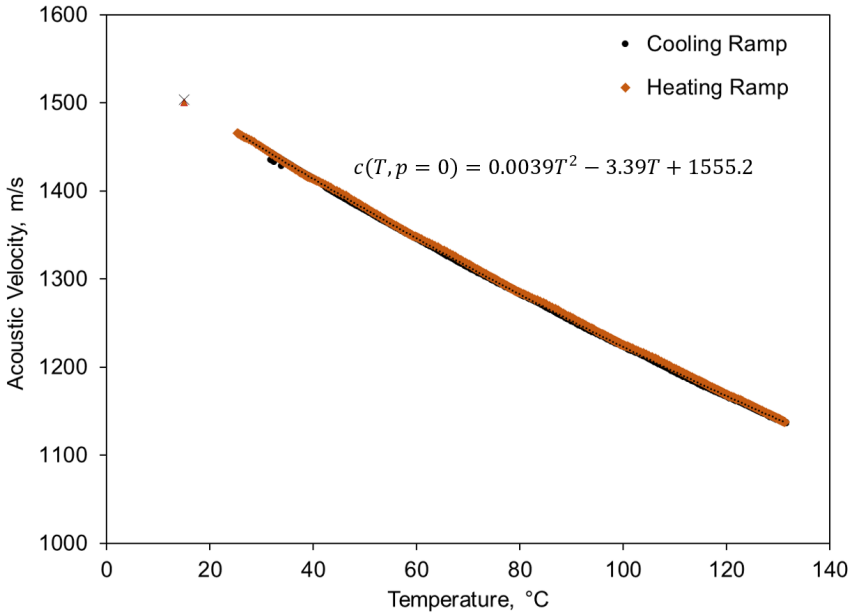

Figure 7.2: Measured acoustic velocity with variable temperature for Shell Melina S 30. Results from a 7-hour linear heating ramp and a 7-hour linear cooling ramp are presented. A second-order fit and corresponding equation of the combined results are also presented.

$$c(T = 20°C, p) = 4.13 \times 10^{-6} p + 1488.8 \tag{7.3}$$

To combine Equations 7.2 and 7.3, the y-intercept, 1555.2 m/s, is taken from Equation 7.2. This is the point at which temperature and pressure are both equal to zero. The variable terms from Equation 7.2 and Equation 7.3 are summed along with this constant, yielding:

$$c(T, p) = 0.0039T^2 - 3.39T + 4.13 \times 10^{-6} p + 1555.2 \tag{7.4}$$

This result is shown graphically in Figure 7.6.

7.1.3 Accounting for Changes in Density

In addition to acoustic velocity, the spring models and exact complex model also require an accurate lubricant density value. Again, this is related to the temperature and pressure of the system. Conveniently, lubricant density may be calculated without any additional testing by combining the following analytical equations:

$$B = \rho \frac{dp}{d\rho} \tag{7.5}$$

$$B = \rho c^2 \tag{7.6}$$

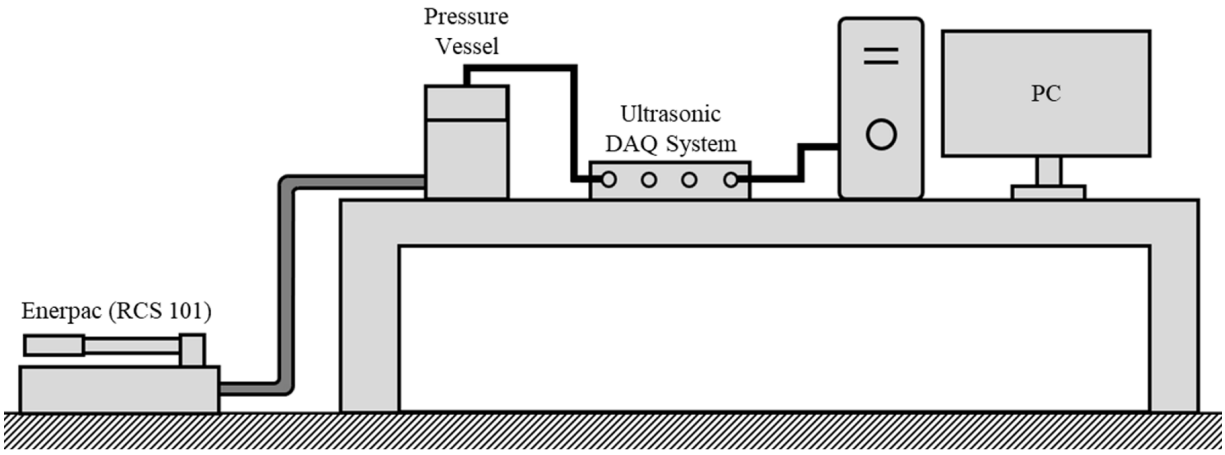

Figure 7.3: Schematic of acoustic velocity-pressure calibration rig.

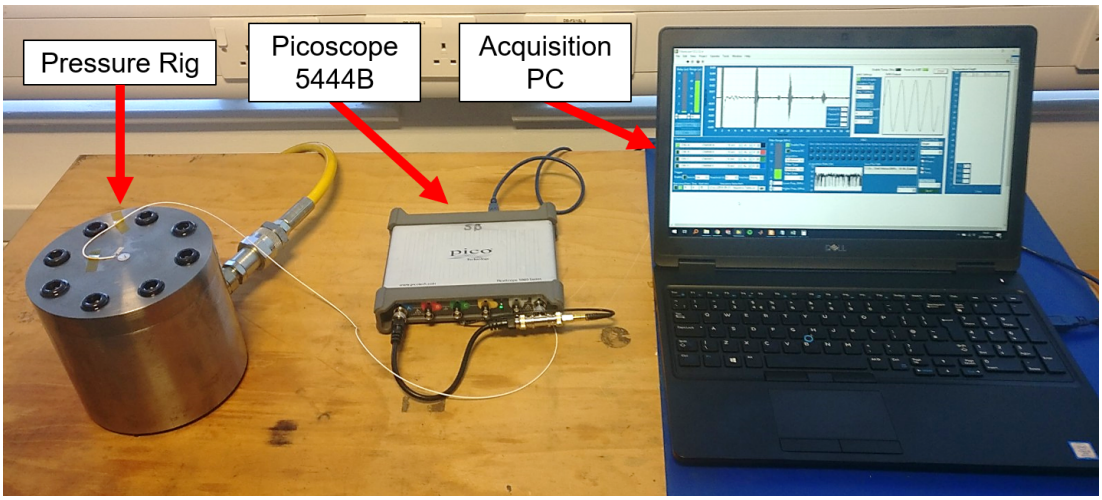

Figure 7.4: Annotated photograph of acoustic velocity-pressure calibration rig.

Where B is bulk modulus and ρ is density. The full step by step derivation is included in Appendix D. Via this method, the formulated relationship for the lubricant was found to be:

$$\rho(T,p) = 162.85 + \frac{888}{1 + 0.0007(T-20)} - \frac{5.88 \times 10^{10}}{p + 3.61 \times 10^{8}} \tag{7.7}$$

This is shown graphically in Figure 7.7.

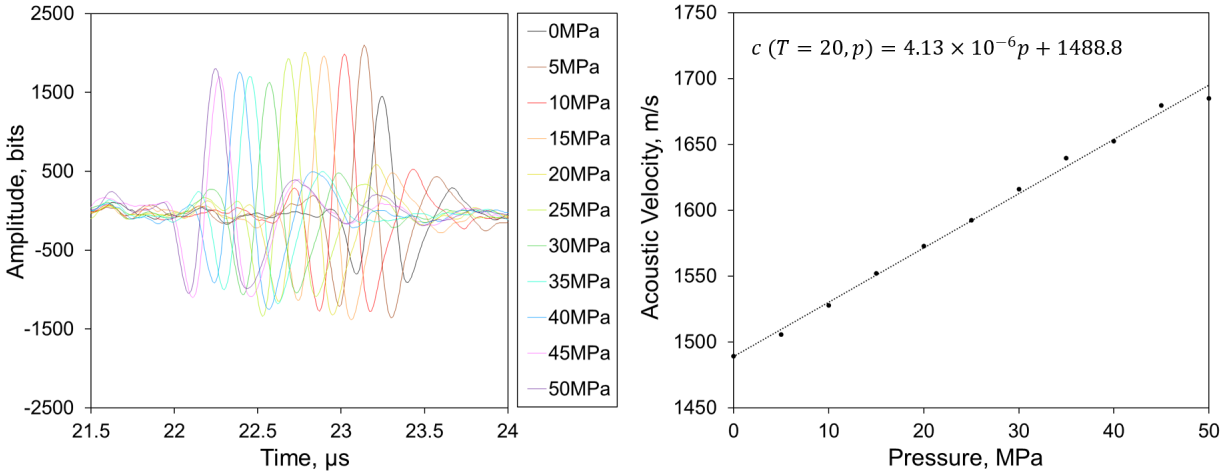

Figure 7.5: Reflected time-domain signal during acoustic velocity-pressure calibration, highlighting the shift in ToF with variable pressure (left). Measured change in acoustic velocity with pressure. A linear fit and corresponding equation are also presented (right).

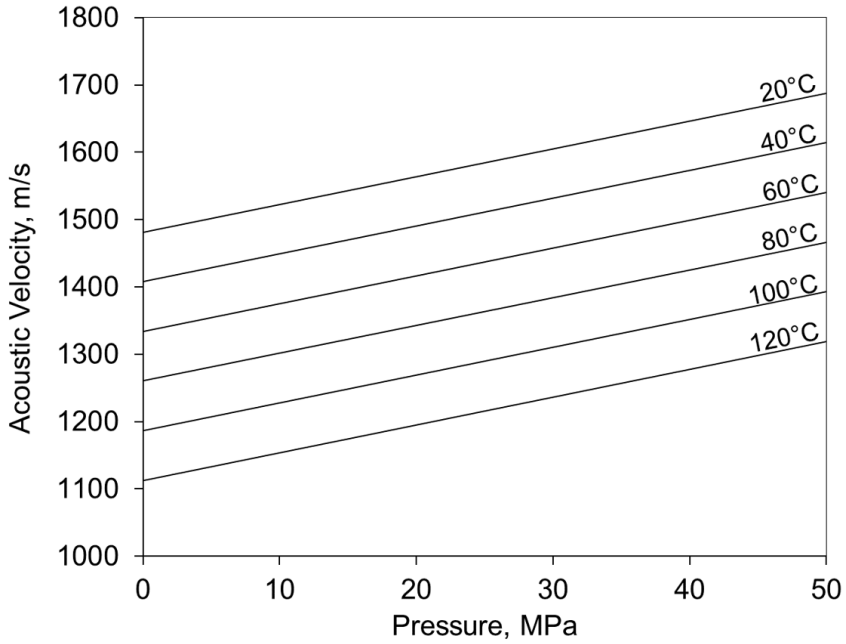

Figure 7.6: Lubricant acoustic velocity against pressure and temperature for Shell Melina S 30. Acquired by combining results from lubricant temperature and pressure characterisations.

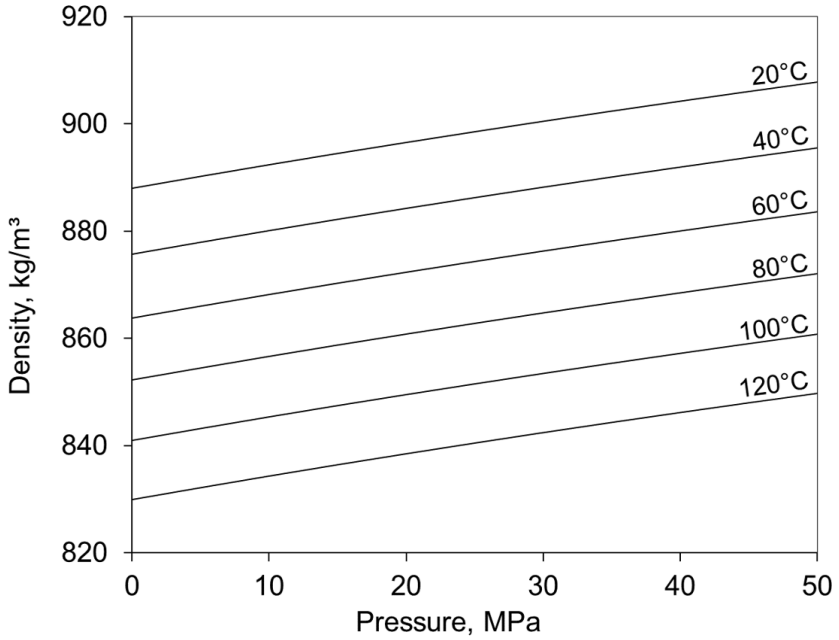

Figure 7.7: Lubricant density against pressure and temperature for Shell Melina S 30.

7.1.4 Viscosity Measurement

A benefit of the ultrasonic technique is that it does not require a lubricant viscosity value. However, viscosity is used in Raimondi-Boyd predictions, which will be used as a comparison in this study. Although data-sheet values were available for Shell Melina S 30, only measurements at 40°C and 100°C were given. This can result in a small uncertainty even when interpolating using a standard VI formula. Also, minor differences between batches can occur. As such, a sample of test oil was taken and viscosity was measured using an SVM 3001 viscometer. The setup is photographed in Figure 7.8. Viscosity against temperature results presented in Figure 7.8 agreed well with data-sheet values, while also providing a more complete characterisation curve.

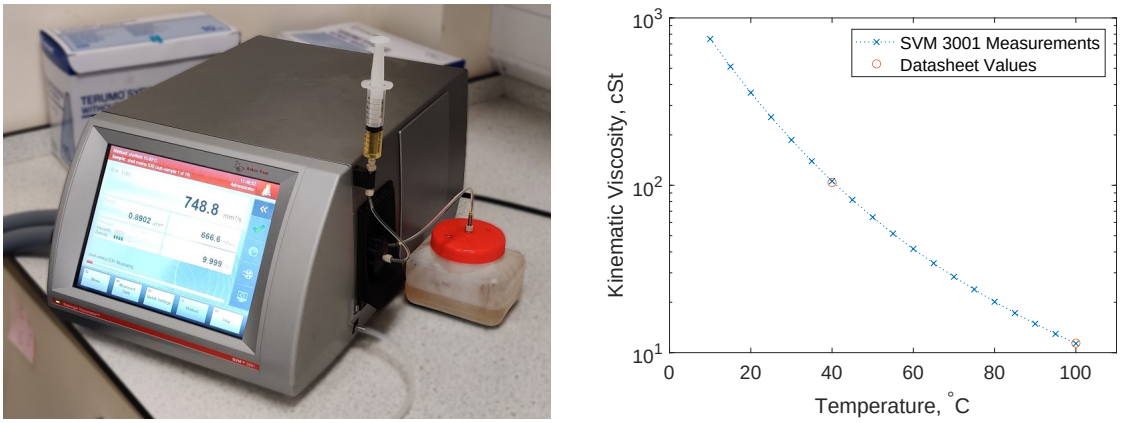

Figure 7.8: Photograph of SVM 3001 viscometer (left). Lubricant viscosity against temperature for Shell Melina S 30 (right).

7.2 Amplitude & Phase Shift in a Rotating Shaft

With the shaft rotating, the signal response from each embedded ultrasonic transducer will change as it progresses around the bearing circumference. This change is evident in the time, frequency amplitude and frequency phase domains, an example snapshot of each is shown in Figure 7.9.

The pattern of this change in reflection coefficient and phase at the centre frequency is shown by a representative example in Figure 7.10. The reflection coefficient is derived from frequency amplitude by taking a modal reference. In this example three distinct regions are indicated, these are:

Thin film region: As the sensor enters the thin film region of the bearing, reflection coefficient amplitude steadily decreases and phase increases, both in line with decreasing film thickness. On the diverging side, the reverse happens, with amplitude increasing and phase decreasing as the film thickens. It should be noted that in this context "thin film" is relative to the thickness around the circumference of the bearing. In some texts the term is reserved for oil films in EHL contacts such as ball bearings, where minimum oil

films can be in the order of 10's to 100's of nanometres [205].

Infinite film region: As discussed previously, the reflection coefficient and phase tend towards constant values as film thickness increases. This manifests as a flat region in the reflection coefficient and phase profiles. This 'infinite film' region is useful as it enables an online reference to be taken each rotation.

Resonance region: Within this section of the bearing circumference, film thickness momentarily coincides with the resonant frequency of the transducer. This creating sharp peaks and troughs in the signal response when observing a single frequency.

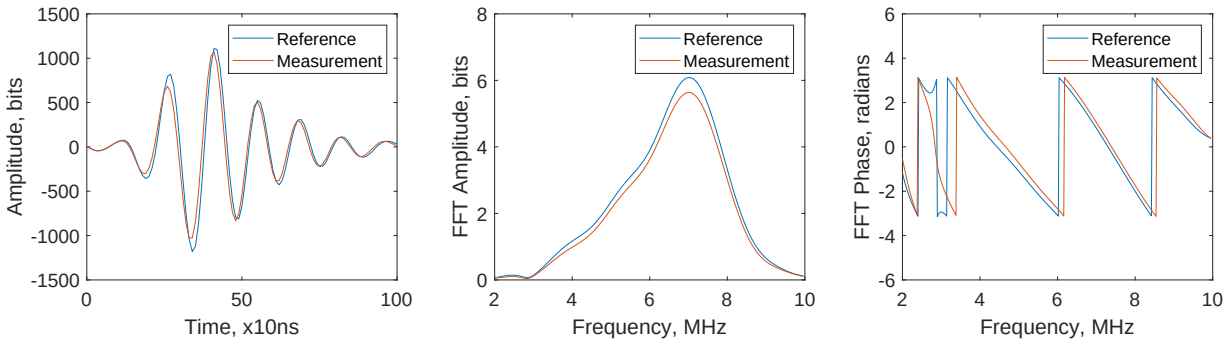

Figure 7.9: Comparison of reference and measurement signal responses in time-domain (left) and corresponding FFT amplitude (centre) and phase (right) plots.

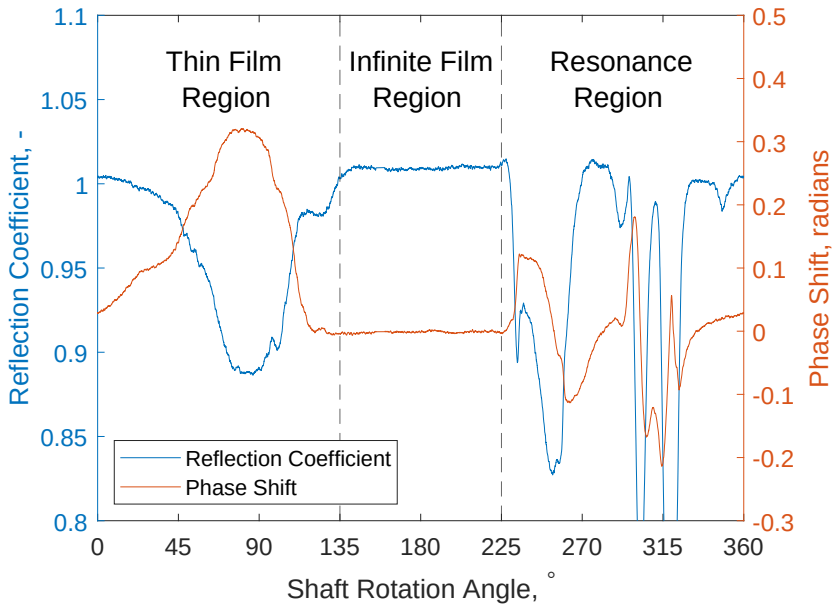

Figure 7.10: Change in reflection coefficient and phase over the bearing circumference. The thin film, infinite film and resonance regions are also indicated.

7.3 Determination of Acoustic Impedance

As shown in Equations 3.17 and 3.18, accurate values of acoustic impedance for both sides of the interface are required for good film thickness measurements when using either the amplitude or phase change models. Obtaining the acoustic impedance of the steel pin, z_1, can simply be found in literature, with sources quoting 46 MRayls for AISI 4340 (EN24) steel [206].

However, the acoustic impedance of the bearing surface, z_2, is more difficult to acquire. Not only is the phosphor bronze layer a more unusual composition and thus is not found in the available literature, but the layer is also a thin sputtered coating. Therefore, it is unlikely z_2 would match the acoustic impedance for the bulk material even if it were available. As such, a more complex measurement approach is required.

Reddyhoff et al. successfully calculated acoustic impedance in a static system by comparing the reflection coefficient and phase change [207]. This was achieved via the following equation:

$$z_2 = z_1 \frac{R^2 - 2Rcos\phi_R + 1}{1 - R^2} \tag{7.8}$$

It is proposed that the same process can be applied in this scenario by comparing the reflection coefficient and phase change within the converging region of the shaft-bearing interface during operation.

Figure 7.11 demonstrates that z_2 remains consistent within the full converging region. As expected the signal-noise ratio improves towards minimum film thickness. This is due to the non-linear relationship between film thickness and amplitude or phase; such that for very thin films a large change in amplitude or phase corresponds to a small change in thickness, whereas for thicker films a small change in either value corresponds to a large change in thickness.

Acoustic impedance measurements within the diverging region are inconsistent, sharply decreasing as the surfaces diverge. It is expected that this is due to cavitation, with emerging air bubbles disturbing the reflected signal. Thus, the diverging region can be ignored and should not be used to determine acoustic impedance.

Theoretically, any data point within the converging region can be used, and for any test condition (such as speed, load or bearing temperature). However, a more rigorous approach has been applied to demonstrate the z_2 value is consistent throughout by testing under a range of operating conditions. For simplicity, the investigation will take only the acoustic impedance value at each minimum film point.

A total of 80 tests under a range of loads, rotations speeds and temperatures were performed. The calculated mean acoustic impedance was 24.36 MRayls, with a standard error of 0.23 MRayls ($\pm 1\%$ of the mean). Figure 7.12 shows calculated acoustic impedance

compared against different variables: Sommerfeld number, temperature, load and speed. Results were analysed for normality and found to be normally distributed. A parametric Pearson correlation analysis was performed to determine whether any significance between any test conditions and acoustic impedance were present. None was found for Sommerfeld number, rotation speed or load (P=0.5692, P=0.2608, P=0.4723). This is also demonstrated by the low R^2 values obtained via a linear regression, also presented in Figure 7.12.

A statistically significant link between z_2 and temperature is shown (P=0.0143), indicating that the observed positive correlation is not due to random sampling. With regards to the strength and magnitude of this association, the gradient and shared variance, quantified by R^2 (in this case 0.0745), are both low. The correlation observed could be explained by changes in material properties, in particular, either a minor change in acoustic velocity, density or both. Therefore, it is suggested this is not a measurement error but a true variation in acoustic impedance. For simplicity, as the change in z_2 is low over the operating temperature range in this study, a constant value for acoustic impedance can be used. Although this may need consideration if testing systems over a wider range of temperatures.

Figure 7.12 does display a rather substantial spread in measured acoustic impedance. This suggests the accuracy of the technique is poor if only one test condition is applied. This variation is higher than that observed by Reddyhoff under static conditions [207], so a higher uncertainty may be due to the dynamic nature of the system. However, the narrow confidence bands indicate that a greatly improved measurement accuracy can still be obtained by performing multiple tests.

Future investigations can be optimised by identifying individual test conditions which produce more accurate results. Narrower confidence bands indicate that decreasing Sommerfeld number, rpm and increasing load does decreases variance in results. The reason for this improvement is that it corresponds to thinner oil film conditions, where the signal to noise ratio is greatest. Therefore, similar tests in future may benefit from operating within this region so fewer tests are needed. It should be noted that fewer tests were performed at 65°C, leading to reduced confidence and wider confidence bands.

The logical question which follows is if the uncertainty in acoustic impedance is acceptable. This is explored in Figure 7.13, for which film thickness is plotted against acoustic impedance for a range of reflection coefficient and phase shift values. This figure shows the gradient is very low, particularly for the phase shift technique. Within the uncertainty range of acoustic impedance, the maximum error in the amplitude model is 2.5% and 0.13% for the phase shift model. This may be considered reasonable given the variability in other test parameters.

An advantage of this method is that the test to obtain acoustic impedance does not have to be exclusive, in fact, the data used in this case was obtained during the normal operating conditions testing presented in Chapter 8. Also, a potential benefit of this technique could be in condition monitoring. By continuously evaluating the acoustic impedance

of the wearing surface, variations may suggest a material change. For example, in this test platform, a sharp increase in acoustic impedance may indicate that the bearing has worn through the white metal layer completely and to the steel backing. This detection may even occur before other symptoms appear, such as temperature or friction (torque) increase. If so, the platform can be shut down and the bearing replaced, thus protecting the system from damage. Of course, a rigorous investigation would be required to confirm this hypothesis.

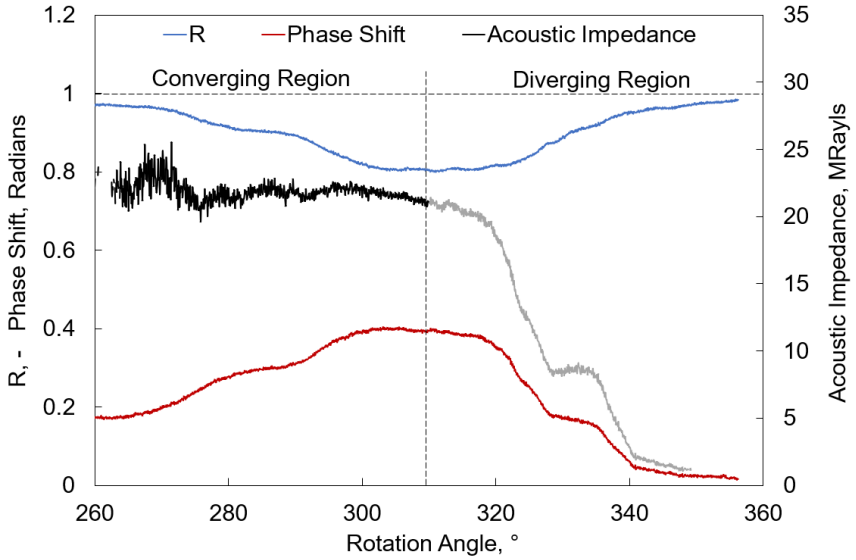

Figure 7.11: Acoustic impedance calculated by observing phase change and reflection coefficient within the minimum film region for an example test case (20 kN, 100 rpm at 65°C). Vertical dashed line represents the location of minimum film thickness.

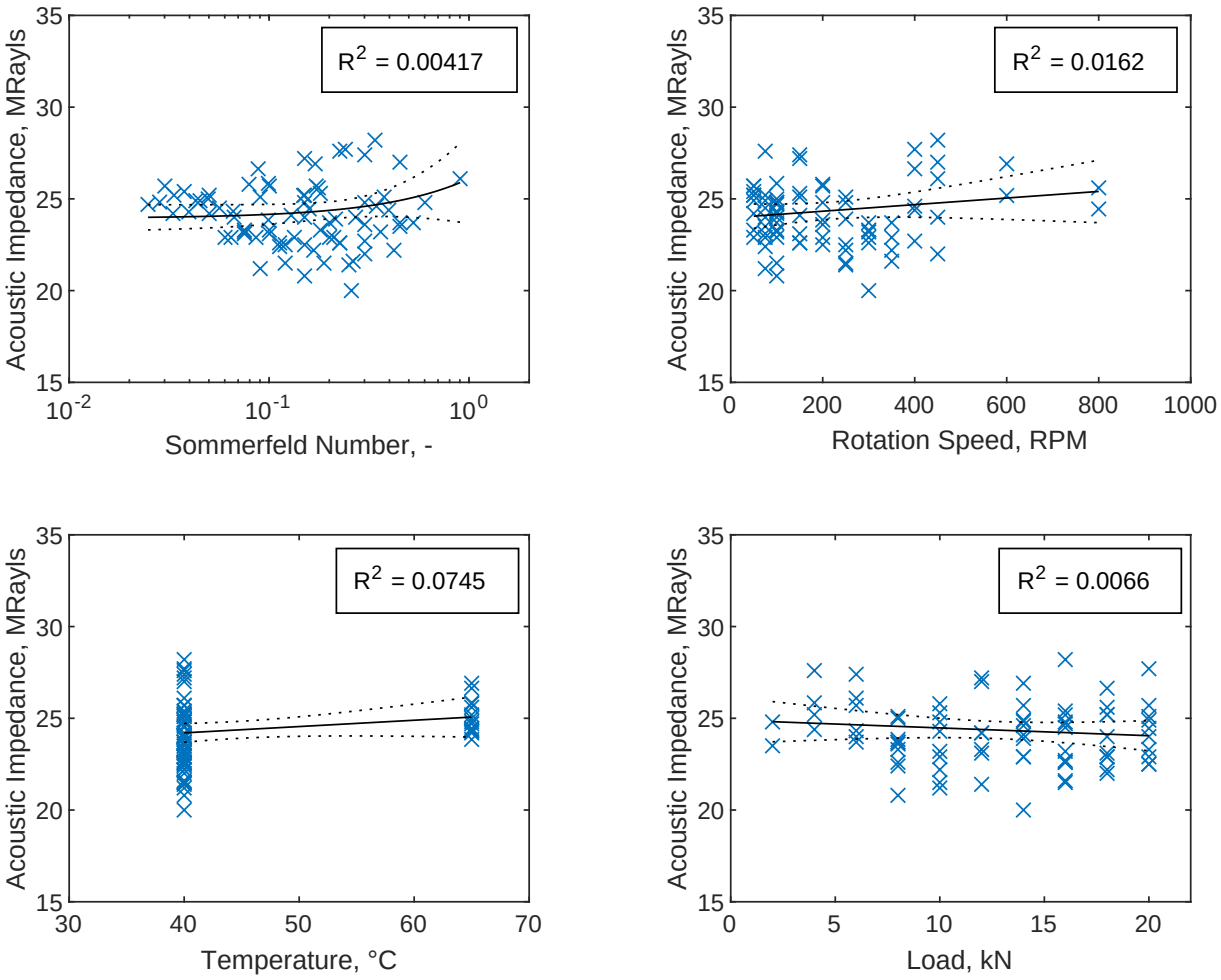

Figure 7.12: Acoustic impedance against Sommerfeld number (top-left), rotation speed (top-right), temperature (bottom-left) and load (bottom-right). Linear regression curve fits, along with corresponding R^2 values are also presented.

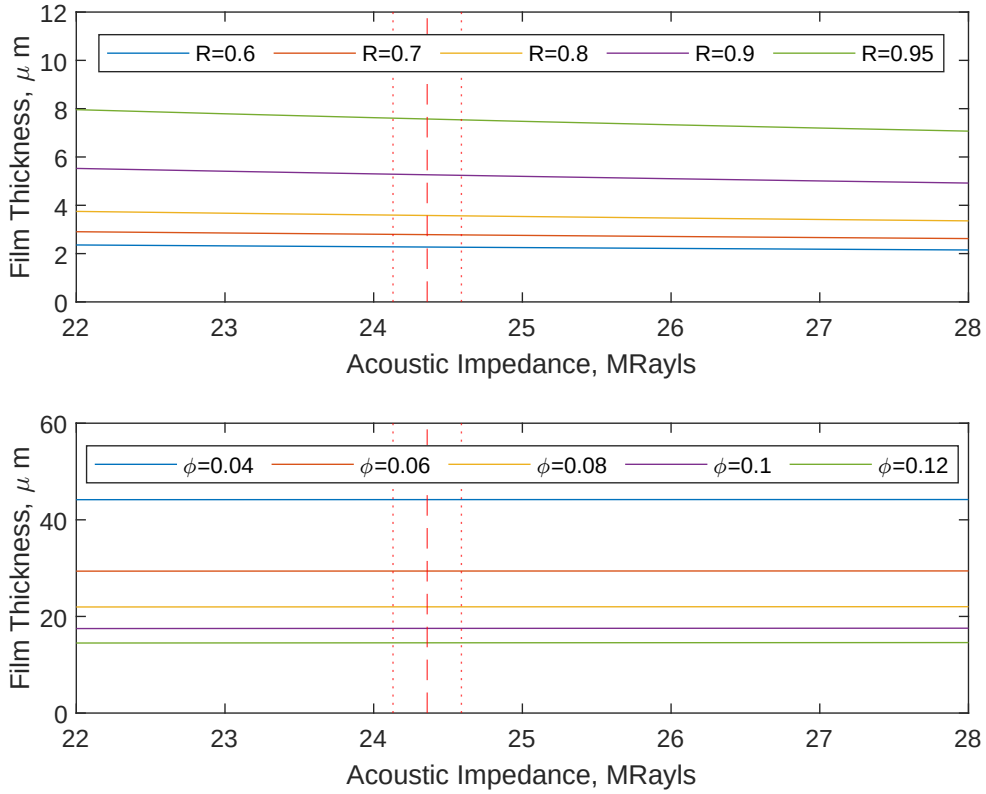

Figure 7.13: The sensitivity of ultrasonic film measurements to uncertainties in bearing acoustic impedance. Shown for the amplitude model (top) and phase change model (bottom).

7.4 Calculating Film Thickness

Now that the key parameter values have been obtained, we can now progress to the meat of the matter and calculate film thickness. The following uses a representative sample of test data from the static loading test rig under normal operation conditions, the full extent of which will be presented in Chapter 8.

A two-stage approach to data processing was created. The first stage is performed in a LabVIEW environment to convert raw A-scan data into reflection coefficient amplitude and phase shift values. The amplitude and phase shift values at the index frequency, 7 MHz, were then saved. LabVIEW is ideal as it allows easy dynamic visualisation of data, so one can check that files have been saved correctly and for obvious mistakes with data acquisition, such as if cables have been unplugged for example. Also, data is captured in .tdms file format during testing, which is native to LabVIEW. A screenshot of the first stage processing software is shown in Figure 7.14.

The second stage uses these values to compute film thickness. A MATLAB environment was used in this stage as it is designed for efficiently manipulating large datasets and can output graphs for reporting. The MATLAB code used to calculate film thickness can be found in APPENDIX E. Stage II Processing MATLAB Program.

One of the key effects not considered in common practice is the relationship of pressure with acoustic velocity, c, and density, ρ. The challenge is that to calculate pressure, one must know the thickness of the oil layer in the bearing. To overcome this, an iterative approach was developed, which is outlined in Figure 7.15. First, the film thickness is calculated via the phase change technique (Equation 3.18) using acoustic velocity and density values which assume pressure in the bearing is zero. This film thickness is then used as an input, along with bearing geometry and operating parameters, into a numerical model to output a three-dimensional pressure map. Example pressure maps under and aligned and misaligned conditions are shown in Figure 7.16.

The minimum film thickness is then recalculated using acoustic velocity and density values compensated by the maximum pressure at the same axial location as the transducer. This is repeated until a convergence criterion is met. The criterion used was that $h_{min,n}$ must be within 0.1% of $h_{min,n-1}$. Convergence was found to be surprisingly rapid and was satisfied within three iterations in most cases. To ensure accuracy a condition that five iterations minimum must be completed was also implemented. Examples of how minimum film thickness converged are presented in Figure 7.17. It can be seen that the film thickness converges equally well for various speeds and loads.

Once the convergence criterion was satisfied, a slice around the bearing circumference was taken from the pressure map. The location of this slice corresponds to the axial position of the transducer. Film thickness can then be calculated using acoustic velocity and density values accounting for pressure at every point around the circumference.

For simplicity, only the film thickness calculated via the phase shift method was iterated, with the amplitude model calculated afterwards using the pressure compensated acoustic velocity and density values. The reverse was attempted for a few cases, with film thickness from the amplitude model iterated and results were near-identical.

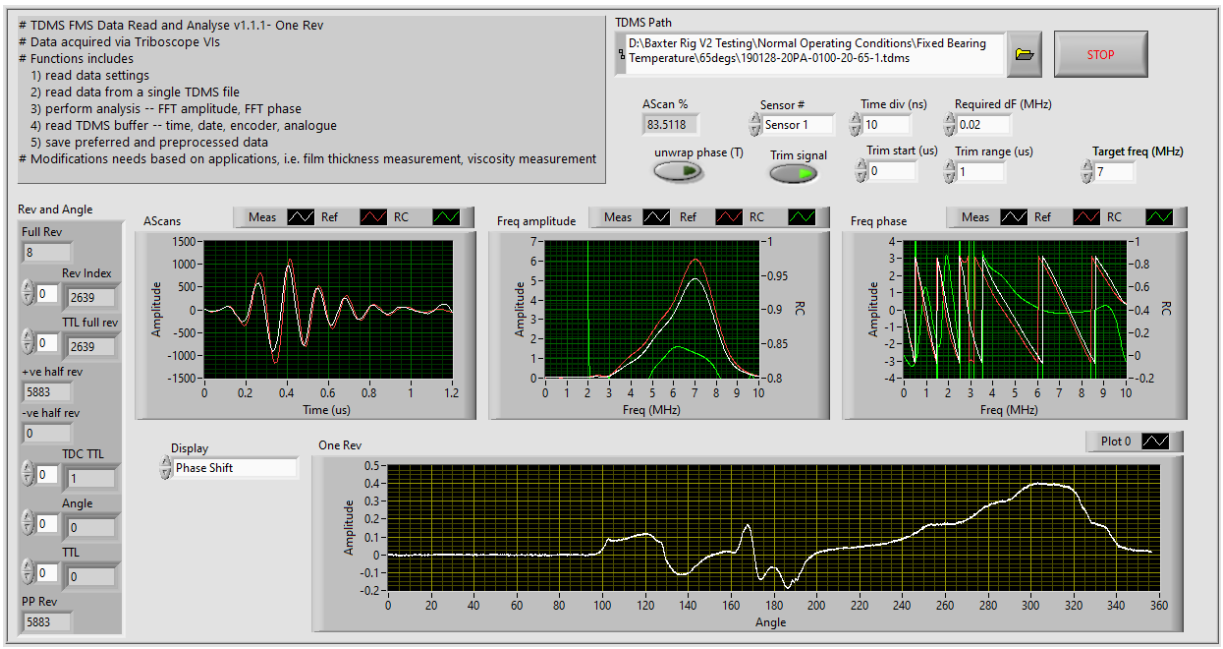

Figure 7.14: Screenshot of LabVIEW processing software.

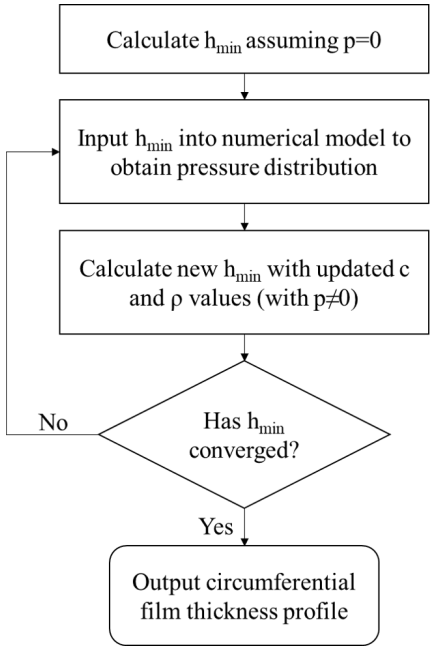

Figure 7.15: Flowchart describing the proposed iterative procedure to account for pressure in ultrasonic film measurements.

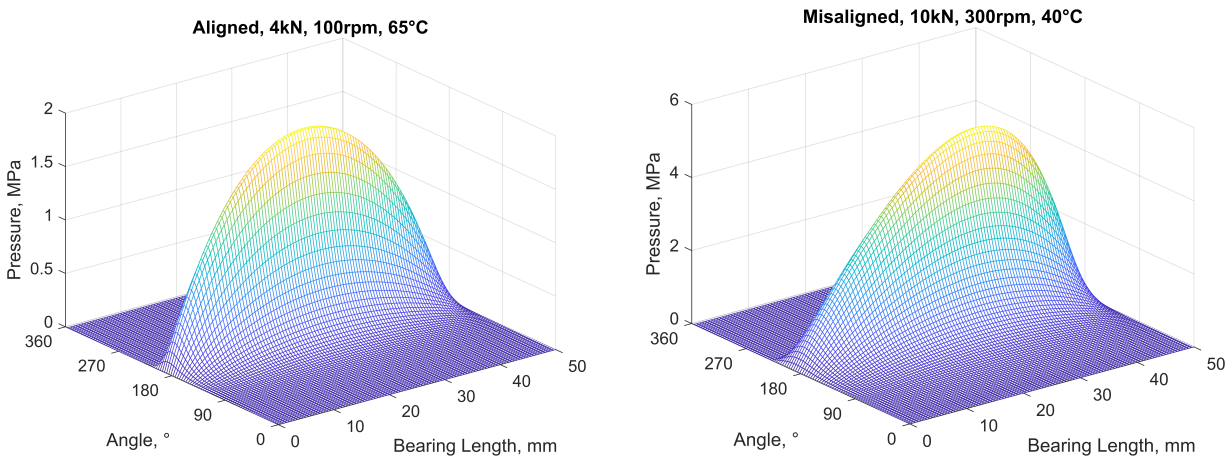

Figure 7.16: Example pressure maps within the bearing contact under aligned (left) and misaligned (right) operating conditions.

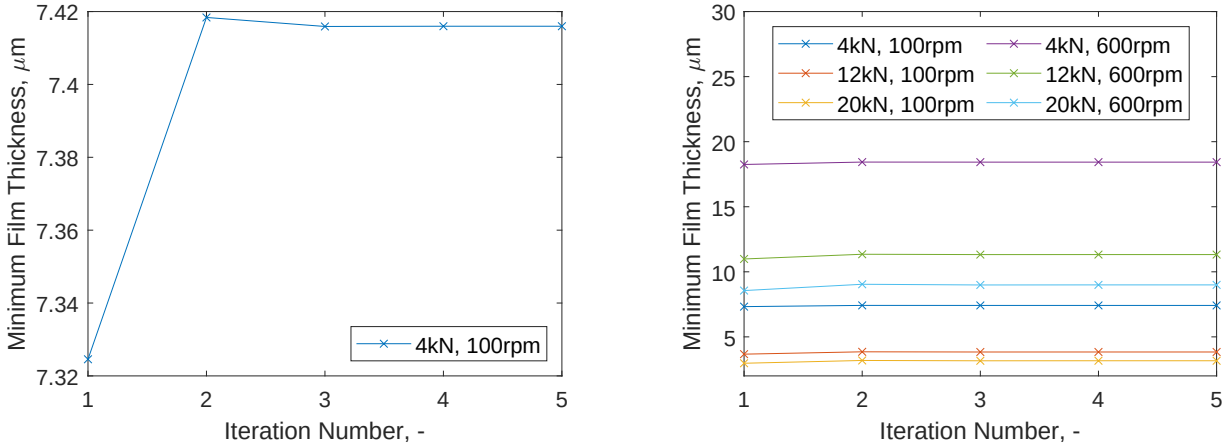

Figure 7.17: Demonstration of how film thickness measurements converge as successive iterations of the pressure compensation process are applied. Film measurements are found using the ultrasonic phase shift technique. A zoomed view of one example (left) and of multiple examples (right) are presented.

7.5 Frequency Dependence of Thin Film Measurement

It has been well established for some time that film thickness measurements should produce the same results no matter what frequency in the spectrum is used. Of course, there may be small discrepancies due to electrical noise. The primary reason centre frequency is most commonly used is that it has the highest amplitude and therefore provides the optimum SNR. However, previous validation tests only used simple plate geometries [208, 102] and even studies using different arrangements still work on this assumption. Thus, it is worthwhile to test whether frequency independence holds for the more complex curved

pin geometry used in this work.

To investigate frequency dependence, the reflected A-scan signal was windowed at different time lengths, then both reflection coefficient amplitude and phase shift spectrograms over the full bearing circumference were calculated. These spectrograms are presented in Figure 7.18. This figure shows that an interference pattern emergences as the A-scan length increases. This interference pattern is clear in both the thin film region (0° to 120°) and resonance region (200° to 300°). The fact that this occurs in both regions may be a clue to its cause.

Theory states that in the thin film region reflection coefficient should increase with increasing frequency [102], leading to a smooth positive gradient; so that when applied to the thin film equations the resulting film thickness value would be consistent. This is only observed at 0.4 μs, suggesting that there is a secondary effect affecting the latter section of the signal response.

Conversely, a smooth negative gradient is expected within the thin film region of the phase shift spectrogram. This is observed between 0.4 μs and 1 μs, suggesting that the phase shift is more weakly affected by this interference effect.

These spectrograms were then used to produce circumferential film thickness profiles, shown in Figure 7.19. For amplitude measurements, it appears that results are frequency-dependent for any A-scan length. However, there are indications that the results at 0.4 μs are due to low SNR rather than interference effects. First, the difference in film thickness profiles on the converging region reduces as film thickness decreases. For the spring amplitude model, SNR is dependent on film thickness, worsening as it tends towards infinity. This has been discussed previously in Section 3.7. A low SNR would be expected at 0.4μs because the amount of signal energy sampled is lower, particularly for frequencies further from the centre frequency. Also, the profiles in the diverging region match very well.

Also shown in Figure 7.19 is a profile derived from the change in Hilbert envelope amplitude. This is an alternative method of acquiring the reflection coefficient. By applying a Hilbert envelope around the time-domain signal and dividing the amplitude by the amplitude of an infinite file reference envelope, one can calculate a frequency-independent value for reflection coefficient. Example measurement and reference A-scans with corresponding envelopes are presented in Figure 7.20 to serve as a typical example. Across all A-scan lengths it appears film thicknesses derived via the Hilbert envelope method are very similar to measurements using the centre frequency, 7 MHz.

Figure 7.21 takes a closer look at the centre frequency, comparing reflection coefficient amplitude and phase over the bearing circumference using window lengths from 0.4 μs to 1.2 μs. Also shown is the reflection coefficient amplitude plot attained via the Hilbert envelope method. For amplitude measurements, film profiles are near identical within the thin film region across all window lengths and the Hilbert profile. This suggests that window length is not critical when applying the spring amplitude method in this system

provided the centre frequency is used.

For phase measurements, film profiles converge on frequency independence as A-scan window length increases. This improvement may be due to the improved SNR as a larger proportion of the signal is sampled. Although, at 1.2μs the film profiles become less similar. This may be due to secondary reflections affecting the result. As such, window length is important in this system when applying the phase shift method. A balance must be struck between windowing enough of the signal to optimise SNR, but not so long that secondary reflections are included.

These findings imply that one should not assume frequency independence, otherwise there is a danger of getting a consistently inaccurate result. Thus, it is important to be rigorous when applying ultrasonic techniques where high accuracy is essential, testing for both frequency and A-scan length independence. It appears in this case that A-scan window length does not have a substantial effect when using the centre frequency, although sampling more of the A-Scan will improve SNR as there is more signal energy. The fact that phase measurements are more consistently frequency-independent may either be true only in this test platform or a universal finding. Further research in other systems would be required to determine this.

It should be noted that although only results at 65°C bearing temperature are presented, other test conditions were also investigated and showed similar patterns. Also, changing the material or lubricant properties (these being acoustic impedance, density and acoustic velocity) did not greatly affect the relative differences between film thickness profiles, so it can be assumed the difference is not due to inaccurate material values.

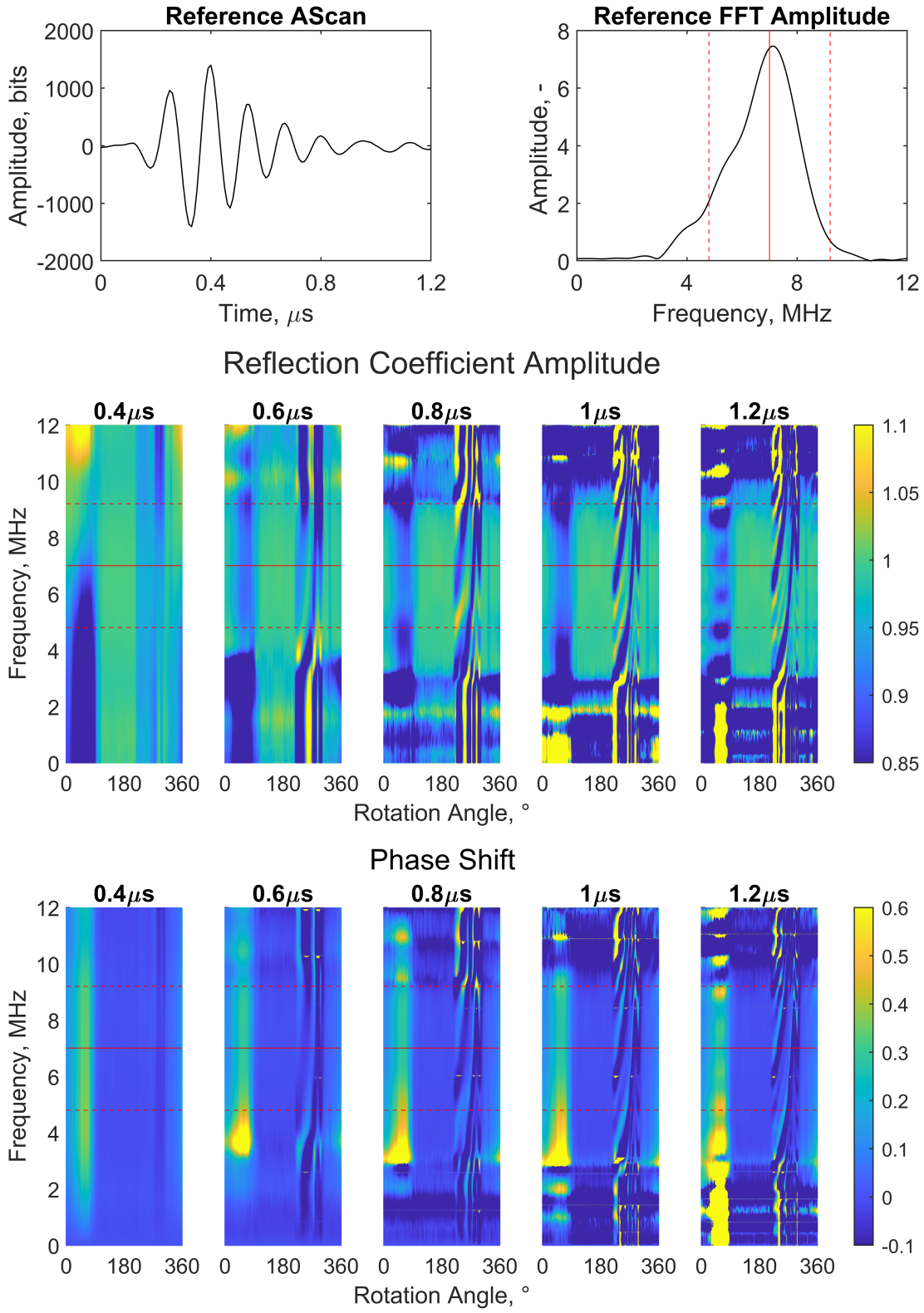

Figure 7.18: Reference A-scan and corresponding FFT amplitude plot, with centre frequency and bandwidth limits indicated (top). Spectrogram of reflection coefficient amplitude (middle) and phase shift (bottom) over a full shaft rotation using different A-scan lengths. Data taken from testing at 200 rpm, 20 kN and 65°C bearing temperature.

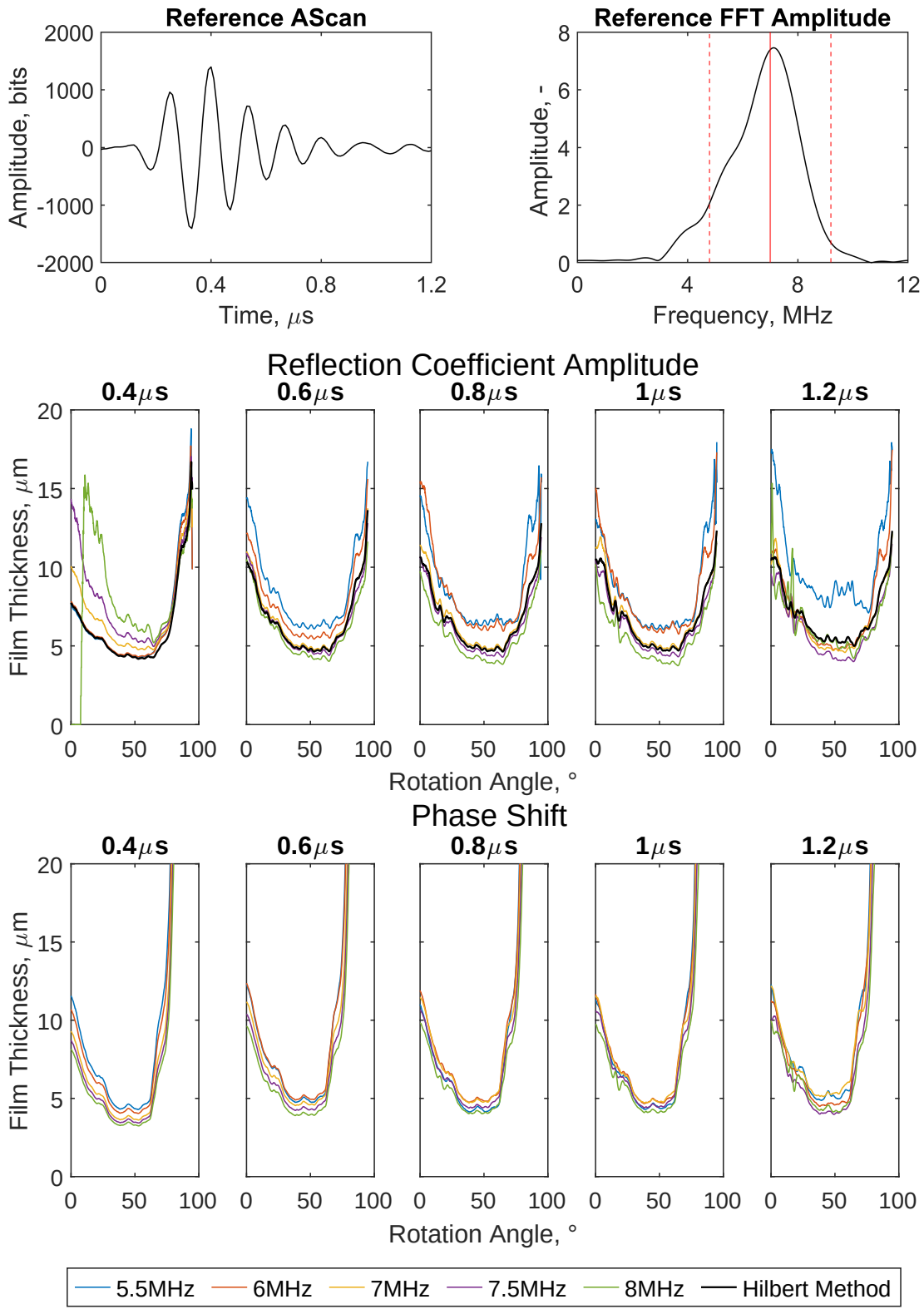

Figure 7.19: Circumferential film thickness profiles obtained via the spring amplitude model (top) and phase shift model (bottom). Each profile applies a different frequency and A-Scan window length in its calculation to test for frequency independence. Also shown is the film thickness profile derived from the Hilbert method.

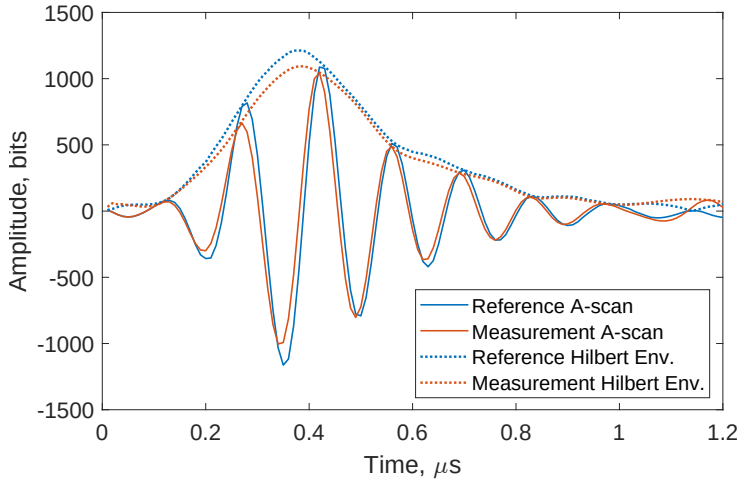

Figure 7.20: A-scan and Hilbert envelope of reflected signal taken within the thin film region, compared against an infinite film reference A-scan and Hilbert envelope.

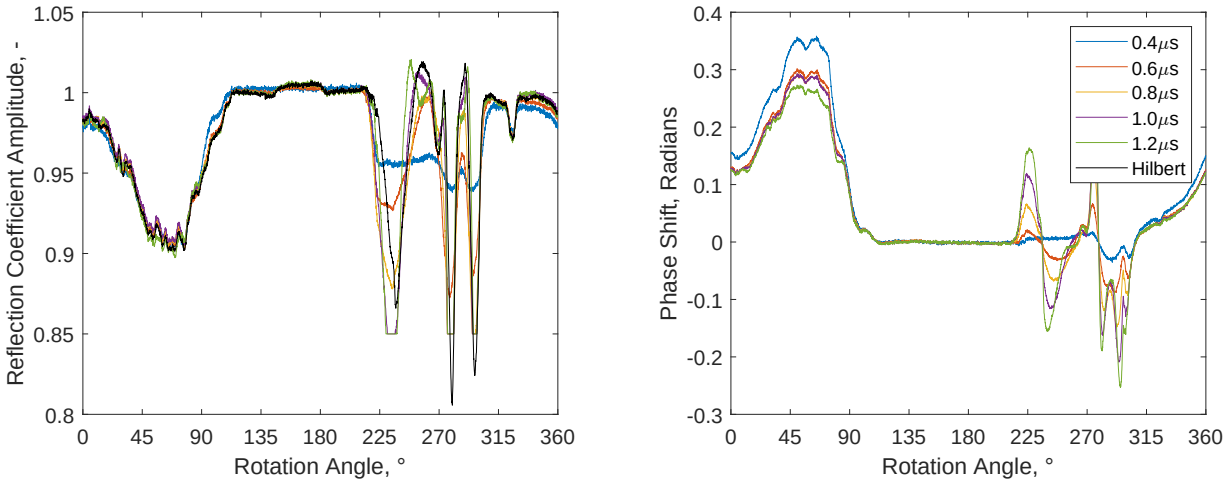

Figure 7.21: Change in reflection coefficient (left) and phase shift (right) over the bearing circumference using the FFT centre frequency, 7MHz, and different A-Scan window lengths. The reflection coefficient profile found using the Hilbert method is also shown.

7.5.1 Observing Wave Patterns in a Simulation

The question which now arises is why does an interference pattern emerge? One hypothesis is that the patterns observed in Figure 7.18 are caused by the geometry of the pin. Specifically, either the internal reflections at the pin sides or because the pin face is curved.

To explore this, waveforms were simulated using k-Wave, an open-source acoustics toolbox for MATLAB. Figure 7.22 shows the simulation with four arrangements. These are:

- Case (a): No side reflections and flat pin face.
- Case (b): No side reflections and curved pin face.
- Case (c): Side reflections and flat pin face.
- Case (d): Side reflections and curved pin face.

For case (a) the reflected wave pattern is as expected, with smooth, consistent peaks and valleys along the sensor width. The response in case (b) is very similar, although the concave shape causes slightly more of the wave energy to bounce towards the centre. This manifests as increased signal amplitude, but again no interference pattern is present.

The response of case (c) is markedly different, with a clear interference pattern observed, which becomes more pronounced as time progresses. The same pattern is also seen in case (d). This interference pattern arises from internal reflections within the pin. Also, waves that reflect off of the sides of the pin have a longer path length and therefore arrive later than waves that travel perpendicular to the sensor. As such, side reflections only affect the latter part of the signal.

It is thought that this interference pattern is also present in the real system, which would account for the trends observed in Section 7.5. Even though the shaft and pin are constructed of the same material (EN24 steel), there may still exist a gap between them. The pin-shaft clearance is designed to be a transition fit and the pin is secured with thread-lock adhesive. Therefore, an adhesive layer in the order of 0.1 μm to 1 μm may exist between the pin and shaft. This layer would have a lower acoustic impedance than steel, meaning some internal reflections are expected.

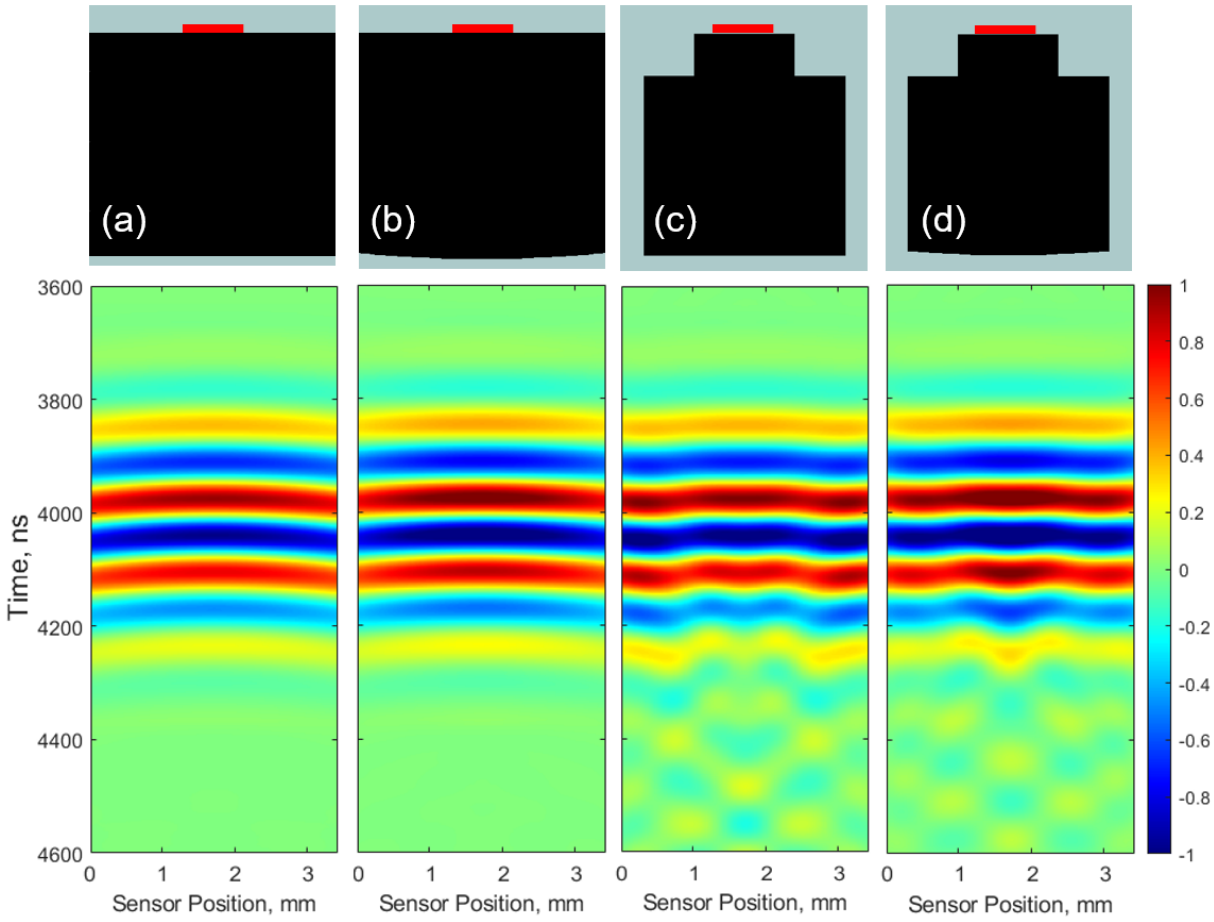

Figure 7.22: A simulation of the reflected wave pattern detected across the sensor length for different modelled geometries. (a) no side reflections and flat pin face, (b) no side reflections and curved pin face, (c) side reflections and flat pin face, (d) side reflections and curved pin face.

7.6 Thick Film Measurements via the Resonant Dip Technique

To measure oil films in the thickest region of the bearing, the resonant dip technique was applied. First, boundaries governing the frequency range in which to search for resonances were drawn. The usable area was defined by observing the frequency amplitude spectrum from a reference signal and finding the points -12 dB below peak amplitude. This is shown in Figure 7.23, with boundaries defined as 4.9 MHz and 9.5 MHz. Given a lubricant temperature of 65°C, leading to an acoustic velocity of 1330 ms^{-1} with Shell Melina S 30, this corresponds to film thickness limits of 70 μm to 136 μm using the resonant dip technique (Equation 3.20). It is possible to use data outside of this frequency range, however, noise would be substantial, making false positives more likely.

A reflection coefficient threshold of 0.85 was also set, along with the condition that shaft

rotation angle must be between 180° and 360°. This angle range corresponds to the thick film region of the bearing. For each FFT, provided these conditions were met, the frequency with the lowest FFT amplitude within the useable bandwidth was then taken as the resonant dip frequency. An example resonant dip is shown in Figure 7.23. Equation 3.20 could then be applied to convert resonant dip frequency to film thickness. Thick film measurements taken during a typical test cycle are presented in Figure 7.24 to serve as an example.

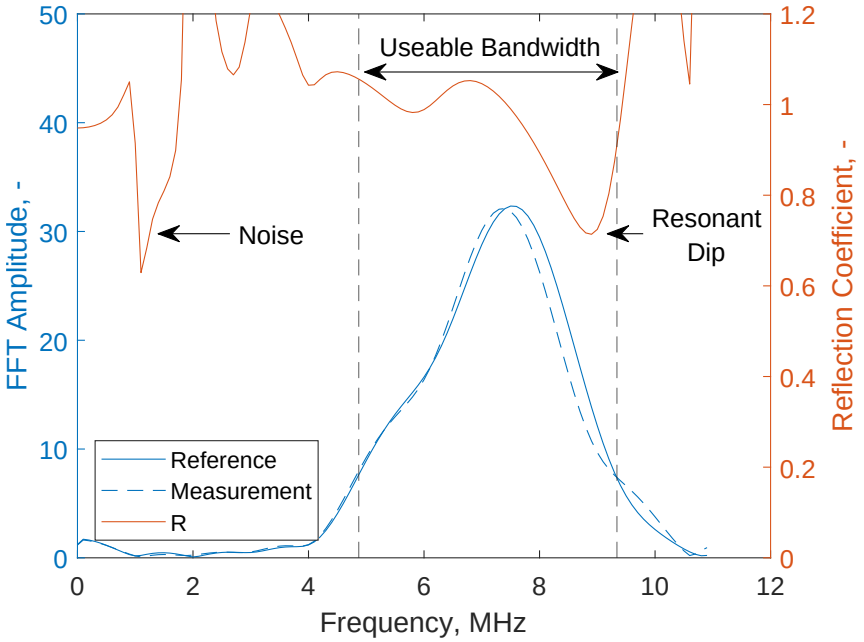

Figure 7.23: Example of a resonant dip observed in the resonance region. The useable bandwidth, -12 dB, is also indicated.

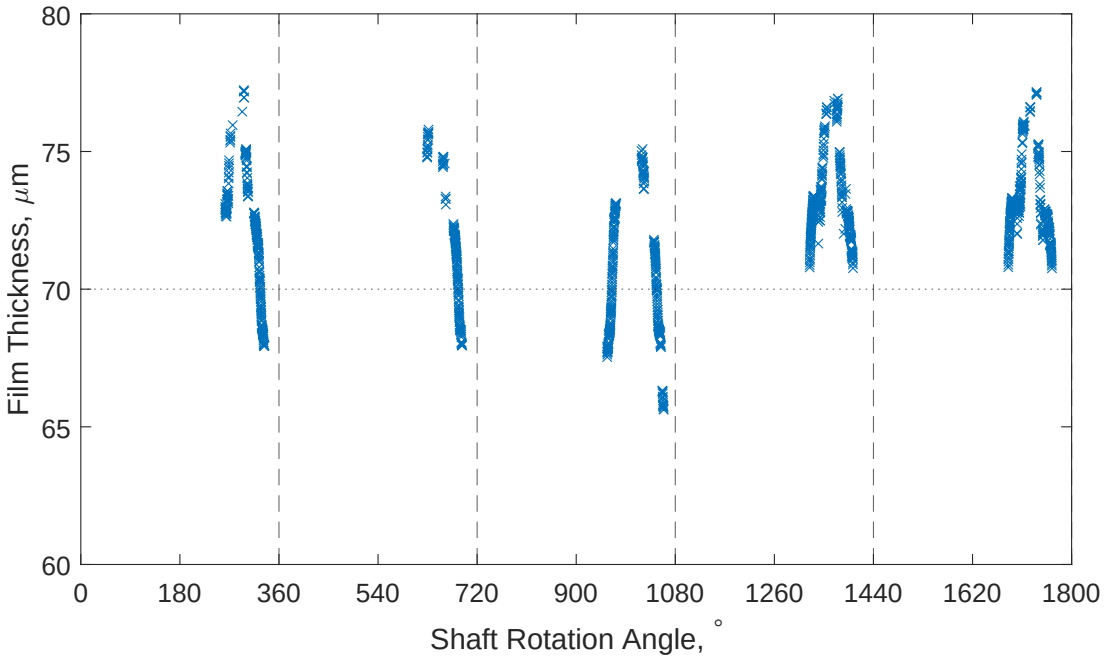

Figure 7.24: Film thickness calculated via the resonant dip technique for five full shaft rotations under normal operating conditions (200 rpm shaft rotation speed, 20 kN applied load).

7.7 Conclusions

This chapter has covered the complete process developed in this study to acquire film thickness measurements via ultrasound in the BAXTER test platform. This includes:

- Preliminary steps performed prior to testing. The density and acoustic velocity of the lubricant were found experimentally over a range of temperatures and pressures typically experienced in a bearing contact. Acoustic velocity and density are required values for most ultrasonic methods. Although the method is only shown for one lubricant, this characterisation has been applied to all oils used in this work.

- The general reflection coefficient amplitude and phase patterns observed around the bearing circumference are presented. Three major regions have been identified: the thin film region, infinite film region and resonance region.

- A method to determine bearing acoustic impedance using reflection coefficient and phase is presented. Acoustic impedance is a required value for the spring amplitude and phase shift techniques.

- The step-by-step process for calculating film thickness via the spring amplitude and phase shift techniques has been presented. This process accounts for the hydrodynamic pressure profile around the bearing circumference using a numerical model and iterative approach. Also, a reference method using measurements from the infinite film region has been introduced.

- Spectrograms of reflection coefficient amplitude and phase shift around the bearing circumference showed the emergence of an interference pattern as time-domain window length is increased. Reflection coefficient amplitude and phase shift at the centre frequency were generally unaffected by this interference pattern, however other frequencies can only be used for film thickness measurements when the time-domain window is narrow.

- An acoustic wave simulation performed in k-wave indicated this interference pattern is due to internal reflections in the pin.

- The process for calculating thick films via the resonant dip technique has been presented.

Chapter 8

Normal Operating Conditions

This chapter details the experiments performed using the BAXTER static loading test platform described in Chapter 6 under normal operating conditions. This refers to tests with constant rotation speed, load and temperature, sufficient lubricant supply and zero misalignment. First, film thickness measurements around the bearing circumference for individual tests are presented. Minimum film thickness measurements from each ultrasonic method are then compared against a theoretical prediction and eddy current sensors. This is followed by an inspection of the shaft and bearing surfaces to understand wear characteristics.

8.1 Results under Normal Operating Conditions

In this study, a matrix of individual tests was performed to understand the behaviour of the bearing system under normal operating conditions. For each test case, the platform was run until equilibrium was achieved, with a particular focus on bearing temperature. Once this had been achieved data was recorded for 5 seconds. By careful control of the oil bath temperature, the bearing temperature could remain consistent. Tests were performed at two bearing temperatures, 40°C and 65°C. Rotation speeds ranged between 100 rpm and 800 rpm at 100 rpm intervals and applied loads from 2 kN to 20 kN at 2 kN intervals. The lubricant used is Shell Melina S 30, a high-performance marine diesel engine mineral oil, characterised in Section 7.1.

Film thickness was calculated from ultrasonic measurements via the process outlined in Section 7.4. This includes accounting for hydrodynamic pressure effects. Additional acquisition hardware measured load, speed, bath temperature, bearing temperature and film thickness via conventional eddy current sensors.

8.1.1 Circumferential Film Measurements

By combining multiple ultrasonic models it is possible to obtain film thickness measurements over a wider range. Figure 8.1 and Figure 8.2 show film thickness around the circumference of the bearing using a combination of the amplitude, phase shift and resonant dip techniques at 200 rpm and 400 rpm respectively. Results are an average of all

cycles captured over the 5 second period. For clarity, the profile is repeated in Figure Figure 8.1 and Figure 8.2, showing two full rotations.

Results are compared against a theoretical Raimondi-Boyd prediction. The boundaries of this prediction are formed by the uncertainty in bearing clearance (-5 μm to +0 μm). It is observed that this uncertainty has a large effect on film thickness in the thick film region of the bearing but a negligible effect within the thin film region.

There is good agreement between the amplitude model, phase shift model and Raimondi-Boyd prediction within the converging thin film region. However, the bearing is slightly tapered and is therefore not perfectly concentric. This is observed in the ultrasonic measurements but not considered in the Raimondi-Boyd prediction.

In the diverging region, film thickness measured via the phase shift model increases more sharply than makes geometric sense and deviates rapidly from the Raimondi-Boyd prediction. It is thought that this is due to cavitation. A similar pattern was observed by Kasolang et al. [144], for which they also concluded was due to cavitation. Pressure reduces as the two surfaces separate, leading to the formation of air bubbles. The interface becomes what is effectively a steel-air boundary and as such, there is a near-total reflection of the acoustic wave. This interferes with the measurement, causing substantial errors. As such, these ultrasonic models are unable to measure film thickness within the diverging region in this case. However, cavitation may be reduced or eliminated by using different operating conditions or oil types, allowing film measurements in this region. Also, an indication that cavitation is occurring is useful in itself. If left unchecked, severe cavitation can incur substantial wear on the bearing surface [36].

The resonant dip profiles in Figure 8.1 and Figure 8.2 lie within the bounds of the Raimondi-Boyd prediction, although both sit closer to the minimum boundary. By combining the minimum and maximum film measurements around the bearing circumference it is possible to obtain a measurement for bearing clearance. In this case, results suggest radial clearance is around 46 μm, which is within the range previously determined (45 μm to 50 μm).

Figure 8.3 presents a comparison of film thickness profiles with loads ranging from 2 kN to 20 kN at 400 rpm and 65°C. In line with theory, an increase in load reduces film thickness as the surfaces are compressed together with greater force. A decrease in attitude angle is also observed as the applied load becomes more significant compared to rotational forces, pulling the minimum film point closer in line with the applied load vector at the top of the bearing.

A sharp valley is observed at the top of the bearing for all load profiles. It is theorised this may be due to the thermocouple cable ejection channel in the bush behind the thin bearing shell located at the top of the bearing. It is possible that the bearing shell deformation is significant as the bearing shell area is unsupported. The position of this cable ejection channel is shown in Figure 8.5.

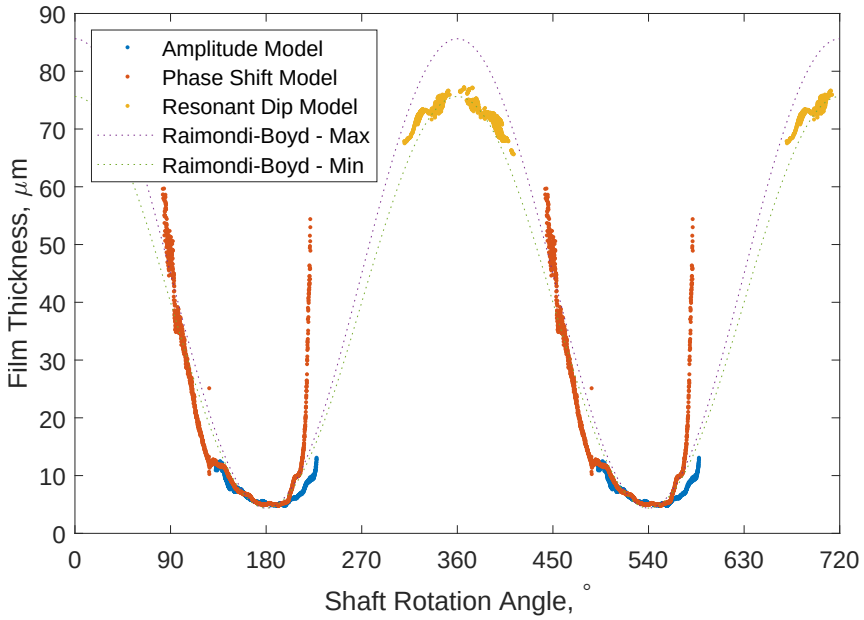

Figure 8.1: Circumferential film measurements via the amplitude, phase shift and resonant dip techniques for an example test case, (20 kN, 200 rpm, 65°C). This is compared against the Raimondi-Boyd solution, for which the minimum and maximum range is defined by uncertainty in radial clearance, $-5\ \mu m$ to $+0\ \mu m$.

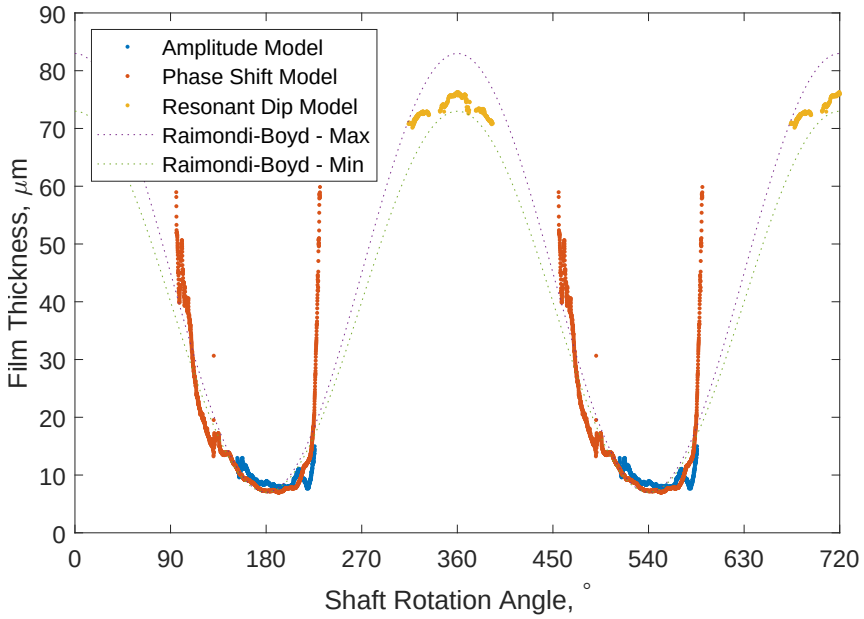

Figure 8.2: Circumferential film measurements via the amplitude, phase shift and resonant dip techniques for an example test case, (20 kN, 400 rpm, 65°C). This is compared against the Raimondi-Boyd solution, for which the minimum and maximum range is defined by uncertainty in radial clearance, $-5\ \mu m$ to $+0\ \mu m$.

A comparison of profiles at different rotation speeds is shown in Figure 8.4. All tests are at 10 kN and 65°C. Converse to the effect of applied load presented in Figure 8.3, an increase in speed leads to an increase in film thickness. This is due to the increased hydrodynamic pressure pushing the surfaces apart. Similarly, by observing the angle between minimum film thickness against the top of the bearing, it is clear that a faster rotation speed also leads to an increase in attitude angle.

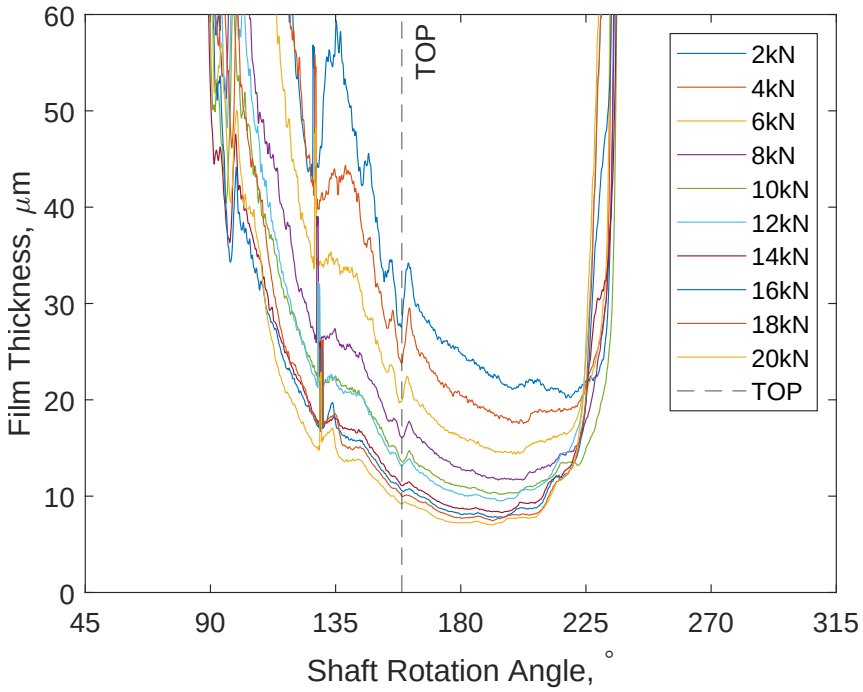

Figure 8.3: Circumferential film measurements via the ultrasonic phase shift technique for loads ranging from 2 kN to 20 kN, all at 400 rpm and 65°C. The top of the bearing (labelled *TOP*) is also indicated.

A novel aspect of this work is accounting for pressure effects in the circumferential film measurement. A comparison between profiles accounting for pressure and not accounting for pressure are shown in Figure 8.6. As expected, the difference between profiles increases with pressure. This is highlighted by the divergence of profiles as they tend to the point of minimum film thickness. Also, the difference between profiles is much smaller for the 2 kN test case in comparison to the 20 kN test case. As such, accounting for pressure in ultrasonic film thickness measurements may be critical in high-pressure journal bearing applications such as in automotive big-end bearings but unnecessary in turbochargers for example.

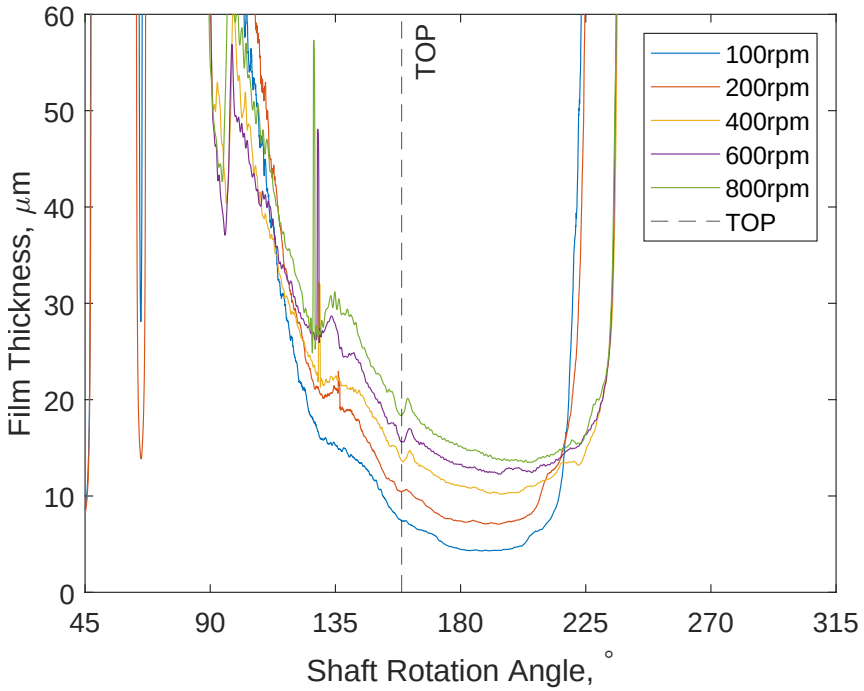

Figure 8.4: Circumferential film measurements via the ultrasonic phase shift technique for loads ranging from 100 rpm to 800 rpm, all at 10 kN and 65°C. The top of the bearing (labelled *TOP*) is also indicated.

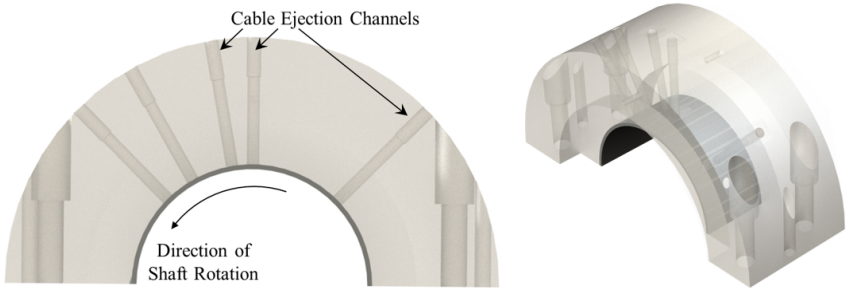

Figure 8.5: Schematic of bearing bush, with cable ejection channels indicated.

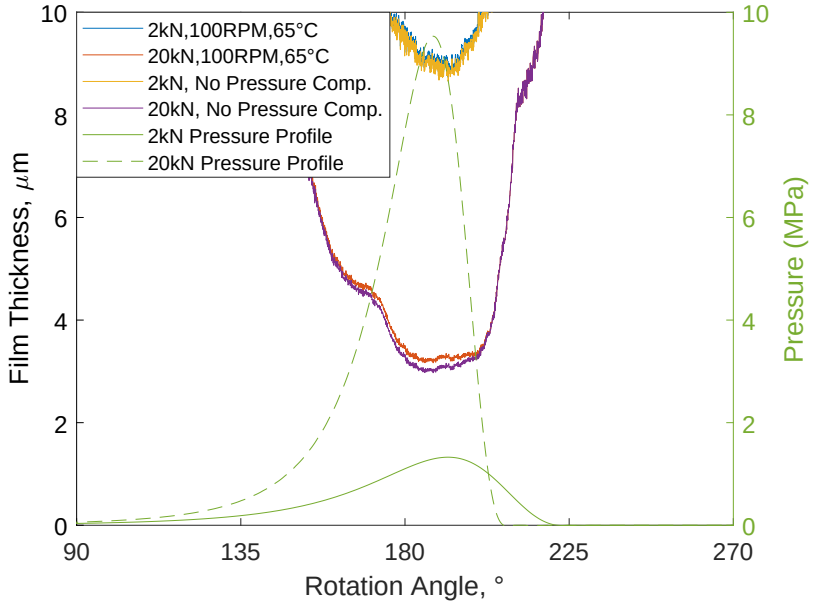

Figure 8.6: Film thickness measurement around the bearing circumference obtained via the ultrasonic phase shift technique for two example test cases (2 kN and 20 kN, both at 100 rpm and 65°C). Pressure compensated and non-pressure compensated film thickness measurements are presented, along with the corresponding pressure profile around the bearing axial plane.

8.1.2 Minimum Film Measurements

Taking the minimum film thickness value from each circumferential profile and collapsing these results onto a Sommerfeld graph enables a simple comparison between ultrasonic techniques. This has been performed in Figure 8.7, which shows minimum film thicknesses calculated via the amplitude, phase and exact-complex method, along with a Raimondi-Boyd theoretical prediction.

Generally, all methods are in good agreement for operating conditions which lead to thin oil films; as indicated by confidence bands overlapping up to around 8 μm. At thicker films, the models slightly diverge. The amplitude model loses accuracy with increasing film thickness as the reflection coefficient tends to unity, with a hard limit defined at 14 μm.

As previously discussed, the exact-complex method has an advantage in that it does not require an acoustic impedance value for either the shaft or bearing. With the exact complex and phase shift measurements so similar, this provides further evidence the value for bearing acoustic impedance derived in Section 7.3 is accurate. An inaccurate value for bearing acoustic impedance would instead lead to a significant difference between methods across the full film thickness range.

It is uncertain why a small difference between phase and exact-complex models arises with thicker films. This could simply be due to the reduced signal-noise ratio increasing measurement uncertainty. However, another cause may be that the R component of the exact-complex technique begins to lose accuracy as R tends towards unity. Although Yu et al. state that the measurement range of the exact complex method should be similar to the phase shift technique, their testing was done in a less complex static system under carefully controlled, ideal conditions. Also, Yu et al. found that the lower bound measurement uncertainty is much larger than the upper bound for the exact-complex method. Thus, one may expect the exact complex method to underpredict film thickness, which is indeed observed in Figure 8.7.

A similar divergence pattern emerges when comparing each ultrasonic measurement against the Raimondi-Boyd prediction. Again this may be due to the decrease in SNR as film thickness decreases. However, it should be stated that the Raimondi-Boyd prediction is of course not the true film thickness value, and does make some potentially significant assumptions (as listed in Section 4.1.2). One particular aspect to consider is that the Raimondi-Boyd prediction does not account for effects due to inlet pressure. All tests were conducted with an oil inlet pressure of 600 kPa. Given that the oil port diameter is 8 mm, this leads to a normal force of 30 N in addition to the measured force applied via the hydraulic cylinder. However, as shown in Figure 6.1, the oil port angled is 63° from vertical, shifting the total load vector. With a magnitude of 30 N, oil port effects may be significant at low loading, although its contribution may be negligible under higher load conditions.

The Raimondi-Boyd prediction also assumes the oil inlet is located at the position of

maximum film thickness. However, the effects of this assumption are expected to be minimal as the true oil inlet position is approximately within this range, as shown in Figure 6.1.

The reflection coefficient amplitudes used to calculate film thickness via the amplitude and exact methods ignore any thermal effects due to the mismatch of the thermal conductivity, and specific heats, between steel and oil. Theoretically, a mismatch in thermal properties can affect the magnitude of the reflected wave [209]. This effect is expected to be small, particularly as results are in good agreement with the phase-shift model, but a detailed investigation has not yet been carried out.

Error bars in Figure 8.7 indicate the SEM (standard error of the mean) for each test case. As previously discussed, each ultrasonic method is generally more accurate when measuring thinner films within this system. However, with measurements taken over a five-second period, high rotation speed tests, for which oil films are thicker, will record more minimum film measurements as more rotations are completed. For example, only 8.3 rotation cycles will occur over five seconds at 100rpm, compared to 66.6 cycles at 800 rpm. As such, high rotation speed tests have more sample measurements, counteracting their inherent higher measurement uncertainty.

The R^2 values shown in Figure 8.7 indicate variation from test to test is low for all measurement techniques, although variation is lowest for the phase shift model. This demonstrates the phase change technique is the most consistent across the full spectrum of thicknesses explored. Variation in both the amplitude and exact-complex methods slightly increase for thicker film tests as SNR decreases.

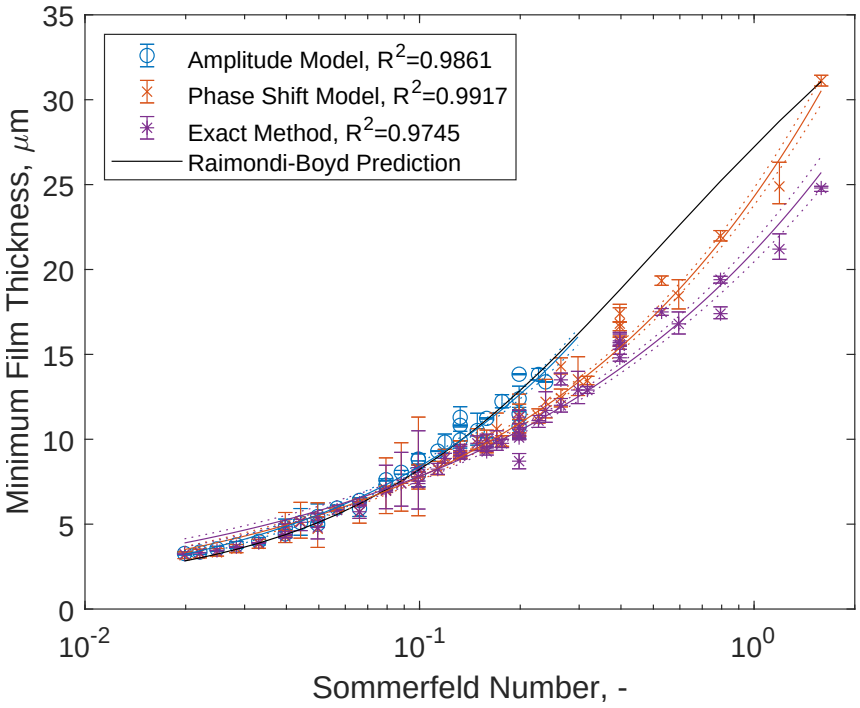

Figure 8.7: Minimum film thickness against Sommerfeld number for bearing testing under normal operating conditions. Theoretical prediction curve is obtained via the Raimondi-Boyd solution, measurements are obtained via the ultrasonic spring amplitude, spring phase shift and exact-complex methods. Error bars indicate variations in film measurement within each test case to ±1 SEM. Log-log nonlinear regression fits for each method are presented, along with dashed lines representing 95% confidence bands.

8.1.3 Test Platform Repeatability

If one wants to compare oils or bearing materials it is important that the test platform produces repeatable measurements, else differences observed could be attributed to variability in the test platform. To explore this, a test set was repeated using the same oil, separated by three days and with the top bearing shell replaced.

A comparison between repeats 1 and 2 is shown in Figure 8.8. Minimum film thicknesses derived via the phase shift method are presented. It should be noted that the test matrices of repeats 1 and 2 differ slightly, with repeat 1 focussing more on thinner film operating conditions and vice-versa. However, there is a substantial overlap between repeats so a good comparison can still be made.

Repeats were compared for similarity via an extra-sum-of-squares F test, with no significant difference between repeats found ($P = 0.280$). As such, a shared curve for both datasets is the preferred model. Narrow 95% confidence bands also indicate low measurement uncertainty. Overall this suggests the test platform produces consistent results, even when separated by long periods of time and the bearing shells have been replaced.

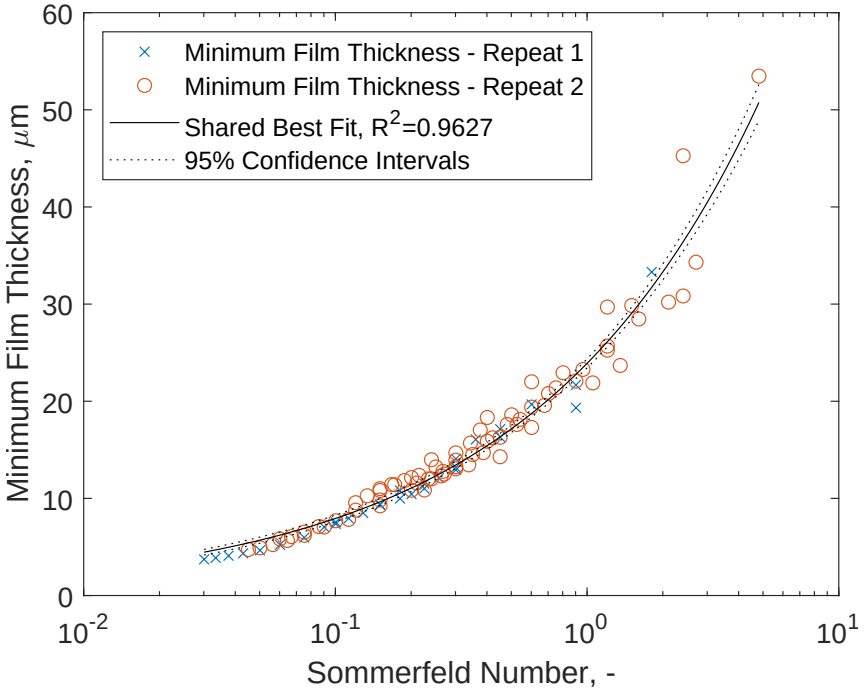

Figure 8.8: Minimum film thickness obtained via the phase shift technique against Sommerfeld number for repeats 1 and 2. A shared log-log regression fit with 95% confidence bands is also presented.

8.1.4 Comparison against Eddy Current Sensor Measurements

During 65°C bearing temperature testing between 100 rpm and 400 rpm, film thickness measurements were also obtained using conventional eddy current sensors mounted on the bearing assembly. Details of this setup, including sensor positions, have been previously described in Section 6.1. The purpose of this experiment is to compare the effectiveness of the ultrasonic technique against a more conventional method.

Figure 8.9 shows minimum film thickness against Sommerfeld number obtained via the phase shift method and using eddy current sensors, along with a Raimondi-Boyd prediction.

First, it is clear that variability is greater for eddy current measurements compared to the ultrasonic phase shift method, as indicated by their R^2 values, 0.8492 and 0.9917 respectively. This suggests phase shift measurements are more consistent. Also, the phase shift measurements fit more closely to the Raimondi-Boyd prediction, with eddy current sensors reporting thicker films in the majority of cases, particularly as Sommerfeld number increases.

To explore this further, the differences between measured and predicted film thickness with respect to the two control variables, load and rotation speed, were analysed. Figure 8.10 shows the normalised difference between measured film thickness and Raimondi-

Boyd prediction plotted against speed and load separately. The R^2 value for the phase change measurements is similar for load and speed, suggesting that both have an effect on the difference between measurement and prediction. This is consistent with the findings in Section 8.1.2, for which differences were attributed to either reduced accuracy as film thickness increases or due to an assumption made by the Raimondi-Boyd prediction.

However, for the eddy current measurements, there is only a significant correlation with respect to load and not with rotation speed. By deduction, because the difference magnitude is only related to load, this divergence is not simply due to an under or over-prediction by the Raimondi-Boyd technique. Instead, some effect is directly introducing error when load is changed. It is expected that this is due to shaft bending or deformation. The eddy current sensors are mounted on the sides of the bearing housing away from the contact, so any differences in deformation magnitude between the two locations would introduce uncertainty. This highlights one of the primary advantages of ultrasonic techniques, in that they can provide direct measurements whilst still positioned away from the contact so as not to interfere with bearing operation.

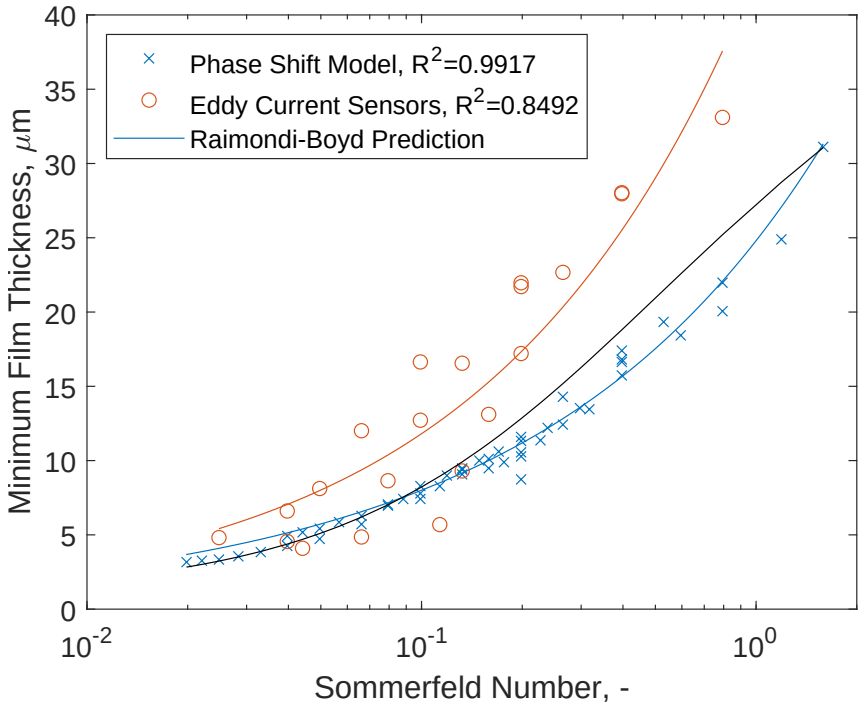

Figure 8.9: Minimum film thickness against Sommerfeld number measured by both the ultrasonic phase shift technique and by conventional eddy current sensors. Log-log nonlinear regression fits, along with corresponding R^2 values are presented. A Raimondi-Boyd prediction is also shown.

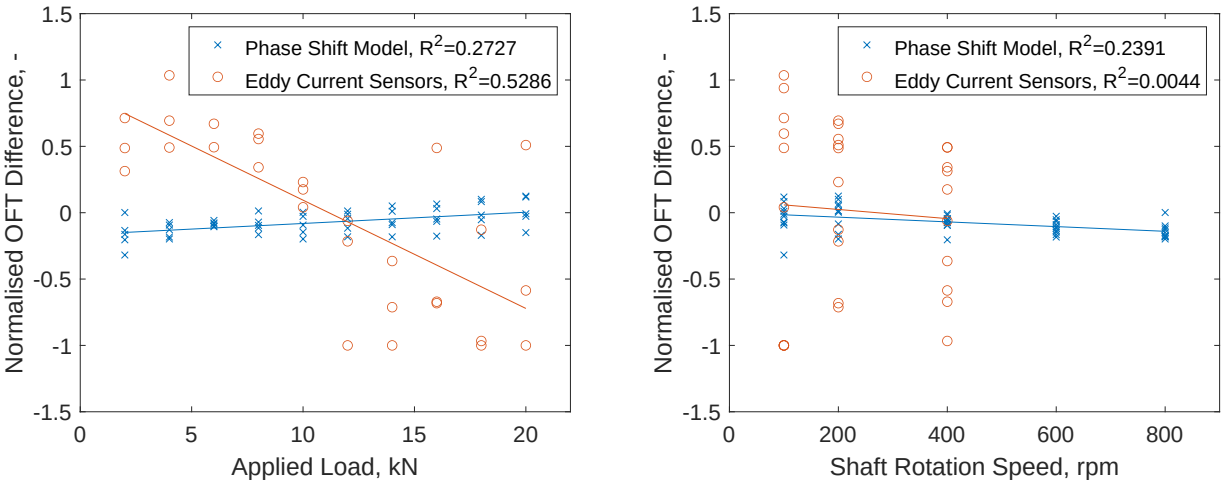

Figure 8.10: Normalised difference in film thickness between measurement and prediction against load (left) and rotation speed (right). Ultrasonic phase shift and conventional eddy current sensor measurements are presented, along with corresponding linear regression fits.

8.1.5 Comparison between Oil Types

A key function of this test platform is to enable the comparison of bearing lubricants in a more realistic experimental setup than simple tribometers. Such an example is presented in Figure 8.11, with the conditions tested shown in Table 8.1. In this study, two oils of different base viscosities were tested at 40°C, with loads ranging from 2 kN to 20 kN and shaft rotation speeds of 200 rpm and 300 rpm. The first oil selected was Shell Melina S 30, with a viscosity of 104 cSt at 40°C and 11.6 cSt at 100°C. The second oil was Chevron Neutral Oil 220R, a paraffinic base oil with a viscosity of 43.7 cSt at 40°C and 6.3 cSt at 100°C.

As expected, the more viscous oil (Shell Melina S 30) consistently generated thicker films under the same operating conditions. This is evident in both the minimum film thickness measurements and observing the more complete circumferential profiles. Both oils show a positive film thickness relationship with rotation speed and a negative relationship with applied load. This agrees with lubrication theory.

Table 8.1: Operating conditions applied in oil type comparison study.

Oil Type	Temperature	Viscosity	Speed	Load
Shell Melina S 30	40°C	104 cSt	200 rpm	2-20 kN (2 kN steps)
			300 rpm	
Chevron Neutral 220R		43.7 cSt	200 rpm	2-20 kN (2 kN steps)
			300 rpm	

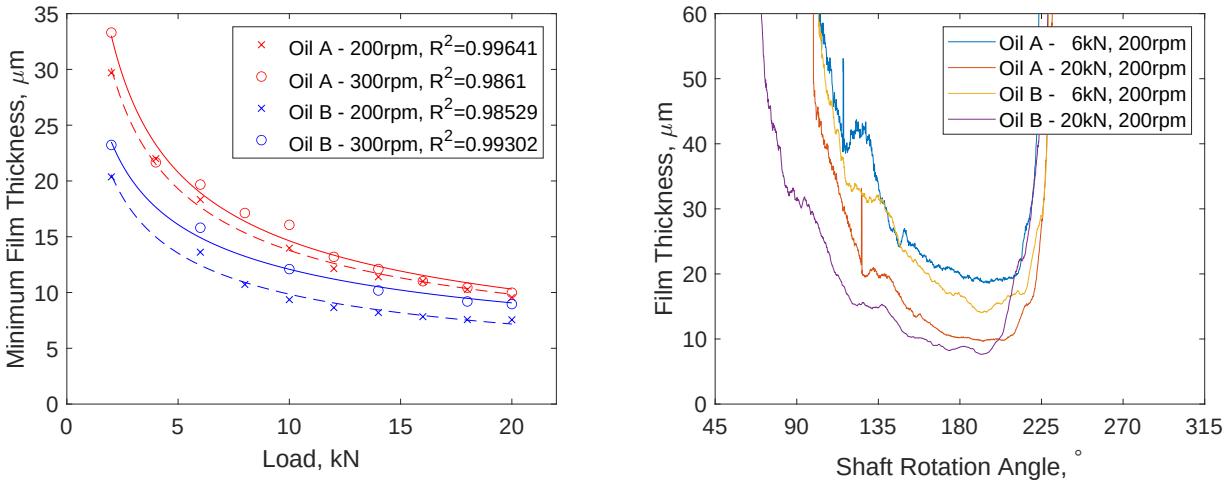

Figure 8.11: Minimum (left) and circumferential (right) film thickness comparison between two oils of different viscosities at 40°C, obtained via the ultrasonic phase shift technique. One-term power series fits for minimum film measurements are presented, along with corresponding R^2 values. Oil A (Shell Melina S 30) and Oil B (Chevron Neutral Oil 220R) viscosities at 40°C are 104 cSt and 43.7 cSt respectively.

8.1.6 Indirect Pressure Measurement

Returning to the procedure for determining film thickness in Figure 7.15 we see that hydrodynamic pressure is calculated as an intermediate step. This parameter is useful within itself. For example, pressure dictates the load carrying capacity of the bearing [36], so if it can be measured then designers can optimise bearing geometry, operating conditions or oil viscosity more effectively.

Peak pressures calculated from the phase model film thickness data presented in Figure 8.7 are shown in Figure 8.12. This is compared against pressures predicted by the Raimondi-Boyd technique. At low loads, the agreement between measurement and prediction is good, with peak pressure increasing with load and decreasing with rotation speed. However, as pressure rises measurement uncertainty increases rapidly. This is because a small change in film thickness leads to a much larger change in pressure, particularly for thinner films. This is evident by comparing the magnitude of film thickness error bars in Figure 8.7 with pressure error bars in Figure 8.12, where the pressure error bars are clearly much larger proportionally.

Unfortunately, these results indicate this technique seems only suitable for approximate measurements of bearing pressure, although comparative measurements over different operating conditions appear to be robust. If the accuracy of the method could be improved, this may mean separate conventional pressure transducers are not required. Future bearing systems could use embedded ultrasonic transducers instead of conventional pressure transducers. Ultrasonic transducers are of similar complexity to implement and have the added capability of film thickness measurements.

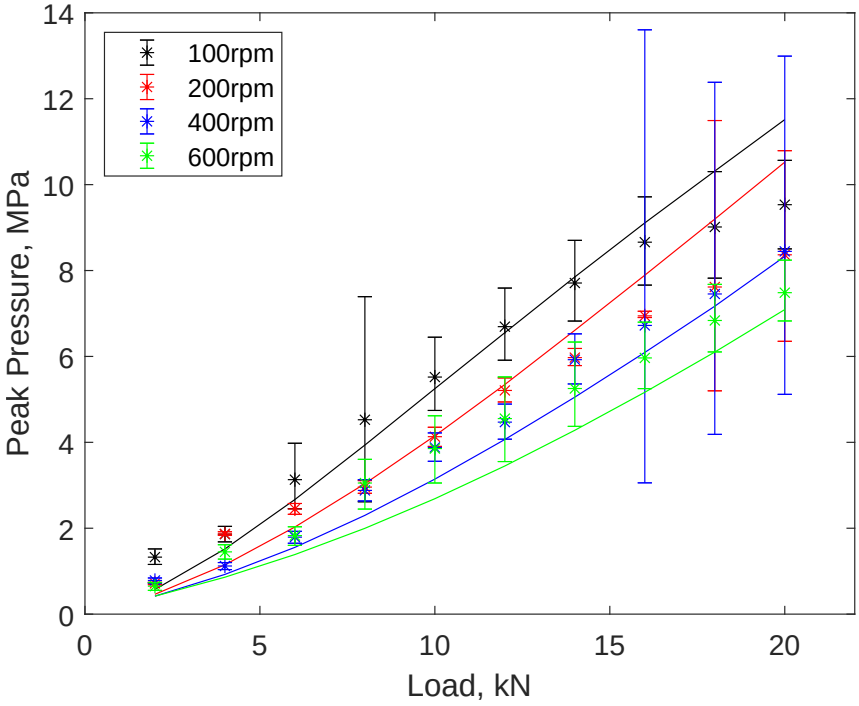

Figure 8.12: Peak pressure measured indirectly using film thickness derived via the ultrasonic phase shift model, compared against a Raimondi-Boyd prediction. Error bars indicate SEM.

8.1.7 Detecting Evidence of Shear Thinning

Due to the operating conditions selected, the ultrasonic film measurements also provide an opportunity to investigate whether signs of shear thinning in this lubricant are present. Referring back to the Sommerfeld number equation:

$$S = \left(\frac{r}{C}\right)^2 \frac{\mu LDN}{F} \tag{8.1}$$

It can be observed that different input variables can result in the same Sommerfeld number and therefore lubricant film thickness. However, shear rate is linked to rotation speed and film thickness by:

$$\gamma = \frac{U}{h} \tag{8.2}$$

Where γ is shear rate, and U is relative surface velocity.

As a result, it is possible for two operating conditions to have the same Sommerfeld number and film thickness but different shear rates. For example, a bearing system operating at 100 rpm and 4 kN should expect the same film thickness as if it operated at 200 rpm and 8 kN, provided all other variables remain consistent. Yet, as the second condition has double the rotation speed its shear rate is also doubled. If shear thinning does occur then

viscosity would decrease and these statements would no longer hold true, with a relative reduction in film thickness occurring.

The test program was structured so that sets of tests with the same Sommerfeld number but different shear rates were performed. Also, a dimensionless film thickness ratio parameter was defined.

$$Film\ Thickness\ Ratio = \frac{h_{min}}{h_{(min,\gamma\approx 0)}} \tag{8.3}$$

Where h_{min} is the minimum film thickness within a particular test and $h_{(min,\gamma\approx 0)}$ is the minimum film thickness of the test case that has the lowest shear rate within a set. If the lubricant is shear stable this ratio should equal approximately one across all tests in the set. Conversely, if shear thinning effects were present, one would expect a negative correlation between shear rate and film thickness ratio.

Figure 8.13 shows the film thickness ratio against shear rate for all test cases. In this study, film thicknesses were calculated via the ultrasonic phase shift method and the oil used is Shell Melina S 30. It was found that there was no significant deviation from the gradient, with no strong correlation between the two variables. Therefore, it can be concluded that shear thinning does not occur in this lubricant, at least up to a shear rate of $3 \times 10^7\ s^{-1}$. This is in line with expectations.

It would be interesting to repeat this test procedure with a lubricant that should shear thin over this range. Although evidence of shear thinning was not identified, the methods described provide a framework to test shear thinning in other oils.

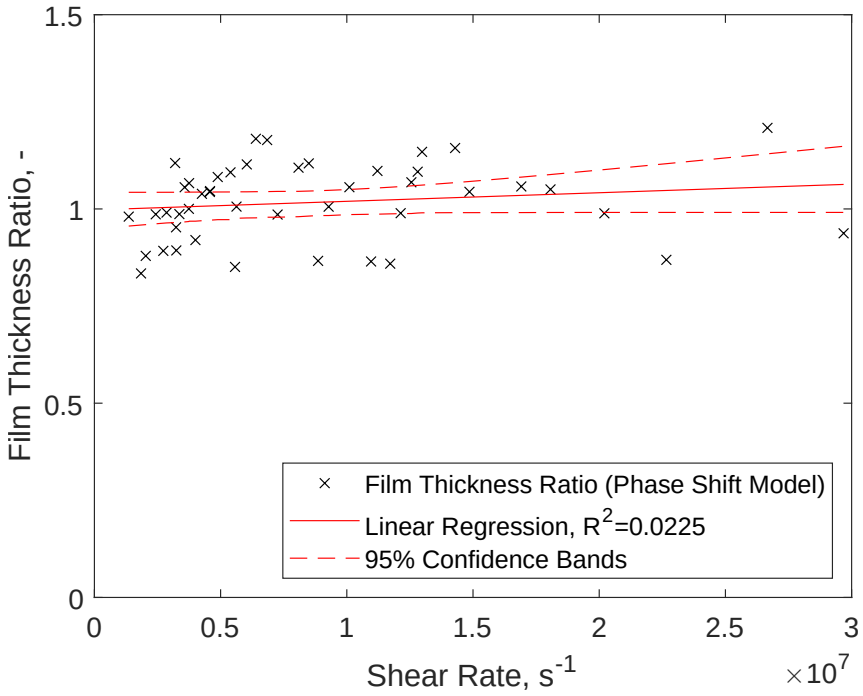

Figure 8.13: Shear Rate against film thickness ratio for the oil used in this investigation.

8.1.8 Detecting Evidence of the Acoustoelastic Effect

Introduced in Section 3.6, the acoustoelastic effect is where the application of stress causes a change in acoustic velocity and therefore also acoustic impedance. Thus, if pressures on the shaft or bearing are of sufficient magnitude a shift in ToF (time-of-flight) would be observed. This ToF shift would lead to errors in the ultrasonic phase shift method because the apparent phase shift would be the sum of the phase shift due to changing film thickness plus the ToF shift due to the acoustoelastic effect. These components are difficult to decouple, hence it is important to determine if the acoustoelastic effect is significant.

To detect signs of the acoustoelastic effect, A-scans from tests with the same Sommerfeld number but different applied loads were selected. This criterion is achieved by balancing load with shaft rotation speed. If acoustoelasticity is negligible then these A-scans should all have the same phase shift, in fact, the entire A-scans should be identical. However, if the acoustoelastic effect is significant then ToF will reduce with increasing load.

Figure 8.14 shows A-scans for tests with different loads but an identical Sommerfeld number. A-scans within the thick film, unloaded region and minimum film, loaded region are shown. Zoomed views of the first A-scan zero-crossings are also presented. To identify the point of zero-crossing more clearly, the temporal resolution of each A-scan has been increased via a windowed sinc interpolation. This method of interpolation was selected as Dou et al. identified in 2020 that it is the optimum model for ultrasonic waves, providing much greater accuracy than linear or cubic spline interpolation [210].

As expected, changes in zero-crossing between the thick film and minimum film A-scans are observed due to a phase shift caused by reduced thickness. By taking the difference in zero crossings between thick film and minimum film A-scans, there was no significant difference between tests. This strongly suggests that the acoustoelastic effect is negligible in this investigation.

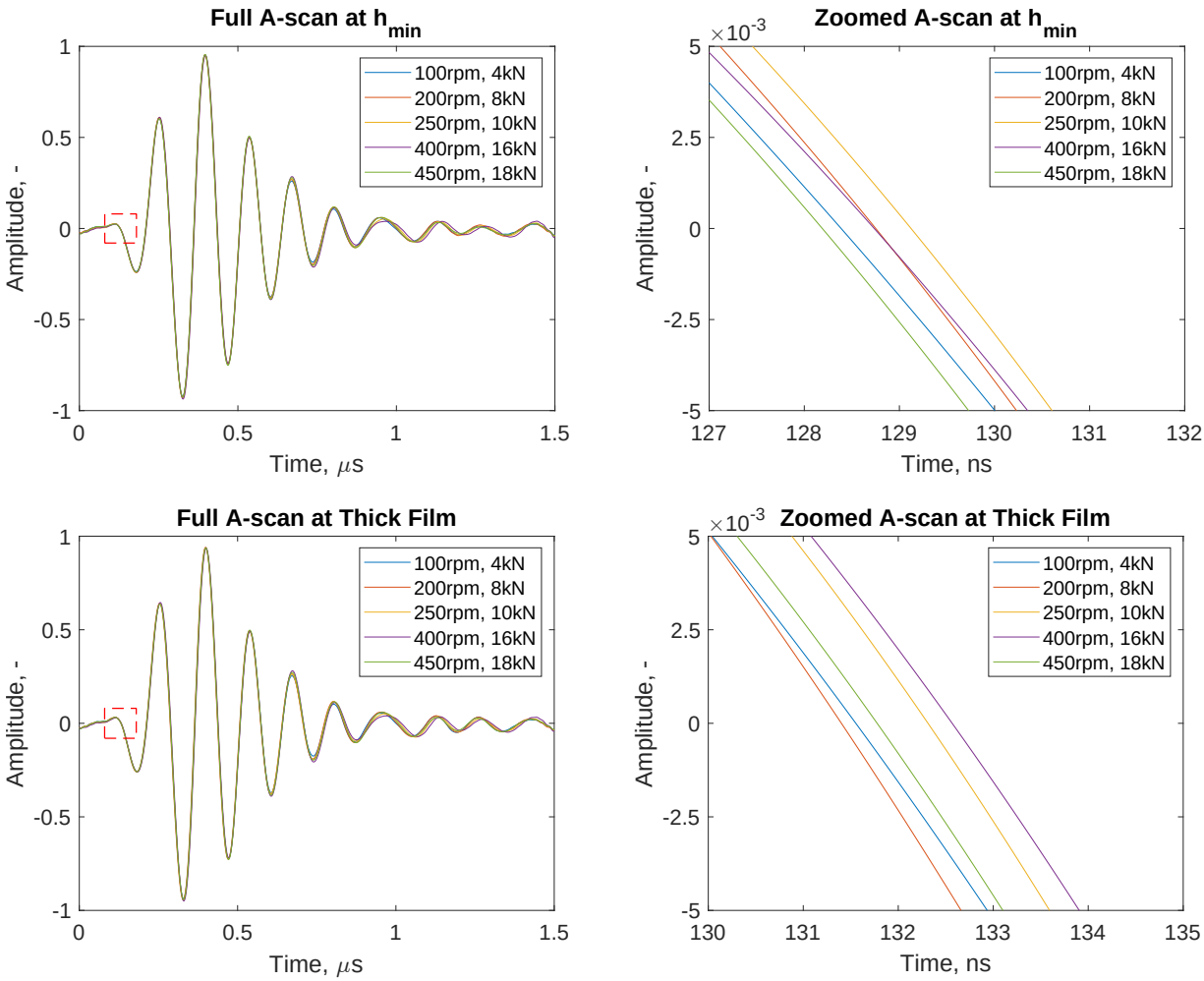

Figure 8.14: A-scans of reflected signals under different operating conditions but identical Sommerfeld numbers. A-scans at the point of minimum film thickness (top) and within the thick film region (bottom) are presented.

8.2 Inspection of Surface Wear

A surface wear analysis of the bearing shells was performed to further understand the system behaviour during operation and to identify any unusual features.

The photographs presented in Figure 8.15 were taken after normal operating conditions testing. These show that the flash layer has been removed in some areas of the bearing

shell. Removal of the flash layer is expected during normal operation as its function is for aesthetics and to protect the bearing from corrosion prior to installation. In fact, it is unusual to maintain so much of this flash material as the layer is so soft that it may be easily removed by lightly rubbing the surface with a cloth. The flash layer pattern provides an opportunity to observe where wear is most substantial and if the wear pattern lines up with expectations. Features of particular interest have been identified in these photographs.

First, wear is clearly more significant on the top bearing. This is expected as the bearing is pulled down onto the shaft and as such the thin film region is found on the top bearing. Similarly, annotation A indicates wear is greater on the right side of the top bearing than the left side. Shaft rotation causes the location of minimum film thickness to shift away from the top of the bearing, creating an attitude angle. In this case minimum film thickness shifts to the right, which agrees with the wear pattern observed.

Another observation is that wear appears symmetrical along the axial direction, highlighted by annotation B. This indicates that the system is axially aligned. Wear in the bearing axial centre is marginally greater, suggesting a thicker film at the bearing edges. This is explored in more detail later in Section 9.1.

To identify changes in roughness due to wear, the bearing shells were profiled before and after testing using an Alicona InfiniteFocus SL optical surface measurement system. Significant changes in roughness may affect hydrodynamic flow of the lubricant, introducing uncertainty when comparing different lubricants. Also, a sharp increase in roughness could suggest severe wear has occurred. Figure 8.16 presents the change in R_a (arithmetic mean) and R_q (root mean square) roughness for the top bearing shell.

Prior to testing, axial and radial roughnesses are near identical, by both R_a and R_q measures. This is expected as the sputtering process used in depositing the overlay during bearing manufacture should create an isotropic surface profile. After testing, a small but significant decrease in R_a and R_q is observed along the radial direction. It is thought that this is because the peaks of the asperities are removed by adhesion due to the relative motion between the bearing and shaft surfaces along the radial direction. As roughness slightly decreases it can be concluded that mild wear has occurred.

In the axial direction, however, both R_a and R_q slightly increase. To investigate this further, zoomed photographs of the top bearing shell were taken before and after testing via the Alicona InfiniteFocus SL. These are presented in Figure 8.17. The used bearing shell image clearly shows thin wear scars along the radial plane, most likely formed due to abrasive wear. The peaks and troughs of these scars would contribute to the overall roughness measurement in the axial direction but not the radial direction.

Under the operating conditions investigated in this chapter, the oil film is sufficiently thick that the bearing is still conformably within the hydrodynamic lubrication regime, even with the slightly elevated axial roughness. In support of this, the repeatability study

previously discussed in Section 8.1.3 found that once the bearing shells had run-in film thickness measurements remained consistent. However, under more severe conditions this variation in roughness could affect the point at which the system transitions into the mixed regime.

Figure 8.17 also shows that wear is generally consistent across the bearing surface. However, annotation C indicates a small wear pocket in the surface. As the oil used in normal operating conditions testing is new and the lubricant circulation system includes an oil filter, it is most likely the wear scar is caused by a broken asperity from either the bearing or shaft, although it is still possible this scar is caused by a third body contaminant. The feature appears similar to one observed by Liu et al., in which they attributed their wear scar to micro-ploughing [211]. Feature C is offset from the axial centre and thus is not detected by the circumferential ultrasonic film measurements in this study.

The shaft was also inspected visually before and after testing. Previous research has shown that even small scratches can upset the hydrodynamic flow, modifying the pressure field and maximum pressures experienced in the bearing system [139]. No scratches or other wear scars were observed. This is expected due to the greater hardness of the shaft in comparison to the bearing shells.

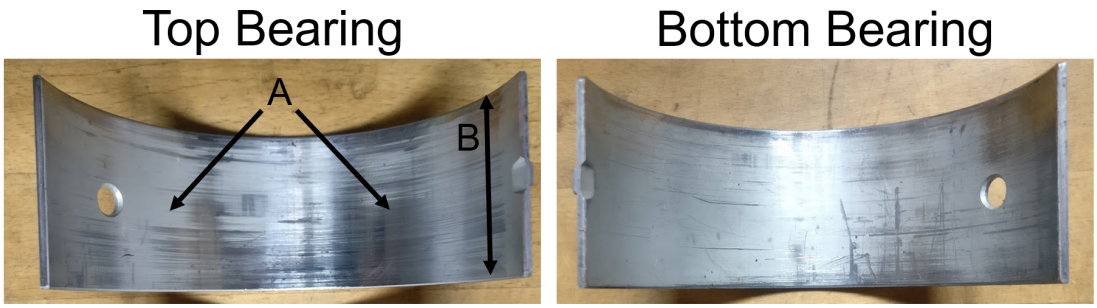

Figure 8.15: Photographs of the top and bottom bearing shells after normal operating conditions testing. Areas of interest A, B and C are annotated.

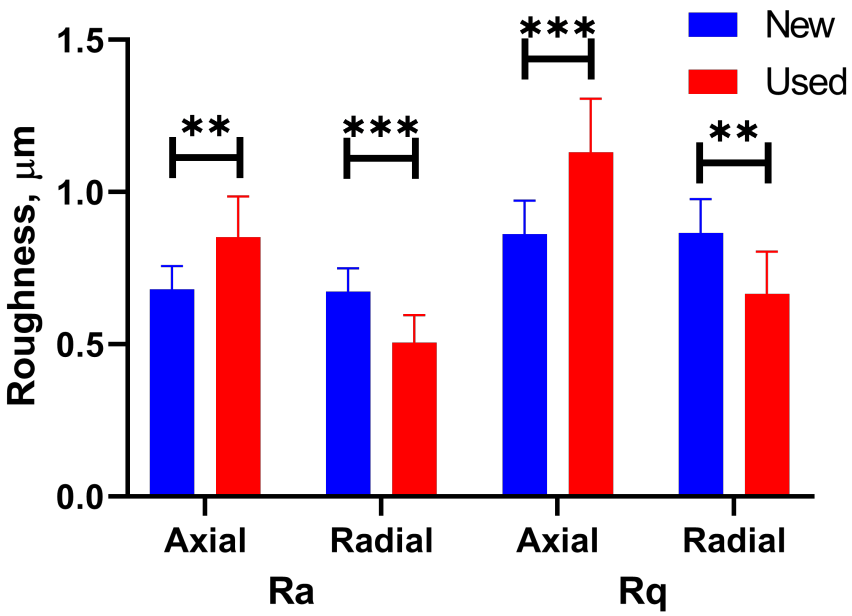

Figure 8.16: Bearing shell roughness measurements before and after normal operating conditions testing. Measurements are taken along the axial and radial directions.

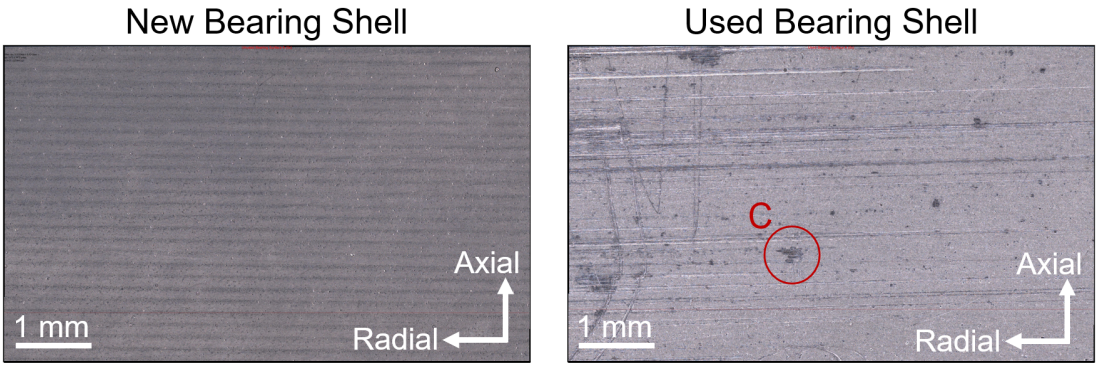

Figure 8.17: Images of top bearing shell before and after normal operating conditions testing, taken using an Alicona InfiniteFocus SL. Feature of interest C is indicated.

8.3 Conclusions

This chapter has covered the results and analysis from tests performed on the BAXTER static loading test rig under normal operating conditions. This includes:

- The capture of near-complete circumferential film thickness measurements around the bearing circumference for a range of rotation speeds and applied loads. These were obtained via a combination of ultrasonic methods, namely the amplitude, phase shift and resonant dip techniques. Hydrodynamic pressure has also been accounted for, although the resultant improvement in film thickness measurement is minor. As such, pressure effects can be ignored in lightly to moderately loaded bearings in the calculation of film thickness via ultrasound unless high accuracy is required. Circumferential film thickness profiles were compared against a Raimondi-Boyd prediction and were in good agreement.

- Minimum film measurements via the amplitude, phase shift, exact-complex and Raimondi-Boyd prediction have been shown to agree well, particularly for thinner films. This is also the first instance in which the exact-complex technique has been verified by a third party or applied to a dynamic system.

- Duplicate testing has demonstrated excellent platform repeatability. This is essential if the test platform and ultrasonic methods are to be used for comparative measurements, such as investigating different oil types or bearing materials.

- Two oils of different viscosity have been evaluated. As expected, a consistently thinner minimum film thickness was observed with the low viscosity oil.

- Evidence of either shear thinning or acoustoelastic effects were not found. A framework for applying the test platform to measure shear thinning in lubricants up to $3 \times 10^7 s^{-1}$ has been developed.

- Wear analysis found bearing roughness changes during operation and thus a run-in period is required. Also, wear is evenly distributed across the axial direction of the bearing, suggesting good alignment.

Chapter 9

Severe Operating Conditions

This chapter details findings from testing performed using the BAXTER rig, introduced in Chapter 6, under more severe operating conditions. This includes inclined shaft misalignment, offset load, starvation and run-down testing. These conditions are often considered undesirable and are generally not as well understood compared to normal operating conditions due to their increased complexity.

9.1 Misalignment Testing

In this investigation, the shaft was inclined incrementally so that the effect of misalignment on film thickness across the bearing length could be observed. This was achieved by inserting metal shims of known thickness under one roller bearing support block, raising it by set amounts. Also, to stop the bearing assembly from self-aligning, the flexible linkage which transfers the applied load was replaced by a rigid linkage, both photographed in Figure 9.1 for comparison. This rigid linkage restricts any tilting motion by the bearing assembly.

For misaligned testing three transducer pins along the shaft's axial plane were used, these are Pins A, B and C (see Figure 9.2); thus allowing a comparison of the film thickness profile in this plane. To ease comparison, the profile of Pin B has been shifted 90° to align with Pins A and C. The lubricant used in this investigation is Shell Melina S 30.

Figure 9.2 demonstrates that inducing misalignment has a significant effect on circumferential film thickness profiles. In this figure, a comparison between an aligned and misaligned case is shown. For the aligned case each film thickness profile is very similar, whereas for the misaligned case film thickness profiles vary substantially along the axis of the shaft. In the aligned case there is a small difference between the central pin, Pin B, and the offset pins, Pin A and C. It is expected that this is due to deformation of the bearing shell. This deformation is symmetrical along the bearing width, hence Pin A and Pin C showing near-identical film thickness profiles.

Focusing on Pin C, for which film thickness is lowest along the axial direction, one can

observe how this changes with misalignment angle. In Figure 9.3, it can be seen that an increase in inclination leads to a reduction in film thickness across the entire circumference. However, as misalignment increases further, the film thickness reduction is not as substantial due to the non-linear relationship between pressure and film thickness, as demonstrated by both the Raimondi-Boyd prediction [113] and the Reynolds equation [212]. At 130° rotation angle, a small but sharp peak in film thickness is observed in Figure 9.3. This feature is consistent across all profiles. It is thought that this is either due to a scratch or an embedded 3^{rd} body particle in the bearing surface.

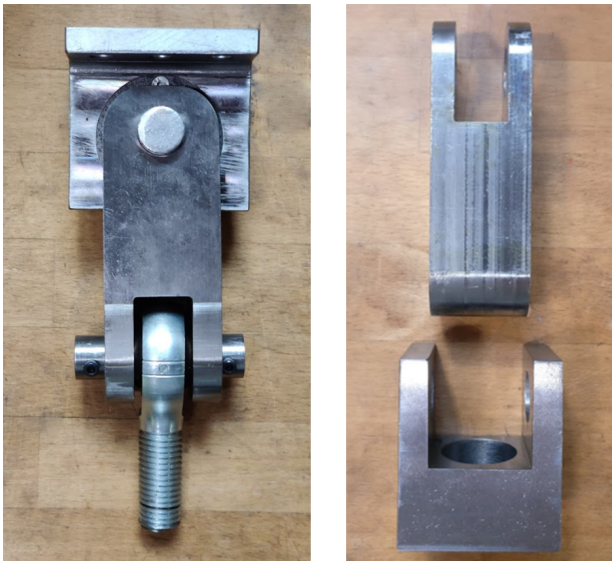

Figure 9.1: Photograph of flexible linkage used in normal operating conditions testing (left) and rigid linkage used in misaligned and offset load testing (right).

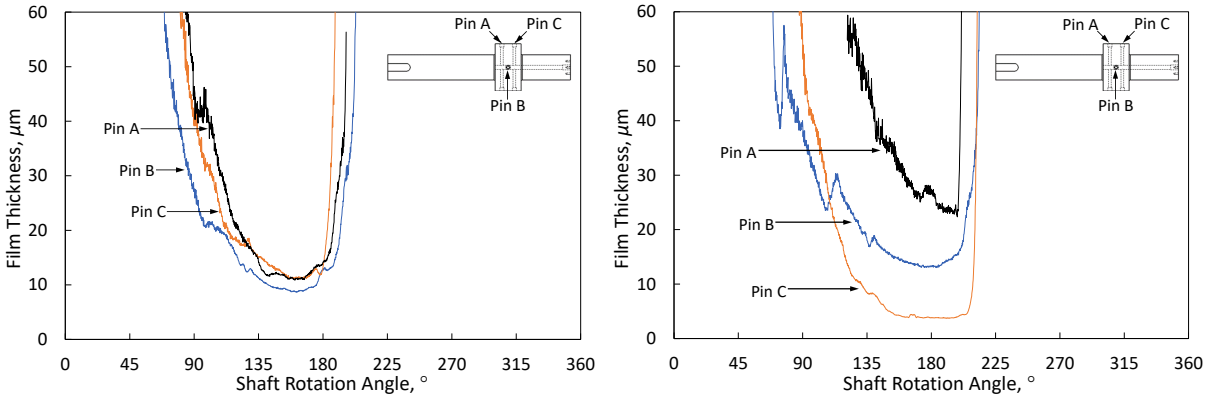

Figure 9.2: Film thickness within the thin film region for three locations along the bearing width under aligned (left) and 0.085° misaligned (right) conditions. Measurements are obtained via the phase shift model.

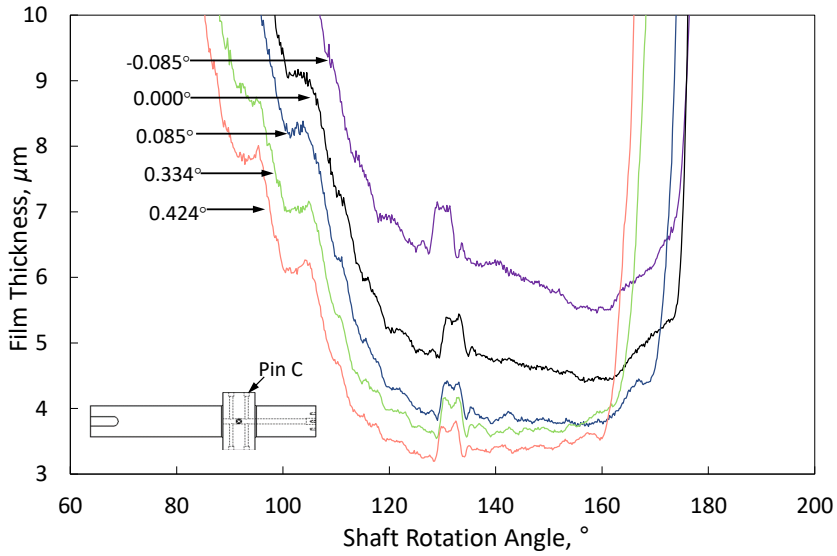

Figure 9.3: Circumferential film thickness profiles for Pin C under a range of misalignment angles, obtained via the phase change model.

9.2 Offset Load Testing

An alternative method to induce misalignment in a bearing system is to offset the applied load in the axial plane. Even if a system is perfectly aligned it may be required to withstand offset loads. For example, stern tubes in marine applications experience significant lateral loads during turning manoeuvres [213].

In this study, misalignment was achieved by including an offset of 8 mm in the loading arm using a redesigned linkage component, photographed in Figure 9.4.

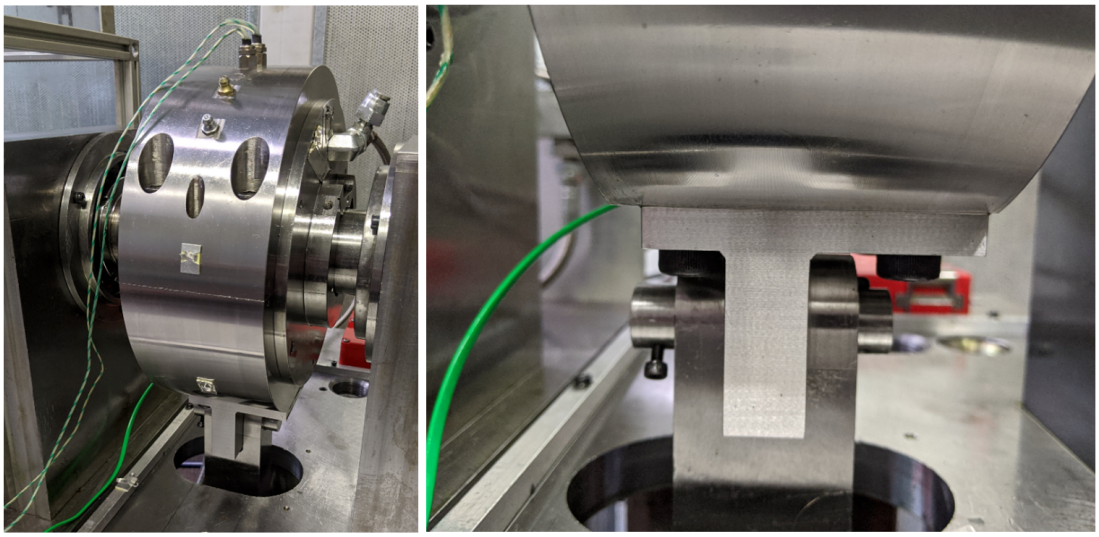

Figure 9.4: Photograph of bearing assembly with offset load linkage fitted (left). Zoomed view photograph of offset load linkage (right).

Minimum film thickness along the axial plane for various speeds and loads is shown in Figure 9.5. In a similar manner to angled misalignment testing in the previous section, film thickness is measured at three locations along the axial direction via Pins A, B and C. A linear fit of these results is also applied. The goodness of fit of this linear approximation appears to be most accurate for lower loads, as indicated by their greater R^2 values. As load increases, the axial profile appears to become more non-linear. It is thought that this is due to shaft bending, bearing deformation or a combination of the two.

Measurements in Figure 9.5 are also compared against numerical predictions. The numerical model applied follows the routine described by Stachowiak and Batchelor for misaligned bearings [10]. Measured and predicted results are similar in magnitude and gradient, although generally, the numerical model predicts a thinner film. This may be because the model makes the following assumptions:

- The fluid is isoviscous.
- The fluid is Newtonian.
- Bearing and shaft deflection is negligible.
- Geometric features such as oil ports are ignored.
- Zero bearing and shaft roughness.

Additional measurements under offset loading conditions are presented in Figure 9.6. This demonstrates more clearly the trend towards a non-linear axial profile as Sommerfeld number decreases (due to higher load or slower rotation speed). Furthermore, the gradient of the axial profile decreases with increasing load. This may be due to elevated lubricant viscosity at the thin film side due to the greater hydrodynamic pressure.

Following the same procedure outlined in Section 8.1.6, the measured film thickness may be used to approximate hydrodynamic pressure in the bearing contact. Results under offset loading conditions for rotation speeds of 100 rpm and 300 rpm at loads between 4 kN and 20 kN are presented in Figure 9.7.

Both pressure at the axial centre of the bearing and peak pressure are shown, along with comparisons against numerical predictions. Also, full pressure distribution maps for two test cases are shown in Figure 9.8. The measured and predicted pressures at the bearing axial centre are in good agreement. However, predicted peak pressures are much greater than calculated from experimental results, on average 107% higher. This highlights the strong relationship between film thickness and hydrodynamic pressure, particularly under thin film conditions. Thus, there is great value in improving the measurement accuracy of ultrasonic methods, such as more robust referencing techniques or accounting for the effect of pressure on density and acoustic velocity in calculations.

Differences may also be due to the assumptions made by the numerical model, such as a lack of consideration for shaft bending or viscosity dependence on pressure. Also, as

this model is isoviscous it does not account for the temperature variation across the axial plane. In a misaligned system the highest temperatures are around the peak pressure region, which leads to a local reduction in lubricant viscosity, increasing misalignment further [214, 68]. As such it may be worthwhile to compare results against a more sophisticated thermohydrodynamic (THD) model in future.

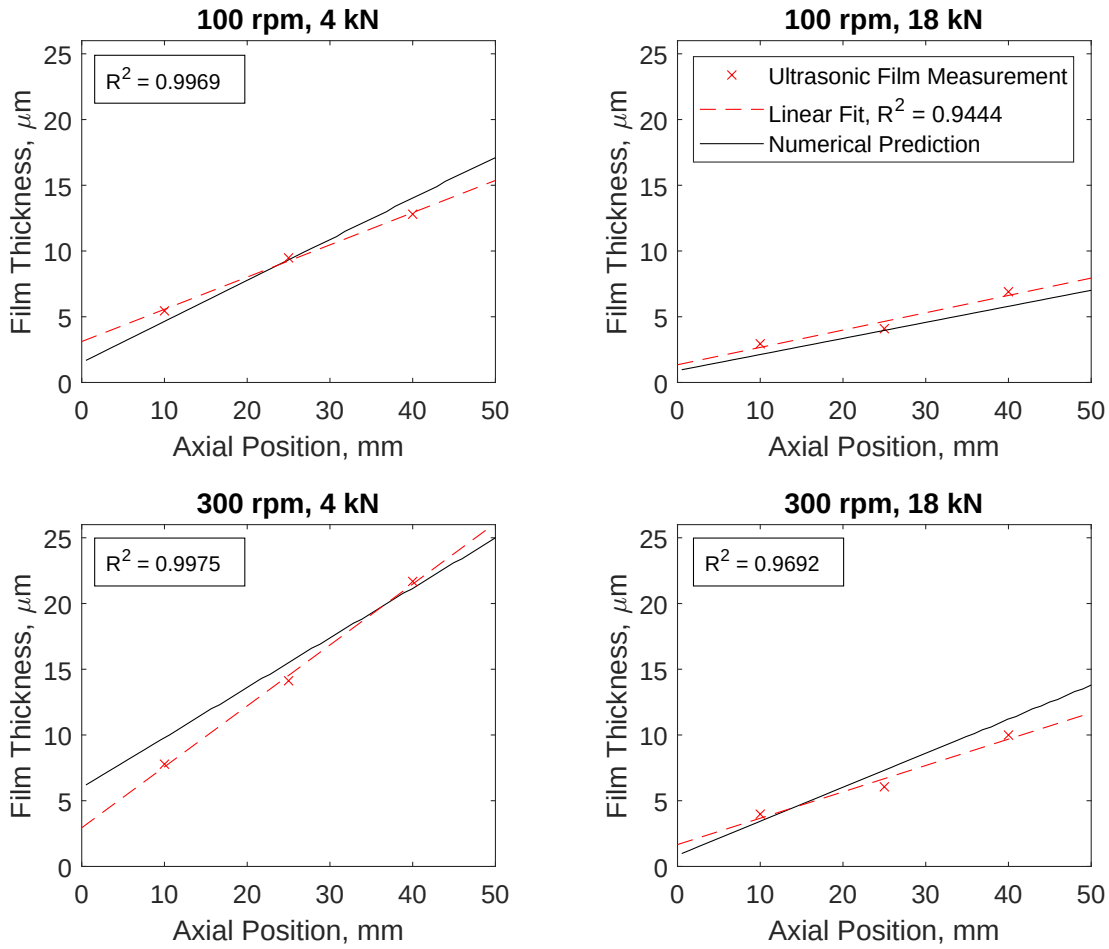

Figure 9.5: Film thickness along the axial plane under offset loading conditions. Measured via three shaft-mounted ultrasonic transducers, with linear fits applied. Predictions from a numerical model are also presented.

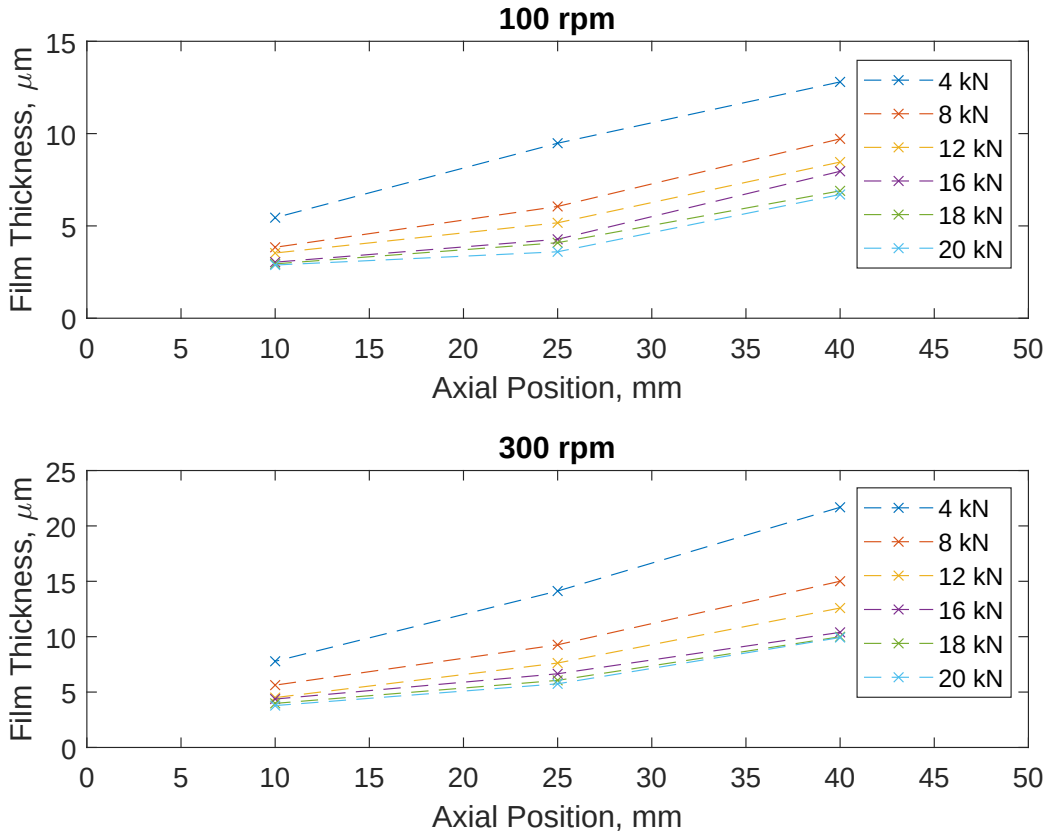

Figure 9.6: Measured film thickness across the axial plane for a range of applied loads, with a load offset of 8 mm.

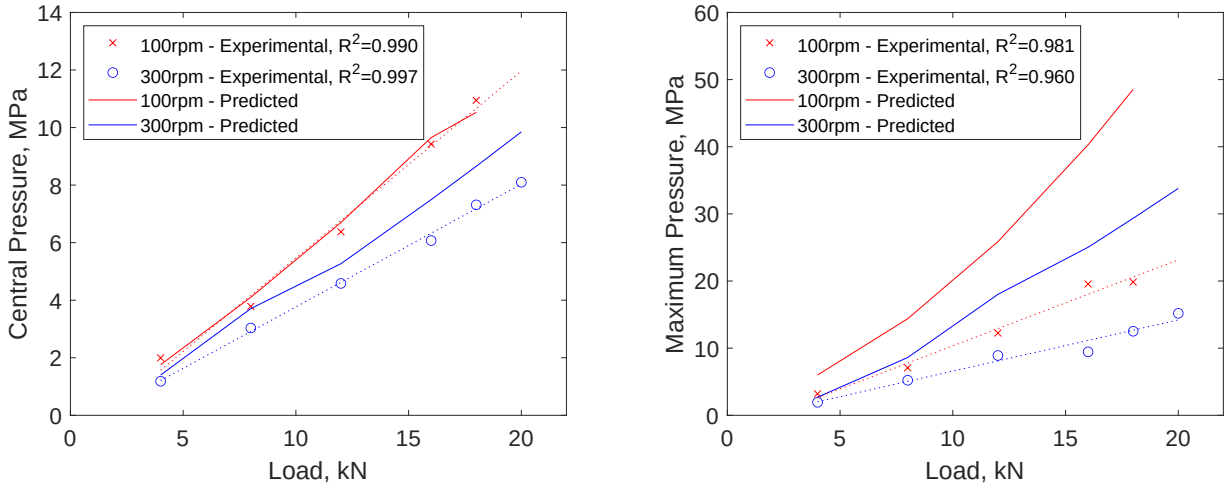

Figure 9.7: Change in central pressure (left) and maximum pressure (right) with applied load, with a load offset of 8 mm. Results derived from ultrasonic film thickness measurements and from numerical predictions are presented.

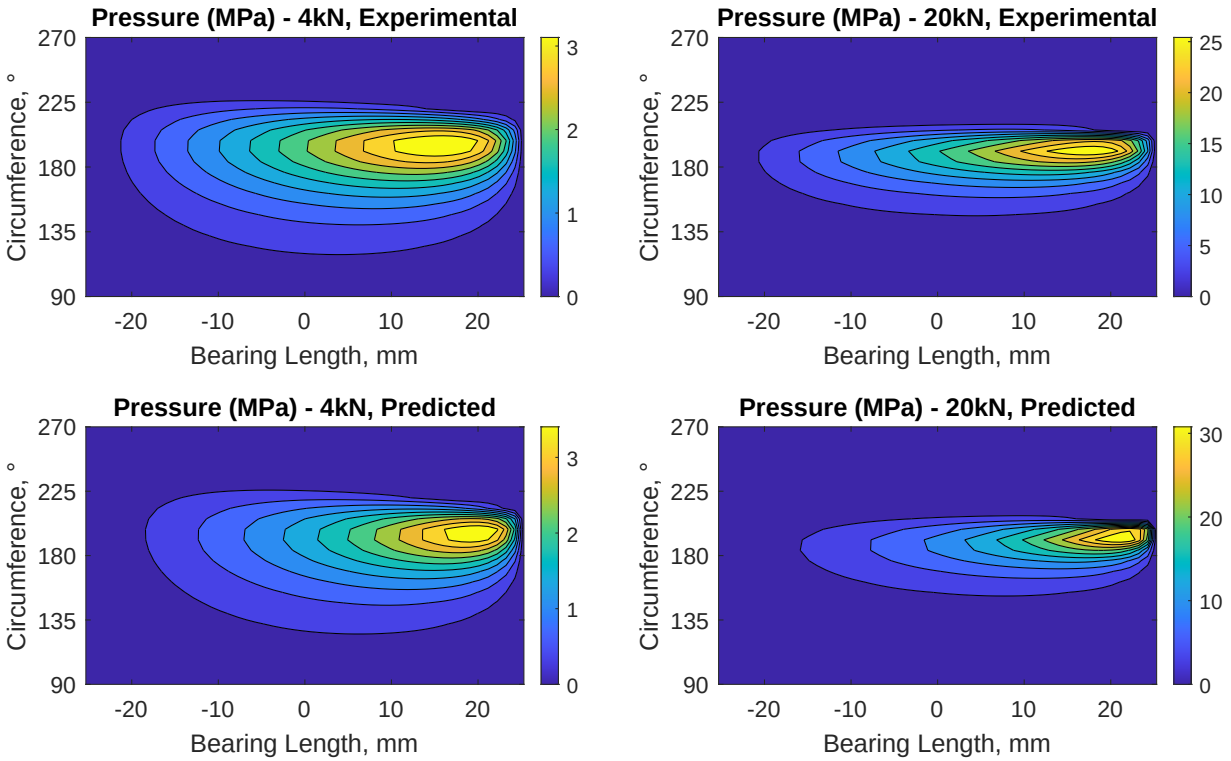

Figure 9.8: Pressure map of journal bearing under 4 kN and 20 kN applied load, with a load offset of 8 mm and a shaft rotation speed of 300 rpm. Results are derived from ultrasonic measurements (top) and a numerical model (bottom).

9.3 Run-down Testing

As shaft rotation speed decreases hydrodynamic pressure also drops. Therefore, during a run-down cycle, such as when an internal combustion engine is stopped, film thickness steadily decreases and the system transitions through each lubrication regime.

In this study, the BAXTER rig operates at a constant speed of 300 rpm with an applied load of 20 kN. Then, when equilibrium is reached, the rotation speed is reduced at a constant rate to 0 rpm over 90 seconds. Film thickness via the phase shift technique and torque are recorded during the cycle. The same oil as characterised in Section 7.1 (Shell Melina S 30) is used in this investigation.

The change in torque and film thickness during two run-down cycles are shown in Figure 9.9, one at 40°C bearing temperature and one at 60°C. This shows that, as expected, film thickness decreases steadily throughout each cycle. Also, torque gradually reduces then sharply increases as the system enters the mixed lubrication regime. Due to reduced viscosity, this transition occurs earlier for the 60°C bearing temperature cycle (88.3 rpm) compared to the 40°C bearing temperature cycle (79.3 rpm).

Film thickness and rotation speed at the inflection point for a wider test set is presented in Figure 9.10. In this, oil viscosity is controlled by varying bearing temperature. An extra-sum-of-squares F test identified a linear fit was preferred to model the relationship between film thickness at inflection point and viscosity, whereas the relationship between rotation speed at inflection point and viscosity was best modelled by a logarithmic fit.

As expected, a greater viscosity allows the system to remain within the hydrodynamic regime at slower rotation speeds. Also, film thickness at the inflection point appears to be dependant on viscosity. A statistically significant positive correlation (P=0.0002) between viscosity and oil thickness at inflection is observed.

9.3.1 Predicting Lubrication Regime Transition

As discussed in Section 2.2, the thickness at which a system transitions between lubrication regimes is strongly linked to the roughness of the shaft and bearing surfaces. This thickness may be predicted via the lambda ratio (Equation 2.5). It is commonly stated that a lambda ratio above 3 is sufficient for there to be no significant interaction between asperities [40, 215], at which point the system is operating within the hydrodynamic regime.

Using the lambda ratio, along with the roughnesses of the shaft and bearing surfaces, a prediction for the film thickness at which the system should transition to the mixed lubrication regime may be calculated:

$$h_{min} = \lambda\sqrt{R_b^2 + R_s^2} = 3 \times \sqrt{0.506^2 + 0.1^2} = 1.54\ \mu m \pm 0.26\ \mu m. \tag{9.1}$$

This calculation uses the bearing roughness along the radial direction after running in, as

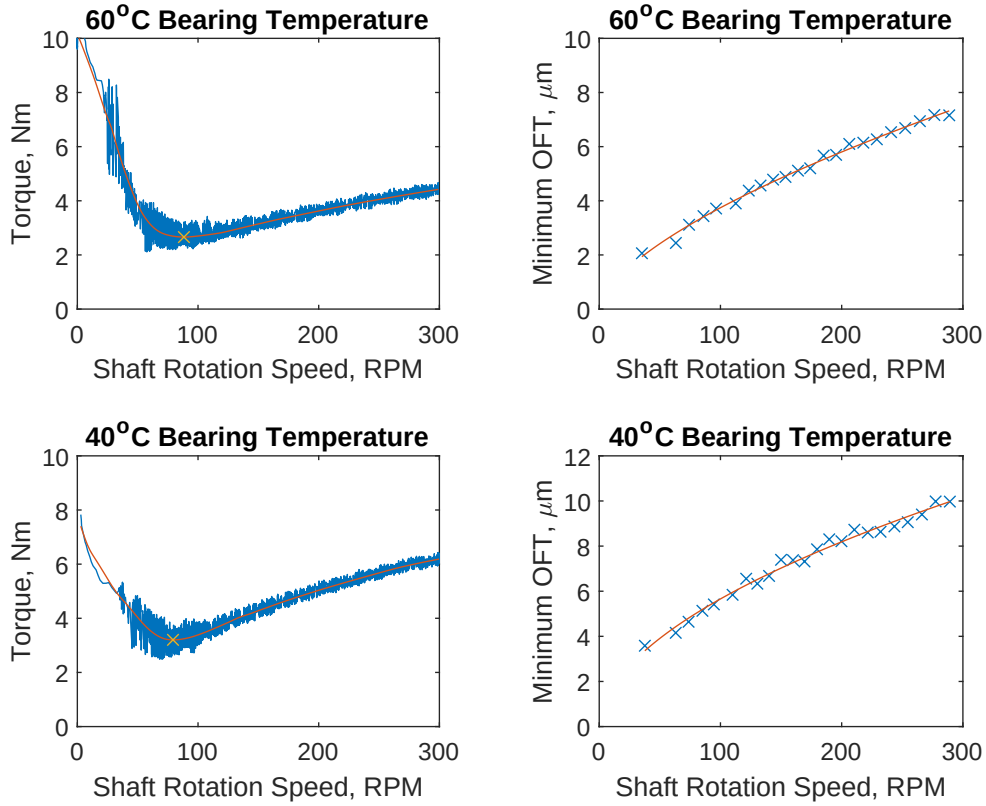

Figure 9.9: Change in torque and film thickness during a run-down cycle with an applied load of 20 kN at 40°C and 60°C bearing temperature.

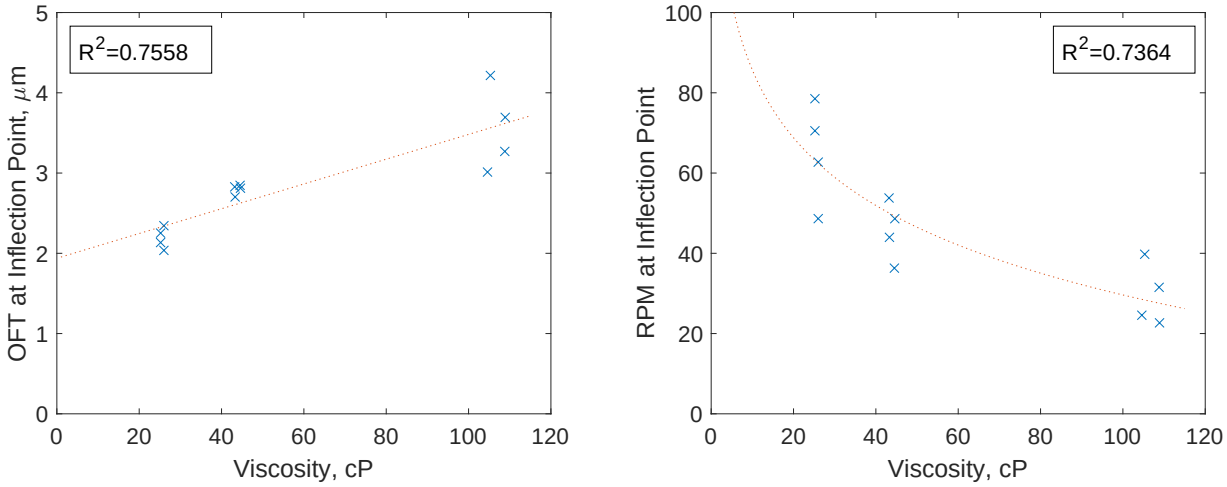

Figure 9.10: Film thickness (left) and shaft rotation speed (right) at the torque inflection point for different lubricant viscosities under aligned conditions.

found in Section 8.2. The radial direction was selected as this is the direction of relative motion between surfaces. An uncertainty of ± 0.26 μm exists due to uncertainty in bearing roughness measurements. It was also observed that as the bearing roughness is much greater than that of the shaft this dominates the calculated transition film thickness value.

Returning to Figure 9.10, it is clear that a value of 1.54 μm is significantly lower than any case measured in this study. Alternatively, if one uses the bearing axial roughness (0.85 μm), predicted transition film thickness is 2.57 μm $\pm$0.40 μm, which is within the range of thicknesses observed. This highlights that a one-dimensional arithmetic mean roughness value is too simple for an accurate prediction, particularly when roughness is anisotropic. Furthermore, other sources argue that a lambda ratio of 3 is too low, such as Yan et al. suggesting full film lubrication is reached when the lambda ratio equals 5 or above [216].

Also, these predictions still assume that transition thickness is independent of operating conditions. One potential explanation for the observed correlation in Figure 9.10 is an occurrence of significant asperity deformation during operation. Flattening asperities due to hydrodynamic pressure would result in reduced roughness during operation. Raimondi and Boyd showed that decreased viscosity leads to an increased peak pressure given the same applied load [113]. This leads to greater asperity deformation, thus creating a smoother surface, which in turn causes transition film thickness to be reduced. This trend is evident in Figure 9.10, shown by the positive correlation between transition film thickness and viscosity. Peak pressure in this study is approximately within 10 MPa and 20 MPa. Such pressures would lead to some level of deformation, although not so high that plastic deformation would be expected [217].

9.3.2 Run-down under Offset Loading Conditions

To encourage the earlier transition to mixed lubrication, run-down tests were repeated using the offset loading setup described in Section 9.2. It was expected that due to the localised high pressure and therefore thinner oil film at the bearing edge, solid-solid contact should occur more readily under the same operating conditions.

Figure 9.11 presents film thickness at the axial centre and the thin film edge of the bearing at the point of torque inflection plotted against lubricant viscosity. As with the aligned case, a linear fit was preferred for the relationship between these variables.

A strong positive correlation between minimum film thickness at the axial centre of the bearing and viscosity was found. The positive correlation with film thickness at the bearing edge is weaker but still statistically significant (P=0.0037). This agrees with the findings from run-down testing performed under aligned conditions, again demonstrating the transition between lubrication regimes is more complex than simple lambda ratio models.

Also shown in Figure 9.11 is the shaft rotation speed at this inflection point plotted against viscosity. In this case, a logarithmic fit was preferred. As expected, the rotation speed at inflection is greater under the offset-load configuration. This highlights the importance of good shaft alignment, showing a misaligned bearing may experience significant wear even when operating within design parameters if undiagnosed. Also, the same negative correlation between rotation speed at inflection and viscosity as seen in aligned conditions

is observed, with the system able to operate within the hydrodynamic regime under slower rotation speeds with increased lubricant viscosity.

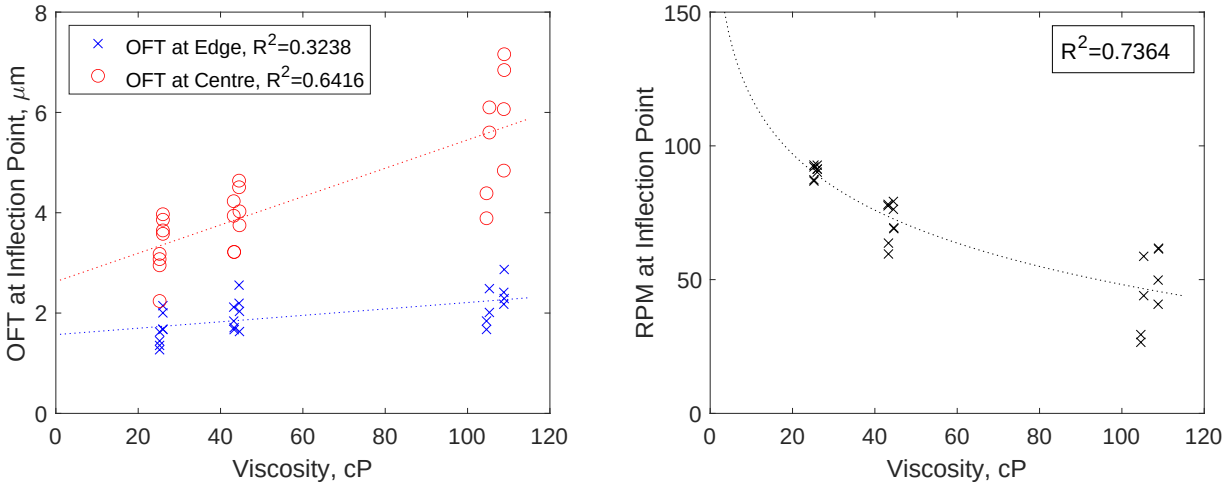

Figure 9.11: Film thickness (left) and shaft rotation speed (right) at the torque inflection point for different lubricant viscosities under offset loading conditions.

9.4 Starvation Testing

As discussed in Section 2.3.2, journal bearings must receive a sufficient supply of lubricant. If for some reason oil supply is restricted, such as a blocked inlet or cold weather causing slow circulation of oil due to increased viscosity, then solid-solid contact will occur. This starvation can be catastrophic, leading to very rapid wear rates, high temperatures or even seizure. The ability to detect starvation early may be incredibly useful so that the system can be stopped or adjusted to avoid any significant damage.

To investigate what happens at the onset of starvation, the test platform was run with the oil circulation pump turned off. An outlet hole was also opened at the bottom of the bearing assembly to allow oil to escape. A shaft rotation speed of 400 rpm and applied load of 10 kN were maintained throughout. Over time the bearing chamber drained of oil until starvation occurred. It should be noted that the platform was stopped reasonably quickly once signs of starvation appeared so as not to permanently damage the test platform. In future, more aggressive tests could be performed which allow the contact to be starved for a longer period.

Figure 9.12 shows the change in bearing temperature and minimum film thickness over the test cycle. It appears some mild form of starvation takes place between 10 and 20 seconds, in which film thickness decreases and bearing temperature increases. As metal-metal contact occurs the surfaces heat up due to friction. A reduction in film thickness is likely the result of elevated temperatures decreasing oil viscosity. The magnitudes of these changes are reasonably small, often starvation leads to a more dramatic increase in

temperature. This may be due to some residual oil still left in the contact. Running the test for a longer period may lead to a sharper increase in temperature.

The advantage of shaft mounted sensors is that they can measure signal response around the full circumference of every rotation. Indications that oil supply is reduced may be found outside of the minimum film region. Figure 9.12 shows the circumferential phase shift profile towards the start of the test (20^{th} rotation) and near the end of the test (410^{th} rotation). Even though the profiles are very similar within the thin film region, there is a clear difference within the resonance region. Initially, the bearing is fully flooded, meaning a solid-oil-solid interface is present around the full circumference. This results in resonance when film thickness matches the resonant frequency of the sensor. However, as oil availability reduces, the interface away from the thin film region becomes a solid-air-solid interface. This means near full ultrasonic reflection occurs and resonance no longer happens. It is thought changes in signal response are less present in the thin film region as shaft rotation entrains even the small amount of remaining oil into the contact.

Figure 9.12 also shows the corresponding frequency-domain signals taken within the resonance region at rotations 20 and 410. Again, there is a clear difference observed between the start and end of testing. A resonant dip is initially observed but disappears as oil availability reduces. Using an FFT amplitude profile to detect significant changes in signal response may be a simpler and more robust approach if starvation detection is to be automated in a bearing system. The maximum allowable amplitude can be defined at a particular rotation angle where resonance occurs. Then, an alarm can be triggered if the amplitude exceeds this threshold at that same angle during operation.

Unfortunately, these tests were performed before the installation of the torque transducer. However, it is expected that there would be not have been a significant increase in torque. Not only was the temperature change marginal, but the film thickness was also well within the hydrodynamic regime. Of course, under more aggressive starvation conditions one may expect a substantial torque increase.

In summary, monitoring minimum film thickness, temperature or torque may be the wrong approach. By the time significant changes are observed it is probably too late and the bearing is already being damaged. Instead, observing the thick film side can identify a drop in oil supply before severe starvation occurs. This is something one may not detect with bearing mounted ultrasonic transducers unless transducers are positioned around the full bearing circumference. This can be more expensive, requires more processing power and more space for transducers and cabling. Conversely, a single sensor mounted within the shaft provides a measurement around the full circumference, often at lower cost and complexity.

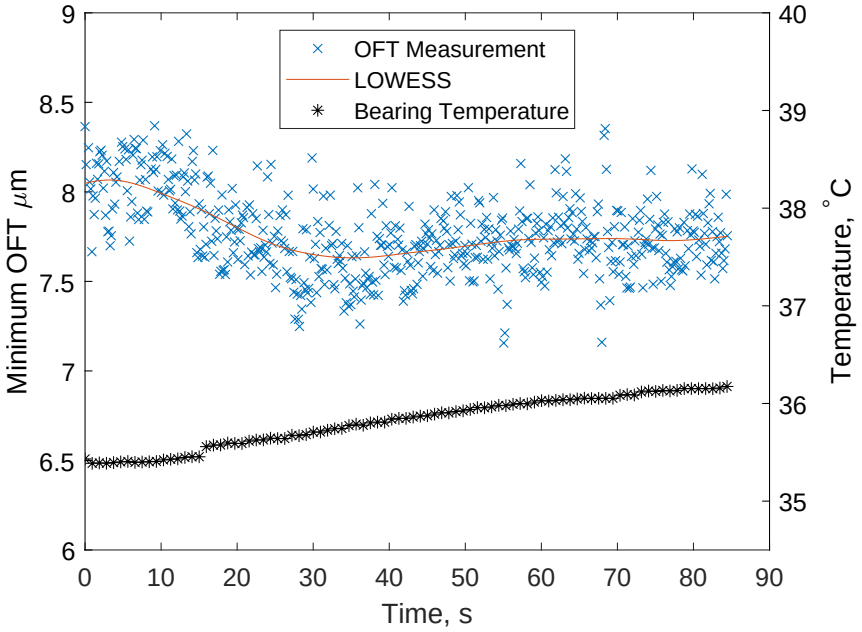

Figure 9.12: Change in minimum film thickness and bearing temperature during starvation testing. 400 rpm shaft rotation speed and 10 kN applied load were maintained throughout. A LOWESS regression curve fit of film thickness is also presented.

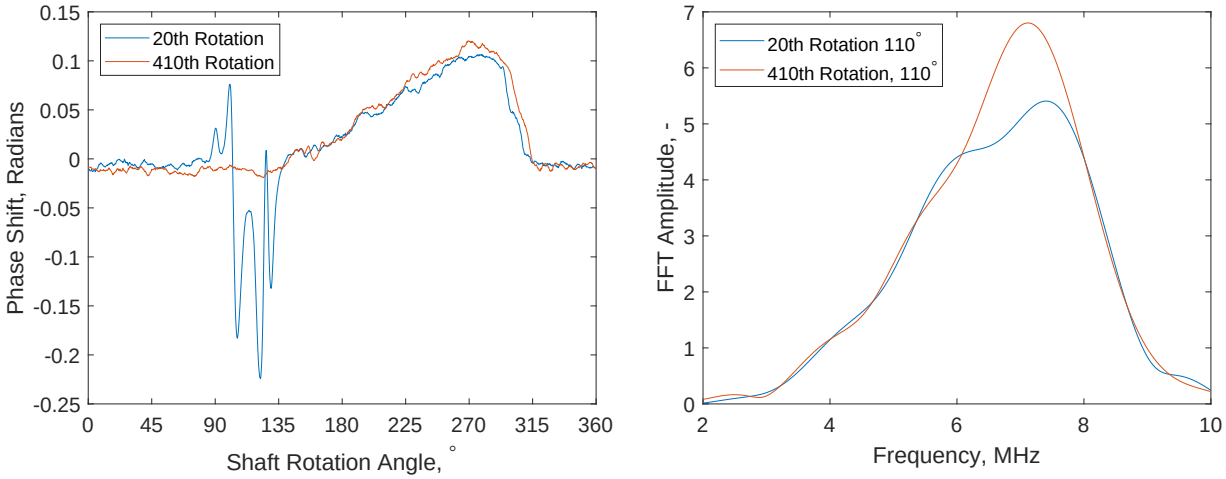

Figure 9.13: Change in circumferential phase shift profile (left) and FFT amplitude within the resonance region (right) during starvation testing.

9.5 Conclusions

This chapter has covered the results and analysis from tests performed on the BAXTER static loading test rig under a range of severe operating conditions. This includes:

- Shaft misalignment: by elevating one roller support bearing and using a rigid loading linkage, shaft misalignment could be induced. Misalignment angle could be calculated by measuring oil film thickness across the axial plane via three ultrasonic transducers embedded in the shaft.

- Offset loading: using a modified loading linkage, the applied load was offset by 8 mm from the bearing axial centre. Film thicknesses measured across the axial plane under a range of loads and speeds were compared against a numerical model, with good agreement observed. However, small differences between film thickness at the bearing edge led to significant differences in peak pressure, with the numerical model predicting much greater pressures. This may be due to the assumptions made by the model, for example, neither deformation nor pressure effects on viscosity are not considered.

- Run-down: by steadily reducing rotation speed, the bearing system transitioned through the different lubrication regimes. It was demonstrated that the point of torque inflection could be used to identify the point between the hydrodynamic and mixed regimes. Film thickness at this transition point was found to be viscosity-dependent. Additional tests performed with an 8 mm offset load showed the same trends, although the transition to mixed lubrication occurred more rapidly.

- Starvation: by draining the bearing assembly of oil during operation, early signs of starvation were observed. Monitoring ultrasonic signal response in the thick film region provided a clear sign that lubricant supply had reduced. This is a superior solution to the conventional methods of monitoring temperature or torque as the onset of starvation can be identified much earlier.

Chapter 10

Dynamic Loading Conditions

This chapter introduces the second test platform developed for this work. Known as BETTY (BEamish Test rig Two), this system is designed to investigate fluid film behaviour in bearings under dynamic loads. Ultrasonic transducers are instrumented on the top and side surfaces of the bearing and embedded in the shaft to measure film thickness. The main design features, ultrasonic sensor hardware and instrumentation process are presented. This is followed by results under a range of operating conditions, with a particular focus on the effect of dynamic loads on film thickness, including comparisons against a numerical model.

As with the BAXTER static loading test platform presented in Chapter 6, the author was responsible for leading the design and implementation of the BETTY system as part of this project. This includes conceptualisation, specification development, component design and manufacture, software, assembly, preliminary testing and troubleshooting.

10.1 Overview of BETTY Rig Design

A photograph of the BETTY rig in operation is provided in Figure 10.1. The bearing assembly consists of a solid bronze bush instrumented with twelve longitudinal ultrasonic sensors. Running inside this is an EN24T steel shaft instrumented with an array of eight longitudinal sensors. Ultrasonic hardware and implementation will be discussed in more detail in Section 10.2.

Dimensions of the bronze bush are provided in Figure 10.3. This geometry includes a single circumferential groove running around the axial centre of the bearing. As discussed in Section 2.3.2, the inclusion of a circumferential groove is suitable for bearings subject to dynamic loads due to the wide range of attitude angles they experience. The groove allows oil to reach the changing minimum film region more easily, reducing the chance of starvation.

The shaft is also supported by two needle roller bearings (SKF RNA 6914) on either side of the bronze bush, along with needle thrust bearings (SKF AXK 5578) at each end

of the shaft. These thrust bearings prohibit the shaft from rubbing directly onto the sides of the housing in the event of axial movement. A section view of the housing assembly is shown in Figure 10.2.

Along with ultrasonic transducers to measure film thickness, the test platform also includes conventional measurement hardware. Thermocouples are located within the heater manifold, annotated in Figure 10.5, to measure oil inlet temperature. Thermocouples are also positioned at the edges of the bearing, touching the running face of the shaft to record bearing operating temperature. A Futek TRS605 transducer measures torque as well as providing a TTL (transistor-transistor logic) pulse once per degree of shaft rotation. This is used in conjunction with a Cherry GS1001 hall effect sensor which provides a TTL pulse each full revolution. Additionally, a Honeywell PX3 pressure transducer monitors oil inlet pressure and a Parker ASIC pressure transducer indirectly measures applied bearing load. The loading system design is discussed in more detail in Section 10.1.1.

The analogue measurement devices are controlled by a National Instruments cRIO-9035 controller linked to an acquisition PC. The cRIO-9035 features an FPGA (field-programmable gate array), enabling the system to run efficiently with very high capture rates, up to 10 MHz. The acquisition hardware is photographed in Figure 10.5 and a measurement hardware flow diagram describing how each component is linked is provided in Figure 10.6.

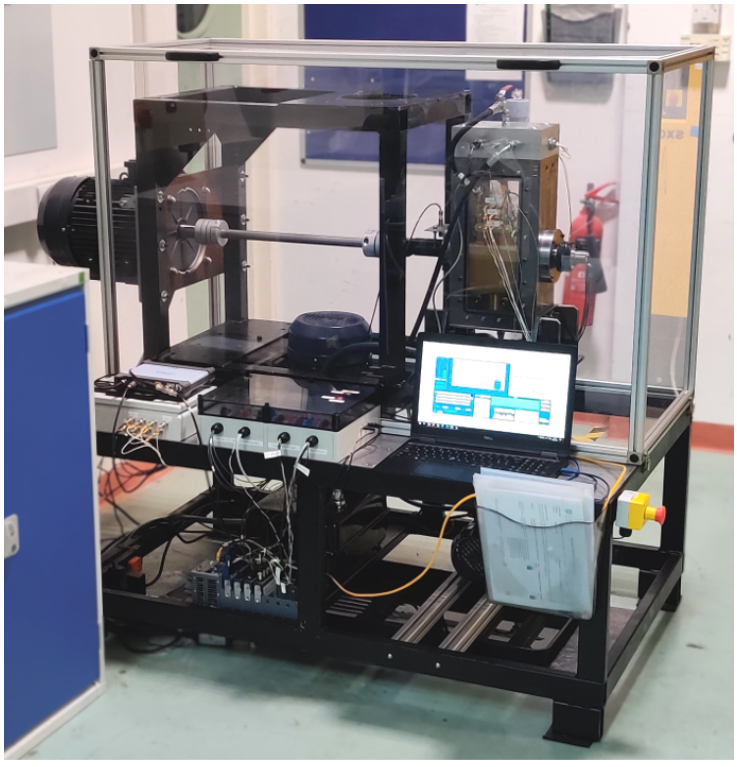

Figure 10.1: Photograph of BETTY dynamic loading test rig in operation.

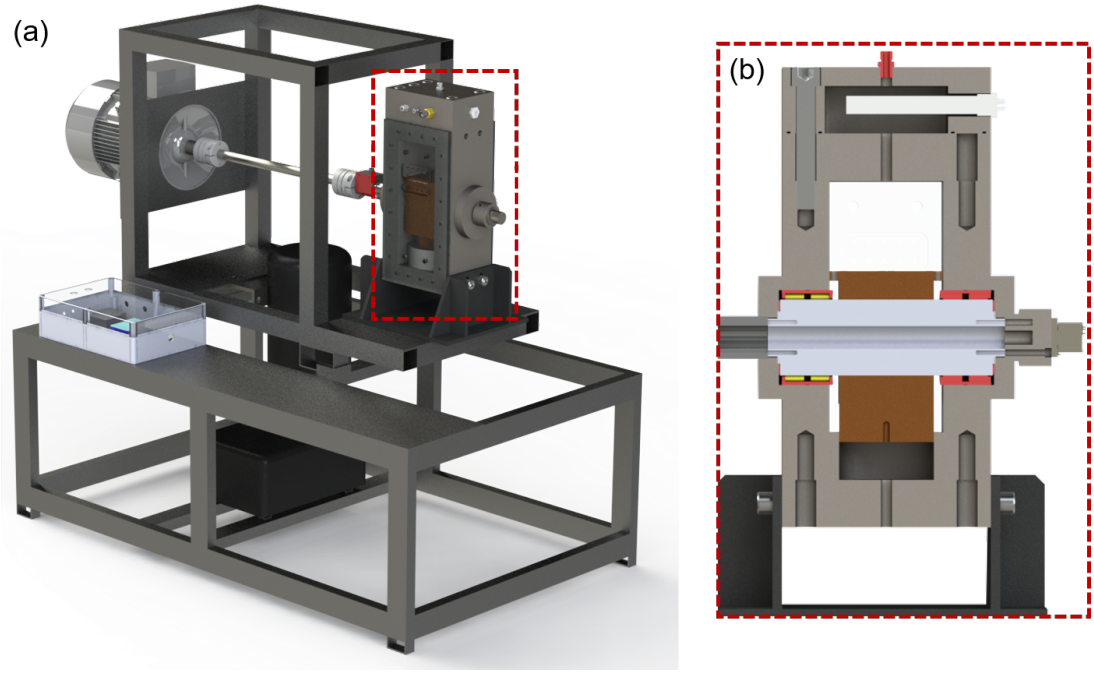

Figure 10.2: CAD render of BETTY test platform. a) Dimetric projection of full assembly. b) Section view of bearing housing. Cabling and hydraulic hose circuit omitted for clarity.

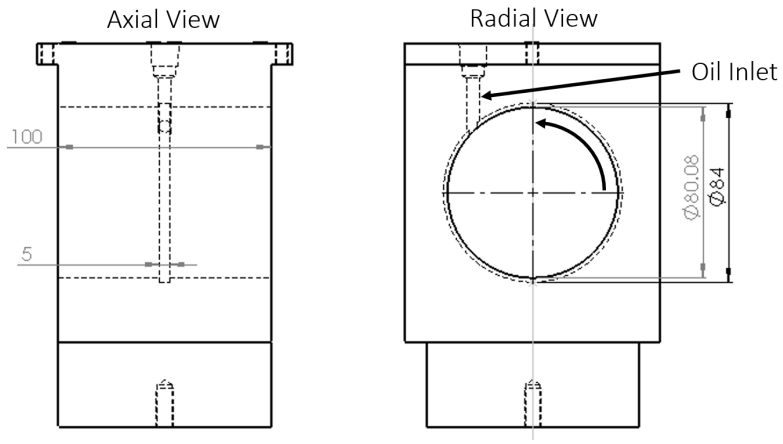

Figure 10.3: Dimensioned schematic of bearing in BETTY test platform. Curved arrow indicates the direction of shaft rotation.

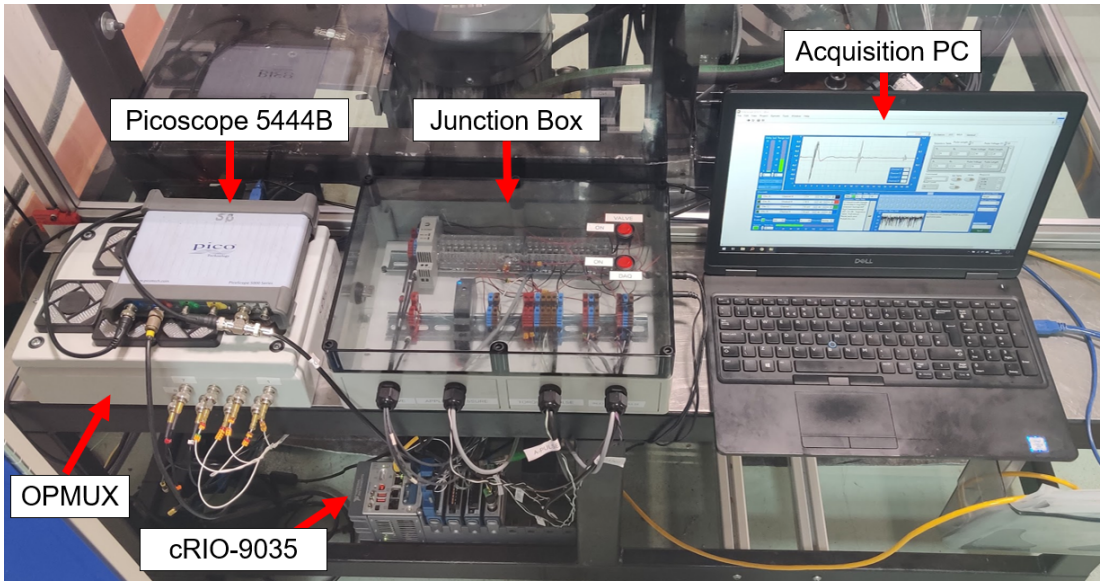

Figure 10.4: Photograph of Betty rig acquisition hardware.

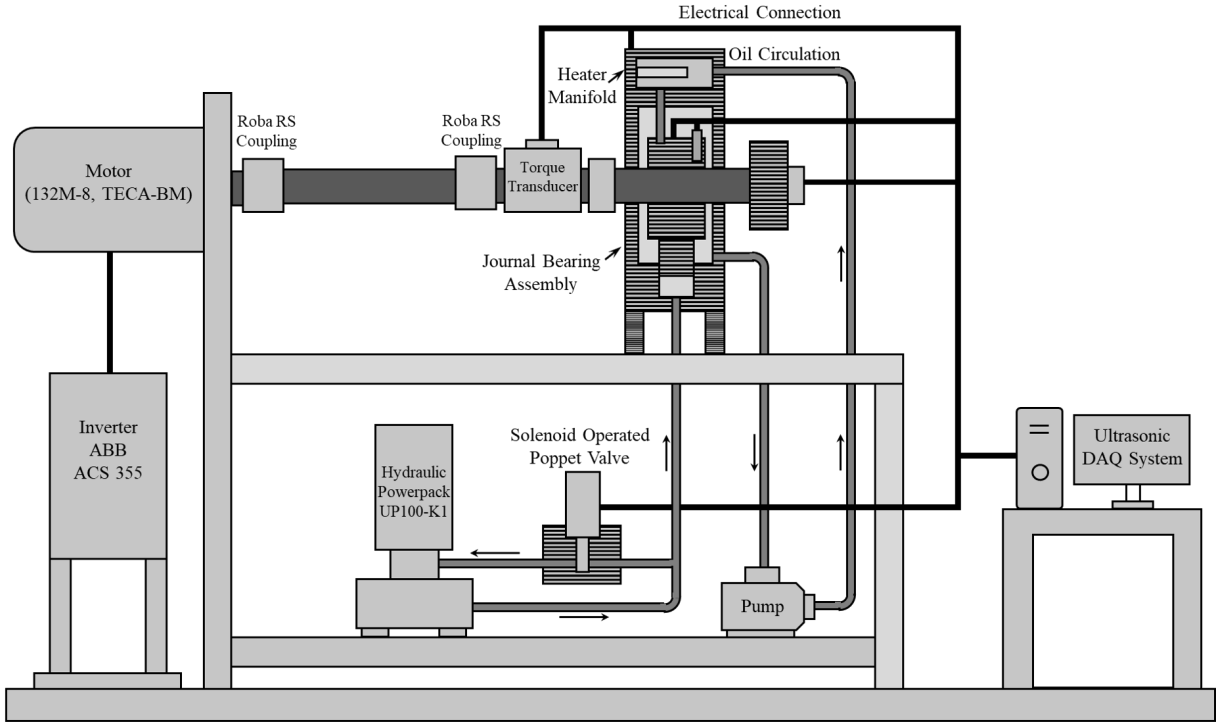

Figure 10.5: Schematic of BETTY test platform.

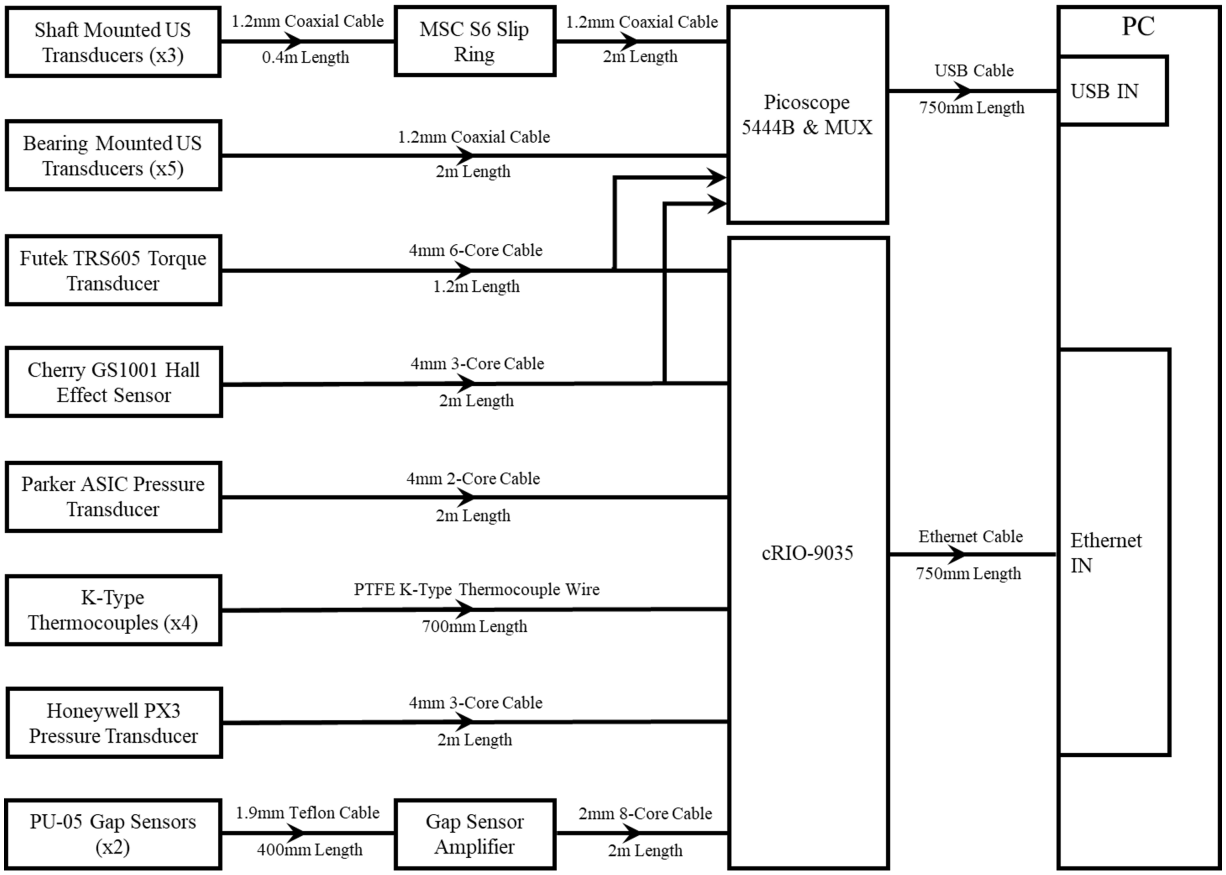

Figure 10.6: Measurement hardware flow diagram for BETTY test platform.

10.1.1 Dynamic Loading System

The primary advantage of the BETTY rig over the previously introduced BAXTER rig is its dynamic loading capabilities. This is achieved via a hydraulic power pack which applies pressure to the bottom face of the bearing, pushing it upwards like a piston. The applied pressure can then be varied by controlling an electro-proportional valve (Sun Hydraulics RBAPXWN). Opening the valve allows fluid to flow more freely through the circuit, relieving pressure, whereas closing the valve blocks flow, thereby increasing pressure. The magnitude of applied pressure is controlled by adjusting the voltage output to the valve via a National Instruments cRIO-9035 controller and NI-9263 voltage output module.

Pressure in the hydraulic circuit can be easily converted to applied load by multiplying by the area of the bearing bottom face (7854 mm^2). A nitrile seal fitted between the bearing and bore prevents cross-contamination between the lubrication circuit and hydraulic loading circuit; however, as some leakage may occur the same oil is used in both circuits as a precaution.

A sample of the load cycles trialled is presented in Figure 10.7. These are constant load, sine wave and square wave loading patterns. In this case, loading patterns are synchronised to shaft rotation angle via an encoder, with the sine wave pattern repeating every 360° and the square wave every 720°. Load is only applied for one-quarter of the square wave cycle to simulate real four-stroke engine loading more closely. Examples with a shaft rotation speed of 100 rpm and 700 rpm are presented.

At 100 rpm both the sine and square wave loading patterns closely follow the desired input. However, at 700 rpm there is a significant rise-time for the square wave loading pattern. This is because the valve does not close instantly and also because the oil is not perfectly incompressible. Although acceptable for this work, rise time could be mitigated in future by reducing the hose length between the power-pack and journal assembly, thus reducing the volume of the working fluid, or by using a faster acting valve.

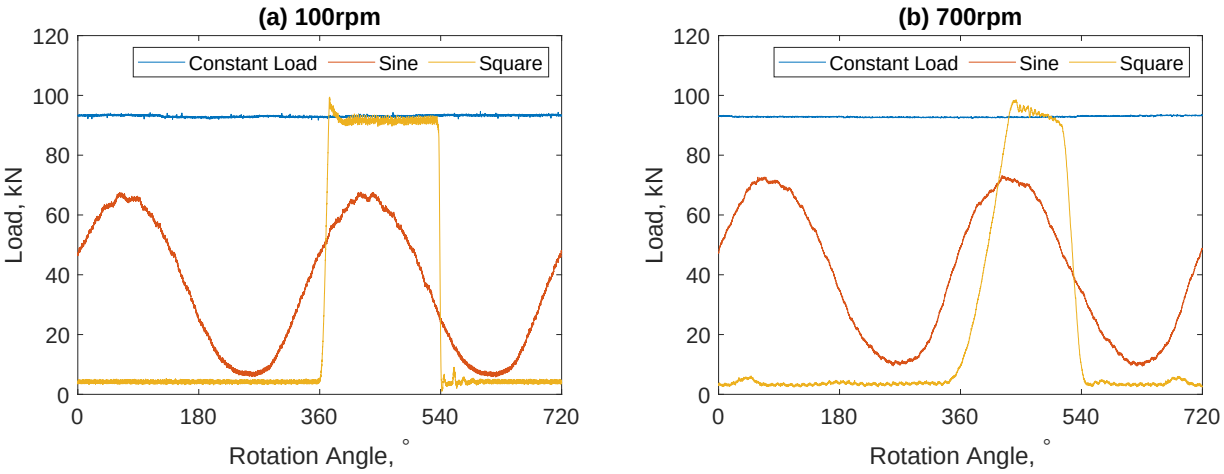

Figure 10.7: Example load cycles from BETTY test platform (constant load, sine wave and square wave) at 100 rpm and 700 rpm.

10.1.2 Determination of Bearing Material Properties

As previously discussed, accurate ultrasonic measurements rely on good knowledge of material properties, specifically acoustic impedance, density and acoustic velocity. A well-defined material is also useful when building equivalent numerical models, for which elastic properties such as Young's modulus are required. The bearing used in the BETTY test platform is solid aluminium bronze, however, the exact alloy was unknown. Thus, a study to determine bearing composition was performed. This involved imaging a sample of the material using an SEM (scanning electron microscope) and evaluating the proportions of each element within the alloy via EDS (energy-dispersive X-ray spectroscopy). The step-by-step process is outlined graphically in Figure 10.8.

First, shavings of the material were taken directly from the bearing outer surface using a new file to reduce any chance of contamination. These shavings were then imaged using an SEM. Multiple EDS spectra were taken from these images and the proportions of each element by weight were averaged across tests. Next, these proportions were compared against a range of common aluminium bronze alloys to find the best fit.

This study identified the bearing material as C95400 ($CuAl_{11}Fe_4$). Not only does it agree with the proportions measured via EDS, but C95400 is one of the most popular alloys used in aluminium bronze bearings. Material properties of C95400 are generally well documented in the literature, including a known density of 7450 kgm^{-3} [218, 219].

The acoustic velocity and acoustic impedance of C95400 however could not be found in the literature. As such, these values were obtained by applying the time of flight technique to a time-domain signal taken from a bearing mounted sensor during testing. This time-domain signal is presented in Figure 10.9. The figure shows time-of-flight between the first and second reflections is 7.815 μs. As path length is 40 mm, acoustic velocity is found simply by applying Equation 3.9:

$$c = \frac{d}{t} = \frac{0.04}{7.185 \times 10^{-6}} = 5118.36\ ms^{-1} \tag{10.1}$$

With density already known, Equation 3.3 can now be applied to calculate acoustic impedance:

$$z = \rho c = 7450 \times 5118.36 = 38.13 \times 10^{6}\ Rayls \tag{10.2}$$

This more direct approach also reduces sources of uncertainty. For example, acoustic velocity, and by extension acoustic impedance, are subject to change with temperature. This would be particularly difficult to account for with standard values found in the literature due to the complex temperature gradient between the ultrasonic transducer and shaft-bearing interface.

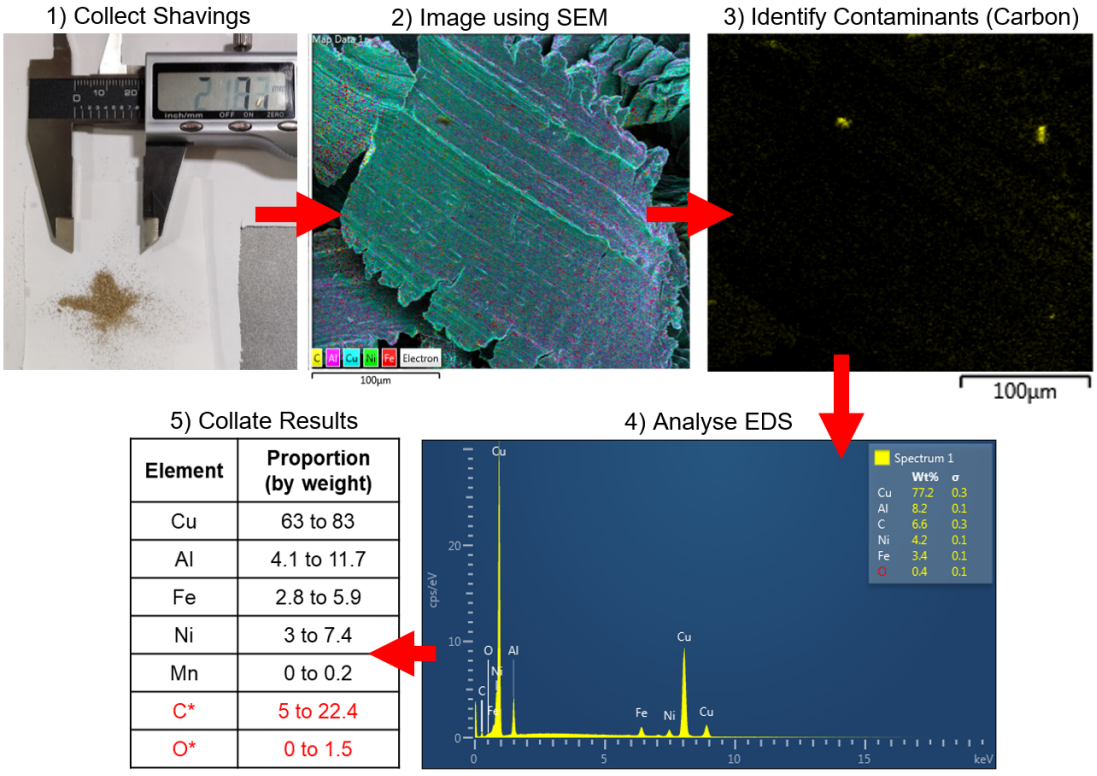

Element	Proportion (by weight)
Cu	63 to 83
Al	4.1 to 11.7
Fe	2.8 to 5.9
Ni	3 to 7.4
Mn	0 to 0.2
C*	5 to 22.4
O*	0 to 1.5

Figure 10.8: Step by step process used to determine bearing material.

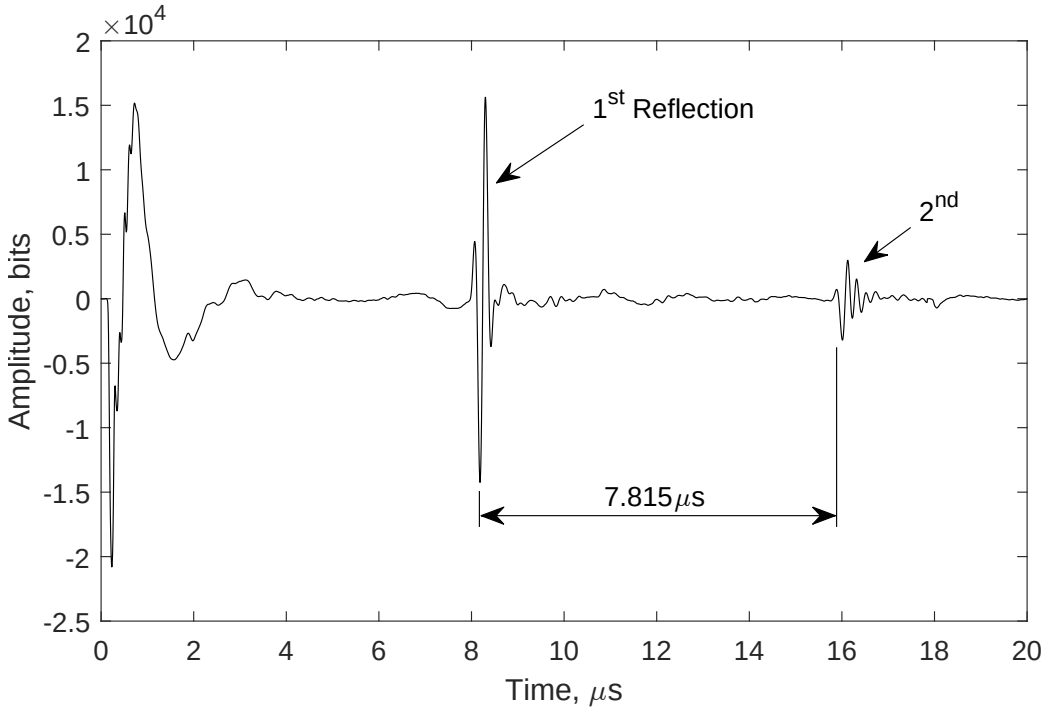

Figure 10.9: Time-domain signal captured from a transducer bonded to the aluminium bronze bearing used in the BETTY test rig. The time-of-flight between the first and second reflections is indicated.

10.2 Ultrasonic Sensor Instrumentation

The BETTY rig is instrumented with ultrasonic transducers on both the shaft and bearing to provide film thickness measurements. The positions and dimensions of each sensor element is shown in Figure 10.10 and components photographed in Figure 10.11.

A total of twelve elements are instrumented on the bronze bush, four on each side and four on the top face. As the film thickness is expected to be greater at the top of the bearing in comparison to each side, the optimum sensor frequency is different.

10.2.1 Optimum Frequency for Top Bearing Sensors

As the bearing is pushed upwards onto the shaft, the minimum film thickness will occur towards the bottom of the bush, although with some attitude angle present. Thus,the maximum film thickness will occur on the opposite side, near where the top bearing sensors are located. Given that design diametric clearance is 95 μm, the expected measurement range can be easily calculated geometrically.

The maximum expected film thickness at the top of the bearing is equal to the diametric clearance. This would occur when very high loads are applied and rotation speed is low. Conversely, the minimum expected film thickness at the top of the bearing would be half the diametric clearance. Theoretically, this would occur when no load is applied, with

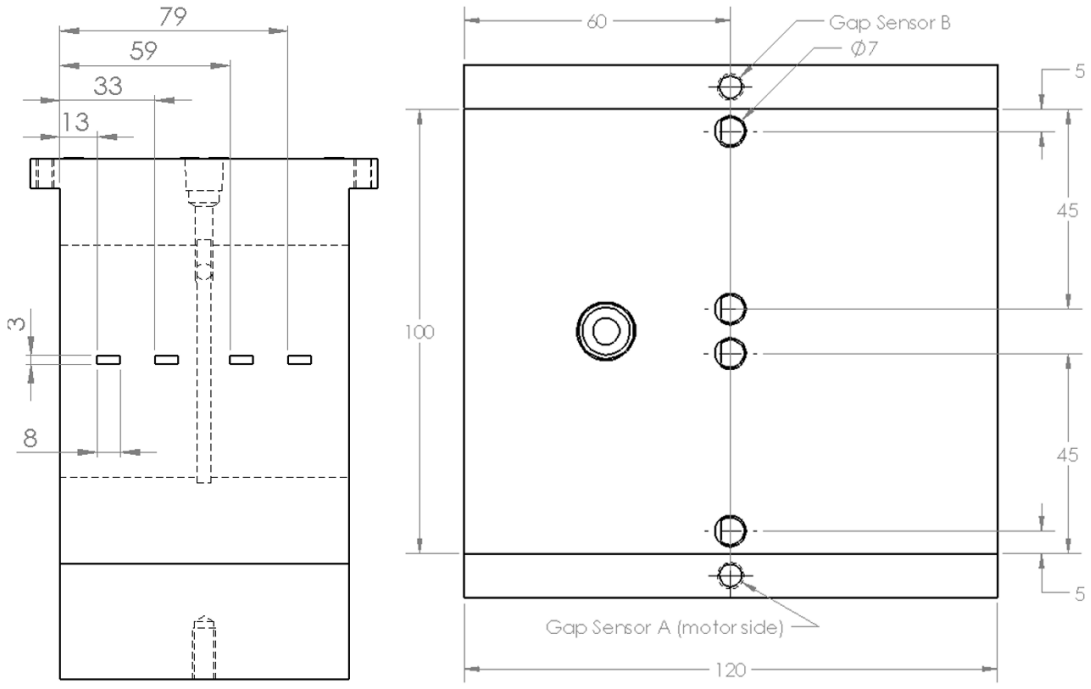

Figure 10.10: Positions and dimensions of bearing mounted ultrasound sensors on BETTY rig. Position of eddy current gap sensors also indicated. Thermocouples are also located alongside each gap sensor.

shaft and bearing perfectly concentric.

As such, the expected range is between 47.5 μm and 95 μm. It was decided that the resonant dip technique would be most suitable as it does not require a reference measurement and piezoceramic elements of a suitable frequency were readily available.

Referring back to Equation 3.20, the acoustic velocity of the lubricant is required for converting resonant dip frequency to film thickness. The same lubricant is used in this investigation as with the BAXTER rig, which at 50°C has an acoustic velocity of 1495 ms^{-1}. Therefore applying Equation 3.20, resonant dip frequency will range between 7 MHz and 14.6 MHz. As such, soft PZT 10 MHz centre frequency elements were selected. The low quality factor of soft PZT leads to a wider bandwidth, ensuring sufficient energy across the required frequency range.

10.2.2 Optimum Frequency for Side Bearing Sensors

The expected film thickness at each side of the bearing is lower than that of the top, estimated to be between 20 μm and 60 μm depending on operating conditions. A film thickness of 20 μm corresponds to a frequency of 35 MHz if applying the resonant dip technique. Given the significant path length, it is likely such a high frequency wave would

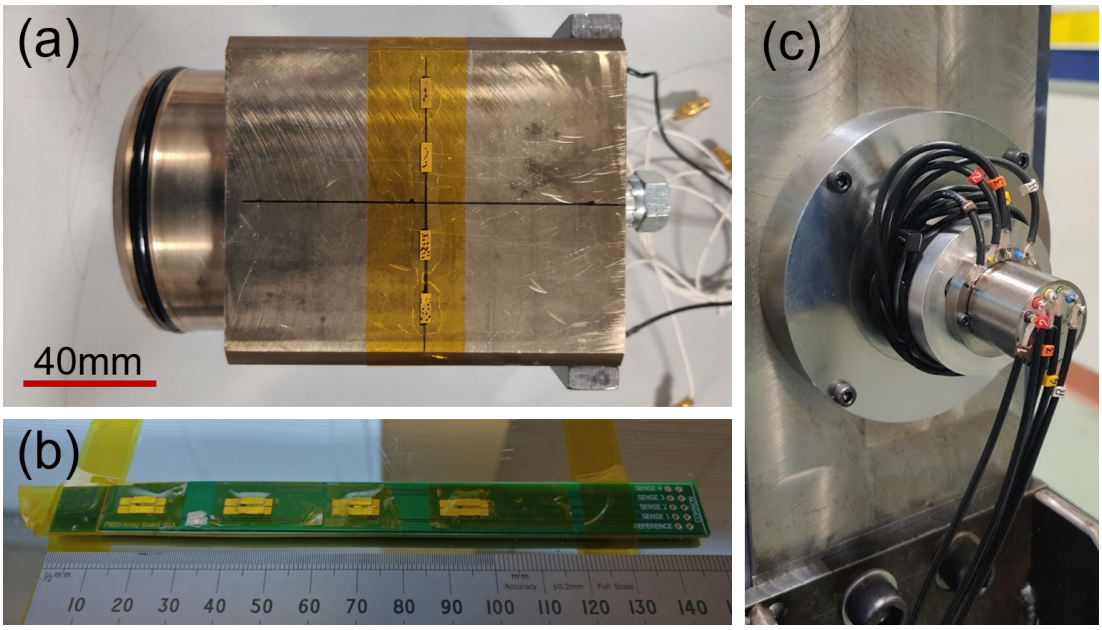

Figure 10.11: (a) Photograph of BETTY test platform bearing during sensor instrumentation. (b) Photograph of PCB with ultrasonic sensor elements, before shaft installation. (c) Photograph of slip ring.

be too attenuative, leading to poor signal quality. Therefore, it was decided that frequency should be optimised for the phase shift technique.

For these reasons, 5 MHz sensor elements were selected. At this frequency, a phase shift of 0.025 corresponds to a film thickness of 97.35 μm, and maximum phase shift of 0.98 corresponds to 0.92 μm.

10.2.3 Shaft Mounted Ultrasonic Sensors

Unlike the pin design used in the BAXTER rig, sensors within the shaft of the BETTY rig employ a PCB design, photographed in Figure 10.11. The dimensions and positions of each element in the array are shown in Figure 10.12, along with photographs taken at each stage of the instrumentation process.

Wraparound longitudinal elements with a centre frequency of 10 MHz were selected as circumferential film thickness profiles were expected to be similar to those observed in the BAXTER rig (which used 7 MHz elements). Each sensor was bonded to the pads of the PCB with MG Chemicals 8331 liquid conductive adhesive, which cures at room temperature. Elements were then coated with Duralco 4525-IP epoxy adhesive, then the PCB was immediately inserted and clamped into the square bore of the hollow shaft. The shaft was then placed into a programmable oven to allow the epoxy to cure at a high temperature overnight. Once installed in the BETTY rig, the cables from the PCB were connected to the pulsing hardware via a slip ring, photographed in Figure 10.11.

This PCB design has practical advantages over the previously used pin design, as well as more conventional shaft embedded eddy current sensors (see Figure 4.4). First the array can be installed in any hollow shaft without having to machine into the shaft's running face and regrinding the surface, provided at least one of the internal faces is flat. In this case, a square bore was machined via wire erosion. Arrays are also easier to replace if the sensors fail. The PCB can either be removed and replaced or even remain in the shaft and a new array bonded onto one of the remaining internal surfaces. Additionally, the mass of the PCB is very low and is positioned close to the radial centre. Therefore in low to medium rotation speed applications any shaft imbalance introduced is negligible, even with large arrays. If the application involves very high rotation speeds, for which a balancing process is already typical, then a counterweight can be easily installed in the bore.

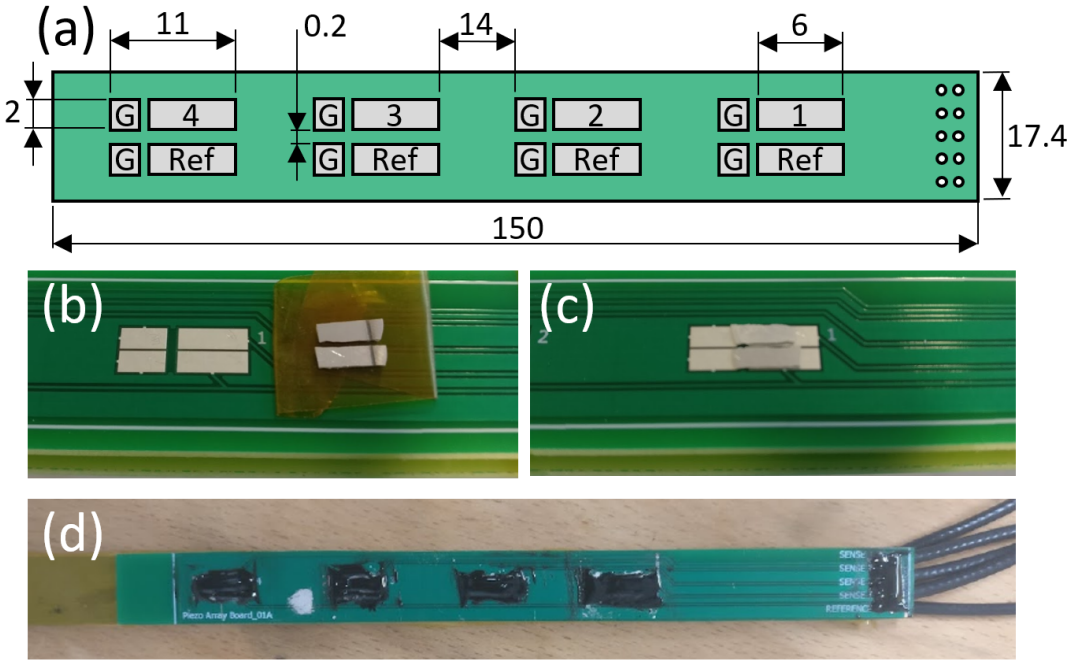

Figure 10.12: (a) Dimensioned schematic of PCB used in BETTY test platform, units in mm. (b) Piezoelectric elements positioned before silver epoxy deposition. (c) Piezoelectric elements after curing of silver epoxy. (d) Elements on PCB coated with Duralco 4525-IP adhesive before shaft installation and curing.

10.2.4 Ultrasonic Acquisition

In the BETTY rig system, ultrasonic transducers are excited sequentially by an Optel Op-MUX Multiplexer. The signal response is then captured by a Picotech Picoscope 5444B. Both devices are photographed in Figure 10.4.

Excitation pulses are triggered by the rotation of the shaft. This is in contrast to the BAXTER rig, for which pulsing was controlled by the UPR's internal clock. For the

BETTY rig a TTL signal is produced per single degree rotation by a shaft encoder integrated into the torque transducer.

This signal feeds into an NI9401 digital output module, which is programmed to output eight TTL signals in quick succession (at 24 μs intervals). These eight signals are sent to the OpMUX and Picoscope to trigger ultrasonic signal generation and capture. Sketch outputs from the encoder and NI9401 are shown in Figure 10.13. Multiplying one TTL signal to an eight signal pulse train in this manner allows the system to capture an ultrasound response on all eight channels at essentially the same shaft position.

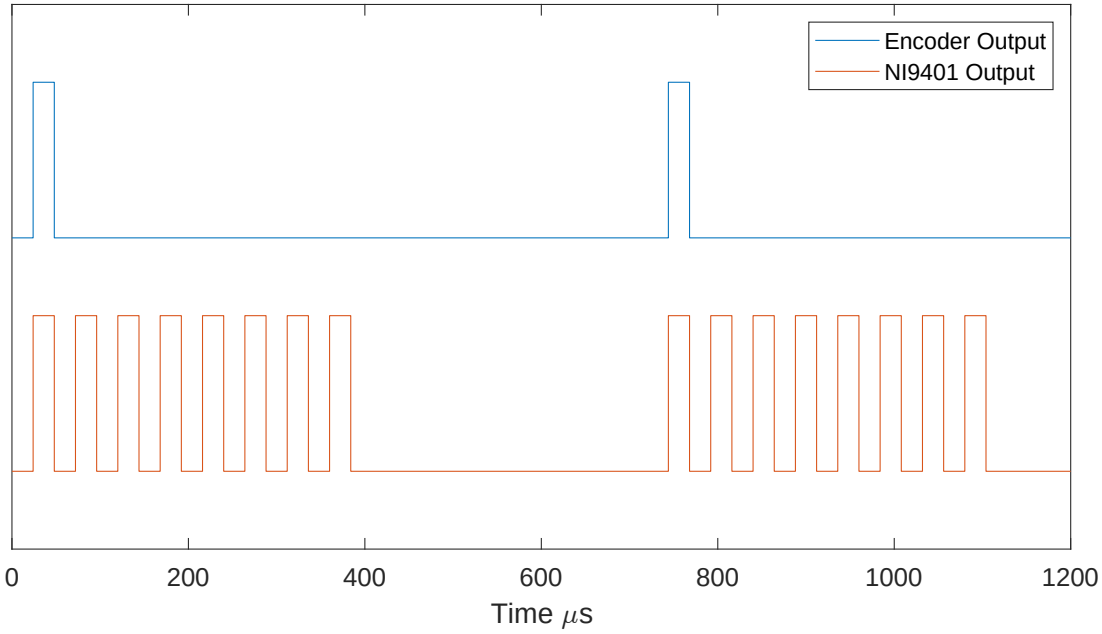

Figure 10.13: Encoder and NI9401 digital module outputs used in OpMUX triggering.

10.2.5 Introducing the Snapshot Reference Technique

As previously discussed, the top bearing sensors employ the resonant dip technique for film thickness measurements, which does not require a reference measurement. Also, the shaft mounted sensors using the phase shift method obtain an infinite film reference in the same manner as the shaft mounted sensors in the BAXTER test rig.

However, the side mounted bearing sensors remain within the phase shift measurement range at all times during operation. As a result, either a conventional pre-test reference or an alternative method is required. Unfortunately, due to the sensitivity of the phase shift technique to effects such as changes in temperature gradient through the bearing material, a pre-test reference was found to be inadequate. As such, an alternative technique was created.

The following new referencing method proposed will henceforth be referred to as the

'snapshot' reference technique in this work, as it takes the film thickness information from other sensors at a single moment in time and uses geometry to infer a reference phase for the sensor in question. The step-by-step process for this technique is shown in Figure 10.14.

To model the system geometrically, the shaft and bearing surfaces can be treated as two concentric circles. Assuming the distance between circles (i.e. film thickness) is small compared to their radii, the distance between circles around the circumference can be approximated via the following:

$$f(\phi) = A\ sin(\phi + k) + b \tag{10.3}$$

Where ϕ is bearing angle and A, b and k are constants unique to a particular geometry. These constants can be calculated via the following three equations given that minimum film thickness, attitude angle and film thickness at the top of the bearing are known:

$$A = \frac{h_{top} - h_{min}}{sin\left(\phi_{top} + \frac{(2n+1)\pi}{2} - \theta\right) - sin\left(\frac{(2n+1)\pi}{2}\right)} \tag{10.4}$$

$$b = h_{min} - A\ sin\left(\frac{(2n+1)\pi}{2}\right) \tag{10.5}$$

$$k = \frac{(2n+1)\pi}{2} - \theta \tag{10.6}$$

Where h_{top} is film thickness at the top of the bearing, h_{min} is minimum film thickness, ϕ_{top} is the angle at the top of the bearing (in this work defined as 0°) and θ is attitude angle. Film thickness at the position of each side sensor can then be calculated via Equation 10.3, in this work defined as 90° and 270°.

The phase equation (Equation 3.18) can be rearranged to make Φ the subject:

$$\Phi = atan\left(\frac{2z_1 z_2^2(\omega/K)}{(z_1^2 - z_2^2) + z_1^2 z_2^2(\omega/K)^2}\right) \tag{10.7}$$

For which:

$$K = \frac{\rho c^2}{h} \tag{10.8}$$

Where K is stiffness. Also note the distinction between bearing angle ϕ, ultrasonic wave phase angle φ and ultrasonic wave phase shift Φ.

Applying side film thickness found geometrically to Equation 10.7 and Equation 10.8 thus allows phase shift to be calculated. Subtracting the phase measured from the side sensor from this phase shift then provides a reference phase value. This reference phase, in theory, would be equal to a phase measurement taken at a solid-air or solid-infinitely thick oil film boundary.

The full derivation of these equations, along with a worked example, is presented in APPENDIX F. Derivation of Oil Film Gap Equations.

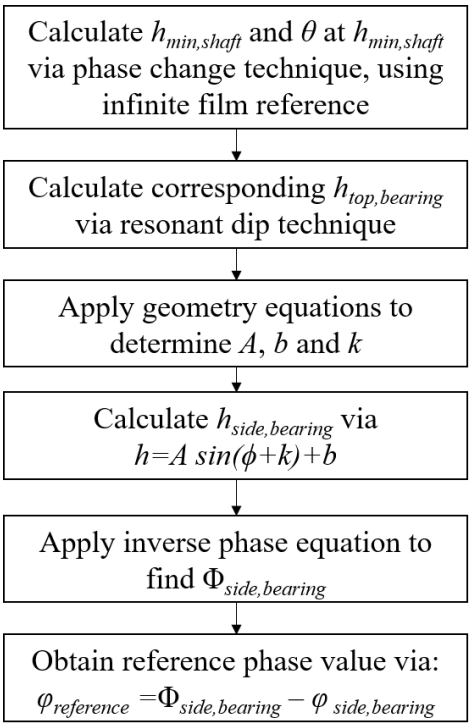

Figure 10.14: Flow diagram detailing the routine for applying the snapshot reference technique.

10.3 Dynamic Loading Rig Test Results

The following covers results obtained via the BETTY test platform under a range of static and dynamic loading conditions. First, measurements from shaft mounted transducers are presented, including a comparison between different pulse configurations and sensor locations. This is followed by bearing mounted sensor measurements which enable continuous monitoring of minimum film thickness and attitude angle. Results are then compared against predictions from a numerical model and measurements from bearing mounted gap sensors.

10.3.1 Shaft Sensor Film Thickness Measurements

Shaft mounted ultrasonic transducers enable monitoring of film thickness around the bearing circumference as the shaft rotates. The transducer array on the BETTY rig, previously introduced in Figure 10.12, can operate in both pulse-echo (PE) and pitch-catch (PC) configurations. For pulse-echo the same transducer generates and receives the signal, whereas for pitch-catch one transducer generates and a different transducer receives the reflected signal. In this study the reference transducer elements (denoted "Ref" in Figure 10.12) generate the signal in pitch-catch mode.

It was anticipated that different pulsing configurations might produce different results. Figure 10.15 shows circumferential phase shift and corresponding film thickness profiles

measured by various transducers in the array using both pulse-echo and pitch-catch configurations. In this test, a constant load of 50 kN was applied, with a shaft rotation speed of 60 rpm and bearing temperature of 50°C. Measurements over five full shaft rotations are presented. Film thickness is calculated via the phase shift method.

The profiles for all sensors and configurations appear to be reasonably consistent across multiple rotations, indicating good system stability and no significant oil whirl. Results are compared against a Raimondi-Boyd numerical prediction, with the profile shape and minimum film thickness in good agreement. However, the attitude angle appears to be significantly different. It is thought this may be because the piston style loading system restricts horizontal movement of the bearing.

To investigate differences between transducer locations and pulsing configurations in a more rigorous manner, a test program with a wide range of static loading conditions and rotation speeds was performed. Figure 10.16 shows the average difference between measured minimum film thickness for each configuration and predicted film thickness obtained via a Raimondi-Boyd model.

From Figure 10.16, it is clear that all configurations consistently measure thinner minimum films than predicted by the numerical model. This may be due to the assumptions made by the Raimondi-Boyd model, such as assuming constant viscosity and zero deformation. Also, there was no significant difference between sensor locations. This uniformity across sensor locations indicate the system is sufficiently aligned in the axial plane. However, there was a significant difference observed between pulse-echo and pitch-catch configurations for the same receiving sensors, with pulse-echo reporting thicker films.

It is hypothesized that in this system the pulse-echo configuration is not actually measuring the true minimum film location because the transducer elements are radially offset. A simplified schematic of the required wave path for measurement is presented in Figure 10.17. This highlights that the receiving sensor in pitch-catch detects the proportion of wave energy which reflects centrally around the minimum film location, whereas in pulse-echo the centre of the measured area is slightly to the side of the minimum film location. As such, subsequent results use the average film thickness of element 2 and element 3 in the pitch-catch configuration.

Figure 10.18 shows two examples of partial circumferential film thickness profiles under square-wave loading conditions, one at 50 kN peak load with a rotation speed of 60 rpm and one at 100 kN peak load with a rotation speed of 600 rpm. In both cases, load is applied for 180° and removed for 540°. As expected, the minimum film is thinner for the 60 rpm case due to its lower Sommerfeld number. In both cases there is a substantial reduction in film thickness when the bearing is loaded compared to when it is unloaded.

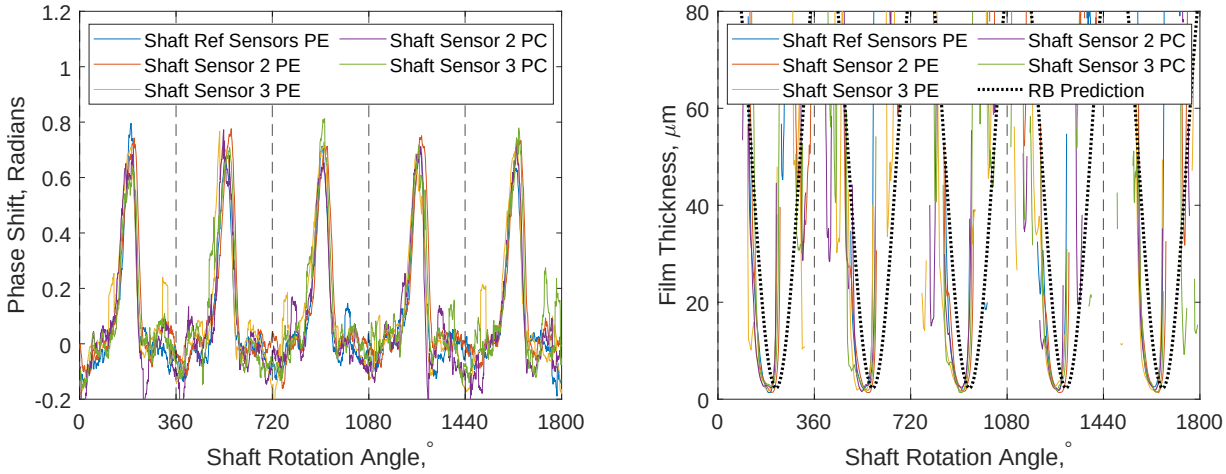

Figure 10.15: Phase shift (left) and corresponding film thickness(right) for different shaft sensors and pulsing configurations in the BETTY rig. Operating conditions are 50 kN constant applied load, 60 rpm shaft rotation speed and 50°C bearing temperature. Vertical dashed lines represent rotation angle when shaft sensors are at the bearing top.

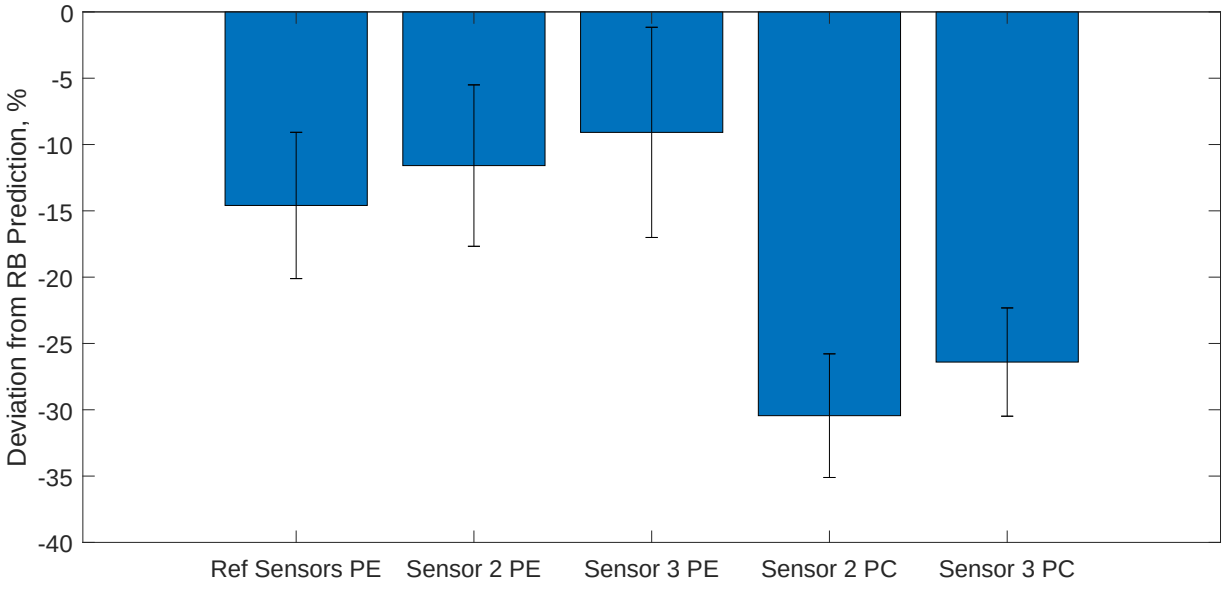

Figure 10.16: Deviation from Raimondi-Boyd prediction for minimum film measurements measured via shaft mounted transducers. Test conditions are under static loading at rotation speeds 60 rpm to 600 rpm and 50 kN to 100 kN applied load. Error bars indicate the standard error of the mean. Pulse-echo (PE) and pitch-catch (PC) pulsing configurations are shown.

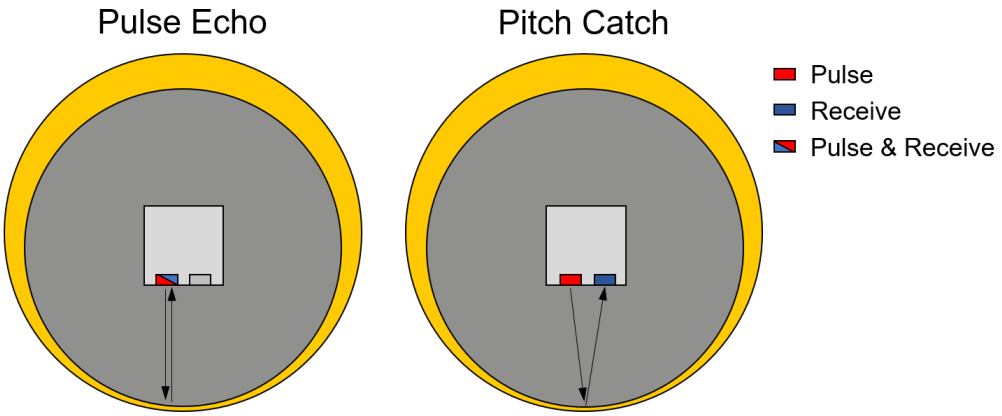

Figure 10.17: Simplified schematic showing the ultrasonic signal path for shaft mounted transducer elements in the BETTY test platform. Rotation angle corresponds to the instant of minimum film thickness measured around the bearing circumference. Both pulse-echo and pitch-catch configurations are shown. Some dimensions are intentionally not to scale for clarity.

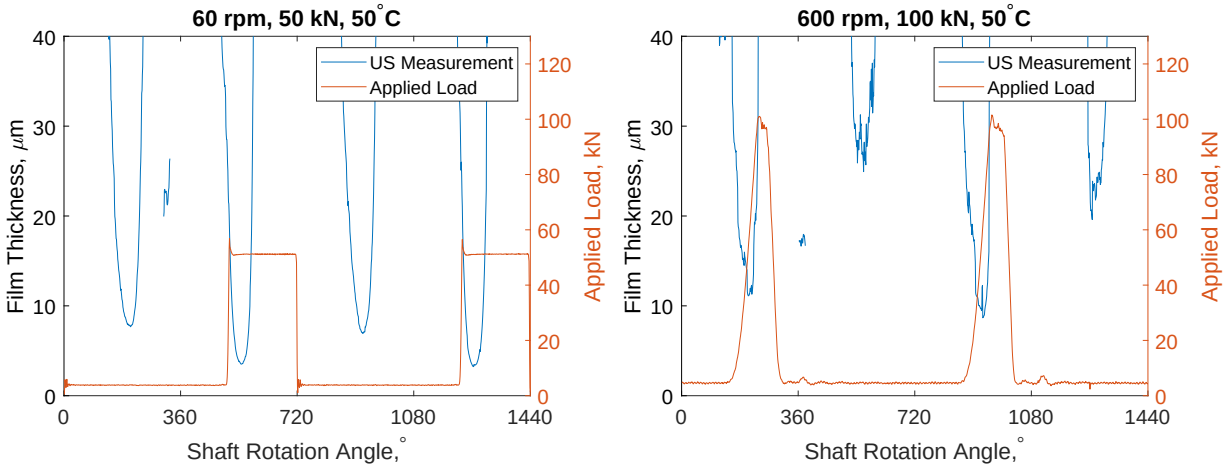

Figure 10.18: Circumferential film thickness under dynamic loading conditions, measured via shaft mounted ultrasonic transducers in the BETTY rig.

10.3.2 Bearing Sensor Film Measurements

The limitation with using shaft mounted sensors exclusively is that they struggle to provide continuous minimum film measurements when operating conditions are rapidly changing. For example, if the load increases sharply when the shaft sensor is in the diverging region, then cavitation effects will inhibit the shaft sensors from detecting a quantifiable change. Thus, additional sensing hardware is required. For the BETTY test platform, this is achieved with bearing mounted ultrasonic transducers.

In this study, only the bearing sensors on the top face and one side face were used. This side face corresponded to the converging region of the bearing. Outputs on the diverging side were deemed ineffectual due to cavitation effects. However, these unused sensors may be useful in future, particularly if the rotation direction is reversed.

Figure 10.19 shows four examples of film thicknesses measured under dynamic loading conditions as captured by the top mounted bearing sensors. These thicknesses were calculated via the resonant dip technique. Square wave and sine wave loading patterns across four full rotations at two different rotation speeds (60 rpm and 600 rpm) are presented.

Examining these results, an increase in applied load leads to an increase in film thickness. This is because the top bearing sensors are located at the opposite side to the minimum film thickness region. Also, tests at higher rotation speeds demonstrate a consistently thinner film for the same reason. It should be noted that this measurement changes with load due to both a change in minimum film thickness and attitude angle.

For the square wave loading results, it is evident that film thickness takes time to reach equilibrium when the load is changed. This is due to the squeeze film effect, which means the required volume of lubricant is unable to completely enter or exit the contact instantly. This effect is observed when the load is applied and removed. Squeeze film effects are less obvious for sine wave loading patterns due to their more gradual changes in load; however, a slight lag is still observed.

Comparing the squeeze time for square wave cases in Figure 10.19, it appears the film takes longer to recover when the load is reduced for the 60 rpm case than for the 600 rpm. Although the 60 rpm and 600 rpm cases take similar degrees of rotation to recover, on average 223° and 232° respectively, this corresponds to a recovery time of 0.621 seconds and 0.065 seconds respectively. It is thought this difference is because a faster rotation speed may draw more lubricant into the contact, allowing the oil film to recover faster.

Figure 10.20 shows bearing film measurements for tests under the same square wave dynamic load but with different bearing temperatures, 50°C and 70°C. As expected, a higher temperature leads to a thicker measured film, which suggests a thinner minimum film on the opposite side of the bearing. Also, for the 100 rpm case, squeeze time is longer when the bearing temperature is at 50°C than at 70°C when the load is increased. On average, the loaded squeeze times are 0.28 seconds and 0.23 seconds respectively. This trend is also

observed when the load is removed, with a recovery time of 0.38 seconds and 0.22 seconds for 50°C and 70°C respectively. This is because a lower viscosity oil can enter and exit the contact more quickly when load conditions change.

For the 700 rpm tests shown in Figure 10.20, the loaded squeeze time is also significantly longer for the 50°C case, at 0.031 seconds, compared to 0.023 seconds at 70°C. However, the average recovery times are very similar, at 0.055 seconds and 0.056 seconds respectively. This could be due to the variable nature of the real system or at higher speeds lubricant viscosity is less important in oil film recovery after a loading event.

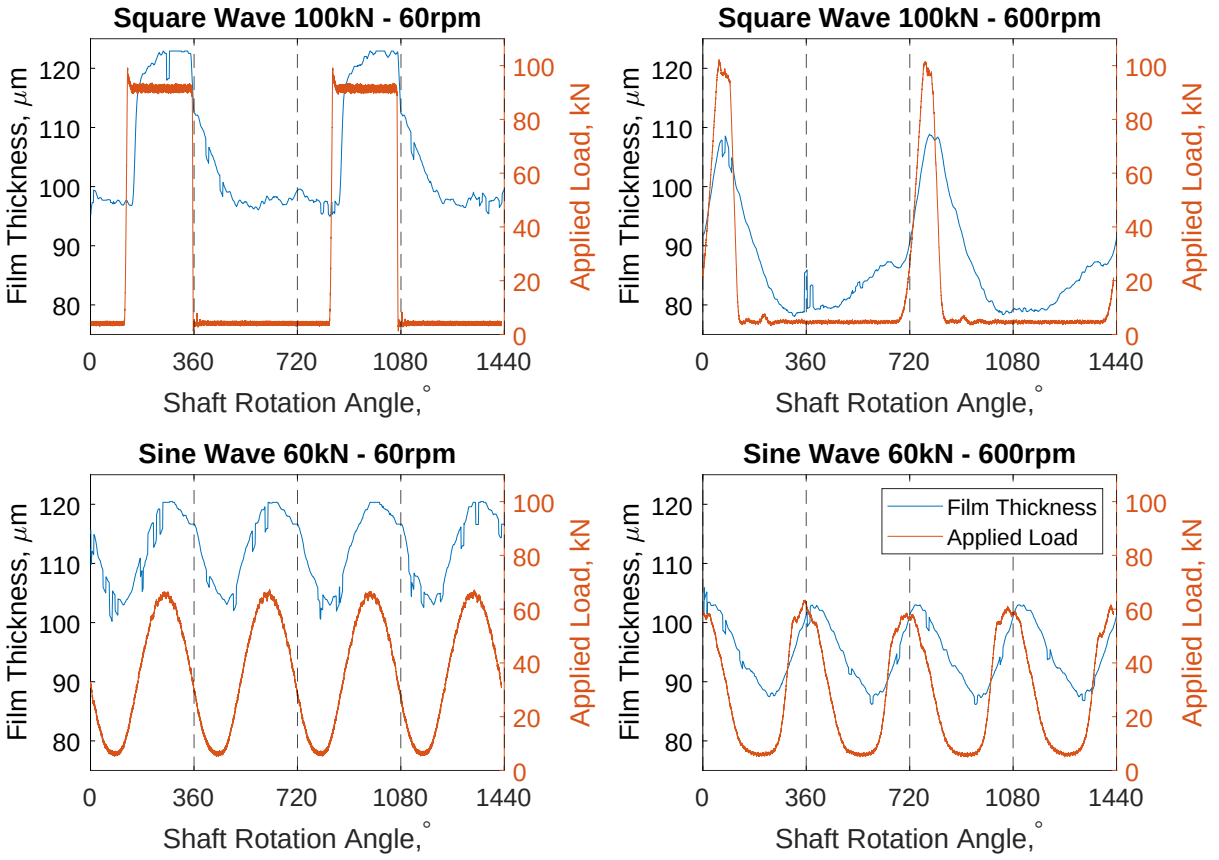

Figure 10.19: Comparison of film thickness at the top of the bearing for four different dynamic loading cases, with variable load shape and rotation speed. Film measurements were taken via ultrasonic transducers mounted on the bearing top surface. Applied load measurements for each case are also shown.

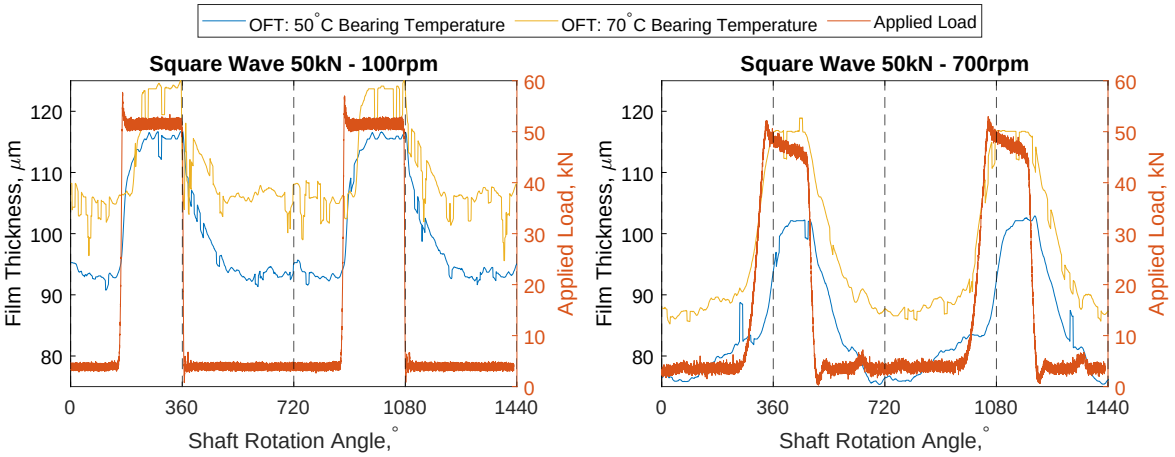

Figure 10.20: Comparison of film thickness at the top of the bearing for dynamic loading cases with different bearing temperatures, 50°C and 70°C. Low rotation speed (100 rpm) and high rotation speed (700 rpm) examples are provided. Film measurements are taken via ultrasonic transducers mounted on the bearing top surface. Applied load measurements for each case are also shown.

10.3.3 Minimum Film Measurements

By applying the snapshot reference technique introduced in Section 10.2.5, shaft and top bearing sensor measurements can be combined to obtain a reference for the side bearing sensors, thus enabling continuous minimum film and attitude angle measurements. Figure 10.21 presents minimum film thickness and attitude angle measurements for four dynamic loading test cases; two square wave and two sine wave loading patterns, each at 60 rpm and 600 rpm. These measurements are plotted against applied load.

In Figure 10.21, both minimum film thickness and attitude angle are consistently higher for the 600 rpm tests. As previously discussed, this is in line with lubrication theory which states that the resultant increased hydrodynamic pressure pushes the shaft and bearing surfaces apart with greater force.

A consistent decrease in film thickness is observed when applied load increases, with an obvious squeeze film effect causing the oil film to take time to change. The same can be seen for the attitude angle measurements, which tend towards equilibrium at the same rate.

Figure 10.22 shows the same film thickness and attitude angle data, although plotted against torque instead of the applied load. As expected, an increase in load leads to an increase in torque. Each test appears to be operating within the hydrodynamic regime, except the square wave 60 rpm test case when a load is applied. Torque is substantially higher for this test case compared to its 600 rpm counterpart. By considering the Stribeck curve in Figure 2.3, a lower rotation speed would only result in a higher torque if the system is operating within the mixed regime. In contrast, the 60 rpm and 600 rpm sine wave tests are operating within the hydrodynamic regime, evidenced by the higher torque

for the 600 rpm test.

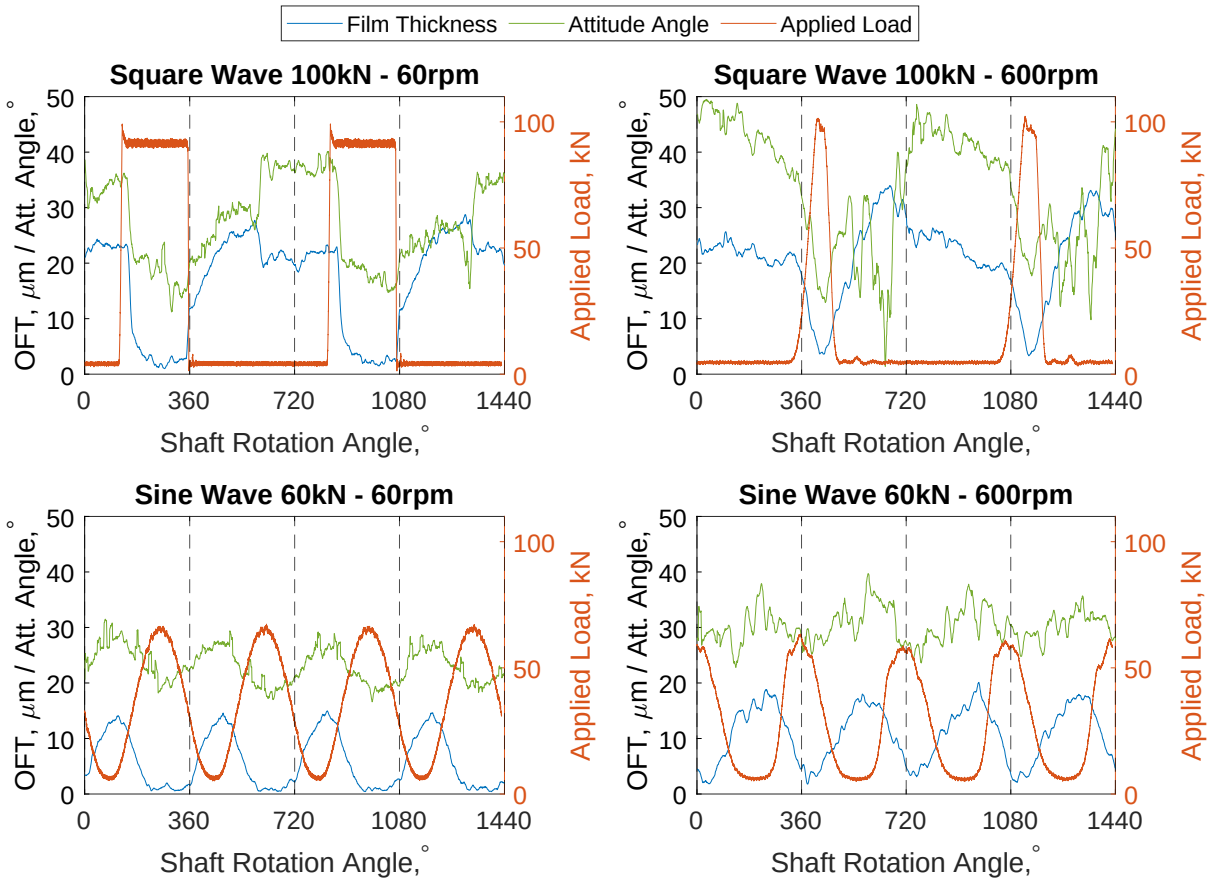

Figure 10.21: Comparison of minimum film thickness and attitude angle for four different dynamic loading cases, with variable load shape and rotation speed. Film measurements are taken via ultrasonic transducers mounted on the top and side of the bearing. Applied load measurements for each case are also shown.

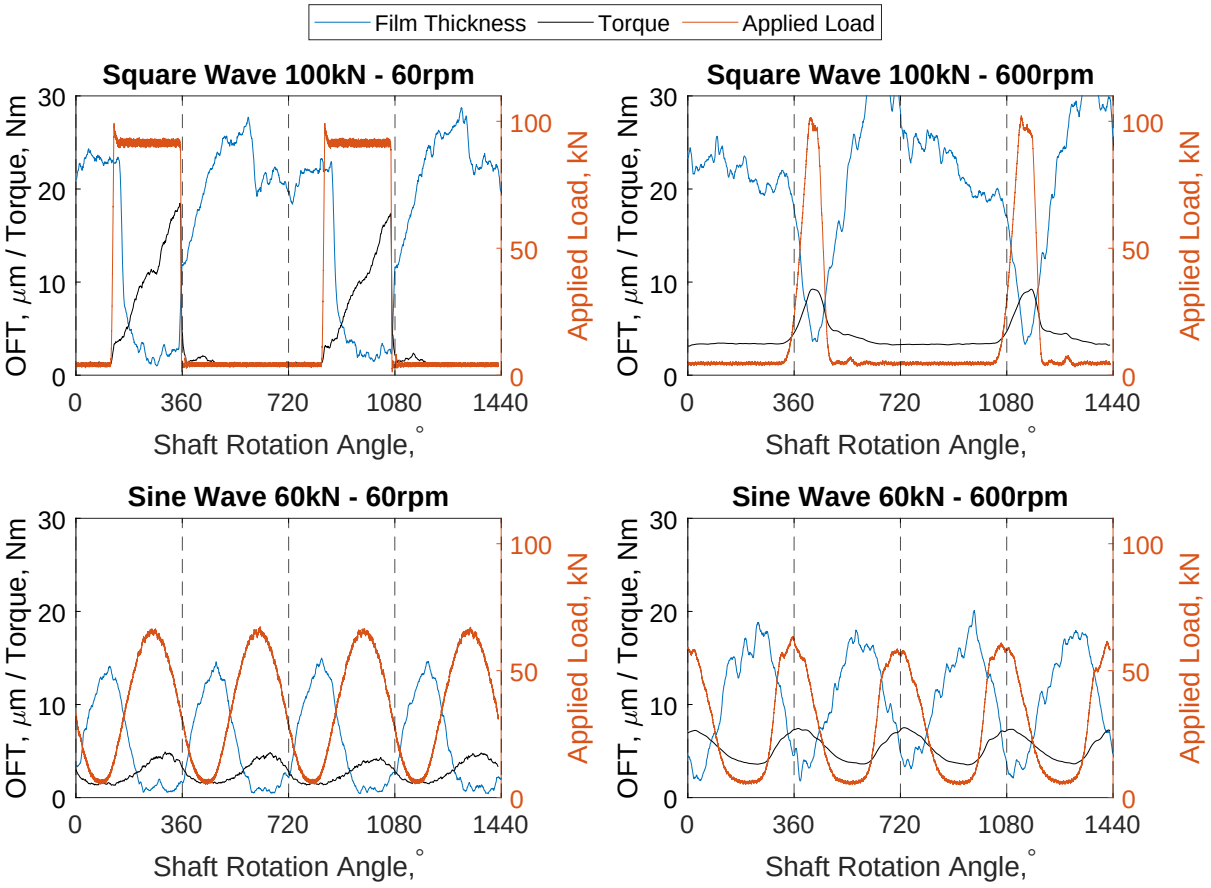

Figure 10.22: Comparison of minimum film thickness and torque for four different dynamic loading cases, with variable load shape and rotation speed. Film measurements are taken via ultrasonic transducers mounted on the top and side of the bearing. Applied load measurements for each case are also shown.

10.3.4 Comparison against a Numerical Model

Minimum film thickness measurements have been compared against predictions calculated via a numerical model. As previously discussed, even if a change in operating parameters, such as applied load, can be assumed to be instant, the change in film thickness is not. This is due to the squeeze film effect and can substantially increase complexity when attempting to model film behaviour.

For simplicity, only square-wave loading patterns were modelled in this study as these provide a region in which the film may reach equilibrium before the next loading or unloading instance. Minimum film thickness within each load state at equilibrium was calculated using the Raimondi Boyd technique, and the change in film thickness between load states was predicted using a numerical technique presented by Khonsari & Jang [86]. The results could then be combined to produce a continuous film thickness profile over multiple load cycles. Two examples are presented in Figure 10.24, along with the corresponding experimental results.

The following describes the predictive method in more detail. The squeeze-film numerical technique presented by Khonsari & Jang requires the initial and final eccentricity ratios. These are calculated in this study via the Raimondi-Boyd technique. Then, small intervals between the initial and final eccentricity ratio values are created. In this case, steps of $\Delta\varepsilon = 0.01$ were found to be appropriate. At each interval, the corresponding dimensionless load capacity $\overline{W}$ is calculated. This was achieved using a relationship shown graphically in Figure 10.23. As the length-diameter ratio, Λ, in the BETTY rig is 1.25, the values for dimensionless load capacity were found by linear interpolation between curves Λ=1 and Λ=1.5. The value for $\overline{W}$ is then applied to the following equation to obtain the speed at which film thickness is changing, known as the approach velocity:

$$V = \frac{WC^3}{\mu r L \overline{W}} \tag{10.9}$$

Where W is applied load, C is radial clearance, μ is dynamic viscosity, r is bearing radius, L is bearing length and $\overline{W}$ is the dimensionless load capacity.

Consequently, time duration can then be calculated via the following:

$$\Delta t = \frac{2C(\varepsilon_2 - \varepsilon_1)}{V_1 + V_2} \tag{10.10}$$

Where ε_1 and ε_2 are the initial and final eccentricity ratios within that interval respectively. V_1 and V_2 are the initial and final approach velocities within that interval respectively.

This process is repeated at every interval. The sum of all time duration values provides the total squeeze time. With a known eccentricity ratio, and therefore minimum film thickness, at each time interval, the change in thickness between load states can be graphed, as in Figure 10.24.

As with all numerical models, this method requires assumptions to be made. In this case, these are:

- The film thickness is small compared to other dimensions in the system, such as bearing diameter and length.
- The fluid is incompressible.
- The fluid is Newtonian.
- Fluid flow is laminar.
- Shaft and bearing deformation are negligible.

Assessing Figure 10.24, the experimental and predicted results are in good agreement when the applied load is high. However, the difference between measured and predicted

film thickness is generally greater when the bearing is unloaded. It is thought that this is due to the non-linear relationship between operating conditions and film thickness. For example, it takes a far greater load increase to reduce film thickness from 3 μm to 2 μm than it does to reduce from 20 μm to 19 μm. The same is also true for rotation speed. Additionally, the phase shift technique is most accurate for thinner films.

Also, in many cases, when the load is removed, the measured film thickness peaks then settles down to a lower constant value. This was unexpected and was not predicted by the numerical model. There may be some sort of bouncing effect as the load is quickly removed, although more work is required to confirm this.

For the 60 rpm test, a small delay between the load applied and the change in film thickness is present. This is also observed in a limited number of other test cases. The cause of this is uncertain. It could be due to a synchronisation error between data streams either during acquisition or processing; however, the change in film thickness when the load is removed initiates immediately.

The measured and predicted film thickness gradient profiles between load states appear to be in good agreement, although the predicted total squeeze time appears to be slightly shorter. This is true for both the loading and unloading events. Small differences may be due to the complex nature of a bearing experiencing dynamic loads. For example, even a small change in bearing temperature results in a substantial change in viscosity, which, as Equation 10.9 shows, would substantially affect approach velocity. Thus, the temperature profile around the entire bearing would be required for an optimum prediction. To achieve this, ambient temperature, how the fluid flows within the bearing and effects due to oil ports must be known, to name a few. This would also require a much more advanced numerical model than the one used in this study. This highlights the advantage of a robust measurement technique, which does not require such detailed knowledge of the system.

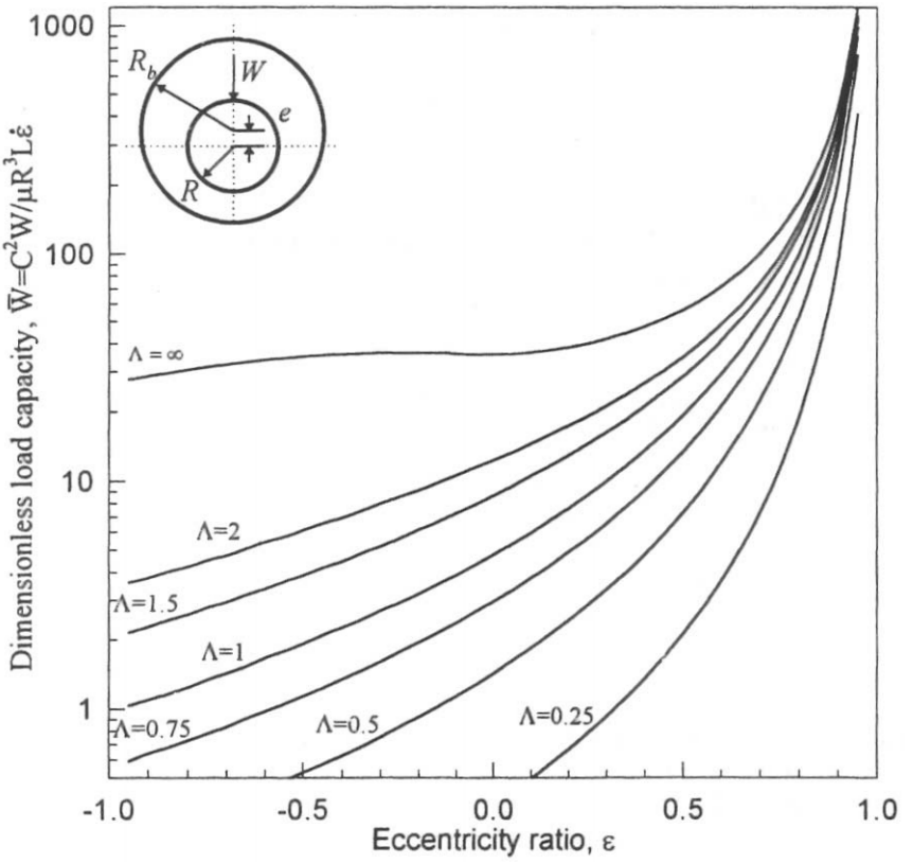

Figure 10.23: The relationship between eccentricity ratio and dimensionless load capacity for a full journal bearing at different length-diameter ratios (Λ).

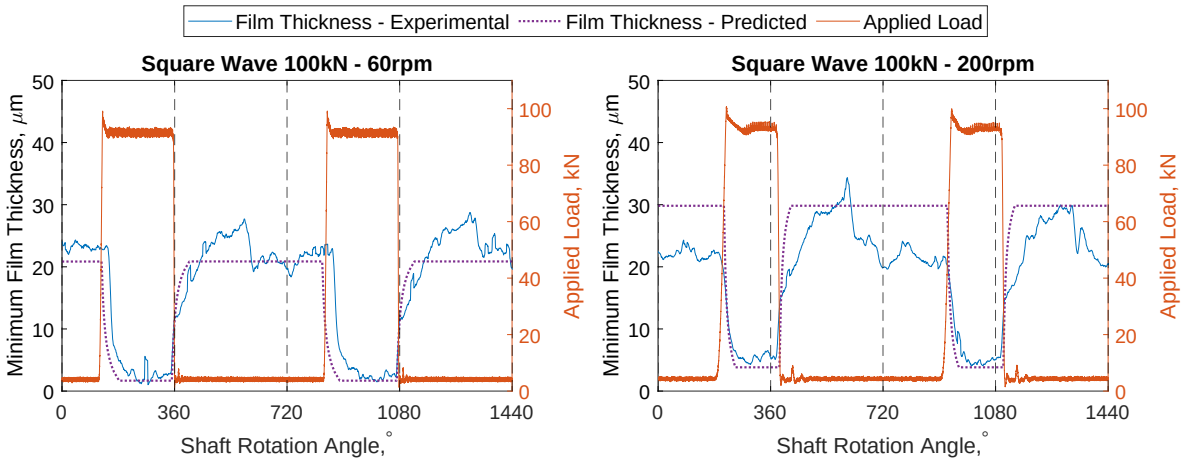

Figure 10.24: Comparison between experimental minimum film thickness measurements and a numerical prediction for two test cases under dynamic loading conditions. Measurements over four full rotations are presented. Operating conditions include a shaft rotation speed of 60 rpm (left) and 200 rpm (right), an applied square-wave loading pattern with 100 kN peak load and bearing temperature of 50°C.

10.3.5 Comparison against Eddy Current Sensor Measurements

As with the BAXTER rig, film measurements via the ultrasonic technique were also compared against conventional eddy current (gap) sensor measurements during BETTY rig testing. These gap sensors were positioned at either side of the bearing in line with the top ultrasonic sensors, as shown in Figure 10.10.

Figure 10.25 compares film thickness measurements obtained by eddy current gap sensors against ultrasonic measurements taken during a square wave loading cycle. In this test, the shaft rotation speed is 150 rpm, and load varies between 5 kN and 25 kN. Loading frequency is 2.5 Hz, synchronised with the acquisition software's internal clock rather than the encoder as done in previous experiments.

Gap sensors A and B both exhibit film thickness profiles similar to that of the ultrasonic measurements, although generally reporting a slightly thicker film. Also, gap sensor A and B measurements are somewhat inconsistent, even though previous experiments indicated that the shaft-bearing system was aligned, so results should be identical. As previously discussed, inaccuracies may be caused by shaft or bearing deformation. This is not accounted for due to the indirect nature of the eddy current sensor measurement technique. Additionally, the voltage output of an eddy current sensor is sensitive to changes in temperature. Although thermocouples were mounted in close proximity to the sensors and a careful pre-test calibration was performed, uncertainties in temperature may still lead to reduced measurement accuracy.

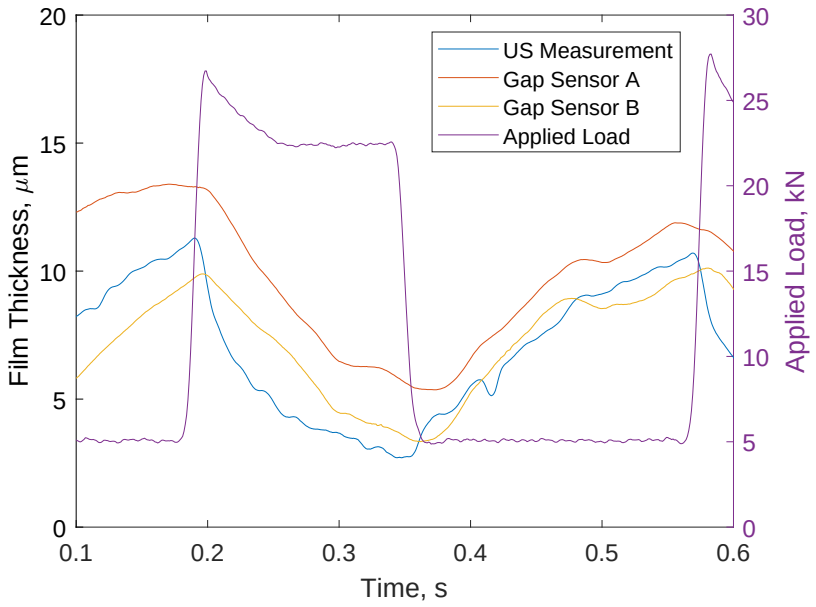

Figure 10.25: Comparison between ultrasonic and eddy current gap sensor measurements on BETTY rig. Gap sensor A located on motor side of bearing, gap sensor B located on slip-ring side.

10.4 Revisiting Cavitation

For the BAXTER rig, cavitation appeared to be so significant that phase shift would almost instantly tend towards zero in the diverging region. However, for tests using the BETTY test platform, phase shift increased less sharply, indicating that cavitation was less severe. With a finite gradient available, as evident in Figure 10.18, it was deemed worthwhile to examine cavitation in more detail using results from the BETTY rig.

Theoretically, within the high pressure region, all air is dissolved in the lubricant; thus, the proportion of air in the suspension (known as the air volume fraction, β) is zero. However, within the diverging region, air escapes as pressure reduces, thereby increasing the volume fraction of air in the suspension. In journal bearings this peak in volume fraction is typically in the range of around 8% [144].

The acoustic velocity of an oil-air mixture is lower than that of oil with no suspended air. In fact, acoustic velocity can be used to calculate volume fraction via the Urick equation [220]:

$$\beta = -\frac{\pm\sqrt{a^2 + 4ab\gamma^2 - 2ab + b^2} + a + b^2}{2ab} \tag{10.11}$$

$$a = \frac{\rho_{air} - \rho_{oil}}{\rho_{oil}} \tag{10.12}$$

$$b = \frac{\kappa_{air} - \kappa_{oil}}{\kappa_{oil}} \tag{10.13}$$

$$\gamma = \frac{c_{oil}}{c_{suspension}} \tag{10.14}$$

Where β is the air volume fraction, and κ_{air} and κ_{oil} are the compressibilities of air and oil respectively. The Urick equation assumes air bubbles are evenly distributed across the thickness of the layer and have a negligible diameter. This will be considered in more detail in Section 10.4.1.

To obtain a value for acoustic velocity in the diverging region, one can use the expected film thickness by assuming the converging and diverging regions are identical, mirrored around the point of minimum film thickness. This value of film thickness can then be applied to a rearranged form of the phase shift equation, in which acoustic velocity is the subject:

$$c = \sqrt{h\frac{\omega z_1 z_2 \pm \sqrt{\omega z_1 z_2^2 - tan^2\Phi(z_1^2 - z_2^2)(\omega z_1 z_2)^2}}{tan\Phi(z_1^2 - z_2^2)}} \tag{10.15}$$

This equation provides the speed of sound of the suspension, which can then be applied to the Urick equation (Equation 10.11) to provide volume fraction at that rotation angle.

Two examples of this are shown in Figure 10.26, with rotation speeds of 60 rpm and

200 rpm. Both are operating under a 50 kN static load. Also shown is the pressure profile around the bearing circumference at the same axial location as the transducer. This profile is calculated the same numerical model previously used to compensate for pressure effects in Section 7.4.

Both cases in Figure 10.26 show that cavitation initiates at the point at which the simulation predicts pressure to reach zero. This agrees with theory as the air dissolved in the lubricant only escapes when the pressure drops below its vapour pressure, which is similar in magnitude to the ambient pressure. The peak magnitude of air volume fraction is in the order of 1% to 10%, this is within the range one would expect in a journal bearing of this size [144].

No significant relationship between air volume fraction and rotation speed or applied load was detected. However, this study only intends to explore whether ultrasonic methods can provide air volume fraction measurements at least within the correct order of magnitude and whether cavitation is detected within the expected region. A future investigation could develop the process, thereby enabling circumferential volume fraction measurements to higher accuracy. From this, links between air volume fraction and operating conditions could be explored in more detail.

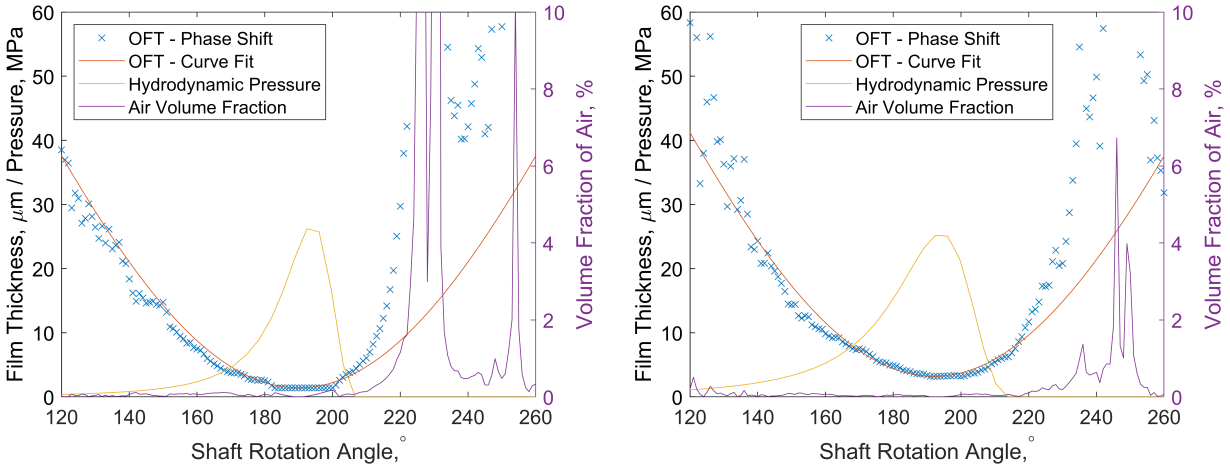

Figure 10.26: Film thickness and air volume fraction for two shaft rotation speeds, 60 rpm (left) and 200 rpm (right). Both tests use a static applied load of 50 kN. These are compared against hydrodynamic pressure profiles calculated via a numerical model. Also shown is a sine curve fit of the film thickness measurements within the converging region, reflected at the attitude angle.

10.4.1 Assessing scattering effects

The results presented so far have assumed that the magnitude of cavitation effects are purely due to the air volume fraction. However, Kasolang et al. posited that the cavitation patterns observed are a function of both air volume fraction and wave scattering off individual air bubbles [144]. That said, Urick stated that scattering is negligible when

bubble size is infinitesimally small compared to the wavelength of the ultrasonic wave, in the order of 100 times smaller. Although it is difficult to determine the exact size of the bubbles in the contact, their diameter cannot exceed the thickness of the interface at that bearing angle. This upper limit ranges from 8 μm to 40 μm in the area of interest for this system. Given a lubricant acoustic velocity of 1400 ms^{-1} and index frequency of 5 MHz, the wavelength is:

$$\lambda = \frac{c_{oil}}{f} = \frac{1400}{5 \times 10^6} = 280 \ \mu m \tag{10.16}$$

Where λ is the wavelength. Thus, the maximum possible bubble size is not negligible compared to the wavelength, at approximately 10% of the scale. However, the actual bubble size may be much smaller than this, causing scattering to be negligible.

As scattering is wavelength dependent, it follows that if scattering is significant then calculated air volume fraction should change with index frequency, with more scattering for higher frequencies. Figure 10.27 shows partial circumferential film thickness profiles and corresponding volume fractions calculated using different index frequencies. In both the 60 rpm and 200 rpm cases, the measured volume fraction is inversely proportional to index frequency. This agrees with theoretical expectations, as scattering causes the wave to be dispersed, causing less of the energy to be returned, reducing the apparent reflection coefficient.

Volume fraction profiles between index frequencies are more similar for the 60 rpm case. The agreement is most evident towards the start of the diverging region, where the maximum possible bubble size is lower due to the smaller gap between surfaces. The similarity in profiles suggests that bubbles in the 60 rpm case may be smaller on average than in the 200 rpm case, leading to less scattering.

In all, this study serves as a starting point in attempting to quantify cavitation in journal bearings using ultrasound. To reduce the effect of scattering it may be beneficial in future to embed a transducer with a much lower centre frequency, possibly around 500 kHz, so that bubble size would certainly be negligible to wavelength.

As an aside, Figure 10.27 shows film thickness is consistent in the converging region particularly around minimum film thickness, with slight variations attributed to different SNRs. This indicates the measurements are frequency independent.

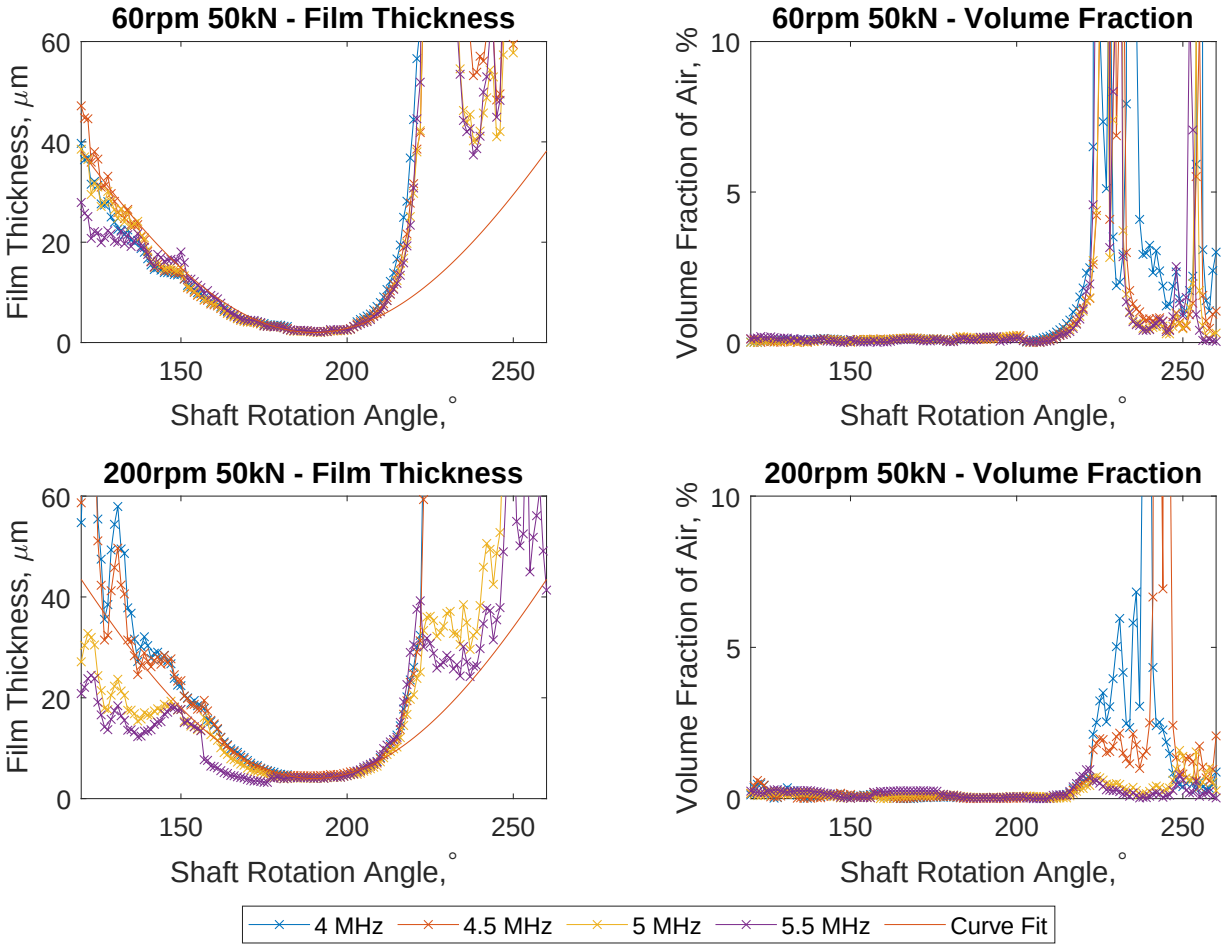

Figure 10.27: Film thickness and air volume fraction for two shaft rotation speeds, 60 rpm (top) and 200 rpm (bottom), calculated using different index frequencies. Both tests use a static applied load of 50 kN. Also shown is a sine curve fit of the film thickness measurements within the converging region, reflected at the attitude angle.

10.5 Conclusions

This chapter has covered the development and application of the BETTY dynamic loading test rig. The following has been achieved:

- A journal bearing test platform capable of dynamic loading has been developed.
- This test platform has been instrumented with bearing and shaft mounted ultrasonic transducers, along with conventional measurement hardware such as thermocouples and a torque transducer.
- A new referencing method, the snapshot technique, has been created. This is suitable for transducers with oil films which constantly sit within the spring model measurement range during operation. The method uses bearing geometry and film thickness measurements from other sensors to provide a reference. This eliminates the need for a separate pre-installation reference.
- Minimum film thickness and attitude angle have been measured for a range of dynamic loading conditions. This includes different lubricant temperatures, rotation speed and loading profiles.
- Minimum film thickness results have been compared against a numerical model, with good agreement between predictions and ultrasonic measurements. Results were also compared against conventional eddy current sensor measurements. Although there was reasonable agreement, shaft and bearing deformation introduced some uncertainty to the eddy current sensor measurements.
- Bearing cavitation was revisited. The air volume fraction around the bearing circumference was quantified using a method based on the Urick equation. The peak magnitude of air volume fraction was in the order of 1% to 10%, which is similar to previous findings.

Chapter 11

Conclusions

11.1 Contribution to Current Knowledge

The aim of this project was to develop the capabilities of the ultrasonic technique in the analysis of oil films within journal bearings. This was achieved by the design and implementation of two bespoke bearing test platforms, the first to understand static loading and severe operating conditions, the second to investigate dynamic loading.

Via these test platforms, several advancements in applying ultrasonic techniques to tribological components were made. First, a more complete and rigorous approach in determining film thickness from reflected ultrasonic waves was developed. This included a new method to determine material acoustic impedance by using the changing reflection coefficient amplitude and phase during operation. This method could readily be applied to many three layer systems where the acoustic impedance is uncertain or subject to change during operation.

Additionally, pressure effects around the bearing circumference were accounted for using a novel iterative technique. It was determined that pressures in the order of 1 MPa to 10 MPa, typical for journal bearings, have a significant effect on lubricant density and acoustic velocity. Therefore, pressure should be considered when calculating journal bearing film thickness via ultrasonic methods, something not accounted for in previous investigations.

Also, this study has demonstrated that by combining the amplitude, phase and resonant dip techniques, one can obtain a near-complete film thickness profile around the bearing circumference with a single transducer, even if film thickness spans three orders of magnitude. Uncertainty in the diverging region arose from cavitation effects; however, film thickness could be assumed to be symmetrical around the minimum point in most cases.

The quantification of air volume in the film rupture region was attempted, with reasonable values calculated. However, actual bubble size was unknown, thus scattering effects may reduce the accuracy of this method. That said, simply detecting cavitation and the angle

at which it occurs is useful within itself, enabling predictions of where cavitation wear is most likely to occur under certain conditions.

By raising the support bearings on the BAXTER rig, it was demonstrated that ultrasonic techniques could be used to detect and quantify shaft misalignment. This was extended by offsetting load axially by 8 mm to the bearing assembly. By comparing experimental results against a numerical model, it was found that even minute differences in film thickness at the bearing edge had a substantial effect on the peak pressure. The numerical model did not consider deformation or pressure effects on viscosity, which may explain why predicted peak pressures were greater than when measured experimentally. This highlighted the danger of making assumptions with predictive numerical models, showing that a rigid model is generally unsuitable for misaligned bearings.

Run-down operating conditions were simulated by steadily reducing rotation speed. By monitoring torque, a spike in friction signified a transition into the mixed lubrication regime. The film thickness at this point was dependent on lubricant viscosity.

Oil starvation can lead to rapid and severe damage to bearing systems if it is not detected and resolved. Starvation on the BAXTER test platform was induced by draining the bearing assembly of oil during operation. Early signs of starvation could be detected by monitoring the thick film region of the bearing. As there was only a marginal change in both minimum film thickness and bearing temperature, it was unlikely that torque significantly increased. Thus, circumferential film measurements may allow the onset of starvation to be identified far earlier than with conventional methods.

Finally, the capabilities of ultrasonic film measurements in dynamically loaded bearings were explored. The minimum film thickness and attitude angle could be reliably measured across a range of shaft rotation speeds, lubricant temperatures and loading profiles. This study made use of a new referencing technique, the snapshot method. This method enabled the side bearing sensors to be referenced during operation even though film thickness at their locations never left the measurable region. This would not be possible using previous in-situ referencing techniques and would have required a pre-test reference, which can be both cumbersome and lose accuracy over time.

The design of the BAXTER and BETTY rigs can also be useful for inspiring the next generation of test platforms. For example, the BAXTER rig is currently being used as a template for a new tilting pad bearing platform in development at the University of Sheffield.

11.2 Future Work

11.2.1 Installation of Additional Hardware

Even though the BAXTER test platform has a wide band of operating conditions, there is potential to extend this further. For example, the shaft rotation speed under steady-state conditions is limited by the motor to 75 rpm. Below this, the motor fan does not spin fast enough to provide adequate cooling. Also, the rotation speed is less consistent, with some levels of stuttering observed below 50 rpm. Although entering the mixed lubrication regime was achieved during shut-down in Chapter 9, slower constant rotation speeds would be required for the system to stay in this regime for sustained periods. One solution would be to install a reduction gearbox such as the 10:1 ratio worm-gearbox photographed in Figure 11.1. Mixed lubrication is currently undergoing intense study in the automotive industry as they work to meet emissions regulations by minimising viscous losses. As such, adapting the test platform to investigate such conditions could be beneficial. Conversely, replacing the current 4-pole motor with a 2-pole motor would increase maximum rotation speed from 1500 rpm to 3000 rpm, enabling higher shear rate and high Sommerfeld number conditions to be investigated. An example 2-pole motor of the appropriate specifications is shown in Figure 11.1.

The BAXTER rig also only currently features shaft-mounted ultrasonic sensors. The addition of bearing mounted sensors would allow consistent film thickness measurements to be taken at precise locations in a similar manner to the BETTY rig. A comparison between bearing and shaft mounted measurements would act as a further validation tool to assess the accuracy of the ultrasonic technique. Bearing mounted sensors would also serve as an example to industrial partners looking for a condition monitoring tool and who may prefer the shaft to be unmodified. Instrumenting sensors on the rear of a bearing shell is generally a more simple and less intrusive process than for shaft-embedded sensors. To assess the feasibility of this, a bearing shell was instrumented with an array of piezo-ceramic elements, photographed in Figure 11.2. Despite their small size and the low thickness of the bearing shell, clear and distinct reflections were observed. Also, the bearing housing used in the BAXTER rig already has cable ejection channels suitable for bearing mounted sensors, so no further machining or new components would be required.

Another useful addition could be ultrasonic shear transducers to assess viscosity. Unlike the reflection coefficient in longitudinal waves, which varies with film thickness, the reflection coefficient in shear waves can be related to lubricant viscosity. This has been attempted previously in journal bearings under normal operating conditions, although with significant variability in the results, particularly for low viscosity oils [221, 222]. Shear transducers were successfully instrumented on a BAXTER bearing rig as a trial, shown in Figure 11.2. The shear sensors can be identified in this photograph by their darker colour.

Further to this, the use of micro arrays in ultrasonics is increasing in popularity. High density arrays of sub-millimetre piezoceramic elements enable the techniques previously discussed in Section 5.1, such as beam steering and full matrix capture. However, man-

ufacturing these arrays at a reasonable cost can be challenging, particularly for bespoke systems that require unusual array patterns. Through a collaboration with the École nationale d'ingénieurs de Saint-Étienne (ENISE), early trials of machining bulk piezoceramic elements using a milling machine was performed. This technique used a 100 μm thick diamond tipped slitting saw. The process is photographed in Figure 11.3. After optimising machining parameters such as feed rate, tool rpm and depth of cut, 5 MHz shear piezoceramic elements could be cut consistently to a size of 90 μm before debonding. A surface profile of an ultrasonic transducer array with decreasing element sizes is shown in Figure 11.3.

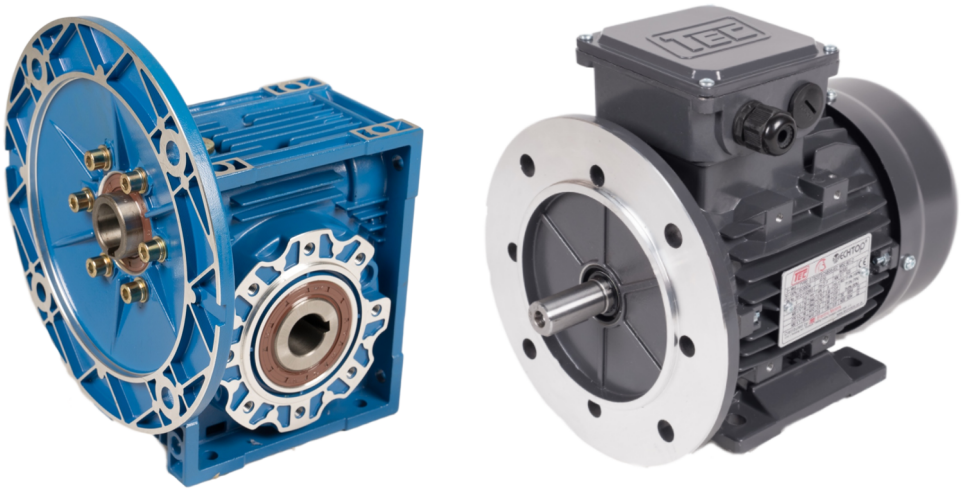

Figure 11.1: Photograph of worm gearbox (left) [223]. Photograph of 2-pole motor (right) [224].

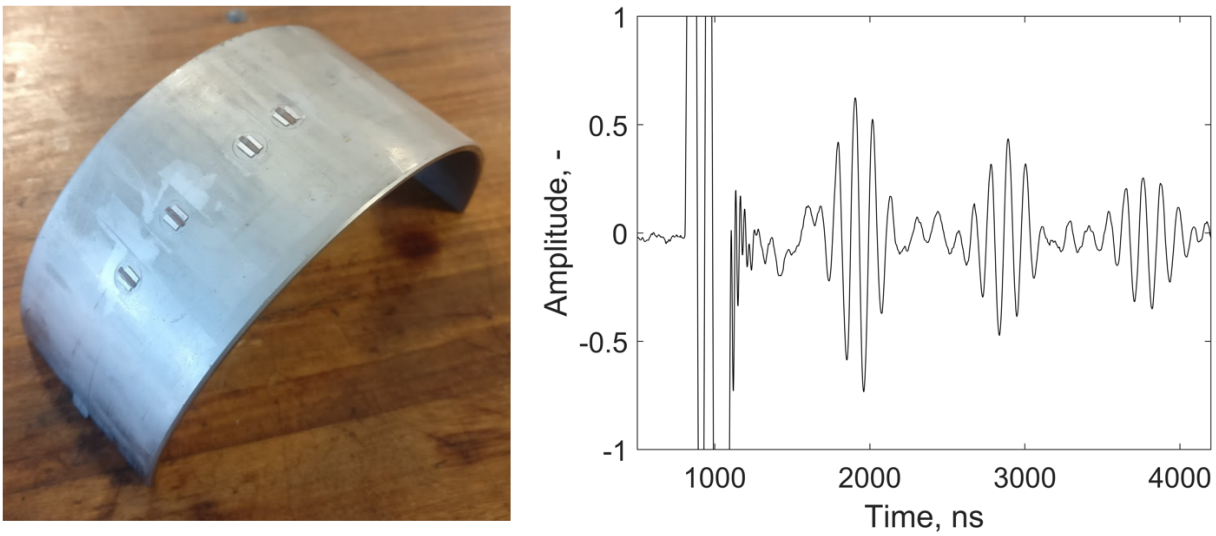

Figure 11.2: Photograph of bearing shell for BAXTER rig instrumented with longitudinal and shear ultrasonic transducers (left). Corresponding A-scan from a longitudinal bearing mounted sensor (right).

Figure 11.3: Photograph of bearing shell during array machining process (left). Surface profile of ultrasonic array taken using an Alicona InfiniteFocus SL (right).

11.2.2 Application to Real Systems

Although the use of ultrasound in test platforms to measure film thickness has been proven to be a useful tool in understanding lubricant and bearing behaviour, the potential of this technology is not confined to laboratory environments. As the ultrasonic method matures it can be more readily applied to real engineering systems.

The outcomes of this work should stay relevant for some time, particularly as journal bearings aren't going anywhere. Even though the phase-out of internal combustion engines in passenger cars is in full swing, it is predicted that the majority of off-highway heavy duty vehicles and marine vessels will still be powered by ICEs for decades [225, 226]. Therefore, there is plenty of time and value in optimising bearing efficiency in ICEs while the transition to electrification or other alternative technologies continues.

Also, journal bearings are being trialled in new applications. For example, the current roller bearings in wind turbines are susceptible to significant wear due to their extreme contact pressures. This leads to considerable maintenance costs and downtime. As wind turbines are growing in both size and popularity, research into whether journal bearings are a viable alternative is a trending area of interest [227, 228]. Ultrasonic methods could play a big part in understanding journal bearing behaviour in this new application, including as a monitoring tool.

References

[1] P. Alexander, A. Reddy, C. Brown, R. C. Henry, and M. D. Rounsevell, "Transforming Agricultural Land Use through Marginal Gains in the Food System," *Global Environmental Change*, vol. 57, jul 2019.

[2] S. Sunder and G. Waymire, "Marginal Gains in Accuracy of Valuation from Increasingly Specific Price Indexes: Empirical Evidence for the U.S. Economy," *Journal of Accounting Research*, vol. 21, no. 2, p. 565, 1983.

[3] C. Pentecost, D. A. Richards, and J. Frost, "Amalgamation of Marginal Gains (AMG) as a Potential System to Deliver High-quality Fundamental Nursing Care: A Qualitative Analysis of Interviews from High-Performance AMG Sports and Healthcare Practitioners," *Journal of Clinical Nursing*, vol. 27, no. 11-12, pp. 2387–2402, jun 2018. [Online]. Available: http://doi.wiley.com/10.1111/jocn.14186

[4] M. Marcella and A. Johnson, "Developing High-Performance Motorcycle Oils," *SAE Technical Papers*, no. 0505, jan 2020. [Online]. Available: https://www.sae.org/publications/technical-papers/content/2019-32-0505/

[5] K. Holmberg and A. Erdemir, "The Impact of Tribology on Energy Use and CO2 Emission Globally and in Combustion Engine and Electric Cars," *Tribology International*, vol. 135, pp. 389–396, jul 2019.

[6] C. Taylor, "Automobile Engine Tribology—Design Consideration for Efficiency and Durability," *Wear*, vol. 221, pp. 1–8, 1998.

[7] C. Knauder, H. Allmaier, D. E. Sander, and T. Sams, "Investigations of the Friction Losses of Different Engine Concepts. Part 1: A Combined Approach for Applying Subassembly-resolved Friction Loss Analysis on a Modern Passenger-car Diesel Engine," *Lubricants*, vol. 7, no. 5, may 2019.

[8] The European Parliament and the Council of the European Union, "REGULATION (EU) 2019/631 - Setting CO2 Emission Performance Standards for New Passenger Cars and for New Light Commercial Vehicles," apr 2019. [Online]. Available: https://eur-lex.europa.eu/legal-content/EN/TXT/PDF/?uri=CELEX:32019R0631{\&}from=EN

[9] P. Bielaczyc and J. Woodburn, "Trends in Automotive Emission Legislation: Impact on LD Engine Development, Fuels, Lubricants and Test Methods: a Global

View, with a Focus on WLTP and RDE Regulations," *Emission Control Science and Technology*, vol. 5, no. 1, pp. 86–98, 2019.

[10] G. W. Stachowiak and A. W. Batchelor, *Engineering Tribology*. Butterworth-Heinemann, 1993.

[11] H. K. Lotze, H. Guest, J. O'Leary, A. Tuda, and D. Wallace, "Public Perceptions of Marine Threats and Protection from around the World," *Ocean and Coastal Management*, vol. 152, no. September 2017, pp. 14–22, 2018. [Online]. Available: https://doi.org/10.1016/j.ocecoaman.2017.11.004

[12] T. G. Safford, J. D. Ulrich, and L. C. Hamilton, "Public Perceptions of the Response to the Deepwater Horizon Oil Spill: Personal Experiences, Information Sources, and Social Context," *Journal of Environmental Management*, vol. 113, no. September, pp. 31–39, 2012.

[13] J. Chun, J. H. Oh, and C. K. Kim, "Oil Spill Response Policies to Bridge the Perception Gap between the Government and the Public: A Social Big Data Analysis," *Journal of Marine Science and Engineering*, vol. 8, no. 5, 2020.

[14] United States Environmental Protection Agency Office of Wastewater Management, "Environmentally Acceptable Lubricants," *Encyclopedia of Lubricants and Lubrication*, no. November, pp. 526–526, 2014.

[15] D. S. Etkin, "Worldwide Analysis of In-port Vessel Operational Lubricant Discharges and Leakages," *Proceedings of the 33rd AMOP Technical Seminar on Environmental Contamination and Response*, vol. 1, no. 2007, pp. 529–553, 2010.

[16] A. Yano, E. Iwawaki, M. Mihara, and S. Yoshihara, "Study on the Load Carrying Capacity of Sliding Bearing Lubricated by Synthetic Ester Oils," *Tribology Online*, vol. 10, no. 5, pp. 377–389, 2015.

[17] R. Oza, "Bacteria Bacterium Microbiology," 2020. [Online]. Available: https://pixabay.com/illustrations/bacteria-bacterium-microbiology-1832824/

[18] S. Nakamura and T. Minamino, "Flagella-driven Motility of Bacteria," *Biomolecules*, vol. 9, no. 7, jul 2019. [Online]. Available: /pmc/articles/PMC6680979/?report=abstracthttps://www.ncbi.nlm.nih.gov/pmc/articles/PMC6680979/

[19] Venarca, "Turbocharger: How Exhaust Gases Increase Engine Power," 2017. [Online]. Available: https://www.venarca.com/turbocharger-engine-power

[20] T. Walke, "The Most Powerful Diesel Engine in the World," 2006. [Online]. Available: http://web.archive.org/web/20100716202400/http://people.bath.ac.uk/ccsshb/12cyl/index.html.o

[21] J. A. Williams, *Engineering Tribology*. Oxford: Oxford University Press, 2000.

[22] T. Tevrüz, "Tribological Behaviours of Carbon Filled Polytetrafluoroethylene (PTFE) Dry Journal Bearings," *Wear*, vol. 221, no. 1, pp. 61–68, oct 1998.

[23] R. H. Savage, "Graphite Lubrication," *Journal of Applied Physics*, vol. 19, no. 1, pp. 1–10, jan 1948. [Online]. Available: http://aip.scitation.org/doi/10.1063/1.1697867

[24] G. Gao, Z. Yin, D. Jiang, and X. Zhang, "Numerical Analysis of Plain Journal Bearing under Hydrodynamic Lubrication by Water," *Tribology International*, vol. 75, pp. 31–38, jul 2014.

[25] K. Radil, S. Howard, and B. Dykas, "The Role of Radial Clearance on the Performance of Foil Air Bearings," *Tribology Transactions*, vol. 45, no. 4, pp. 485–490, 2002. [Online]. Available: https://www.tandfonline.com/doi/abs/10.1080/10402000208982578

[26] S. C. Vladescu, N. Marx, L. Fernández, F. Barceló, and H. Spikes, "Hydrodynamic Friction of Viscosity-Modified Oils in a Journal Bearing Machine," *Tribology Letters*, vol. 66, no. 4, p. 127, dec 2018. [Online]. Available: https://doi.org/10.1007/s11249-018-1080-4

[27] P. P. Wegener, *What Makes Airplanes Fly?* New York: Springer US, 1991.

[28] N. Marx, L. Fernández, F. Barceló, and H. Spikes, "Shear Thinning and Hydrodynamic Friction of Viscosity Modifier-Containing Oils. Part II: Impact of Shear Thinning on Journal Bearing Friction," *Tribology Letters*, vol. 66, no. 3, pp. 1–11, 2018. [Online]. Available: http://dx.doi.org/10.1007/s11249-018-1040-z

[29] G. H. B. Dean, E. W; Davis, "Viscosity Variations of Oils with Temperature," *Chemical and Metallurgical Engineering*, vol. 36, pp. 618–619, 1929.

[30] OelCheck, "Viscosity – Viscosity Changes – Viscosity-Temperature Behaviour," 2018. [Online]. Available: en.oelcheck.com/wiki/Viscosity

[31] F. X. Borras, M. B. D. Rooij, and D. J. Schipper, "Rheological and Wetting Properties of Environmentally Acceptable Lubricants (EALs) for Application in Stern Tube Seals," *Lubricants*, 2018.

[32] N. Marx, ·. Luis Fernández, F. Barceló, and ·. H. Spikes, "Shear Thinning and Hydrodynamic Friction of Viscosity Modifier-Containing Oils. Part I: Shear Thinning Behaviour," *Tribology Letters*, vol. 66, p. 92, 2018. [Online]. Available: https://doi.org/10.1007/s11249-018-1039-5

[33] RheoSense, "Viscosity of Newtonian and Non-Newtonian Fluids," 2020. [Online]. Available: https://www.rheosense.com/applications/viscosity/newtonian-non-newtonian

[34] P. Liu, J. Lu, H. Yu, N. Ren, F. E. Lockwood, and Q. J. Wang, "Lubricant Shear Thinning Behavior Correlated with Variation of Radius of Gyration via Molecular Dynamics Simulations," *The Journal of Chemical Physics*, vol. 147, p. 84904, 2017. [Online]. Available: https://doi.org/10.1063/1.4986552https://doi.org/10.1063/1.1421362

[35] G. Willis, *ExxonMobil Lubrication Fundamentals.* New York: Marcle Dekker Inc., 1980.

[36] G. Stachowiak and A. Batchelor, *Engineering Tribology*, 3rd ed. Elselvier, 2006. [Online]. Available: http://www.scopus.com/inward/record.url?eid=2-s2.0-84882176267{\&}partnerID=40{\&}md5=9d442c18156945d76e0853ad8ba5822e

[37] Y. Wang, Q. J. Wang, C. Lin, and F. Shi, "Development of a Set of Stribeck Curves for Conformal Contacts of Rough Surfaces," *Tribology Transactions*, vol. 49, no. 4, pp. 526–535, 2006.

[38] T. STOLARSKI, *Tribology in Machine Design.* Butterworth-Heinemann, 1999.

[39] P. Cann, E. Ioannides, B. Jacobson, and A. A. Lubrecht, "The lambda ratio - a critical re-examination," *Wear*, vol. 175, no. 1-2, pp. 177–188, 1994.

[40] D. Zhu and Q. J. Wang, "On the λ Ratio Range of Mixed Lubrication," *Proceedings of the Institution of Mechanical Engineers, Part J: Journal of Engineering Tribology*, vol. 226, no. 12, pp. 1010–1022, dec 2012. [Online]. Available: http://journals.sagepub.com/doi/10.1177/1350650112461867

[41] Permaglide, "Advantages over Ball Bearings," 2019. [Online]. Available: https://www.permaglide.com/en/plain-bearings/advantages-over-ball-bearings/

[42] SKF Group, "SKF Composite Plain Bearings," SKF Group, Gothenburg, Tech. Rep., 2012.

[43] I. Pierre and M. Fillon, "Influence of Geometric Parameters and Operating Conditions on the Thermohydrodynamic Behaviour of Plain Journal Bearings," *Proceedings of the Institution of Mechanical Engineers, Part J: Journal of Engineering Tribology*, vol. 214, no. 5, pp. 445–457, may 2000. [Online]. Available: http://journals.sagepub.com/doi/10.1243/1350650001543322

[44] P. S. Chu and E. Kay, "Optimum Clearance Fits for Journal Bearings in Relation to B.S.1916 and to Lubrication Theory," *Wear*, vol. 27, no. 3, pp. 329–343, mar 1974.

[45] S. Singhal and R. Mistry, "Oil Whirl Rotordynamic Instability Phenomenondiagnosis and Cure in Large Induction Motor," *2009 Record of Conference Papers - Industry Applications Society 56th Annual Petroleum and Chemical Industry Conference, PCIC 2009*, pp. 1–8, 2009.

[46] S. M. DeCamillo, A. Dadouche, and M. Fillon, "Journal Bearings in Power Generation," in *Encyclopedia of Tribology.* Springer US, 2013, pp. 1877–1888. [Online]. Available: https://link.springer.com/referenceworkentry/10.1007/978-0-387-92897-5{_}56

[47] P. C. Mishra and H. Rahnejat, "Tribology of Big-end Bearings," in *Tribology and Dynamics of Engine and Powertrain: Fundamentals, Applications and Future Trends.* Elsevier Ltd., jan 2010, pp. 635–659.

[48] G. Miranda, "The Detection of Journal Bearing Cavitation with use of Ultrasound Technology," Ph.D. dissertation, Case Western Reserve University, 2016.

[49] J. Welsh, *Plain Bearing Design Handbook*. Boston: Butterworth-Heinemann Ltd, 1983.

[50] W. Zhou, X. Wei, L. Wang, and G. Wu, "A Superlinear Iteration Method for Calculation of Finite Length Journal Bearing's Static Equilibrium Position," *Royal Society Open Science*, vol. 4, no. 5, 2017.

[51] Autoparts Pro, "IPSA Crankshaft," 2020. [Online]. Available: https://www.autopartspro.co.uk/ipsa-13876929

[52] ——, "IPSA Crankshaft Bearing Set," 2020. [Online]. Available: https://www.autopartspro.co.uk/ipsa-8027525

[53] N. Lakshminarayanan, P; Nayak, *Critical Component Wear in Heavy Duty Engines*. John Wiley & Sons, 2011.

[54] A. Harnoy, *Bearing design in machinery, Engineering tribology and lubrication*. Marcel Dekker Inc., 2003. [Online]. Available: https://goo.gl/K5tg5M

[55] D. W. Gebretsadik, J. Hardell, and B. Prakash, "Tribological Performance of Tin-based Overlay Plated Engine Bearing Materials," *Tribology International*, vol. 92, pp. 281–289, 2015. [Online]. Available: http://dx.doi.org/10.1016/j.triboint.2015.06.014

[56] Goltens, "Rebabbitting Bearings And Stern Tubes," 2020. [Online]. Available: https://www.goltens.com/services/diesel-engine-services/rebabbitting-bearings-and-stern-tubes/

[57] J. Thomson, R. Zavadil, M. Sahoo, A. Dadouche, W. Dmochowski, and M. Conlon, "Development of a Lead-free Bearing Material for Aerospace Applications," *International Journal of Metalcasting*, vol. 4, no. 1, pp. 19–30, 2010.

[58] G. Wright, *Fundamentals of Medium/Heavy Duty Diesel Engines*. Burlington: Jones & Bartlett Learning LLC, 2017.

[59] W. J. Bartz, *Engine Oils and Automotive Lubrication*. Boca Raton: Taylor & Francis Group, 1993.

[60] Kingsbury Inc., "A General Guide to the Principles, Pperation and Troubleshooting of Hydrodynamic Bearings," Kingsbury Inc., Philadelphia, Tech. Rep., 2019.

[61] W. Bearings, "Tilt Pad Journal Bearings," 2019. [Online]. Available: https://www.waukbearing.com/en/engineered-fluid-film/product-lines/journal-bearings/tilt-pad-journal-bearings/

[62] Engine Parts UK, "Engine Bearings - Conrod, Mains, Thrust Washers, Bushes," 2020. [Online]. Available: https://www.enginepartsuk.net/engine-bearings-conrod-mains-thrust-washers-bushes-shells

[63] H. Basri and P. B. Neal, "Oil Flow in Axial Groove Journal Bearings." International Conference on Mechanical Engineering and Automation, 2014.

[64] M. Russo, "Oil Grooves for Bronze Bushings," jun 2013. [Online]. Available: https://www.nationalbronze.com/News/410/{\#}comments

[65] L. Roy, "Effect of Axial Groove on Steady State and Stability Characteristics of Finite Two-Lobe Hybrid Journal Bearing," *Journal of Applied Mechanical Engineering*, vol. 4, no. 1, 2014.

[66] F. P. Brito, A. S. Miranda, and M. Fillon, "Analysis of the Effect of Grooves in Single and Twin Axial Groove Journal Bearings under Varying Load Direction," *Tribology International*, vol. 103, no. November, pp. 609–619, 2016. [Online]. Available: http://dx.doi.org/10.1016/j.triboint.2016.08.010

[67] P. R. Meernik, "Lubricant Flow to Connecting-Rod Bearings through a Rotating Crankshaft," *SAE Technical Paper Series*, 1986.

[68] J. Jang and M. Khonsari, "On the Characteristics of Misaligned Journal Bearings," *Lubricants*, vol. 3, no. 1, pp. 27–53, 2015. [Online]. Available: http://www.mdpi.com/2075-4442/3/1/27/

[69] R. Pigott, "Bearings and Lubrication Bearing Troubles Traceable to Design can Be Avoided by Engineering Study," *Mech. Eng*, vol. 64, pp. 259–269, 1942.

[70] P. G. Nikolakopoulos and C. A. Papadopoulos, "A Study of Friction in Worn Misaligned Journal Bearings under Severe Hydrodynamic Lubrication," *Tribology International*, vol. 41, no. 6, pp. 461–472, jun 2008.

[71] DNV GL, "Ensuring Satisfactory Aft Stern Tube Bearing Lubrication Performance," oct 2019. [Online]. Available: https://www.dnvgl.com/expert-story/maritime-impact/Ensuring-satisfactory-aft-stern-tube-bearing-lubrication-performance.html

[72] J. ung Lee, B. Jeong, and T. H. An, "Investigation on Effective Support Point of Single Stern Tube Bearing for Marine Propulsion Shaft Alignment," *Marine Structures*, vol. 64, pp. 1–17, mar 2019.

[73] S. Poddar and N. Tandon, "Study of Oil Starvation in Journal Bearing Using Acoustic Emission and Vibration Measurement Techniques," *Journal of Tribology*, vol. 142, no. 12, pp. 1–11, 2020.

[74] C. L. Liu, F. Guo, and P. L. Wong, "Characterisation of Starved Hydrodynamic Lubricating Films," *Tribology International*, vol. 131, no. December 2018, pp. 694–701, 2019.

[75] M. He, J. M. Byrne, and J. A. Vázquez, "Fundamentals of Fluid Film Journal Bearing Operation and Modelling." Houston: 44th Turbomachinery Pump Symposia, 2005.

[76] Melett Precision Engineering Turbochargers, "Insufficient Lubrication," Tech. Rep., 2018.

[77] G. Velasquez, "Monitoring Plain Bearings with Ultrasound," 2014. [Online]. Available: https://www.bearing-news.com/monitoring-plain-bearings-ultrasound/

[78] N. D. S. A. Santos, V. R. Roso, and M. T. C. Faria, "Review of Engine Journal Bearing Tribology in Start-Stop Applications," jan 2020. [Online]. Available: https://doi.org/10.1016/j.engfailanal.2019.104344

[79] J. Rueger, "Clean Diesel - Real Life Fuel Economy and Environmental Performance," in *SAE Government and Industry Meeting*, Washington, DC, 2008.

[80] R. Liu, X. Meng, and Y. Cui, "Influence of Numerous Start-ups and Stops on Tribological Performance Evolution of Engine Main Bearings," *International Journal of Engine Research*, vol. 21, no. 8, pp. 1362–1380, oct 2020. [Online]. Available: http://journals.sagepub.com/doi/10.1177/1468087418810094

[81] A. Adam, M. Prefot, and M. Wilhelm, "Crankshaft Bearings for Engines with Start-stop Systems," *MTZ worldwide*, vol. 71, no. 12, pp. 22–25, dec 2010. [Online]. Available: https://link.springer.com/article/10.1007/BF03228047

[82] D. W. Gebretsadik, J. Hardell, and B. Prakash, "Friction and Wear Characteristics of Different Pb-free Bearing Materials in Mixed and Boundary Lubrication Regimes," *Wear*, vol. 340-341, pp. 63–72, oct 2015.

[83] H. Y. Hwang, "Minimizing Seat Track Vibration that is Caused by the Automatic Start/Stop of an Engine in a Power-split Hybrid Electric Vehicle," *Journal of Vibration and Acoustics, Transactions of the ASME*, vol. 135, no. 6, dec 2013. [Online]. Available: http://asmedigitalcollection.asme.org/vibrationacoustics/article-pdf/135/6/061007/6340442/vib{_}135{_}06{_}061007.pdf

[84] P. L. E. Malcolm, "Understanding Journal Bearings," Applied Machinery Dynamics Co., Durango Colorado, Tech. Rep., 2001. [Online]. Available: AppliedMachineryDynamicsCo.Durango,Durango,Colorado

[85] B. Bhushan and F. Dashnaw, "Material Study for Advanced Stern-Tube Bearings and Face Seals." *ASLE transactions*, vol. 24, no. 3, pp. 398–409, 1981.

[86] R. E. Booser, *Tribology Data Handbook*. New York: The Society of Tribologists and Lubrication Engineers, 1997.

[87] E. Barrett, L.E; Gunter, "Steady-state and transient analysis of a squeeze film damper bearing for rotor stability," National Aeronautics and Space Administration, Washington, DC, Tech. Rep., 1975.

[88] D. Wang, T. G. Keith, Q. Yang, and K. Vaidyanathan, "Lubrication Analysis of a Connecting-rod Bearing in a High-speed Engine. Part I: Rod and Bearing Deformation," *Tribology Transactions*, vol. 47, no. 2, pp. 280–289, 2004.

[89] H. P. Brunskill, "The Real-Time Characterisation of Dry Machine Element Contacts Using Ultrasonic Reflectometry," Ph.D. dissertation, University of Sheffield, 2013. [Online]. Available: http://etheses.whiterose.ac.uk/6494/1/H.BrunskillThesisforSubmission.pdf

[90] J. Krautkriimer, H; Krautkriimer, *Ultrasonic Testing of Materials*, 4th ed. Berlin: Springer-Verlag, 1987.

[91] A. Kumar, P. P. Pathak, and N. Dass, "A Study of Speed of Sound in Water," *Journal of Applied Physics*, 2016.

[92] R. S. Dwyer-Joyce and B. W. Drinkwater, "In situ Measurement of Contact Area and Pressure Distribution in Machine Elements," *Tribology Letters*, vol. 14, no. 1, pp. 41–52, 2003.

[93] P. Laugier and G. Haat, *Bone Quantitative Ultrasound*. Springer, 2011. [Online]. Available: https://pdfs.semanticscholar.org/dd3f/fea179afecc0a6762da70508a53b22c6b887.pdf

[94] R. L. Smith, W. N. Reynolds, and H. N. G. Wadley, "Ultrasonic attenuation and microstructure in low-carbon steels," *Metal Science*, vol. 15, no. 11-12, pp. 554–558, nov 1981. [Online]. Available: http://www.tandfonline.com/doi/full/10.1179/msc.1981.15.11-12.554

[95] M. A. Andrade, F. Buiochi, and J. C. Adamowski, "Particle Manipulation by Ultrasonic Progressive Waves," *Physics Procedia*, vol. 3, no. 1, pp. 283–288, 2010. [Online]. Available: http://dx.doi.org/10.1016/j.phpro.2010.01.038

[96] H.-R. Herzer, M. M. Becker, and E. Schneider, "The Acousto-elastic Effect and Its Use in NDE," *Handbook of Advanced Non-Destructive Evaluation*, pp. 1–17, 2018.

[97] L. Stepanova, A. Kurbatov, and E. Tenitilov, "Methods of Monitoring Longitudinal Stresses in Rails Using Acoustoelastic Effect," in *Advances in Intelligent Systems and Computing*, vol. 1115 AISC. Springer, may 2020, pp. 778–787. [Online]. Available: https://link.springer.com/chapter/10.1007/978-3-030-37916-2{_}76

[98] Chen, Mills, Dwyer-Joyce, and RS, "Direct Load Monitoring of Rolling Bearing Contacts using Ultrasonic Time of Flight," in *Proceedings of the Royal Society A: Mathematical, Physical and Engineering Sciences*, 2015, pp. 471–1364. [Online]. Available: http://eprints.whiterose.ac.uk/90534/https://doi.org/10.1098/rspa.2015.0103https://eprints.whiterose.ac.uk/

[99] B. Praher and G. Steinbichler, "Ultrasound-based measurement of liquid-layer thickness: A novel time-domain approach," *Mechanical Systems and Signal Processing*, vol. 82, pp. 166–177, jan 2017. [Online]. Available: https://linkinghub.elsevier.com/retrieve/pii/S0888327016300991

[100] P. Haines, N; Bell, J; McIntyre, "The Application of Broadband Ultrasonic Spectroscopy to the Study of Layered Media," *The Journal of the Acoustical Society of America*, vol. 6, no. 64, pp. 1645–1651, 1977.

[101] R. S. Dwyer-Joyce, P. Harper, and B. W. Drinkwater, "A Method for the Measurement of Hydrodynamic Oil Films using Ultrasonic Reflection," *Tribology Letters*, vol. 17, no. 2, pp. 337–348, 2004.

[102] T. Reddyhoff, S. Kasolang, R. S. Dwyer-Joyce, and B. W. Drinkwater, "The Phase Shift of an Ultrasonic Pulse at an Oil Layer and Determination of Film Thickness," *Proceedings of the Institution of Mechanical Engineers, Part J: Journal of Engineering Tribology*, vol. 219, no. 6, pp. 387–400, jun 2005. [Online]. Available: http://journals.sagepub.com/doi/10.1243/135065005X34044

[103] M. Yu, L. Shen, T. Mutasa, P. Dou, T. Wu, and T. Reddyhoff, "Exact analytical solution to ultrasonic interfacial reflection enabling optimal oil film thickness measurement," *Tribology International*, vol. 151, nov 2020. [Online]. Available: https://doi.org/10.1016/j.triboint.2020.106522

[104] R. Gohar and M. M. Safa, "Tribology and Dynamics of Engine and Powertrain. Fundamentals, Applications and Future Trends," in *Tribology and Dynamics of Engine and Powertrain: Fundamentals, Applications and Future Trends*, 2010, vol. 1, ch. Fluid Film, pp. 132–170.

[105] Clay Mathematics Institute, "Millennium Problems - Navier Stokes Equation," 2020. [Online]. Available: https://www.claymath.org/millennium-problems/navierstokes-equation

[106] M. Kozma, "Calculation of Oil-Film Thickness in Journal Bearings Running at Varying Rotational Speeds," *Lubricant Sciences*, vol. 14, no. 2, 2002.

[107] M. Woodard, "How to Calculate the EHL Oil Film Parameter," 2014. [Online]. Available: https://www.pumpsandsystems.com/how-calculate-ehl-oil-film-parameter

[108] B. J. Hamrock, "Fundamentals of Fluid Film Lubrication," *NASA Reference Publication 1255*, 1991. [Online]. Available: https://ntrs.nasa.gov/archive/nasa/casi.ntrs.nasa.gov/19910021217.pdf

[109] G. G. Vignolo, D. O. Barilá, and L. M. Quinzani, "Approximate Analytical Solution to Reynolds Equation for Finite Length Journal Bearings," *Tribology International*, vol. 44, no. 10, pp. 1089–1099, sep 2011.

[110] R. Z. Gong, D. Y. Li, H. J. Wang, L. Han, and D. Q. Qin, "Analytical Solution of Reynolds Equation under Dynamic Conditions," *Proceedings of the Institution of Mechanical Engineers, Part J: Journal of Engineering Tribology*, vol. 230, no. 4, pp. 416–427, 2016.

[111] T. He, X. Lu, and J. Zhu, "Mobility Method Applied to Calculate the Lubrication Properties of Bearing under Dynamic Loads," *ISRN Mechanical Engineering*, vol. 2013, pp. 1–5, 2013.

[112] R. S. Paranjpe, S. I. Tseregounis, and M. B. Viola, "Comparison between Theoretical Calculations and Oil Film Thickness Measurements using the Total Capacitance Method for Crankshaft Bearings in a Firing Engine," *Tribology Transactions*, vol. 43, no. 3, pp. 345–356, 2000.

[113] J. Raimondi, A. A. and Boyd, "A Solution for the Finite Journal Bearing and its Application to Analysis and Design," *ASLE Transactions*, vol. 1, no. 1, pp. 159–174, 1958.

[114] J. F. Booker, "Dynamically Loaded Journal Bearings: Mobility Method of Solution," *Journal of Fluids Engineering, Transactions of the ASME*, vol. 87, no. 3, pp. 537–546, 1965.

[115] K. Park, Minje; Jang Siyoul; Min, "Non-Newtonian Fluid Application of The Mobility Method in Engine Journal Bearing," *International Journal of Automotive Technology*, vol. 21, no. 5, pp. 1303–1313, 2020. [Online]. Available: http://link.springer.com/article/10.1007/s12239-012-0027-2

[116] D. Benasciutti, M. Gallina, M. G. Munteanu, and F. Flumian, "A Numerical Approach for the Analysis of Deformable Journal Bearings," *Frattura ed Integrita Strutturale*, vol. 21, pp. 37–45, 2012.

[117] A. Pasini, A. Apollonio, E. Biafora, and L. D'agostino, "Spectral Solution of Reynolds' Film Lubrication Equation for Finite Length Journal Bearing," *AIAA Propulsion and Energy 2020 Forum*, 2020.

[118] AIES Ltd, "BearingDesigner," 2021. [Online]. Available: http://www.aiesl.co.uk/BearingDesigner.html

[119] H. Kumar, S. Yadav, D. Singh, and P. Arora, *Smart Innovations, Systems and Technologies*, 2020, vol. 174.

[120] G. Grassi and P. Vecchio, "Wind Energy Prediction using a Two-Hidden Layer Neural Network," *Communications in Nonlinear Science and Numerical Simulation*, vol. 15, no. 9, pp. 2262–2266, 2010. [Online]. Available: http://dx.doi.org/10.1016/j.cnsns.2009.10.005

[121] R. A. Mufti and M. Priest, "Theoretical and Experimental Evaluation of Engine Bearing Performance," *Proceedings of the Institution of Mechanical Engineers, Part J: Journal of Engineering Tribology*, vol. 223, no. 4, pp. 629–644, 2009.

[122] N. I. of Technology, "Lecture 47 - Design Considerations," Raichur, 2016. [Online]. Available: http://link.springer.com/10.1007/978-3-319-39255-4{_}3

[123] PCS Instruments, "EHD2 Ultra Thin Film Measurement System," 2014. [Online]. Available: http://pcs-instruments.com/wp-content/uploads/2014/03/EHD2{_}Brochure.pdf

[124] B. G. R. Higginson and S. Reed, "An Optical Method of Measuring Film Thickness," *Proceedings of the Institution of Mechanical Engineers*, vol. 182, no. 7, pp. 56–58, 1967.

[125] S. R. Taplin, A. G. Podoleanu, D. J. Webb, D. A. Jackson, and S. R. Nattrass, "Applications of Low Coherence Interferometry to Dynamic Oil Film Thickness Measurement," in *Applications of Photonic Technology 2*. Springer US, 1997, pp. 863–869. [Online]. Available: https://link.springer.com/chapter/10.1007/978-1-4757-9250-8{_}130

[126] K. Nakayama, I. Morio, T. Katagiri, and Y. Okamoto, "A study for measurement of oil film thickness on engine bearing by using Laser Induced Fluorescence (LIF) method," *SAE Technical Papers*, 2003.

[127] "Chapter 11: Interferometry film thickness measurement," in *Tribology Series*, B. Jacobson, Ed. Elsevier, 1991, vol. 19, no. C, pp. 165–196. [Online]. Available: https://doi.org/10.1016/S0167-8922(08)70050-6.

[128] M. T. Fowell, C. Myant, H. A. Spikes, and A. Kadiric, "A Study of Lubricant Film Thickness in Compliant Contacts of Elastomeric Seal Materials using a Laser Induced Fluorescence Technique," *Tribology International*, vol. 80, pp. 76–89, dec 2014.

[129] N. Marx, J. Guegan, and H. A. Spikes, "Elastohydrodynamic Film Thickness of Soft EHL Contacts using Optical Interferometry," *Tribology International*, vol. 99, pp. 267–277, jul 2016.

[130] M. D. Furtuna, "Study of Film Formation in EHD Contacts Using a Novel Method Based on Electrical Capacitance," Ph.D. dissertation, Brunel University, 2011. [Online]. Available: https://core.ac.uk/download/pdf/337482.pdf

[131] Z. Cui, C. Yang, B. Sun, and H. Wang, "Liquid Film Thickness Estimation using Electrical Capacitance Tomography," *Measurement Science Review*, vol. 14, no. 1, 2014. [Online]. Available: http://www.measurement.sk/2014/Ziqiang{_}Cui.pdf

[132] J. A. Spearot and C. K. Murphy, "A Comparison of the Total Capacitance and Total Resistance Techniques for Measuring the Thickness of Journal Bearing Oil Films in an Operating Engine," in *SAE Technical Papers*. SAE International, feb 1988. [Online]. Available: https://www.sae.org/publications/technical-papers/content/880680/

[133] T. Kataoka, T. Kikuchi, and K. Ashihara, "Measurement of Oil Film Thickness in the Main Bearings of an Operating Engine using Thin-film Electrode," *SAE Technical Papers*, vol. 5, no. 1, pp. 425–433, 2011.

[134] H. Moreau, P. Maspeyrot, D. Bonneau, and J. Frène, "Comparison between Experimental Film Thickness Measurements and Elastohydrodynamic Analysis in a Connecting-rod Bearing," *Proceedings of the Institution of Mechanical Engineers, Part J: Journal of Engineering Tribology*, vol. 216, no. 4, pp. 195–208, 2002.

[135] R. R. Navthar and N. V. Halegowda, "Experimental Investigation of Oil Film Thickness for Hydrodynamic Journal Bearings," *Applied Mechanics and Materials*, vol. 110-116, pp. 2377–2382, 2012.

[136] S. Chatterton, P. V. Dang, P. Pennacchi, A. De Luca, and F. Flumian, "Experimental Evidence of a Two-Axial Groove Hydrodynamic Journal Bearing under Severe Operation Conditions," *Tribology International*, vol. 109, no. December 2016, pp. 416–427, 2017. [Online]. Available: http://dx.doi.org/10.1016/j.triboint.2017.01.014

[137] C. Giraudeau, J. Bouyer, M. Fillon, M. Hélène, and J. Beaurain, "Experimental Study of the Influence of Scratches on the Performance of a Two-Lobe Journal Bearing," *Tribology Transactions*, vol. 60, no. 5, pp. 942–955, 2017. [Online]. Available: https://doi.org/10.1080/10402004.2016.1238528

[138] J. Bouyer, M. Fillon, M. Helene, J. Beaurain, and C. Giraudeau, "Behavior of a Two-Lobe Journal Bearing with a Scratched Shaft: Comparison between Theory and Experiment," *Journal of Tribology*, vol. 141, no. 2, feb 2019.

[139] J. Bouyer, Y. Alexandre, and M. Fillon, "Experimental Investigation on the Influence of a Multi-Scratched Shaft on Hydrodynamic Journal Bearing Performance," *Tribology International*, vol. 153, p. 106543, jan 2021. [Online]. Available: https://www.sciencedirect.com/science/article/pii/S0301679X20303753

[140] S. B. Glavatskih, Uusitalo, and D. J. Spohn, "Simultaneous Monitoring of Oil Film Thickness and Temperature in Fluid Film Bearings," *Tribology International*, vol. 34, no. 12, pp. 853–857, 2001.

[141] B. I. Oladapo, V. A. Balogun, A. O. Adeoye, C. O. Ijagbemi, A. S. Oluwole, I. A. Daniyan, A. Esoso Aghor, and A. P. Simeon, "Model Design and Simulation of Automatic Sorting Machine using Proximity Sensor," *Engineering Science and Technology, an International Journal*, vol. 19, no. 3, pp. 1452–1456, 2016. [Online]. Available: http://dx.doi.org/10.1016/j.jestch.2016.04.007

[142] H. G. Tattersall, "The Ultrasonic Pulse-echo Technique as Applied to Adhesion Testing," *Journal of Physics D: Applied Physics*, vol. 6, no. 7, 1973.

[143] P. Harper, B. Hollingsworth, R. Dwyer-Joyce, and B. Drinkwater, "Journal bearing oil film measurement using ultrasonic reflection," in *Proceedings of the 29th Leeds-Lyon Symposium on Tribology*, vol. 41, 2003, pp. 469–476. [Online]. Available: http://www.sciencedirect.com/science/article/pii/S016789220380161X

[144] S. Kasolang and R. S. Dwyer-Joyce, "Observations of Film Thickness Profile and Cavitation Around a Journal Bearing Circumference," *Tribology Transactions*, vol. 51, no. 2, pp. 231–245, mar 2008. [Online]. Available: http://www.tandfonline.com/doi/abs/10.1080/10402000801947717

[145] T. Reddyhoff, R. S. Dwyer-Joyce, J. Zhang, and B. W. Drinkwater, "Auto-calibration of Ultrasonic Lubricant-film Thickness Measurements," *Measurement Science and Technology*, vol. 19, no. 4, 2008.

[146] T. Geng, Q. Meng, Z. Chen, and P. Wang, "Ultrasonic monitoring of lubricating conditions of hydrodynamic bearing," *Journal of Physics: Conference Series*, vol. 305, no. 1, p. 012065, jul 2011. [Online]. Available: https://iopscience.iop.org/article/10.1088/1742-6596/305/1/012065

[147] W. Ouyang, Z. Zhou, Y. Jin, X. Yan, and Y. Liu, "Ultrasonic Measurement of Lubricant Film Thickness Distribution of Journal Bearing," *Review of Scientific Instruments*, vol. 065111, no. March, 2020. [Online]. Available: https://doi.org/10.1063/5.0007481

[148] W. Hu, "Experimental search for High Curie Temperature Piezoelectric Ceramics with Combinatorial Approaches," 2011. [Online]. Available: http://lib.dr.iastate.edu/etd/10246/

[149] H. Xing, P. Huang, C. Zhang, D. Li, Y. Zhang, W. Guo, G. Zhao, and Q. Liao, "Two New High Curie Temperature Piezoelectric Ceramics," *Materials Letters*, vol. 160, pp. 38–40, 2015. [Online]. Available: http://dx.doi.org/10.1016/j.matlet.2015.07.073

[150] T. B. Xu, "Energy Harvesting using Piezoelectric Materials in Aerospace Structures," in *Structural Health Monitoring (SHM) in Aerospace Structures*. Elsevier Inc., mar 2016, pp. 175–212.

[151] University of Cambridge, "Effect of Temperature on the Dielectric Constant," 2004. [Online]. Available: https://www.doitpoms.ac.uk/tlplib/dielectrics/temperature.php

[152] Del Piezo, "Material Specification Sheet," West Palm Beach, 2017. [Online]. Available: https://delpiezo.com/yahoo{_}site{_}admin/assets/docs/Material{_}Specification{_}Sheet.254613.pdf

[153] Sensor Technology Ltd., "Piezoelectric Fundamentals," 2020. [Online]. Available: https://sensortechcanada.com/technical-notes/piezoelectric-fundamentals/

[154] H. N. Shekhani and K. Uchino, "Evaluation of the Mechanical Quality Factor under High Power Conditions in Piezoelectric Ceramics from Electrical Power," *Journal of the European Ceramic Society*, vol. 35, no. 2, pp. 541–544, 2015. [Online]. Available: http://dx.doi.org/10.1016/j.jeurceramsoc.2014.08.038

[155] PI Ceramic GmbH, "Piezoceramic Materials," 2020. [Online]. Available: https://www.piceramic.com/en/products/piezoelectric-materials/

[156] C. M. Sayers and C. E. Tait, "Ultrasonic Properties of Transducer Backings," *Ultrasonics*, vol. 22, no. 2, pp. 57–60, 1984.

[157] Boston Piezo-Optics Inc., "Alumina Wear Plates," 2020. [Online]. Available: https://www.bostonpiezooptics.com/alumina-wear-plates

[158] M. M. Schirru, R. S. Mills, O. Smith, R. S. Dwyer-Joyce, and &. M. Sutton, "In situ Measurement of Journal Bearing Lubricant Viscosity by Means of a Novel Ultrasonic Measurement Technique Using Matching Layer," *Tribology Transactions*, vol. 61, no. 1, pp. 157–167, 2018. [Online]. Available: https://doi.org/10.1080/10402004.2017.1285970

[159] J. Zhou, X. Guo, C. Du, and X. Wang, "Ultrasound Beam Steering using a Fiber Optic Ultrasound Phased Array," *Optics Letters*, vol. 44, no. 21, p. 5390, 2019.

[160] T. Stratoudaki, M. Clark, and P. Wilcox, "Laser Induced Ultrasonic Phased Array using Full Matrix Capture Data Acquisition and Total Focusing Method," *54th Annual British Conference of Non-Destructive Testing, NDT 2015*, vol. 24, no. 19, pp. 351–357, 2015.

[161] Tribosonics, "Products & Systems," 2020. [Online]. Available: https://www.tribosonics.com/products-systems/

[162] Micro-Measurements, "Strain Gage Adhesive Datasheet," Tech. Rep., 2017. [Online]. Available: http://www.vishaypg.com/docs/11010/bond200.pdf

[163] ——, "Strain Gage Adhesive for Stress Analysis and Transducer Applications," 2017. [Online]. Available: http://www.vishaypg.com/docs/11013/bond610.pdf

[164] M. H. Amini, "Design and Manufacture of an Ultrasonic Transducer for Long-term High Temperature Operation," Ph.D. dissertation, University of Toronto, 2016.

[165] C. Bosyj, N. Bhadwal, T. Coyle, and A. Sinclair, "Brazing Strategies for High Temperature Ultrasonic Transducers Based on LiNbO3 Piezoelectric Elements," *Instruments*, vol. 3, no. 1, p. 2, 2018.

[166] C. Oakley, J. Mueller, D. Dietz, and J. Kuhnke, "A Minimally Invasive Ultrasound Probe using Non-coax Cabling," *Proceedings of the IEEE Ultrasonics Symposium*, vol. 2, pp. 1011–1016, 2001.

[167] Sole Engineering, "What is The Significance Of Coaxial Cable?" 2020. [Online]. Available: http://www.soleengineering.com.my/what-is-the-significance-of-coaxial-cable/

[168] Newark, "Ribbon Cable, Round Conductor Flat, Unshielded," 2020. [Online]. Available: https://www.newark.com/3m/3365-40/flat-cable-40-conductor-100ft/dp/03F5912{\#}

[169] Farnell, "Pro Power Multicore Cable, Screened, 15 Core," 2020. [Online]. Available: https://uk.farnell.com/pro-power/7001249/cable-def-7-2-15c-15core-25m/dp/1190268

[170] Optel, "Ultrasonic Multiplexer OPMUX v12.0 Manual," pp. 1–30, 2013.

[171] S. W. Smith, *The Scientist and Engineer's Guide to Digital Signal Processing*. California Technical Pub., 1997.

[172] H. Brunskill, "Friction and Wear Analysis of the Micro-Oil Extralube ZX1." Ph.D. dissertation, University of Sheffield, 2008.

[173] Olympus IMS, "Pulser and Receiver Operation ," 2021. [Online]. Available: https://www.olympus-ims.com/en/ndt-tutorials/flaw-detection/pulser-and-receiver/

[174] A. Hunter, "Ultrasonic Measurements of the Strip Thickness, Lubricant Film Thickness, Roll Deflection and Roll Stress in the Roll Bite in the Cold Rolling of Steel," Ph.D. dissertation, University of Sheffield, 2018. [Online]. Available: http://etheses.whiterose.ac.uk/22009/

[175] H. Jain, E. G. Tarpara, and V. H. Patankar, "Design and Development of Ultrasonic Bipolar Square-wave Pulser for Non-destructive Testing of Concrete Structures," *Review of Scientific Instruments*, vol. 91, no. 9, p. 094704, sep 2020. [Online]. Available: http://aip.scitation.org/doi/10.1063/5.0006782

[176] Ness Engineering, "RMS-Avg Values of Waveforms," 2014. [Online]. Available: http://www.nessengr.com/techdata/rms/rms.html

[177] A. W. Doerry, "Generating Precision Nonlinear FM Chirp Waveforms," Sandia National Laboratories, Albuquerque, Tech. Rep. September, 2006.

[178] J. Kanja, R. Mills, X. Li, H. Brunskill, A. K. Hunter, and R. S. Dwyer-Joyce, "Non-contact Measurement of the Thickness of a Surface Film using a Superimposed Ultrasonic Standing Wave," *Ultrasonics*, vol. 110, p. 106291, feb 2021.

[179] S. D. Pye, S. R. Wild, and W. N. Mcdicken, "Adaptive Time Gain Compensation for Ultrasonic Imaging," *Ultrasound in Medicine and Biology*, vol. 18, no. 2, pp. 205–212, 1992.

[180] S. Sahu, M. Dubey, M. I. Khan, J. Kumar, and W. S. Email, "Comparative Evaluation of Filters for Liver Ultrasound Image Enhancement," vol. 2, no. 1, pp. 161–165, 2013.

[181] D. M. Boore and C. A. Goulet, "The Effect of Sampling Rate and Anti-aliasing Filters on High-Frequency Response Spectra," vol. 12, pp. 203–216, 2014.

[182] R. A. Mucci, "A Comparison of Efficient Beamforming Algorithms," *IEEE Transactions on Acoustics, Speech, and Signal Processing*, vol. 32, no. 3, pp. 548–558, 1984.

[183] J. Smith, "Fourier Theorems for the DFT," in *Mathematics of the Discrete Fourier Transform (DFT) with Audio Applications*, 2nd ed., 2007. [Online]. Available: http://ccrma.stanford.edu/{~}jos/mdft/Fourier{_}Theorems{_}DFT.html

[184] T. Plantegenet, M. Arghir, M. A. Hassini, and P. Jolly, "The Thermal Unbalance Effect Induced by a Journal Bearing in Rigid and Flexible Rotors: Experimental Analysis," *Tribology Transactions*, vol. 63, no. 1, pp. 52–67, 2020. [Online]. Available: https://doi.org/10.1080/10402004.2019.1658836

[185] M. Moazami-goudarzi, "Failure Analysis of GE-F9 Gas Turbine Journal Bearings," *Iranian Journal of Science and Technology Transaction B: Engineering*, no. August, 2015.

[186] C. Soares, "Gas Turbines in Simple Cycle & Combinded Cycle Applications," National Energy Technology Laboratory, Tech. Rep., 1998. [Online]. Available: https://www.netl.doe.gov/sites/default/files/gas-turbine-handbook/1-1.pdf

[187] O. Smith and M. Sutton, "Fuel Economy in Heavy Duty Diesel Engines . Part 1 : Measurement of Oil Film Thickness on an Operating Engine," *IMechE Part J: Engineering Tribolog*, vol. 225, pp. 313–324, 2011.

[188] J. Sun, B. Li, S. Zhu, E. Miao, H. Wang, X. Zhao, and Q. Teng, "Lubrication Performance of Connecting - Rod and Main Bearing in Different Engine Operating Conditions," *Chinese Journal of Mechanical Engineering*, 2019. [Online]. Available: https://doi.org/10.1186/s10033-019-0335-9

[189] T. He, D. Zou, X. Lu, Y. Guo, Z. Wang, and W. Li, "Mixed-lubrication Analysis of Marine Stern Tube Bearing considering Bending Deformation of Stern Shaft and Cavitation," *Tribology International*, vol. 73, pp. 108–116, may 2014. [Online]. Available: http://dx.doi.org/10.1016/j.triboint.2014.01.013

[190] Labcon, "High Temperature High Shear Viscometer ASTM-D4683," 2018. [Online]. Available: http://labcon.in/products/high-temperature-high-shear-viscometer-astm-d4683/

[191] Anton Paar, "Lovis 2000 M/ME," 2020. [Online]. Available: https://www.anton-paar.com/uk-en/products/details/rolling-ball-viscometer-lovis-2000-mme/

[192] RheoSense, "m-VROC Viscometer," 2020. [Online]. Available: https://www.rheosense.com/products/viscometers/m-vroc

[193] Anton Paar, "How to Measure Viscosity," 2020. [Online]. Available: https://wiki.anton-paar.com/uk-en/how-to-measure-viscosity/

[194] Brookfield Engineering, "DVNext Cone/Plate Rheometer," 2019. [Online]. Available: https://www.brookfieldengineering.com/products/viscometers/laboratory-viscometers/dvnext-cone-plate-rheometer

[195] M. Deligant, P. Podevin, and G. Descombes, "CFD Model for Turbocharger Journal Bearing Performances," in *Applied Thermal Engineering*, vol. 31, no. 5. Pergamon, apr 2011, pp. 811–819.

[196] J. Sun, B. Li, S. Zhu, E. Miao, H. Wang, X. Zhao, and Q. Teng, "Lubrication Performance of Connecting-Rod and Main Bearing in Different Engine Operating Conditions," *Chinese Journal of Mechanical Engineering (English Edition)*, vol. 32, no. 1, p. 23, dec 2019. [Online]. Available: https://cjme.springeropen.com/articles/10.1186/s10033-019-0335-9

[197] W. J. Chen, "Rotordynamics and Bearing Design of Turbochargers," in *Mechanical Systems and Signal Processing*, vol. 29. Academic Press, may 2012, pp. 77–89.

[198] E. Sjöberg, "Friction Characterization of Turbocharger Bearings," *Kth*, 2013. [Online]. Available: http://www.diva-portal.org/smash/get/diva2:644848/FULLTEXT01.pdfMar

[199] Y. G. Kim and U. K. Kim, "Design and Analysis of the Propulsion Shafting System in a Ship with Single Stern Tube Bearing," *Journal of Marine Science and Technology (Japan)*, vol. 25, no. 2, pp. 536–548, 2020. [Online]. Available: https://doi.org/10.1007/s00773-019-00659-8

[200] C. Alemany, A. M. González, L. Pardo, B. Jiménez, F. Carmona, and J. Mendiofa, "Automatic Determination of Complex Constants of Piezoelectric Lossy Materials in the Radial Mode," *Journal of Physics D: Applied Physics*, vol. 28, no. 5, pp. 945–956, 1995.

[201] Meggitt A/S, "Pz27 (Navy II) Soft Relaxor Type PZT," Tech. Rep., 2017. [Online]. Available: https://www.meggittferroperm.com/wp-content/uploads/2017/10/MSSDK{_}PZ27{_}Datasheet-201809.pdf

[202] D. Knezevic and Z. Milovanovic, "Analysis of Changes of Bulk Modulus of Mineral Oil – Effects on the Dynamic Behavior of Hydraulic Actuators," in *International Conference on Tribology – Serbiatrib*, no. April 2011, 2015, pp. 4–5.

[203] H. H. Dashti and M. R. Riazi, "Acoustic Velocities in Petroleum Fluids: Measurement and Prediction," 2014. [Online]. Available: http://dx.doi.org/10.1016/j.petrol.2014.10.013

[204] S. Loranger, C. Bassett, J. P. Cole, B. Boyle, and T. C. Weber, "Acoustically Relevant Properties of Four Crude Oils at Oceanographic Temperatures and Pressures," *Citation: The Journal of the Acoustical Society of America*, vol. 144, p. 2926, 2018. [Online]. Available: https://doi.org/10.1121/1.5078606

[205] K. Jablonka, R. Glovnea, and J. Bongaerts, "Quantitative measurements of film thickness in a radially loaded deep-groove ball bearing," *Tribology International*, vol. 119, no. 1, pp. 239–249, 2018.

[206] J. D. N. Cheeke, *Fundamentals and Applications of Ultrasonic Waves*, 2nd ed. Boca Raton: CRC Press, 2017.

[207] T. Reddyhoff, "Ultrasonic Measurement Techniques for Lubricant Films," Ph.D. dissertation, University of Sheffield, 2006.

[208] B. W. Drinkwater, R. S. Dwyer-Joyce, and P. Cawley, "A study of the interaction between ultrasound and a partially contacting solid-solid interface," *Proceedings of the Royal Society A: Mathematical, Physical and Engineering Sciences*, vol. 452, no. 1955, pp. 2613–2628, 1996.

[209] M. Bruneau, *Fundamentals of Acoustics*. Wiley, 2013.

[210] P. Dou, T. Wu, and Z. Peng, "A Time-domain Ultrasonic Approach for Oil Film Thickness Measurement with Improved Resolution and Range," *Measurement Science and Technology*, vol. 31, no. 7, 2020.

[211] Y. Liu, Z. Han, and H. Cong, "Effects of Sliding Velocity and Normal Load on the Tribological Behavior of a Nanocrystalline Al Based Composite," *Wear*, vol. 268, no. 7-8, pp. 976–983, 2010. [Online]. Available: http://dx.doi.org/10.1016/j.wear.2009.12.027

[212] D. Sfyris and A. Chasalevris, "An Exact Analytical Solution of the Reynolds Equation for the Finite Journal Bearing," *Tribology International*, no. May, 2012.

[213] H. Yang, Y. Zhang, and L. Lu, "Numerical Investigation of After Stern Tube Bearing during Ship Turning Maneuver," *Journal of Marine Science and Technology (Japan)*, vol. 25, no. 3, pp. 707–717, 2020. [Online]. Available: https://doi.org/10.1007/s00773-019-00675-8

[214] Z. S. Zhang, X. D. Dai, and Y. B. Xie, "Thermoelastohydrodynamic behavior of misaligned plain journal bearings," *Proceedings of the Institution of Mechanical Engineers, Part C: Journal of Mechanical Engineering Science*, vol. 227, no. 11, pp. 2582–2599, 2013.

[215] T. Zapletal, P. Sperka, I. Krupka, and M. Hartl, "The Effect of Surface Roughness on Friction and Film Thickness in Transition from EHL to Mixed Lubrication," *Tribology International*, vol. 128, no. August, pp. 356–364, 2018.

[216] Y. Yan, "Tribology and Tribo-corrosion Testing and Analysis of Metallic Biomaterials," *Metals for Biomedical Devices*, pp. 178–201, 2010.

[217] M. Bauccio, *ASM Metals Reference Book*, 3rd ed. ASM International, 1993.

[218] Copper Alloys Ltd, "C95400 - Nickel Aluminium Bronze," 2021. [Online]. Available: https://www.copperalloys.net/alloys/c95400

[219] Azo Materials, "Aluminium Bronze UNS C95400 – Copper Alloy," sep 2012. [Online]. Available: https://www.azom.com/article.aspx?ArticleID=6291

[220] R. J. Urick, "A Sound Velocity Method for Determining the Compressibility of Finely Divided Substances," *Journal of Applied Physics*, vol. 18, no. 11, pp. 983–987, 1947.

[221] S. Kasolang, M. A. Ahmad, and R. S. Dwyer Joyce, "Measurement of Circumferential Viscosity Profile in Stationary Journal Bearing by Shear Ultrasonic Reflection," *Tribology International*, vol. 44, no. 11, pp. 1264–1270, 2011. [Online]. Available: http://dx.doi.org/10.1016/j.triboint.2011.04.014

[222] M. M. Schirru and R. S. Dwyer-Joyce, "A Model for the Reflection of Shear Ultrasonic Waves at a Thin Liquid Film and its Application to Viscometry in a Journal Bearing," *Proceedings of the Institution of Mechanical Engineers, Part J: Journal of Engineering Tribology*, vol. 230, no. 6, pp. 667–679, 2016.

[223] TEC Motors Ltd, "Size 90 Worm Gearbox 10 80B5," 2021. [Online]. Available: https://tecmotors.co.uk/products/gearboxes/tec-gearboxes/fcndk-worm-gearboxes/fcndk/size-90-worm-gearbox-10-80b5/

[224] ——, "7.5kw, 2 pole, Foot and Flange Mounted Motor B35 IE2," 2021. [Online]. Available: https://tecmotors.co.uk/products/motors/three-phase/aluminium-motors/ms2/7-5kw-2-pole-foot-and-flange-mounted-motor-b35-ie2/

[225] G. Kalghatgi, "Is it Really the End of Internal Combustion Engines and Petroleum in Transport?" *Applied Energy*, vol. 225, no. May, pp. 965–974, 2018. [Online]. Available: https://doi.org/10.1016/j.apenergy.2018.05.076

[226] F. Leach, G. Kalghatgi, R. Stone, and P. Miles, "The Scope for Improving the Efficiency and Environmental Impact of Internal Combustion Engines," *Transportation Engineering*, vol. 1, no. May, p. 100005, 2020.

[227] A. Kasiri, "Hydrodynamic Plain Bearings for the Main Bearing Arrangement of a 6 MW Offshore Wind Turbine," in *Conference for Wind Power Drives*, Aachen, 2019, pp. 469–482.

[228] T. Schröder, G. Jacobs, A. Rolink, and D. Bosse, ""flexPad" - Innovative Conical Sliding Bearing for the Main Shaft of Wind Turbines," *Journal of Physics: Conference Series*, vol. 1222, no. 1, 2019.

APPENDIX A. Publications

Beamish, S., Li, X., Brunskill, H., Hunter, A., & Dwyer-Joyce, R. (2020). Circumferential film thickness measurement in journal bearings via the ultrasonic technique. *Tribology International*, 148(February), 106295. https://doi.org/10.1016/j.triboint.2020.106295

APPENDIX B. Bearing Assembly FE Analysis

The purpose of this study is to determine the expected mechanical response of the test bearing in the journal rig under the range of loads expected during testing. These loads range from 2 kN to 25 kN. Von Mises stress, total deformation and directional deformation have been investigated.

Problem Setup

Figure 11.4 displays the 3D geometry used in this investigation. Note that the front-facing side plate has been hidden in the results to allow the bearing surface to be viewed more clearly. A bearing load was applied to the top bearing and a cylindrical support fixture applied to the cylinder hook. EN24 Steel material properties were used in this study.

The load contact area was calculated using Hertzian contact mechanics. The contact area for each case is shown in Table 11.1.

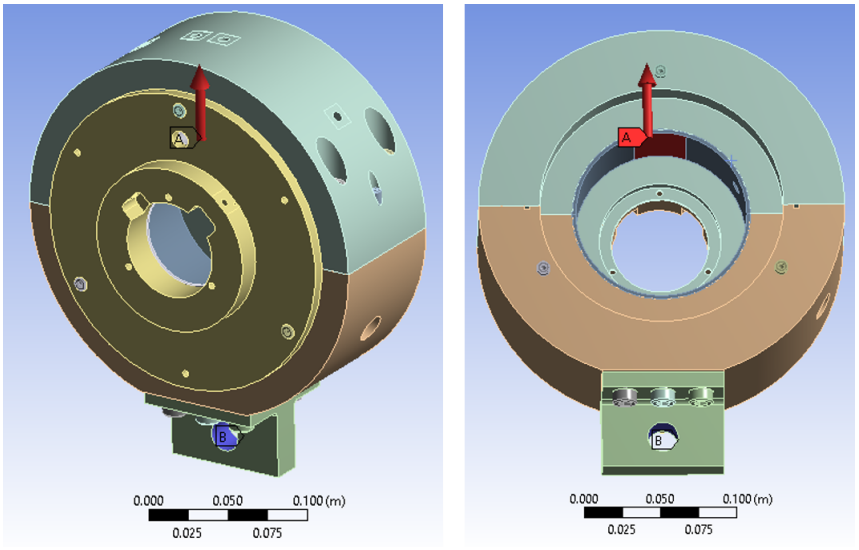

Figure 11.4: 3D geometry of bearing assembly for finite element analysis.

Table 11.1: Contact length and angle for each load case.

Load, kN	Contact Length, mm	Contact angle °
2	10.1	5.2
10	22.7	11.4
25	35.8	17.7

Stress Analysis

The purpose of this stress analysis was to determine the structural strength of the system and confirm that it can withstand the range of applied loads during testing. Simulations with applied loads of 2 kN and 25 kN loads are shown in Figure 11.5.

Deformation Analysis

As with the stress analysis, the deformation study was performed from 2 kN to 25 kN. Both total deformation and directional deformation were investigated. Directional deformation is measured on the axial plane perpendicular to the direction of loading. The directional deformation study aims to highlight the extent at which the bearing is "squeezed" by the applied load, increasing ovality. Total deformation results for 2 kN and 25 kN applied loads are shown in Figure 11.6. Directional deformation results for 2 kN and 25 kN applied loads are shown in Figure 11.7.

Note that the point of zero deformation is at the cylinder hook. As such, deformation in the bearing may be calculated by subtracting the value at the point of interest from the maximum deformation. The following results display the deformation at the top of the bearing and at 53° (the highest minimum film thickness angle expected during testing).

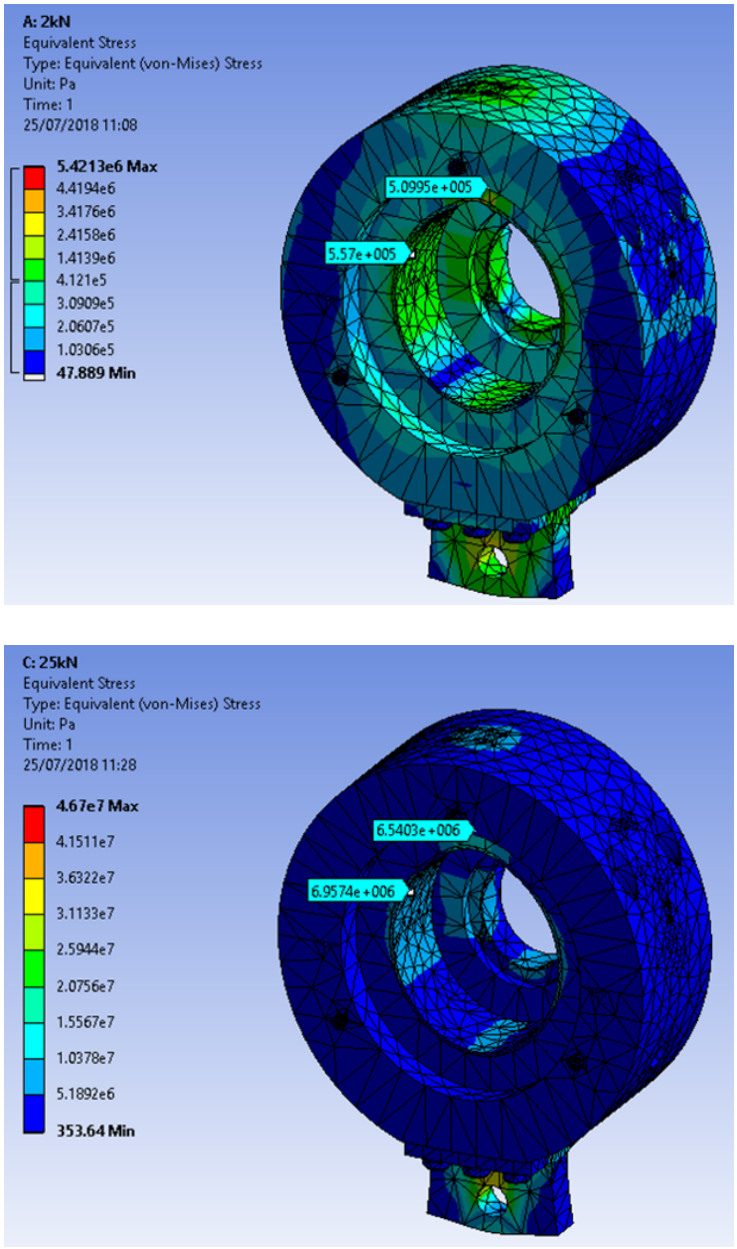

Figure 11.5: Von Mises stress with applied load of 2 kN, top and 25 kN, bottom.

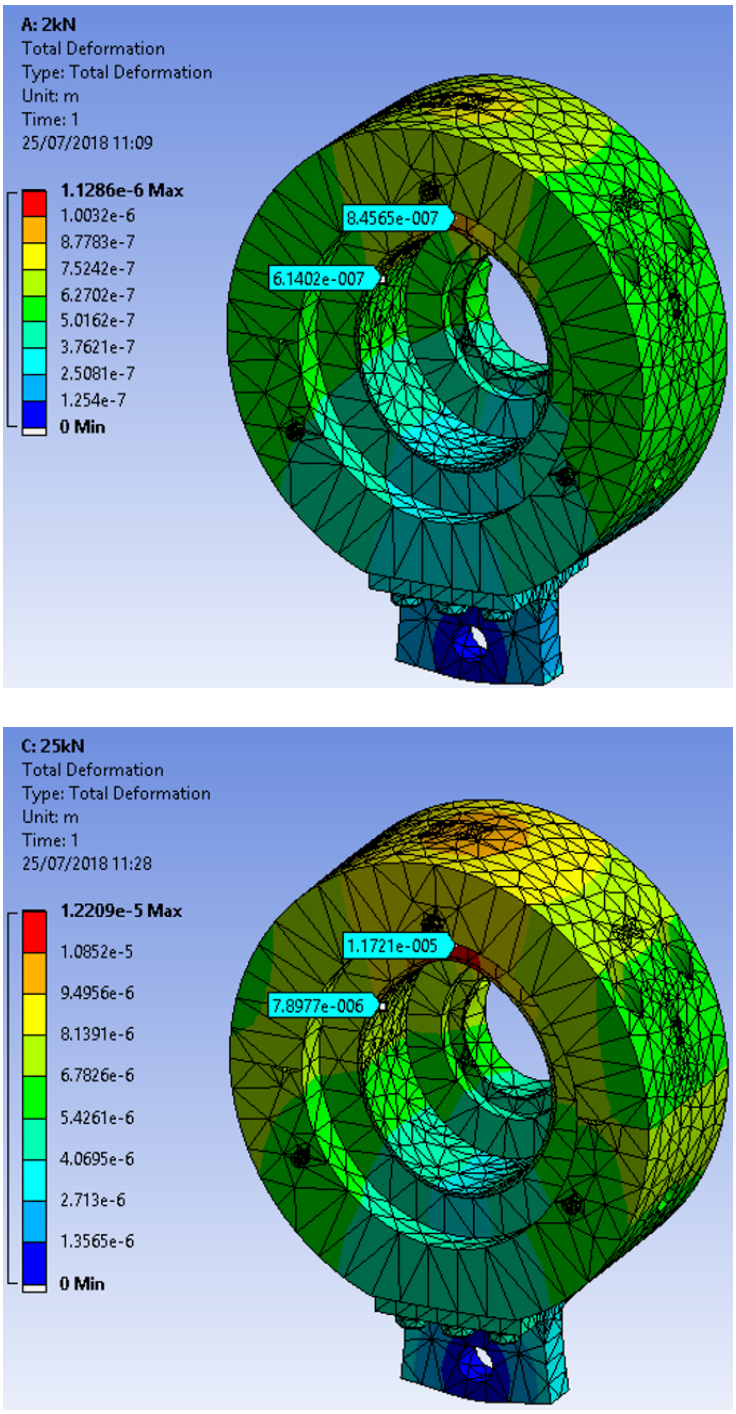

Figure 11.6: Total deformation with applied load of 2 kN, top and 25 kN, bottom.

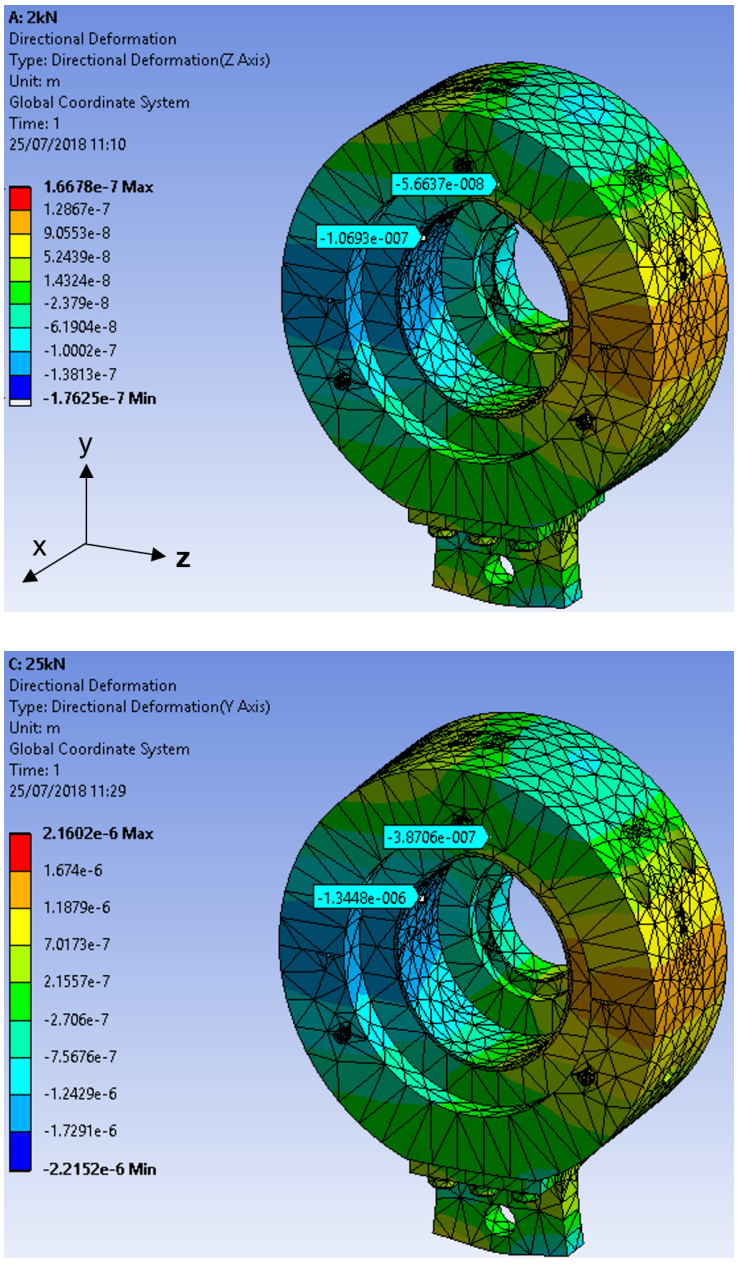

Figure 11.7: Directional deformation with applied load of 2 kN, top and 25 kN, bottom.

Bearing FE Analysis Conclusions

This FEA study indicates that the maximum stress expected during testing is 51 MPa. This is far lower than the yield stress of the material (750 MPa) and as such no plastic deformation or failure would be expected.

As designed, maximum stress occurs in the cylinder hook for all cases. As such, if failure was to occur, for example due to unintentional overloading, the system will fail at this point rather than at more critical components such as the bushes. However, the load required to cause such failure far exceeds the loading capabilities of the system.

The total and directional deformation is greatly dependent on bearing position. For all cases minimum deformation occurs near TDC, close to where minimum film thickness would be expected, as it is supported by the bearing-shaft interface. The maximum deflection on the bearing surface is 12 μm at 25 kN, however the maximum deformation within the range of minimum OFT is approximately 8 μm at 25 kN. Deformation of this magnitude may be considered reasonable.

Linkage FE Analysis

The linkage allows the bearing assembly to move freely when loaded. This is more representative of real journal bearing systems compared to rigs which fully constrain both shaft and bearing.

A study was performed to evaluate the strength of the linkage design shows the stress and deformation experienced by the linkage system when 50 kN is applied, which is twice the magnitude of the maximum applied load during testing. Note that the deformation output image is exaggerated for clarity.

It was found that for this case the maximum von Mises stress was 102.1 MPa, less than 50% of the material's yield strength and as such the design was deemed acceptable.

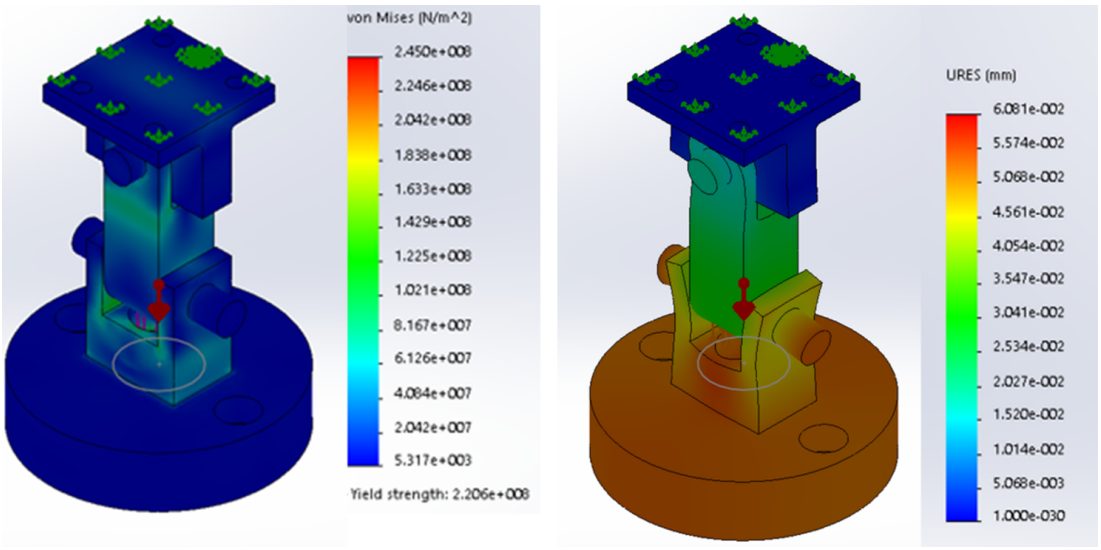

Figure 11.8: Finite element analysis of linkage with 50 kN applied load. Von Mises stress output, left. Deformation output, right.

APPENDIX C. Static Loading Rig Key Machine Drawings

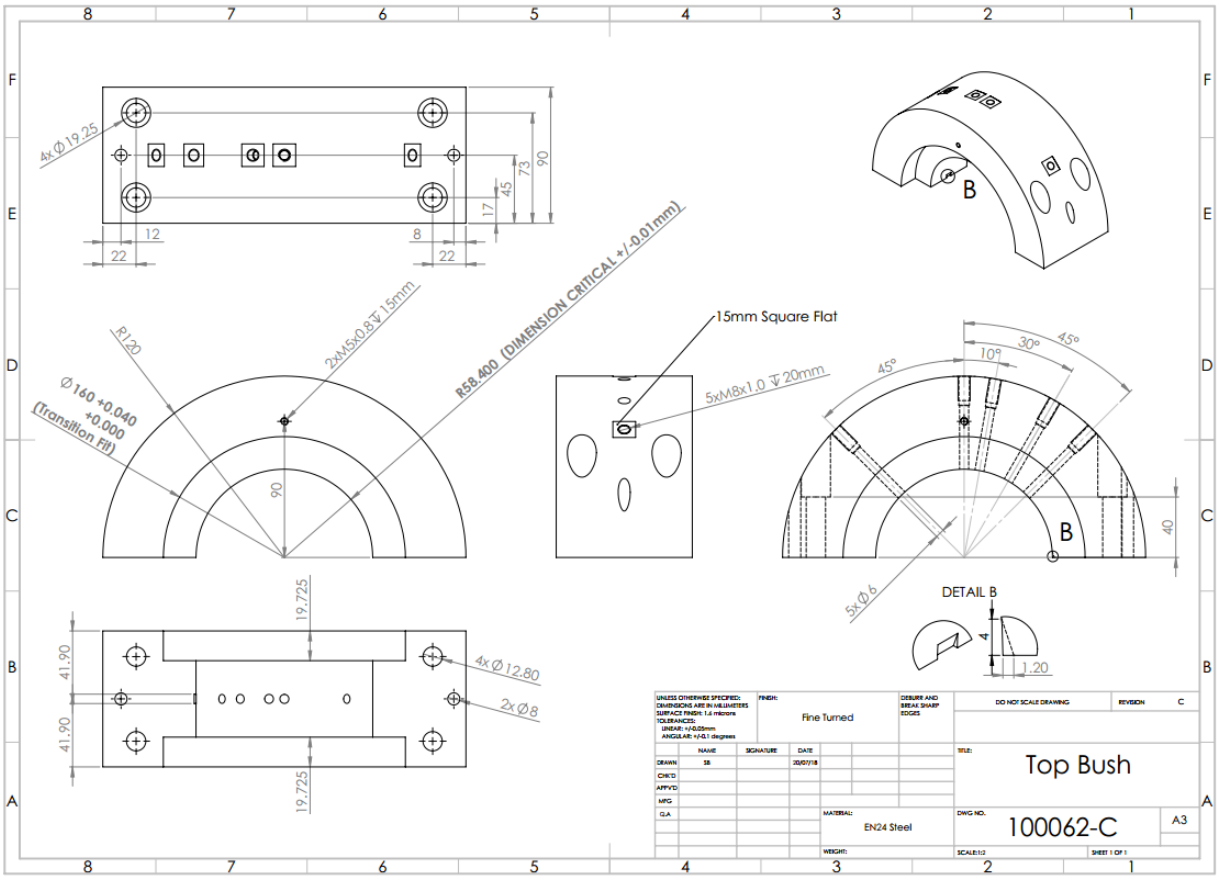

Figure 11.9: Machine drawing of bearing assembly top bush.

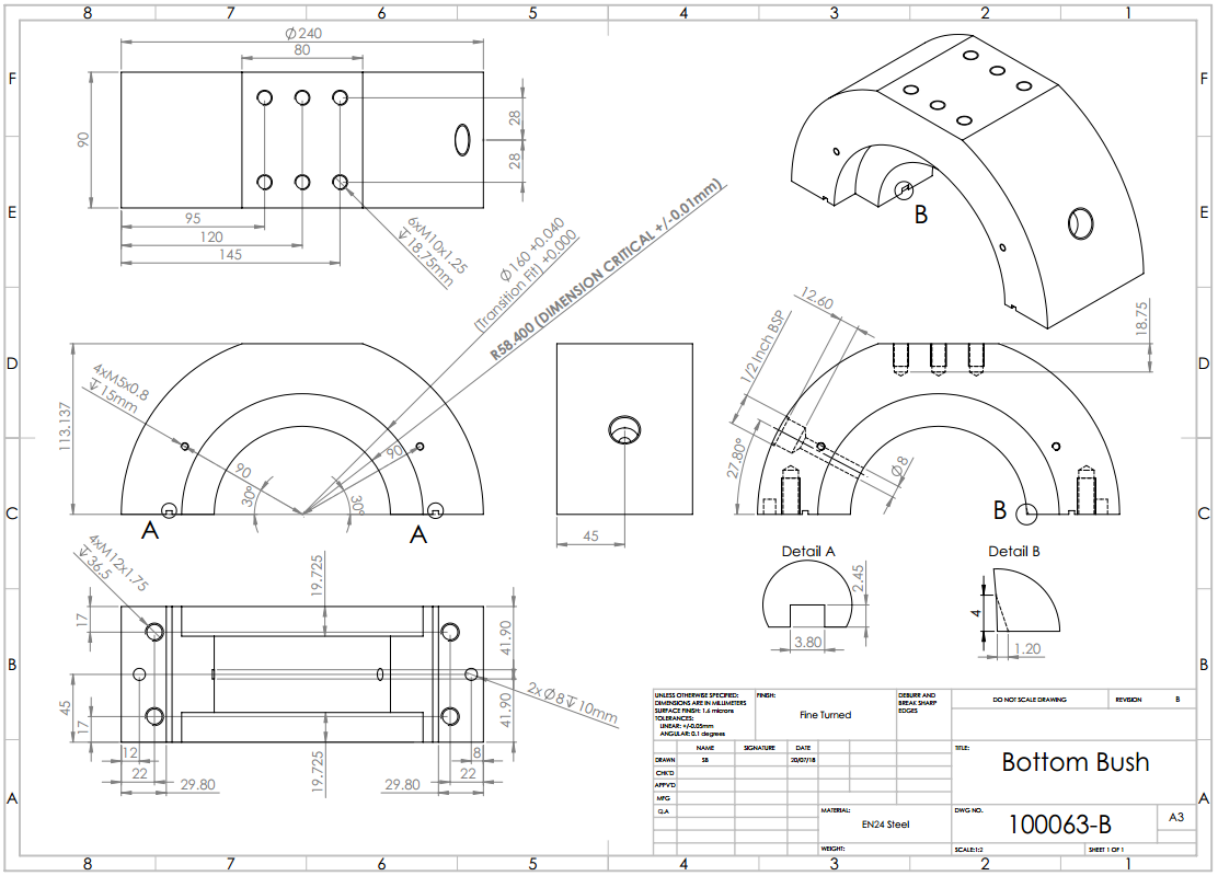

Figure 11.10: Machine drawing of bearing assembly bottom bush.

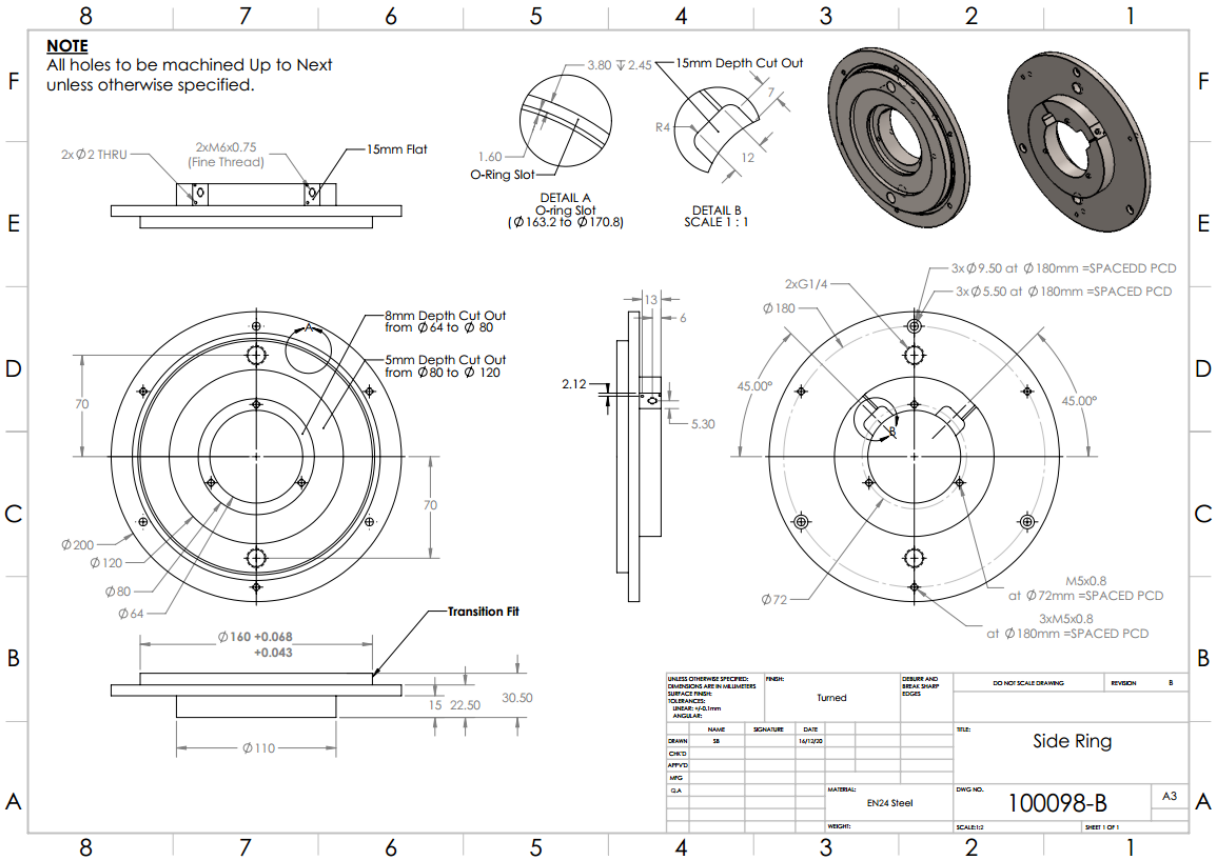

Figure 11.11: Machine drawing of bearing assembly side ring.

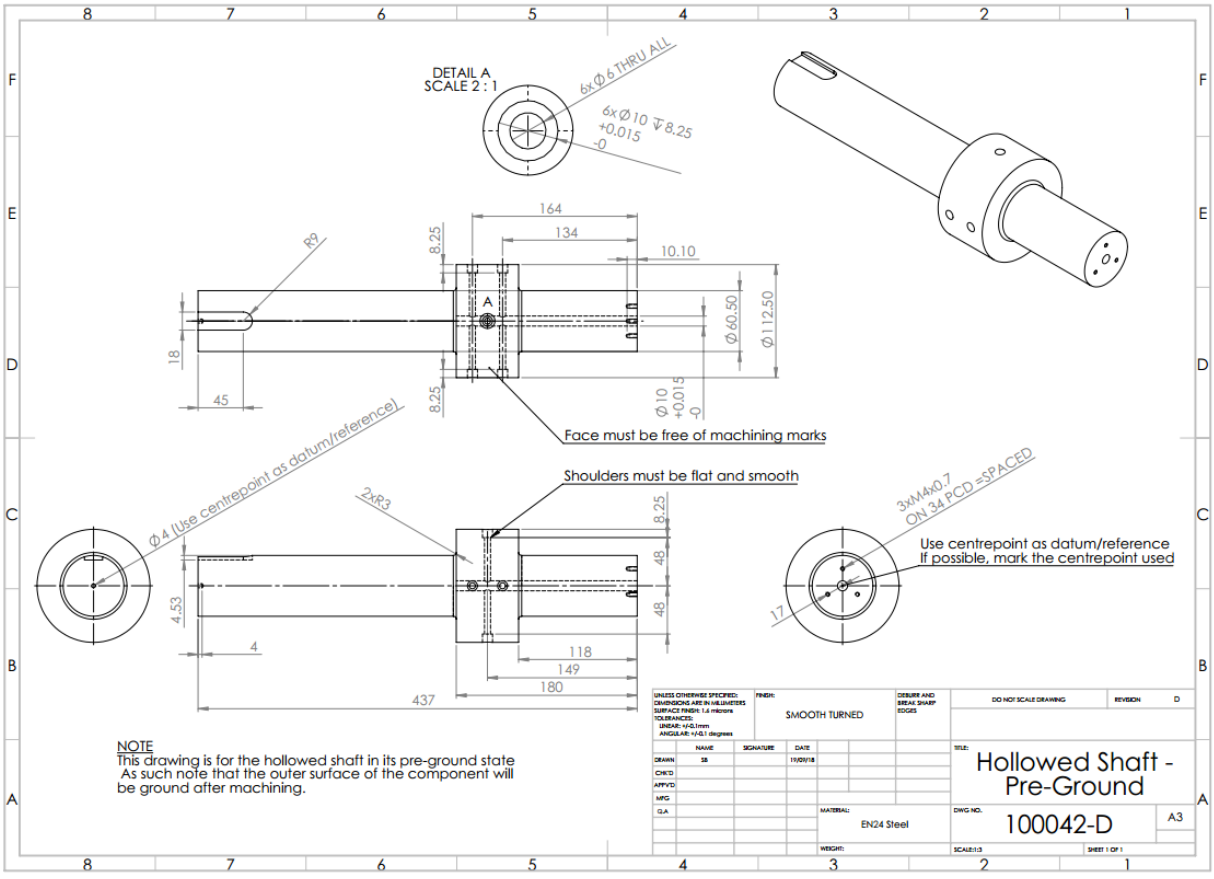

Figure 11.12: Machine drawing of shaft, pre-ground.

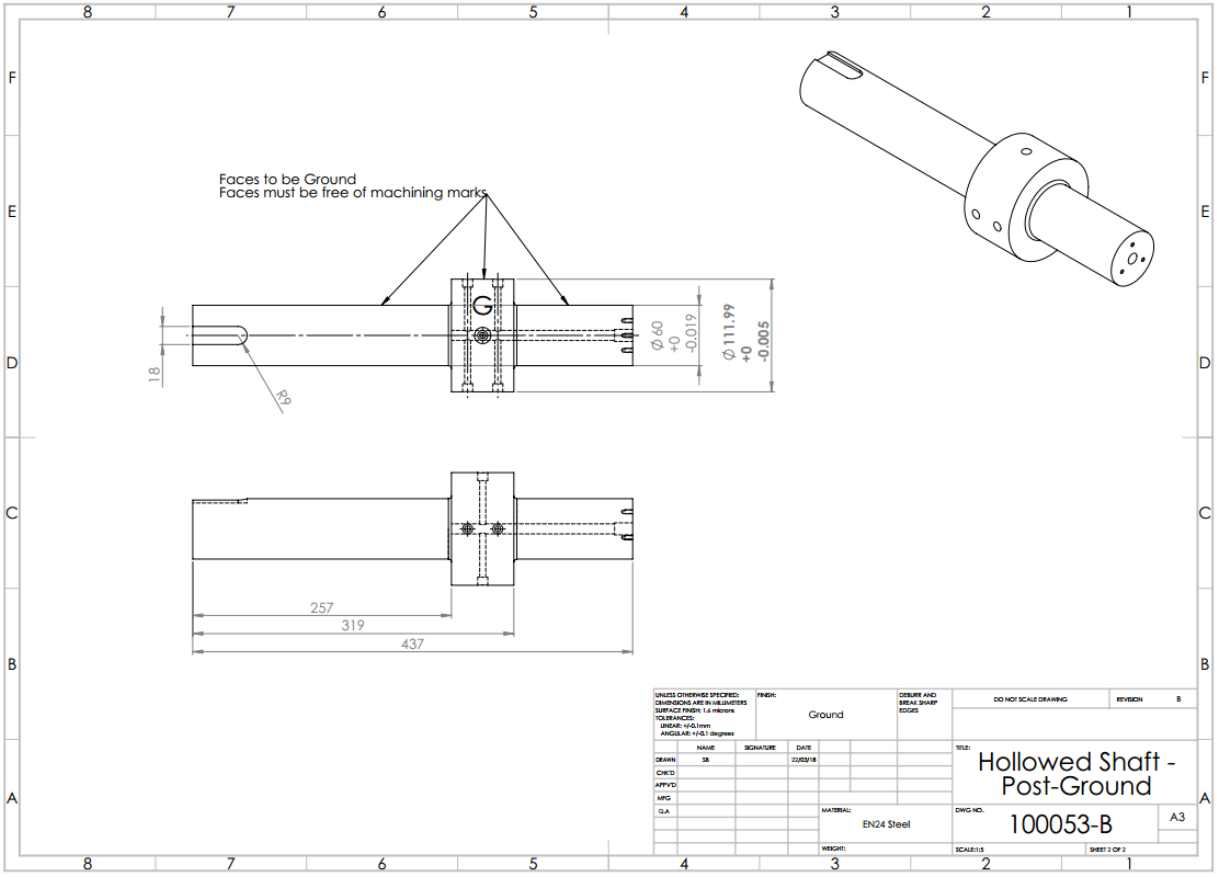

Figure 11.13: Machine drawing of shaft, post-ground.

APPENDIX D. Calculating Temperature & Pressure Relation to Density

The following is a step by step procedure used to calculate density as a function of temperature and pressure for the lubricant discussed in Section 7.1.3.

The bulk modulus of a liquid can be described mathematically by the following two equations:

$$B = \rho \frac{dp}{d\rho} \tag{11.1}$$

$$B = \rho c^2 \tag{11.2}$$

These are then equated:

$$\rho \frac{dp}{d\rho} = \rho c^2 \tag{11.3}$$

Note that the density terms cancel out. The equation is then rearranged and both sides integrated:

$$\int 1 dp = \int \frac{1}{c^2} dp \tag{11.4}$$

In Section 7.1.1 it was found that acoustic velocity in the lubricant under constant pressure can be expressed as:

$$c(T = 20°C, p) = 4.13 \times 10^{-6} p + 1.49 \times 10^3 \tag{11.5}$$

Substituting Equation 11.5 into Equation 11.4 gives:

$$\rho(T = 20°C, p) = \int \frac{1}{4.13 \times 10^{-6} p + 1.49 \times 10^3} dp \tag{11.6}$$

$$\rho(T = 20°C, p) = \frac{-5.88 \times 10^{10}}{p + 3.61 \times 10^8} + A \tag{11.7}$$

Note that A is an unknown constant at this point. A can be found by substituting a known value of density for a specific temperature and pressure. For this particular lubricant, when pressure is equal to 0 MPa and temperature is 20°C, density is 888 kg/m^3. As such:

$$A = \rho(T = 20°C, p = 0) + \frac{5.88 \times 10^{10}}{p + 3.61 \times 10^{8}} \tag{11.8}$$

$$A = 888 + \frac{5.88 \times 10^{10}}{0 + 3.61 \times 10^{8}} \tag{11.9}$$

$$A = 1050.84 \tag{11.10}$$

Substituting this value of A into Equation 11.7 gives:

$$\rho(T = 20°C, p) = \frac{5.88 \times 10^{10}}{p + 3.61 \times 10^{8}} + 1050.84 \tag{11.11}$$

Next, a relationship between density and temperature can be obtained via the following theoretical formula which may be found in literature:

$$\rho_1 = \frac{\rho_0}{1 + \beta(T_1 - T_2)} \tag{11.12}$$

The relevant material properties for this lubricant are:

$$\beta = 0.0007 \frac{1}{°C}$$

$$\rho_0 = 888 kgm^{-3} \; at \; 20°C, 0MPa$$

Therefore:

$$\rho(T, p = 0) = \frac{888}{1 + 0.0007(T - 20)} \tag{11.13}$$

Equations 11.11 and 11.13 are then combined:

$$\rho(T, p) = a + \frac{888}{1 + 0.0007(T - 20)} - \frac{5.88 \times 10^{10}}{p + 3.61 \times 10^{8}} \tag{11.14}$$

Note that a is an unknown constant. As before, this constant is found by substituting in a known value for density for a specific temperature and pressure:

$$\rho(T = 20°C, p = 0) = a + \frac{888}{1 + 0.0007(20 - 20)} - \frac{-5.88 \times 10^{10}}{0 + 3.61 \times 10^{8}} = 888 \tag{11.15}$$

$$a = \frac{-5.88 \times 10^{10}}{3.61 \times 10^{8}} \tag{11.16}$$

$$a = 162.85 \tag{11.17}$$

Substituting a into Equation 11.14 gives the final equation:

$$\rho(T, p) = 162.85 + \frac{888}{1 + 0.0007(T - 20)} - \frac{5.88 \times 10^{10}}{p + 3.61 \times 10^{8}} \tag{11.18}$$

APPENDIX E. Stage II Processing MATLAB Program

Primary Function

```
%% Batch Iterative OFT Finder. The 2nd stage processing software to
% calculate film thickness via the spring amplitude and phase models.
% Required input is .TDMS file type processed using
% "TDMS FMS Data Read and Analyse v1.1.1- One Rev".

tic %Start timer
[baseName, folder] = uigetfile('*.tdms','Select TDMS File to process');
fullFileName = fullfile(folder, baseName);
TDMSFile=TDMS_readTDMSFile(fullFileName);

%Extract phase and amplitude data from .TDMS files
for i=1:(length(TDMSFile.data)-1)/6
    PhaseUnsampled(1:length(TDMSFile.data{1, i*6}),i)...
       = TDMSFile.data{1, i*6} ;
end
for i=1:(length(TDMSFile.data)-1)/6
    SpringUnsampled(1:length(TDMSFile.data{1, (i*6)-1}),i)...
        = TDMSFile.data{1, (i*6)-1} ;
end
fileNames=TDMSFile.groupNames

%Recommended number of iteration is around 5 for Baxter Rig under
%Normal conditons.
NumberOfIterations=5; %Iterations to account for pressure
counter=1;
WidthOfArray=size(PhaseUnsampled,2);

%Spike remove attempts to get rid of false positives from resonances.
%1=yes, 0=no
spikeRemove=1;

%Generate Figures? 1=yes, 0=no
GenerateFigures=1;

%System Properties
z1=46000000; %Pin acoustic impedance (Rayls)
```

```
z2=24360000; %Bearing acoustic impedance (Rayls)
w=2*pi*7e6; %Sensor Angular Frequency (rad/s)
R=0.112/2; %Bearing Radius (m)
L=50.55/(1000);%Bearing Length (m)
loverd=L/(R*2); %Length over diamter
C = 45; %Radial clearance (microns)

%M is the proprtion of the cycle either side of the minimum value to ignore
%(intended to ignore "fake" min oft measurements from resonance peaks)
IgnoreProportion=0.1;

%Read file names to get test parameters
for ii= 1:length (fileNames)
    c=char(fileNames(ii));

    c=split(c,string('-'));
    rpm(ii)= str2double(c(5));
    Load(ii) = str2double(c(4));
    T(ii) = str2double(c(2));

end
%Test Parameters (Load not required)
U=(rpm*R*3.141)/(60); %Entraining Velocity
hminPhaseIterative=zeros(NumberOfIterations,WidthOfArray);
PMaxIterative=zeros(NumberOfIterations,WidthOfArray);
C2=0;
type='CN220';%Oil Type

%Make all columns in Phase change array the same length (sampling)
%Add zeros to end of array (because longest one needs a zero to detect)
PhaseUnsampled=[PhaseUnsampled;zeros(WidthOfArray)];
usPhase=zeros(length(PhaseUnsampled),WidthOfArray);

for n=1:WidthOfArray
X=PhaseUnsampled(:,n);
idx=find(X==0,1,'first');
X=X(1:idx-1);
X=resample(X,length(PhaseUnsampled),length(X));
usPhase(:,n)=X;
end

%Make all columns in Spring model array the same length (sampling)
SpringUnsampled=[SpringUnsampled;zeros(WidthOfArray)];

usSpring=zeros(length(PhaseUnsampled),WidthOfArray);
for n=1:WidthOfArray
X=SpringUnsampled(:,n);
idx=find(X==0,1,'first');
X=X(1:idx-1);
X=resample(X,length(SpringUnsampled),length(X));
usSpring(:,n)=X;
end

%Define size of arrays to be written into
```

```
density=zeros(length(usPhase),WidthOfArray);
c=zeros(length(usPhase),WidthOfArray);
densityNoPressure=zeros(1,WidthOfArray);
cNoPresssure=zeros(1,WidthOfArray);
hPhase=zeros(length(usPhase),WidthOfArray);
hSpring=zeros(length(usPhase),WidthOfArray);
hNoPressurePhase=zeros(length(usPhase),WidthOfArray);
hNoPressureSpring=zeros(length(usPhase),WidthOfArray);
nu=zeros(WidthOfArray,1);
pCentreAll=zeros(length(usPhase),WidthOfArray);

for a=1:WidthOfArray
    %Get rid of spikes in phase data caused by resonance (otherwise will
    %be mistaken for min phase oft). Done by identifying a sudden dip
    %(caused by resonance and removing some data either side of it).
    if spikeRemove==1
        [MinPhase,imin]=min(usPhase(:,a));
        usPhase(:,a)=circshift(usPhase(:,a),round((length(usPhase)/2))-imin);
        usSpring(:,a)=circshift(usSpring(:,a),round((length(usPhase)/2))-imin);
        [MinPhase,imin2]=min(usPhase(:,a));
        M=round(IgnoreProportion*length(usPhase(:,a)));
        usPhase(imin2-M:imin2+M,a)=0.01;

    end
    usphasemax=max(usPhase(:,a));
    PMax=0;

    % Find Oil Viscosity
    Tav = T(a)*1.8+32;
    cTemp=0.0039*T(a)*T(a)-3.6869*T(a)+1555.2+4.13*PMax;%speed of sound
    densityTemp=162.85+867/(1+0.0007*(T(a)-20))-(5.88e10)./...
        ((PMax*1e6)+(3.61e8));
    nu(a)=find_oil_viscosity(type,Tav,densityTemp)/1000;% in Pas

    % Find h when considering P
    for ii=1:NumberOfIterations-1
    c(ii,a)=-3.203*T(a)+1568.2;%speed of sound
    density(ii,a)=162.85+867/(1+0.0007*(T(a)-20))-(5.88e10)./...
        ((PMax*1e6)+(3.61e8));
    nu(a)=find_oil_viscosity(type,Tav,density(ii,a))/1000;% in Pas

    %Calculate Min OFT using Phase Change Method
    htop=(density(ii,a)*c(ii,a)*c(ii,a)*(z1*z1-z2*z2))*tan(usphasemax);
    hbottom1=w*z1*z2*z2;
    hbottom2=(w*z1*z2*z2)^2;
    hbottom3=(z1*z1-z2*z2)*((w*z1*z2)^2)*tan(usphasemax)*tan(usphasemax);

    hmin=htop/(hbottom1-sqrt(hbottom2-hbottom3));
    hminPhaseIterative(ii,a)=hmin;

    %Find Max Pressure
    [PMax]=Max_Pressure_Calculator(C,hmin,U(a),nu(a),loverd,R);
    PMaxIterative(ii+1,a)=PMax;
    end
```

```
PMaxIterative=PMaxIterative(1:length(PMaxIterative)-1);

% Use new hmin to work out pressure in axial centre of bearing
[pCentre]=Pressure_Distribution_Calculator(C,hmin,U(a),nu(a),loverd,R);

% rescale to length of usphase array
pCentre=resample(pCentre,length(usPhase),length(pCentre));
pCentreAll(:,a)=pCentre;

%find index for max phase and max pressures
[PMax,IPMax]=max(pCentre);
[usphasemax,IPhaseMax]=max(usPhase(:,a));

%use circshift to align max phase and min spring with max p
%(by shifting phase & spring)
usPhase(:,a)=circshift(usPhase(:,a),(IPMax-IPhaseMax));
usSpring(:,a)=circshift(usSpring(:,a),(IPMax-IPhaseMax));

%Set threshold for OFT values
threshold=C*(1e-6)*3;

%Calculate Min OFT using Phase Change Method

%First, accounting for pressure around bearing
for n=1:length(pCentre)

    c(n,a)=0.0039*T(a)*T(a)-3.6869*T(a)+1555.2+4.13*pCentre(n);
    density (n,a)=162.85+867/(1+0.0007*(T(a)-20))-(5.88e10)./...
        ((pCentre(n)*1e6)+(3.61e8));

    htop=(density(n,a)*c(n,a)*c(n,a)*(z1*z1-z2*z2))*tan(usPhase(n,a));
    hbottom1=w*z1*z2*z2;
    hbottom2=(w*z1*z2*z2)^2;
    hbottom3=(z1*z1-z2*z2)*((w*z1*z2)^2)*tan(usPhase(n,a))...
        *tan(usPhase(n,a));

    %If statement filters out obvious wrong values
    %(3 time radial clearance and negative values)

    if htop/(hbottom1-sqrt(hbottom2-hbottom3))<threshold && htop/...
            (hbottom1-sqrt(hbottom2-hbottom3))> 0
        hPhase(n,a)=htop/(hbottom1-sqrt(hbottom2-hbottom3));
    else
        hPhase(n,a)=threshold;
    end
end

%Second, NOT accounting for pressure (i.e p=0, which means c and
%density are conastant throughout)
cNoPresssure(a)=0.0039*T(a)*T(a)-3.6869*T(a)+1555.2+4.13*0;
densityNoPressure(a)=162.85+867/(1+0.0007*(T(a)-20))-(5.88e10)./...
    ((0*1e6)+(3.61e8));
```

```
for n=1:length(pCentre)
    %Phase model equation split up to make error checking easier
    htop=(densityNoPressure(a)*cNoPresssure(a)*cNoPresssure(a)*...
        (z1*z1-z2*z2))*tan(usPhase(n,a));
    hbottom1=w*z1*z2*z2;
    hbottom2=(w*z1*z2*z2)^2;
    hbottom3=(z1*z1-z2*z2)*((w*z1*z2)^2)*tan(usPhase(n,a))*...
        tan(usPhase(n,a));

%If statement filters out obvious wrong values
     if htop/(hbottom1-sqrt(hbottom2-hbottom3))<threshold && htop/...
         (hbottom1-sqrt(hbottom2-hbottom3))> 0
          hNoPressurePhase(n,a)=htop/(hbottom1-sqrt(hbottom2-hbottom3));
     else
          hNoPressurePhase(n,a)=threshold;
     end
end

%Calculate OFT using Spring Model
%First, accounting for pressure (note that c and density arrays have
%already been made in phase loop)
for n=1:length(pCentre)
    %Spring model equation split up to make error checking easier
    ha=(density(n,a)*c(n,a)*c(n,a))/(w*z1*z2);
    hb=(usSpring(n,a)*((z1+z2)^2)-((z1-z2)^2));
    hc=1-(usSpring(n,a)*usSpring(n,a));

    %If statement filters out obvious wrong values
    if ha*sqrt(hb/hc) <threshold && ha*sqrt(hb/hc) > 0
        hSpring(n,a)=ha*sqrt(hb/hc);
    else
        hSpring(n,a)=threshold;
    end
end

%Second, NOT accountign for pressure
for n=1:length(pCentre)
    %Spring model equation split up to make error checking easier
    ha=(densityNoPressure(a)*cNoPresssure(a)*cNoPresssure(a))/(w*z1*z2);
    hb=(usSpring(n,a)*((z1+z2)^2)-((z1-z2)^2));
    hc=1-(usSpring(n,a)*usSpring(n,a));

    %If statement filters out obvious wrong values
    if ha*sqrt(hb/hc) <threshold && ha*sqrt(hb/hc) > 0
        hNoPressureSpring(n,a)=ha*sqrt(hb/hc);
    else
       hNoPressureSpring(n,a)=threshold;
    end
end
% Display information about processing progress
fprintf('Just finished Processing Test #%d\n', counter);
fprintf('Tests Remaining #%d\n', WidthOfArray-counter);
toc
fprintf('\n')
```

```
    counter = counter + 1;
end

%Get minimum OFT values
[hminPhase,ihminPhase]=min(hPhase(:,:));
hminSpring=min(hSpring(ihminPhase-(round(length(hSpring)/20)):ihminPhase...
    +(round(length(hSpring)/20)),:));

%Find Sommerfeld Number
N=(rpm/60)';
ProjectedPressure=((Load*1000)/(L*2*R))';
CR=(R)/(C*10^-6);
SO = (CR^2).*nu.*N./ProjectedPressure;

%Raimondi Boyd Calculator
LD = L/(R*2);
RBFilm_thickness=zeros(1,WidthOfArray);
for n=1:length(SO)
    Film_thickness_ratio = find_film_thickness_ratio(SO(n),LD);
    hminRB (n)= (Film_thickness_ratio.*C)/(1000*1000);
end

%Calculate Angle Intervals
Angle=[0:(360/length(hPhase)):360];
Angle=Angle(1:length(hPhase));
Generate_FiguresB(SO,hminSpring,hminPhase,hminRB,hminPhaseIterative,Load,...
    rpm,T,hPhase,hNoPressurePhase,Angle,pCentreAll,NumberOfIterations);
```

Pressure Distribution Calculator

```
%%A Subfunction of Batch_Iterative_OFT Finder. This function is derived
%%from Engineering Tribology by A. W Batchelor and G. W. Stachowiak.

function [PCentre] = Pressure_Distribution_Calculator(C,hmin,U,nu,loverd,R)

% BEGIN OF INPUT DATA
% -------------------
%Bearing angle (360 degrees)
alpha = 360*pi/180;
%t is misalignment
t=0;
% SET MESH CONSTANTS
hmin=hmin*(1000*1000);
epsilon=1-(hmin/C);

inode=120;
jnode=120;
reslim1 = 0.0000001;
reslim2 = 0.000001;
factor1 =1.2;
factor2 =1;
nlim1 =1000;
```

```
nlim2 = 1000;

% END OF INPUT DATA
% -----------------
slender = 0.5/loverd; deltax = alpha/(inode-1); deltay = 1/(jnode-1);
% DIFFERENTIAL QUANTITIES FOR STABILITy CALCULATIONS
% INITIALIZE VALUES OF M(I,J), SWITCH(I,J) AND P(I,J)
M = zeros(inode,jnode); P = zeros(inode,jnode);
% SET INITIAL VALUE OF OFFSET ANGLE
beta = 0;
% ENTER ATTITUDE ANGLE ITERATION CYCLE, CALCULATE H, F AND G VALUES
n2 = 0; betas = 0; residb = reslim2 + 10;
while (residb > reslim2) & (n2 < nlim2),
    n2 = n2 + 1;
    for i = 1:inode,
        xaux = (i-1)*deltax + pi - 0.5*alpha; theta = xaux - beta;
        for j = 1:jnode,
            y = (j-1)*deltay - 0.5; h0 = y*t*cos(xaux) + ...
                epsilon*cos(theta) + 1;
            dhdx0 = -y*t*sin(xaux) - epsilon*sin(theta);
            d2hdx20 = -y*t*cos(xaux) - epsilon*cos(theta);
            dhdy0 = t*cos(xaux); d2hdy20 = 0;
            H(i,j) = h0; G(i,j) = dhdx0/h0^1.5;
            F(i,j) = 0.75*(dhdx0^2 + (slender*dhdy0)^2)/h0^2 + 1.5*...
                (d2hdx20 + d2hdy20*slender^2)/h0;
        end;
    end;
    coeff1 = 1/deltax^2; coeff2 = (slender/deltay)^2;
 % ----------------------------------------
 % SUBROUTINE TO SOLVE THE VOGELPOHL EQUATION
    sum2 = 0; n1 = 0; residp = reslim1 + 10;
    while (residp > reslim1) & (n1 < nlim1),
        n1 = n1 + 1; summ = 0;
        for i = 2:inode-1,
            for j = 2:jnode-1,
                store = ((M(i+1,j) + M(i-1,j))*coeff1 + (M(i,j+1)...
                    + M(i,j-1))*coeff2 -G(i,j))/...
                    (2*coeff1 + 2*coeff2 + F(i,j));
                M(i,j) = M(i,j) + factor1*(store-M(i,j));
                if M(i,j) < 0, M(i,j) = 0; end;
                summ = summ + M(i,j);
            end;
        end;
        residp = abs((summ-sum2)/summ); sum2 = summ;
    end;
 % ----------------------------------------
 % FIND PRESSURE FIELD FROM VOGELPOHL PARAMETER
    for i = 2:inode-1,
        for j = 2:jnode-1,
            P(i,j) = M(i,j)/H(i,j)^1.5;
        end;
    end;
 % ITERATION RESIDUAL ON ATTITUDE ANGLE ITERATION
 % CALCULATE TRANSVERSE AND AXIAL LOADS
```

```
 % ----------------------------------
 % SUBROUTINE TO INTERGRATE FOR FORCES
    for i = 1:inode,
        SUMY(i) = 0;
        for j = 2:jnode, SUMY(i) = SUMY(i) + P(i,j) + P(i,j-1); end;
        SUMY(i) = SUMY(i)*0.5*deltay;
    end;
    axialw = 0; transw = 0;
    for i = 2:inode,
        x = (i-1)*deltax + pi - 0.5*alpha; x2 = (i-2)*deltax...
            + pi - 0.5*alpha;
        axialw = axialw - cos(x)*SUMY(i) - cos(x2)*SUMY(i-1);
        transw = transw + sin(x)*SUMY(i) + sin(x2)*SUMY(i-1);
    end;
    axialw = axialw*deltax*0.5; transw = transw*deltax*0.5;
 % -------------------------
    loadw = sqrt(axialw^2 + transw^2); attang = atan(transw/axialw);
    if axialw > 0, attang1 = attang; end;
    if axialw < 0, attang1 = -attang; end;
    beta = beta + factor2*attang1; residb = abs((beta-betas)/beta);
    betas = beta;
 end;
% ----------------------------------------
% SUBROUTINE TO CALCULATE PETROFF MULTIPLIER
for j = 1:jnode, ICAV(j) = 1000; end;
for j = 2:jnode-1,
    for i = 2:inode,
        if (M(i,j) == 0) & (ICAV(j) == 1000), ICAV(j) = i; end;
    end;
end;
% EXTRAPOLATED VALUES OF ICAV(J) AT EDGES OF BEARING
ICAV(1) = 2*ICAV(2) - ICAV(3); if ICAV(1) < 1, ICAV(1) = 1; end;
if ICAV(1) > inode, ICAV(1) = inode; end;
ICAV(jnode) = 2*ICAV(jnode-1) - ICAV(jnode-2);
if ICAV(jnode) < 1, ICAV(jnode) = 1; end;
if ICAV(jnode) > inode, ICAV(jnode) = inode; end;
% CALCULATE FRICTION COEFFICIENT
% FIND VALUES OF DIMENSIONLESS SHEAR STRESS
for i = 1:inode,
    for j = 1:jnode,
        % CALCULATE dpdx FROM DOWNSTREAM VALUES
        if i > 1, dpdx = (P(i,j) - P(i-1,j))/deltax; end;
        % VALUE OF dpdx FOR i = 1
        if i == 1, dpdx = P(2,j)/deltax; end;
        if i < ICAV(j), TORR(i,j) = 1/H(i,j) + 3*dpdx*H(i,j); end;
        if i == ICAV(j), TORR(i,j) = 1/H(i,j); end; i10 = ICAV(j);
        if i > ICAV(j), TORR(i,j) = H(i10,j)/H(i,j)^2; end;
    end;
 end;
% INTEGRATE FOR TORR(i,j) OVER X AND Y
for i = 1:inode,
    % LINE INTEGRAL IN Y-SENSE
    SUMY(i) = 0;
    for j = 2:jnode, SUMY(i) = SUMY(i) + TORR(i,j) + TORR(i,j-1); end;
```

```
    SUMY(i) = SUMY(i)*0.5*deltay;
end;
friction = 0;
for i = 2:inode, friction = friction + SUMY(i) + SUMY(i-1); end;
friction = friction*0.5*deltax;
% ----------------------------
% CALCULATE DIMENSIONLESS FRICTION COEFFICIENT
myu = friction/loadw;
% SEARCH FOR MAXIMUM PRESSURE
pmax = 0;
for i = 2:inode-1,
    for j = 2:jnode-1,
        if P(i,j) > pmax, pmax = P(i,j); end;
    end;
end;
DimensionlessPMax=pmax;
% CALCULATE PRESSURE IN MPa
C2=C/(1000*1000);

p=(P*6*U*nu*R/(C2*C2))/(1000*1000);

%Find Max Pressure (MPa)
pmax2 = 0;
for i = 2:inode-1,
    for j = 2:jnode-1,
        if p(i,j) > pmax2, pmax2 = p(i,j); end;
    end;
end;
PMax=pmax2;

a=round(size(p)/2);
PCentre=p(:,a(1,2));
end
```

APPENDIX F. Derivation of Oil Film Gap Equations

The following is the full derivation method for the equations presented in Section 10.2.5. These equations allow the calculation of film thickness at any point around a bearing circumference given only minimum film thickness, attitude angle and film thickness at any another known angle. Note that values for clearance, bearing radius or shaft radius are not required. Also, this method assumes the geometries are perfectly circular, with no out-of-roundness due to deformation or machining tolerances

First, the distance between two eccentric circles at a given angle around the circumference may be approximated by the following sine function:

$$f(\phi) = A\ sin(\phi + k) + b \tag{11.19}$$

Where A is amplitude, ϕ is angle, k is x-offset and b is y-offset. This approximation is only applicable when $R_{shaft} >> C$, which is the case in practically all journal bearings. The accuracy of this approximation will be evaluated later in a worked example.

At this point A, k and b are unknown, therefore boundary conditions are required to obtain a solution. In this derivation minimum film thickness, attitude angle and film thickness at bearing top will be defined as known, which matches the directly measurable values from the BETTY test platform. These boundary conditions can be expressed mathematically as:

$$f(\theta) = h_{min} = A\ sin(\theta + k) + b \tag{11.20}$$

$$f(\phi_{top}) = h_{top} = A\ sin(\phi_{top} + k) + b \tag{11.21}$$

Where θ is attitude angle, h_{min} is minimum film thickness and h_{top} is film thickness at the top of the bearing.

The gradient at the point of minimum film is zero. Thus, taking the derivative of Equation 11.19 provides an additional boundary condition:

$$f'(\theta) = 0 = A\ cos(\theta + k) \tag{11.22}$$

Equation 11.22 may be rearranged to make k the subject:

$$0 = A\ cos(\theta + k) = cos(\theta + k)$$

$$\frac{(2n+1)\pi}{2} = \theta + k$$

$$k = \frac{(2n+1)\pi}{2} - \theta \tag{11.23}$$

This shows k has multiple solutions, with two solutions per complete revolution. This corresponds to one solution at minimum film and one at maximum film. The correct n value for a given case depends on how the axes are defined.

For journal bearings rotating in one direction, the attitude angle would not change by any more than $\pi/2$ radians. Thus, defining 0 radians as opposite to the loading vector and increasing in a clockwise direction means the minimum film will always occur at a greater angle than maximum film if the shaft is rotating clockwise, so n should equal 1. Conversely, if the shaft is rotating anti-clockwise minimum film angle will always be smaller than maximum film angle, so n should equal 0. Besides, using the incorrect value for n would result in a nonsensical result, making the mistake obvious.

Equation 11.23 can be substituted into Equation 11.20 to obtain:

$$h_{min} = A\ sin\left(\theta + \frac{(2n+1)\pi}{2} - \theta\right) + b$$

$$h_{min} = A\ sin\left(\frac{(2n+1)\pi}{2}\right) + b \tag{11.24}$$

Which can be rearranged to make b the subject:

$$b = h_{min} - A\ sin\left(\frac{(2n+1)\pi}{2}\right) \tag{11.25}$$

Similarly, Equation 11.23 can be substituted into Equation 11.21 to obtain:

$$h_{top} = A\ sin\left(\phi_{top} + \frac{(2n+1)\pi}{2} - \theta\right) + b \tag{11.26}$$

Substituting 11.25 into 11.26 gives:

$$h_{top} = A\ sin\left(\phi_{top} + \frac{(2n+1)\pi}{2} - \theta\right) + h_{min} - A\ sin\left(\frac{(2n+1)\pi}{2}\right) \tag{11.27}$$

This can be rearranged to make A the subject:

$$A = \frac{h_{top} - h_{min}}{sin\left(\phi_{top} + \frac{(2n+1)\pi}{2} - \theta\right) - sin\left(\frac{(2n+1)\pi}{2}\right)} \tag{11.28}$$

Worked Example

The following worked example is supplied to support understanding of the method and to demonstrate its accuracy. This example uses values typical to the BETTY test platform presented in Chapter 10.

The system geometry, along with values for minimum film thickness, attitude angle and film thickness at the top of the bearing, is shown in Figure 11.14. These values can be applied to Equations 11.23, 11.25 and 11.28 to obtain coefficients k, b and A respectively:

$$k = \frac{(2 \times 1 + 1)\pi}{2} + \frac{5\pi}{4} = 0.7854$$

$$b = 5 \times 10^{-6} - 4.511 \times 10^{-5} sin\left(\frac{(2 \times 1 + 1)\pi}{2}\right) = 5.011 \times 10^{-5}$$

$$A = \frac{82 \times 10^{-6} - 5 \times 10^{-6}}{sin\left(0 + \frac{(2\times1+1)\pi}{2} - \frac{5\pi}{4}\right) - sin\left(\frac{(2\times1+1)\pi}{2}\right)} = 4.511 \times 10^{-5} \tag{11.29}$$

Note that in this example minimum film occurs after the point of maximum film, therefore n is equal to 1, rather than 0. Coefficients k, b and A can now be applied to Equation 11.19:

$$f(\phi) = 4.511 \times 10^{-5} sin(\phi + 0.7854) + 5.011 \times 10^{-5} \tag{11.30}$$

This equation can now be used to find the film thickness at any angle around the bearing circumference. This is shown graphically in Figure 11.15. As previously discussed this method only provides an approximation, albeit a very accurate one. For comparison, the true circumferential film thickness is also plotted, along with the percentage error of the method. The reason for this difference is because Equation 11.19 is actually calculating the length of the line between the shaft and bearing which is normal to the bearing at a given angle, not the shortest distance between the bearing and the shaft at that angle. However, when $R_{shaft} >> C$ these values are practically identical.

These results can also be used to calculate radial clearance by averaging the minimum and maximum film thickness located on opposing sides of the bearing. In this example radial clearance is:

$$C = \frac{h_{min} + h_{max}}{2} = \frac{5 + 95.211...}{2} = 50.1055...\mu m \tag{11.31}$$

As true clearance is 50.1 μm, the error is 5.50 nm (0.011%) which can generally be considered negligible.

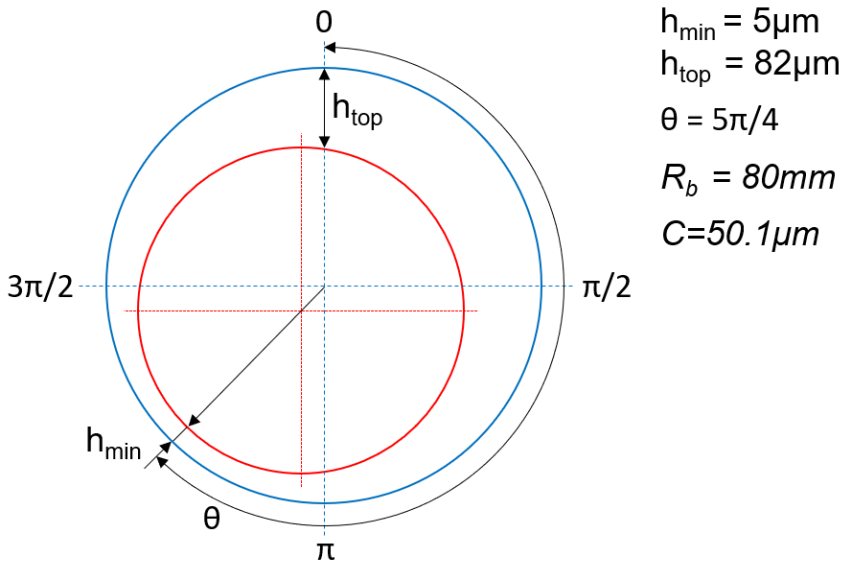

Figure 11.14: Shaft-bearing geometry used in worked example. Geometry is intentionally not to scale for clarity.

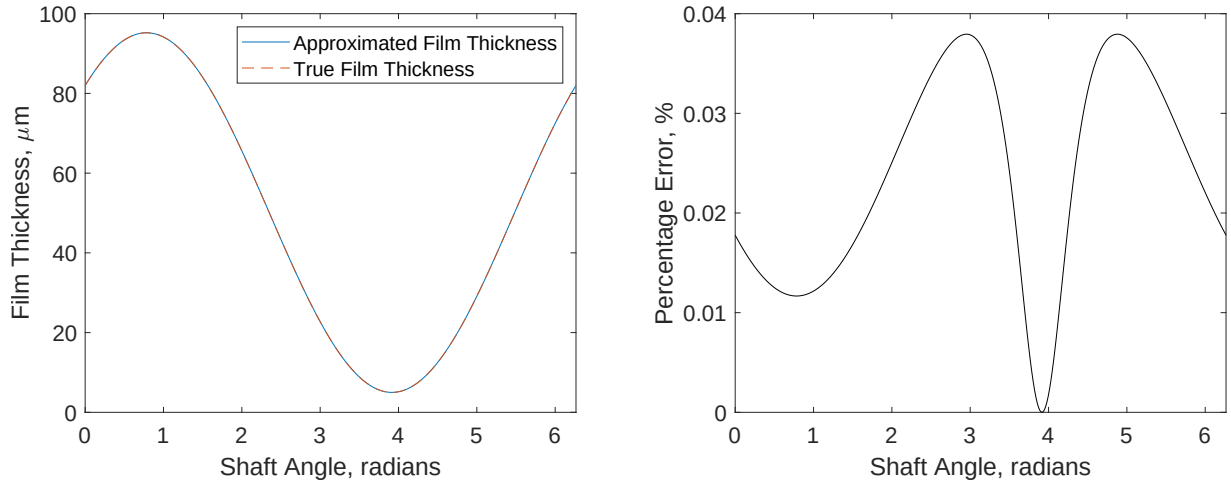

Figure 11.15: Circumferential film thickness using approximation method and from true geometry (left). Percentage error in approximation method around bearing circumference (right).